Coupling of soot oxidation and ammonia-mediated selective catalytic reduction of nitrogen oxides

POLITECNICO DI TORINO

RWTH AACHEN UNIVERSITY

Doctoral Dissertation
Doctoral Program in Chemical Engineering (33rd Cycle)

Erasmus Mundus Joint Doctorate Program within SINCHEM – Sustainable Industrial Chemistry framework

Coupling of soot oxidation and ammonia-mediated selective catalytic reduction of nitrogen oxides

Ferenc Martinovity

* * * * * *

Supervisors

Prof. Raffaele Pirone
Prof. Samir Bensaid, Co-Supervisor
Prof. Regina Palkovits, Co-Supervisor

Doctoral Examination Committee:

Prof. A.B. , Referee, University of….
Prof. C.D. , Referee, University of…
Prof. E.F. , Referee, University of….
Prof. G.H. , Referee, University of…
Prof. I.J. , Referee, University of….

Politecnico di Torino
March, 2021

Coupling of soot oxidation and ammonia-mediated selective catalytic reduction of nitrogen oxides

Der Fakultät für Mathematik, Informatik und Naturwissenschaften der RWTH Aachen University vorgelegte Dissertation zur Erlangung des akademischen Grades eines Doktors der Naturwissenschaften

vorgelegt von

Ferenc Martinovity, M. Sc. aus Senta (Zenta), Serbien

Berichter:

This thesis was written as a collaborative doctoral program within SINCHEM project and carried out at Politecnico di Torino, DISAT as Home institution and RWTH Aachen, ITMC, Chair of Heterogeneous Catalysis and Chemical Technology as Host institution.

This work was funded through a SINCHEM Grant. SINCHEM is a Joint Doctorate programme selected under the Erasmus Mundus Action 1 Programme (FPA 2013-0037).

I hereby declare that, the contents and organisation of this dissertation constitute my own original work and does not compromise in any way the rights of third parties, including those relating to the security of personal data.

…….....

Ferenc Martinovity

Turin, March 2021

Summary

Diesel engines present higher efficiency and fuel economy when compared to gasoline engines, however the emission of toxic pollutants, such as NO_x, particulate matter and unburned hydrocarbons present a serious health hazard. The removal of the NO_x is carried out through the selective catalytic reduction (SCR) with urea or hydrocarbons as reductant, while the particulate matter (soot) is removed by filtration followed by subsequent oxidation. One of the current state-of-the-art technologies for diesel pollution control in the automotive field is the integrated SCR and soot filtration on the so-called SCR on Filter (SCRoF) device. This thesis attempts to address some of the issues related to the coupling of the NO_x SCR and soot oxidation reactions.

Chapter 2 focuses on finding the proper soot oxidation catalyst that is highly active towards soot oxidation and does not interfere with the SCR reaction by oxidizing also the reductant NH_3. It was found that K_2CO_3 loaded on CeO_2-ZrO_2 was highly active for soot oxidation and when mixed with Fe-ZSM-5 SCR catalyst it did not interfere with the NO_x conversion.

Chapter 3 investigates in much more detail the simultaneous interaction of the SCR and soot oxidation catalyst. It is shown that the NO_x conversion over the SCR catalyst can be improved if the soot oxidation catalyst is also active for NO to NO_2 oxidation. The CeO_2-PrO_2 catalyst impregnated with low amount potassium was used as soot oxidation catalyst that was physically mixed with Fe and Cu-ZSM5 and the w/f through the catalyst bed was maintained constant. In such mixtures the soot oxidation temperature was reduced by 150 °C and the SCR reaction improved

In Chapter 4 the hydrocarbon poisoning of Cu-SSZ-13 was investigated and an effective solution proposed. A zeolite and mixed oxide “Composite” catalyst was made by ball-milling Cu-SSZ-13 and CeO_2-SnO_2 in 4:1 mass ratio. In the presence of 700 ppm C_3H_6 as model hydrocarbon the SCR reaction over Cu-SSZ-13 was markedly inhibited, while the Composite catalyst was resistant towards deactivation.

Chapters 5 and 6 involve the development and investigation of $LaCoO_3$ catalyst for NO oxidation and soot oxidation as potential replacement for Pt-based catalysts. The optimal perovskite, $LaCo_{0.75}Al_{0.25}O_3$, obtained through a sol-gel method and calcination at 700 °C, could reach NO_2/NO_x ratio of 0.8 at 300 °C and was shown to be comparable to the Pt/Al_2O_3 catalyst. The SO_2 poisoning took place in 2 stages, in the first stage the SO_2 strongly adsorbed and blocked the active sites for NO oxidation and in the second stage lanthanum sulphates grew on the catalyst surface.

Sommario

I motori diesel presentano un elevata efficienza e risparmio di combustibile rispetto ai motori a benzina. Tuttavia, l'emissione di inquinanti tossici come gli NO_x, particolato ed idrocarburi incombusti rappresenta un pericolo serio per la salute. L'eliminazione degli NO_x avviene attraverso la riduzione selettiva catalitica (ovvero Selective Catalytic Reduction in inglese "SCR") con l'urea o degli idrocarburi come riducenti, mentre che il particolato (soot) viene rimosso attraverso filtrazione e successiva ossidazione. Nello stato dell'arte, una delle tecnologie per il controllo di inquinamento diesel nel settore automotive è l'SCR e filtrazione di soot integrati nel dispositivo denominato "SCR on filter" (SCRoF). Questa tesi affronta alcune delle problematiche correlate all'accoppiamento delle reazioni di SCR di NO_x e ossidazione del soot.

Il Capitolo 2 è focalizzato nel ritrovamento di un catalizzatore adatto per l'ossidazione del soot che sia abbastanza attivo nella suddetta ossidazione e che non interferisca con la reazione SCR ossidando pure l'NH_3, ossia il riducente. È stato trovato che l'inserimento del K_2CO_3 nella CeO_2-ZrO_2 favorisce una elevata attività nell'ossidazione del soot e che quando va aggiunto al catalizzatore per SCR Fe-ZSM-5 non interferisce nella conversione degli NO_x.

Capitolo 3 si investiga nel dettaglio l'interazione che avviene tra i catalizzatori per l'SCR e l'ossidazione del soot. È stato osservato che la conversione di NO_x sul catalizzatore SCR può essere migliorata se il catalizzatore per l'ossidazione del soot è anche attivo nell'ossidazione di NO verso NO_2. Il catalizzatore CeO_2-PrO_2 impregnato con una piccola quantità di potassio è stato utilizzato come catalizzatore per l'ossidazione del soot è stato mischiato fisicamente con le Fe e Cu-ZSM5 e la W/F attraverso il catalizzatore mantenuta costante. Nelle suddette miscele di catalizzatori. La temperatura per l'ossidazione del soot è stata ridotta di 150 °C e la reazione SCR è stata migliorata.

L'avvelenamento della Cu-SSZ-13 con degli idrocarburi, è stato investigato nel Capitolo 4 e una soluzione effettiva è stata proposta. Nel mulino a sfere, è stato preparato un catalizzatore "composito" di zeolite ed ossido misto inserendo Cu-SSZ-13 e CeO_2-SnO_2 con rapporto massico 4:1. Tuttavia, si è osservato che in presenza di 700 ppm di C_3H_6 (usato come modello di idrocarburo) la reazione SCR sulla Ce-SSZ-13 è inibita notevolmente, mentre che il catalizzatore composito si è mostrato resistente alla disattivazione.

I Capitoli 5 e 6 includono lo sviluppo e investigazione del catalizzatore $LaCoO_3$ per l'ossidazione di NO e soot e come potenziale sostituto deo catalizzatori a base di Pt.. La perovskite ottima, ossia la $LaCo_{0.75}Al_{0.25}O_3$ preparata attraverso il metodo sol-gel e calcinata a 700 °C, ha raggiunto un rapporto di 0.8 tra NO_2/NO a 300 °C ed ha mostrato di essere paragonabile al catalizzatore Pt/Al_2O_3. L'avvelenamento con SO_2 è avvenuto in 2 step. Nel primo step è avvenuto l'adsorbimento forte dell'SO_2, bloccando i siti attivi per l'ossidazione di NO, mentre nel secondo step è avvenuto l'accrescimento di solfati di lantanio sulla superficie del catalizzatore.

Auszug

Dieselmotoren präsentieren höhere Effizienz und Kraftstoffverbrauch, wenn zu Benzinmotoren im Vergleich, aber die Emission von toxischen Schadstoffen wie NOx, Partikelmasse und verbrannte Kohlenwasserstoffe stellt eine ernsthafte Gefahr für die Gesundheit. Die Entfernung des NOx wird durch die selektive katalytische Reduktion (SCR) mit Harnstoff oder Kohlenwasserstoffe als Reduktionsmittel durchgeführt wird, während die Partikelmasse (Ruß) durch Filtration, gefolgt von anschließender Oxidation entfernt wird. Eine der modernsten Technologien zur Kontrolle der Dieselverschmutzung im Automobilbereich ist die integrierte SCR- und Rußfiltration auf dem sogenannten SCR am Filter (SCRoF)- Gerät. Diese These versucht, einige der Probleme zu lösen, die mit der Kopplung der NOx-SCR- und Rußoxidationsreaktionen zusammenhängen.

Kapitel 2 konzentriert sich auf die Suche nach dem richtigen Rußoxidationskatalysator, der gegenüber Rußoxidation hochaktiv ist und die SCR-Reaktion nicht durch Oxidation auch des Reduktionsmittels NH_3 stört. Es wurde gefunden, dass auf CeO_2-ZrO_2 beladenes K_2CO_3 für die Rußoxidation hochaktiv war und beim Mischen mit Fe-ZSM-5 SCR-Katalysator die NOx-Umwandlung nicht störte.

In Kapitel 3 die gleichzeitige Wechselwirkung von SCR und Rußoxidationskatalysator viel detaillierter untersucht. Es wird gezeigt, dass die NOx-Umwandlung gegenüber dem SCR-Katalysator verbessert werden kann, wenn der Rußoxidationskatalysator auch für die Oxidation von NO zu NO_2 aktiv ist. Der mit einer geringen Menge Kalium imprägnierte CeO_2-PrO_2-Katalysator wurde als Rußoxidationskatalysator verwendet. Der Rußoxidationskatalysator wurde physikalisch mit Fe und Cu-ZSM5 gemischt und das w/f durch das Katalysatorbett wurde konstant gehalten, dass heißt. In solchen Gemischen wurden die Rußoxidationstemperatur wurde um 150 °C verringert und die SCR-Reaktion verbessert.

In Kapitel 4 wurde die Kohlenwasserstoffvergiftung von Cu-SSZ-13 untersucht und eine wirksame Lösung vorgeschlagen. Ein Zeolith- und Mischoxid- "Verbund" - Katalysator wurde durch Kugelmahlen von Cu-SSZ-13 und CeO_2-SnO_2 im Massenverhältnis 4: 1 hergestellt. In Gegenwart von 700 ppm C_3H_6 als Modellkohlenwasserstoff die SCR-Reaktion über Cu-SSZ-13 deutlich gehemmt, während der Verbundkatalysator gegen Deaktivierung resistent war.

Die Kapitel 5 und 6 befassen sich mit der Entwicklung und Untersuchung des $LaCoO_3$-Katalysators für die NO-Oxidation und Rußoxidation als möglichen Ersatz für Katalysatoren auf Pt-Basis. Der optimale Perowskit $LaCo_{0.75}Al_{0.25}O_3$, der durch ein Sol-Gel-Verfahren und Kalzinieren bei 700 °C erhalten wurde, konnte bei 300 °C ein NO_2/NO_x -Verhältnis von 0,8 erreichen und erwies sich als vergleichbar mit dem Pt/Al_2O_3 -Katalysator. Die SO_2-Vergiftung erfolgte in 2 Stufen, in der ersten Stufe adsorbierte und blockierte das SO_2 die aktiven Stellen stark für die NO-Oxidation und in der zweiten Stufe wuchsen Lanthan-Sulfate auf der Katalysatoroberfläche.

Acknowledgment

This thesis is the result of the research performed between 2017-2020 at Politecnico di Torino and RWTH Aachen. First, I wish to express my gratitude to my supervisors Prof. Raffaele Pirone, Prof. Samir Bensaid and Prof. Regina Palkovits for the unique opportunity to work in their research groups and constant support during the thesis. This work owes much also to Prof. Fabio Alessandro Deorsola, Dr. Tahrizi Andana, Prof. Barbara Bonelli and Prof. Marco Armandi who, together with the supervisors, were always available for solving issues of practical and theoretical matters and open discussions. I would like to thank Prof. Stefania Albonetti and Prof. Francesco di Renzo for the management, dedication and organization of the SINCHEM programme and the school every year. I would like to thank my former mentors Prof. Goran Bošković, Prof. Radoslav Mićić, Dr. Ferenc Kiss and Prof. Radovan Omorjan for teaching me about catalysis, how to think critically and encouraging me to carry out reseach abroad and the improtance of scientific mobility for personal and scientific development.

I am grateful for the constant assistance in the laboratory and for the fruitful discussions with my co-workers both at Polito and ITMC, especially those who worked in Blunox lab: Miguel Marin, Freddy Liendo, Melodj Dosa, Enrico Sartoretti and Fabio Salomone. I would like to thank especially to Tran Quang Nguyen from ICG Montpellier for our fruitful collaboration, chapters 5 and 6 are based on our joint research. I have received also constant support from Kristine Tolod, Samantha Molina Gutierrez, Paola Blair Vasquez, Valeria Maslova, Daniel Bulla, Ulisse Montanari, Payal Baheti, Wei Hua, Medet Zukush, Ana Pacheco, Marcello Favaro and other SINCHEM PhD students whom I had pleasure meeting. The published chapters were all revised by unknown reviewers who corrected the manuscripts and often had constructive comments or suggestions for improvements, their valuable contributions are acknowledged.

Finally, I would like to thank my parents, brother and sister for enabling a happy and carefree childhood, despite the historical circumstances. My wife Jelena and my son Lazar for their love and boundless support during the PhD.

Contents

List of Figures

Chapter 1

1. Pollutants, issues and pollution abatement technologies

Chapter summary

The problem of the engine emissions and the pollutants are shortly presented here along with their effects on human health, their formation during the combustion process and the limits that are regulated. The diesel engine aftertreatment configuration, the role of each unit and the relative catalysts used are described and discussed. The wide variety of catalytic options available for the soot oxidation and NO_x reduction are presented with their respective advantages, disadvantages and areas of application. The functioning, phenomena and issues related to SCRoF are presented and discussed.

1.1 Emissions and regulations

Internal combustion engines invariably emit pollutants during operation. Two engine types most commonly used today, whether mobile or stationary, are the gasoline engines (based on the Otto cycle) and Diesel engines. The pollutants of concern are carbon monoxide (CO), volatile organic or hydrocarbon compounds (VOC or THC), nitrogen oxides (NO, NO_2 or their sum NO_x), sulphur oxides (SO_2, SO_3, SO_x) and the combination of particulate matter (PM) and naphthalene colloquially called “soot”. The mentioned pollutants are toxic, especially to the respiratory organs and aggravating existing chronic conditions such as asthma or bronchitis. The estimated daily adjusted life years lost through the world is, on average, 2 years, significantly higher than cancer and other medical conditions [1–4]. Air pollution is however not distributed evenly since higher population density urban conglomerations are affected more than rural areas. Furthermore, the distribution of air pollution is coupled with economic disparities: less developed countries have lower access to more advanced engine and aftertreatment technologies that in turn leads to lower air quality. Further factors contributing to these phenomena are rapid urbanization, without appropriate infrastructure development, that we can currently observe in some developing regions [5–7]. Indeed, according to the WHO report on the most polluted cities around the world 9 out of the top 10 cities with worst air pollution are located in India (Figure 1.1) [8].

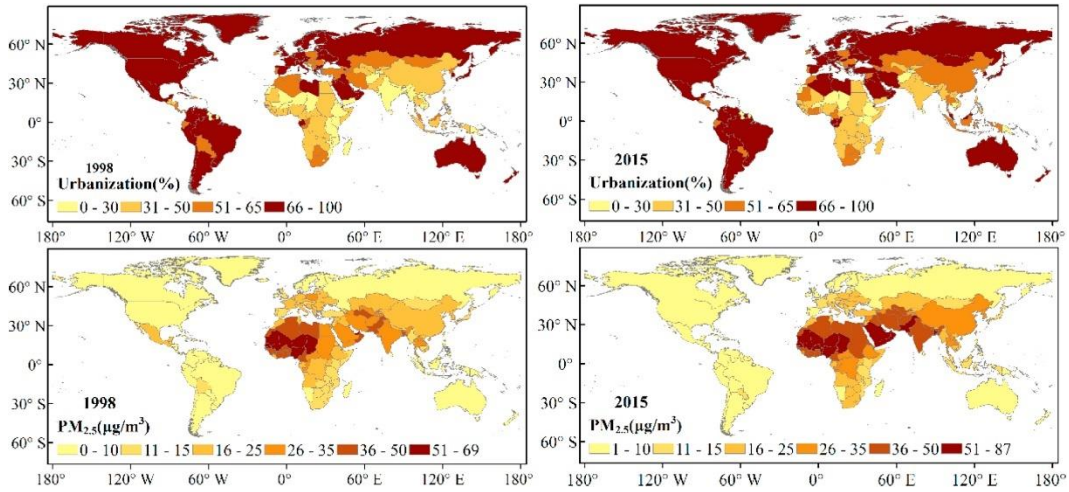

Figure 1.1. Correlation between urbanization rate and PM 2.5 emissions. Adapted from [9]

For these reasons ever more stringent emission limits are introduced since the 1990s. Different regulations are implemented worldwide, however the spearheading regulations are introduced in EU, USA and Japan. The limits imposed by these regulations are equivalent with minor differences, partly due to economic reasons and market/standard compatibility. The latest reference standard is Euro 6, first introduced in 2014 and updated to Euro 6d in 2020 [10–14].

Besides emission limits, the testing method is of paramount importance since it is difficult to ensure that the recorded emissions in the driving cycle tests, which last 10-20 minutes, match that of on-road emissions. One of the earliest testing procedures was introduced in the 1970s, and the NEDC and FTP tests were the standard ones for long time in Europe and USA, respectively. It is questionable how much the short testing procedure reflect emissions of real driving conditions. Deviations were quickly recognized, and the testing protocols are regularly updated. In 2015 the UN developed the world harmonized light-duty vehicles test procedure (WLTP) for increased standardization of the velocity profiles during testing, the test procedure and vehicle setup, environmental conditions, fuel properties, measurement error tolerance, etc [11,14–18]. Depending on the intended use of the vehicle, different WLTP classes are available, these are:

-Class 3 for low, medium, high and extra high engine loads for simulation of urban, extra-urban, rural and highway conditions.

-Class 2 for low, medium and high velocities.

-Class 1 for low and medium velocities.

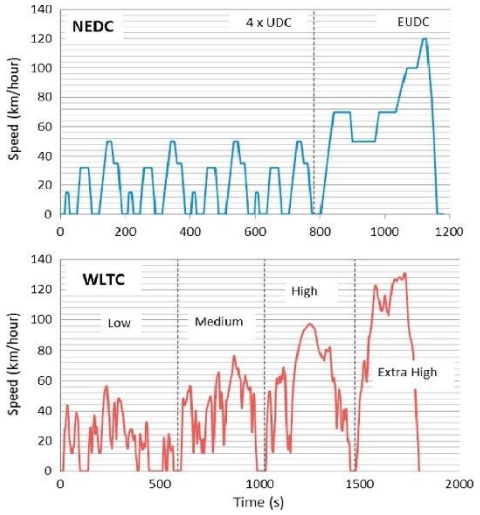

Parameters	NEDC	WLTC
Duration (s)	1180	1800
Distance (km)	11.03	23.27
Average speed (km/h)	33.6	46.5
Maximum speed (km/h)	120.0	131.3
Stop duration (%)	23.7	12.6
Constant driving (%)	40.3	3.7
Acceleration (%)	20.9	43.8
Deceleration (%)	15.1	39.9
Average positive acceleration (m/s^2)	0.59	0.41
Maximum positive acceleration (m/s^2)	1.04	1.67
Average positive "speed*acceleration" (m^2/s^3)	1.04	1.99
Maximum positive "speed*acceleration" (m^2/s^3)	9.22	21.01
Average deceleration (m/s^2)	-0.82	-0.45
Minimum deceleration (m/s^2)	-1.39	-1.50

Figure 1.2. Comparison of the main parameters and velocity profiles of NEDC and WLTC. Adapted from [17]

The different classes are of interest for the catalyst development since the engine load determines the exhaust temperature. The catalysts for the NO_x or soot control must be adapted for the most frequently expected temperature and pollutant concentration in the aftertreatment unit as well as they must account for the potential exotherms.

This mismatch and very strict emission limits were the primary reason of the diesel emission testing scandal, “Dieselgate”, where Volkswagen – and other manufacturers as well – optimized the aftertreatment system, catalyst, software and control for the best performance in the driving cycle testing and neglected the realistic conditions. This resulted in a misconception that diesel engines are more polluting than gasoline engines, which is true if we consider only the engine-out pollutant concentrations [19]. With proper aftertreatment the diesel emissions are in-fact less polluting than gasoline emissions.

1.2. Pollutant formation and sources

Formation of NO_x: NO_x are formed from the N_2 in air mainly during the combustion process and a lower amount originate from the nitrogen contained in the fuel. Their formation is favoured at cylinder temperature above 1600 °C and in oxygen rich conditions. The origination of in-cylinder NO_x is disputed, and several mechanisms are proposed. One mechanism involves the formation of nitrogen radicals through the -OH* radical transfer from the combustion mixture. The N* can subsequently reform either into N_2 or NO_x. Another mechanism is through organonitrogen compounds that release NO_x upon combustion. In any case, the thermodynamic equilibrium of $N_2 + O_2 \leftrightarrow 2NO$ suggests that NO formation is not possible under the temperature of 1400 °C [20–24]. The NO_2

emission can indirectly trigger ozone formation through the interaction with hydrocarbons and UV irradiation [25].

Since gasoline engines typically operate in stochiometric conditions ($\lambda = 1$) the reduction of NO_x to N_2 is easier to perform. Diesel engines typically operate in lean conditions ($\lambda = 1.4$) and the exhaust gas is oxygen rich which makes the NO_x reduction challenging. NO_x emissions can be reduced by engine modifications, most commonly by recycling the exhaust gas (EGR) which reduces the in-cylinder combustion temperature and the NO_x formation. This comes at a cost since the soot emissions are increased in this manner. EGR is typically not enough to reach the latest NO_x emission standards and further abatement of the exhaust gas is required [26].

Hydrocarbon emissions: hydrocarbons in the exhaust stream originate from the unburnt fuel and lubricant. Their concentration and molecular composition can vary greatly, ranging from light olefins and paraffins to high molecular weight naphthalene and other polycyclic aromatic hydrocarbons (PAH). Hydrocarbon emissions are more of concern in gasoline engines when the combustion occurs in oxygen poor conditions and are of less concern in diesel engines. Their concentration in the diesel exhaust is still noticeable and must be considered in the design of the aftertreatment system configuration since they can poison the downstream catalysts and influence their operation [11,18,27].

Carbon monoxide: CO is emitted when the fuel is combusted in rich conditions, hence in diesel engines it is of less concern and the concentration is much less when compared to CO concentration in gasoline engines (ca. 0.1% vs 2%). In the diesel exhaust CO is found in consistent low concentration (ca 100-1000 ppm) with occasional spikes (up to 1%) that occur under non-ideal conditions, such as sudden changes in engine load, cold start, etc [12,28].

Formation of SO_2: SO_2 is formed during the combustion of organosulfur compounds found in the fuel. The content of sulphur in the diesel fuel is regulated by local standards and it is typically set at maximum of 10 ppm. Some exceptions exist where low-cost high-sulphur diesel fuel (also known as “bunker fuel”) is permitted, most notably in the maritime transport since naval vessels are typically far from population centres to cause health issues. Despite its high toxicity, it is not directly regulated by the emission standards, but indirectly by setting its maximum concentration in the fuel. Furthermore, the SO_2 is a strong poison to most of the aftertreatment catalysts and meeting the NO_x limits would not be possible if the SO_2 concentration was high [29,30].

Formation of particulate matter/soot: soot is formed as a result of the partial combustion and pyrolysis polymerization of the diesel fuel and unburnt lubricant. There is typically a trade-off between the NO_x and soot emissions. At high cylinder temperatures the soot is fully combusted however the NO_x formation is enhanced and vice-versa at lower temperatures (Figure 1.2) [22,31–34]. The soot composition can vary greatly depending on the engine operation parameters, the quality of fuel, additives, lubricants, etc., and the mass ratio between the graphitic carbon, volatile organic compounds (VOCs) and ash that compose the PM can vary in a wide range. The ash originates from the lubricant

additives and its main component is $CaSO_4$, its mass ratio is typically around 0-5 wt%. VOCs are mostly composed of high molecular weight aliphatic or PAHs that vaporize in the temperature region 300-400 °C and contributes ca 5-25 wt% to the soot mass [35–37]. The toxicity of soot depends not only from its composition, but also from the size. For this reason, the regulations limits are the aerodynamic diameter of the particulates PM10 and PM2.5 where the number represents the median diameter in μm. The pathogenicity and final effects on health is not fully understood, however it has been shown that soot enters the lungs where it inhibits the oxygen uptake. Furthermore, the PM2.5 are of greater concern since the smaller particles can enter the bloodstream and induce inflammation [1,3,38].

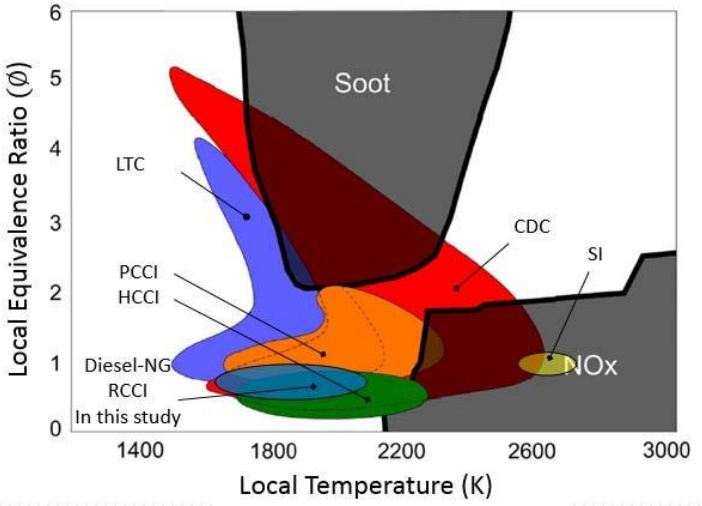

Figure 1.3. Emission map of the dependence of soot and NO_x formation from the combustion temperature and equivalence ratio. Adapted from [39].

1.3. Diesel pollutant treatment system and reduction methods.

1.3.1. General structure and components of the aftertreatment system

The aftertreatment system of the pollutants emitted by the diesel engine is complex, typically consisting of several “bricks” with different functionalities. The units are structured monoliths with channel width of several hundred μm or alternatively metallic foams or nets, each with its unique advantages/disadvantages. The monoliths are produced by extruding the ceramic paste through shaped moulds.

The monoliths must be made of materials that are resistant to high temperatures, thermal and mechanical stress, chemically inert and have low thermal expansion coefficient. They are typically made of cordierite or SiC with various additives. After extrusion, the catalyst together with appropriate binder (e.g. boehmite) are washcoated onto the monolith. It is desirable that the coating adheres strongly and

is uniformly distributed so that diffusional limitations are minimized. Thinner monolith walls are desirable from the pressure drop and diffusional point of view, however thin walls are prone to structural weaknesses [40,41].
The monolith can have all the channels open on both sides ("flow-through" configuration) or consequently plugged on alternating ends to force the gas through the porous material thereby performing filtration ("wall-flow" configuration). Since a high resistance to the exhaust flow results in power and fuel losses, the main goal of the shaping is to minimize the pressure drop of the exhaust without compromising the catalytic performance [40,41].
In general, the design and development for the automotive catalysis is different from conventional catalytic reactors, that is well established in petrochemical or pharmaceutical industry, where constant or controllable temperature is set, the feedstock composition is predictable and constant for extended periods. The automotive converters need to operate in wide temperature range (100-700 °C), with rapidly changing and relatively unpredictable temperature and exhaust pollutants composition. The aftertreatment reactor types and the choice of the catalyst for NO_x reduction and soot oxidation depends from variety of factors, such as engine configuration, intended use (urban, highway, railway etc), rated power etc. and no single, universal solution exists.
The main sections, catalysts and different configuration options of the aftertreatment unit are the following:
1. Diesel oxidation catalyst (DOC): The main purpose of the DOC is to oxidize CO, unburnt hydrocarbons and NO to NO_2 oxidation to improve the downstream processes. Most used catalysts are based on platinum group metals (PGMs, mainly Pt-Rh) since they offer superior performance and relatively high stability. The PGMs are impregnated on high surface area, thermally stable support, typically γ-Al_2O_3 with promoters (e.g. La_2O_3, CeO_2) to prevent agglomeration and phase transition that results in drastic loss of surface area. Typical PGM loadings are between 70-450 g/m^3 which means that the DOC cost can be very high. In order to reduce the DOC cost, substitutes for the PGM have been proposed, most notably lanthanum based doped $LaMnO_3$, $LaCoO_3$ $LaFeO_3$ and La_2CuO_4 perovskites [42–45].
2. Particulate matter removal section: Particulate matter is removed on monolith diesel particulate filters (DPF) by accumulating it in a filter cake form. During soot accumulation the backpressure and resistance to gas flow increases and periodic regeneration is required to burn off the soot. This is commonly achieved by injecting additional fuel to reach the temperature required for rapid soot oxidation. The exotherm generated by the rapid soot oxidation can raise the temperature by several hundred degrees and potentially damage the filter. Many studies have been published about the exotherm evolution and the thermal front expansion during the regeneration and its control and avoiding local hot spots still represents a challenge. Soot oxidation catalysts can be added on the filter (catalysed DPF, cDPF) to enhance the passive oxidation of soot during normal operation and delay or avoid active regeneration [46–49]. The cDPF can be used only when the NO_x levels and the temperature are appropriate and it is typically

limited to heavy duty diesel (HDD) applications, where the aftertreatment temperature is most of the time between 250-350 °C. In contrast, for light duty diesel (LDD) and low load applications the temperature is typically between 200-300 ° C that is not enough for passive regeneration, and in these cases active regeneration is preferable [47,50].

3. NO_x reduction section: DPF is typically followed by a selective catalytic reduction (SCR) section for the reduction of NO_x to non-toxic N_2. The NO_x decomposition to N_2 is thermodynamically favoured, however kinetically limited. Direct decomposition of NO_x to N_2 is practically impossible since the presence of O_2 and H_2O in the exhaust further inhibits the reaction. Reductants are used to promote the catalytic NO_x reduction, and the most used are NH_3 and hydrocarbons ranging from light to heavy alkanes and alkenes. Others, such as H_2, ethanol and CO, are also suggested in literature, however they have never been implemented for widespread use due to their poor performance. For each type of reductant different catalysts are used, each one having certain advantages/disadvantages [10,51–57].

4. Additional equipment: There are many associated ancillary components in the aftertreatment system. Sensors are typically installed to continuously monitor key parameters such as temperature, NO_x and NH_3 emissions, pressure drop, lambda sensor, etc. These parameters are transmitted to the on-board controllers for adjustments. Careful calibration of the control, response and prediction models are required to ensure optimal performance and avoid the issue of pollutant cross-sensitivity. More and higher quality sensors can provide better information and aftertreatment system efficiency at the expense of increased cost [58–60].

Other vital component is the reductant injector, which has to ensure timely response and dosing. The reductant injected must be evenly mixed before the converter inlet to ensure high dispersion, evaporation and accessibility for the catalyst. The injection rate and pulses, shape of the static mixers, etc. are subject of numerous CFD optimization studies since the performance of the downstream treatment units are highly dependent on the injector-mixer efficiency [61,62].

1.3.2. Particulate matter oxidation catalysts

The oxidation of the particulate matter on the filter can be enhanced by a variety of catalysts to reduce the pressure drop increase. The main issue is that there is a mismatch between the soot oxidation temperature in O_2 (400-700 °C) and the typical diesel exhaust temperature (200-400 °C). The soot oxidation temperature can be lowered by catalytically increasing the NO_2/NO_x ratio since NO_2 is a much stronger oxidant for soot and can initiate soot oxidation as low as 250 °C based on reactions R1-2 [37,47,63].

$C + NO_2 + O_2 \rightarrow CO_2 + CO + NO$ R1

$2\ NO + O_2 \rightarrow NO_2$ R2

The current state-of-the-art cDPF rely on this mechanism and utilize Pt/Al_2O_3 based catalysts with high NO to NO_2 oxidation activity, although $LaMO_3$ (M= Co, Mn, Fe) perovskites have been suggested as low-cost alternatives due to comparable activity. The oxidation reaction is indirect, i.e. the NO is oxidized to NO_2 and reacts with the soot from the gas phase and this increases the range of effectiveness since the catalyst does not have to be in direct contact with the soot. The reaction rate between gaseous NO_2 and soot is rather slow and only a portion of the NO_2 generated can be utilized for the oxidation. Another limitation of this approach is that the levels of NO_x in the exhaust stream and temperature are not always high enough for effective oxidation [47,64,65].

However, for some catalysts it has been demonstrated that the NO_2-soot oxidation reaction can be catalytically enhanced by alkali metal or silver doping [66]. The adsorbed NO_3^- can react with soot directly from the catalyst in the adsorbed nitrate form, rather than desorbing and reacting indirectly from the gas phase. In this way almost all the NO_2 can be utilized for the soot oxidation [54,67–69].

To overcome the issue of limited concentration of NO_2 in the exhaust, catalysts have been developed to enhance the catalytic oxidation of soot with O_2. Many different types of catalysts can be found in the literature and they can be broadly classified in the following groups:

1. Silver-based soot oxidation catalysts: catalysts based on Ag exhibit some of the best O_2-assisted soot oxidation performances found in the literature. Silver is impregnated on a suitable carrier and the choice of the support is important since it determines the oxidation state, oxygen transfer rate, and the surface availability of silver. Some of the best performing supports are CeO_2, ZrO_2, SnO_2 and Al_2O_3, while supports with small pores, like zeolites, are not appropriate since ionic silver is not active for soot oxidation. The optimal silver loadings reported are between 5-10 wt% since this ensures the abundance of Ag_2O and Ag, while lower loadings favour Ag^+ and $Ag^{\delta+}$ which are highly dispersed resulting in a lack soot oxidation capability [56,70–73].

It is suggested that the remarkable performance of silver is derived from its ability to generate highly active superoxide O_2^{2-}. These radicals have long range and they are equally effective when mixed in loose contact with soot. It has been demonstrated that the activated oxygen has a long range of action and can enhance the oxidation of soot even when physically separated with an ash barrier few hundred μm wide. Other advantages of silver-based catalysts for use on cDPF are high stability, high activity towards the total oxidation of hydrocarbons, CO and NO, as well as some activity in NO reduction with hydrocarbons in lean conditions [56,70–72].

2. Alkali metal-based soot oxidation catalysts: Alkali metals have been shown as very active catalysts for soot oxidation with O_2. They can also promote the NO_2-soot reaction since the adsorbed nitrates become highly active for soot oxidation and during NO_2-assisted soot oxidation promoted with potassium the NO_2/NO_x quickly reduces close to 0. The oxidation mechanism is disputed in the literature. The prevailing theory suggests charge transfer through reactive molecules such as O_2^{2-}, CO_3^{2-}, NO_3^- etc, which activates the soot for oxidation

(R3), while halides passivize the catalyst, e.g. KCl is inactive. The choice of support and loading is also vital: supports like ZrO_2, CeO_2, SnO_2 and K loading of 5-10 wt% can ensure the best performance [74–78].

$K\text{-}NO_3 + C \rightarrow CO_2 + K_2O + NO$ R3

The cost of potassium-based soot oxidation catalysts is comparably lower than that of silver-based. The disadvantages are that they are not oxidative towards CO, NO and hydrocarbons. Furthermore, they are quite unstable and some of the potassium salts have low melting point and are highly soluble that can result in the migration, aggregation, and progressive deactivation of the active component. It has also been shown that during the reaction with soot low quantities of potassium can vaporize. Two most promising methods suggested in the literature for its stabilization are either the embedment of potassium in aluminosilicate such as nepheline or kaolinite or the fixation of potassium in stable glass [76,79–81].

3. Doped CeO_2-based soot oxidation catalysts: Doping CeO_2 with various oxides, such as Cu, Mn, Fe, Zr, Pr, La and Sn, can increase the number of surface reactive oxygen and improve the soot oxidation activity. These metals can insert into the CeO_2 lattice and enhance the associated oxygen release phenomena. The synthesis method of the catalysts seems to be another key factor since certain facets and morphologies promote the soot oxidation relative to others. Solution combustion, coprecipitation, solid mixing, sol-gel etc are all methods reported for the doped CeO_2 oxides. Various morphologies are thus obtained by tuning the pH, ageing time, concentration, calcination temperature and flakes, rods, fibres, cubes and spheres have been reported [72,82,83].

It should be noted that most of the scientific reports utilize model soot such as Printex-U or Vulkan 7H and the catalytic effect on real diesel soot can be lower due to the presence of the soluble organic fraction and intrinsically different reactivity [37].

1.3.3. Lean NO_x trap (LNT) aftertreatment catalysts

Lean NO_x traps are multicomponent catalysts that operate under alternating lean-rich conditions of the exhaust. An alkaline component, typically Ba or K, is added on Al_2O_3 support for trapping the NO_x during the lean phase. While other alkali earth and alkali metals can also trap the NO_x, the rate of capture and release temperature are less favourable. The second redox component, typically Pt or Rh, produces nitrates in the lean regime and reduces it to N_2 via the hydrocarbons in the rich regime. Reference composition cited is the system $Pt/BaO/Al_2O_3$ in a 1/20/100 weight proportion, although this can change depending on the application requirements. Different dopants and modifications have been proposed such as the use of $MgAl_2O_4$ spinel as support, doping with SnO_2 or CeO_2 as oxygen and sulphate buffer, etc [84].

The rate of reductant dosing is also a key factor and different ratios of lean/rich dosing times have been proposed, typically the ratio is 60/5 s or 5/1 s. The latest

technology, developed by Toyota and labelled Di-Air, uses rapid (0.5-3 Hz) injections of hydrocarbons. In this way the formation of the intermediate -NCO involved in the NO_x reduction is enhanced and better performance and stability has been demonstrated [85,86].
The advantage of LNT-based NO_x reduction catalysts is that the cold start and low temperature emissions are trapped and reduced when the aftertreatment unit is more efficient after heating up. The disadvantages when compared to urea-based reduction are: lower NO_x conversion performance, higher fuel penalty (2% vs 0.5% of urea-SCR), lower thermal stability, strong deactivation by SO_2, higher N_2O production and higher complexity that makes the control demanding [10,87].

1.3.4. Urea based NO_x reduction catalysts

Urea-based catalysts utilize ammonia originating from the aqueous urea solution (AdBlue) thermal decomposition according to the reaction:

$(NH_2)_2CO \rightarrow NH_3 + HNCO$ R4

$HNCO + H_2O \rightarrow CO_2 + NH_3$ R5

The exhaust temperature has to be above 200 °C for the urea solution to decompose and produce ammonia and to avoid the formation of ammonium nitrate:

$NO_2 + NH_3 + H_2O \rightarrow NH_4NO_3$ R6

Ammonium nitrate deposition is undesirable since with the rise of temperature its decomposition can produce N_2O emissions:

$NH_4NO_3 \rightarrow N_2O + 2H_2O$ R7

The above mentioned R4-R7 reactions represent a major limitation for the SCR reaction since it is restricted below 200 °C by both the limited urea hydrolysis and NH_4NO_3 deposition. For the urea hydrolysis reaction, ZrO_2 has been found to be an efficient catalyst, achieving nearly 100% NH_3 production at 150 °C and can be currently found in the SCR formulations [88–90]. The NH_4NO_3 formation has been mainly discussed in negative connotation due to high N_2O yield during the thermal decomposition (between 200-300 °C). Recently, however, an interesting concept has been demonstrated whereby NH_4NO_3 deposits are exploited for enhancing the NO_x conversion. The basic concept is that when $NO_2/NO_x > 0.5$ the NO_x is deposited as NH_4NO_3, while when $NO_2/NO_x < 0.5$ the SCR reaction can utilize the nitrates from the deposit to enhance the Fast SCR pathway [91]. The gaseous ammonia is adsorbed on the acidic Brønsted or Lewis sites of the catalyst where it acts as a reductant for the NO_x SCR. In general, a second redox component is required for completing the SCR redox cycle ($V^{+5/4}$, $Fe^{+3/2}$ or $Cu^{+2/1}$ in the case of zeolites) and facilitating the reduction. The interaction between the acidic sites and the redox sites are important and their strength has to be balanced for optimal performance. Several and diverse theories have been put forward identifying the key reaction intermediates in the NH_3 SCR catalytic cycle. The formation of HONO, NO_3^-, ammonium nitrates or nitrites, different types of site interaction have all been proposed. Considering the amount of evidence

supporting the different mechanisms, it appears that a unified mechanism would be difficult to construct if not impossible. Rather, the limiting reactants and mechanisms are different over different type of sites involved (e.g. Lewis vs Brønsted acids) and even for the same catalyst, the SCR mechanism changes with temperature and low temperature SCR pathways are different than the high temperature one [92–95].

The performance of the NH_3 SCR is also dependent, to a various degree, from the inlet NO_2/NO_x ratio. When the ratio of NO_2/NO_x is 0.5 the SCR reaction is kinetically the fastest and it is called "Fast SCR", when NO_2/NO_x ratio is 0 it is "Standard SCR" and when NO_2/NO_x is 1 it is the "NO_2 SCR". The global reaction stoichiometry is presented in R8-10:

$4NH_3 + 4NO + O_2 \rightarrow 4N_2 + 6H_2O$ R8 Standard SCR

$4NH_3 + 2NO + 2NO_2 \rightarrow 4N_2 + 6H_2O$ R9 Fast SCR

$4NH_3 + 3NO_2 \rightarrow 3.5N_2 + 6H_2O$ R10 NO_2 SCR

Most commonly the NO_2/NO_x ratio is ca. 0.1 at the engine outlet and this is increased in the DOC and cDPF. Before the SCR the ratio it typically between 0 and 0.5 depending on the temperature and DOC performance, meaning that the SCR reactions are a mixture of standard and fast SCR. Most of the scientific literature deals with standard SCR since from the practical point there is an interest to downsize (or even completely eliminate) the costly DOC.

The following catalysts are best performing in the NH_3-mediated SCR reactions with their unique advantages and disadvantages in real applications:

1. Vanadium based SCR catalyst:

Vanadium based catalysts are amongst the earliest NH_3-SCR catalysts to be practically implemented. Their formulation is typically V_2O_5 supported on anatase TiO_2 with V loading of 1-5 wt% and commonly doped with 5-15 wt% WO_3. The TiO_2 has a key role since it has to provide high surface area and high dispersion of monolayer V=O and V-OH that is mandatory for high activity. The anatase TiO_2 phase, active in the SCR reaction, provides mainly Lewis adsorption sites and some Brønsted by converting V=O species to V-OH and enhances the SCR reaction by electron transfer between the $V^{+4/5}$ and $Ti^{+3/4}$. The role of WO_3 is disputed and different promoting mechanisms are suggested such as promoting the electron transfer, enhancing the zeolite acidity by introducing Brønsted sites and by increasing the dispersion of the active site by acting as spacer and anchoring the V [92,96–98].

The main application of the V_2O_5-WO_3/TiO_2 is currently in the aftertreatment of stationary emitters such as coal, fuel oil or biomass-based power plants or boilers, industrial sources, incinerators, etc. These fuels are not refined, hence the flue gases typically contain large amounts of chemical impurities such as SO_2, Hg^0, As, etc. and the V based catalysts are robust towards such contaminants [99,100].

V-based catalysts are irreversibly deactivated when the temperature exceeds 500 °C due to V melting and loss of dispersion. Above 500 °C the TiO_2 support rapidly loses surface area and undergoes phase transition from anatase to rutile phase. This limits the application to stationary sources where the temperature can

be controlled. Mobile aftertreatment units, where the temperature varies rapidly in wide range, it has been largely replaced with more thermally stable zeolites. Other major disadvantage is a relatively narrow operational window in which high NO_x conversion can be achieved, specifically 300-450 °C, since under 300 °C the activity is not satisfactory, while above 450 °C the NO_x conversion decreases due to the predominant NH_3 oxidation [99].

2. Zeolite-based SCR catalysts

Zeolites are aluminosilicates with well-defined porous structure, multiscale hierarchy and peculiar chemical features. The insertion of Al^{3+} into the silicate framework results in charge deficiency that is compensated by a proton associated to every zeolite aluminium. These features allow the use of zeolites in variety of forms such as solid-acids or ion exchange of certain metals for specific applications. For the NH_3 catalysed SCR reactions the ion exchanged Fe^{3+} and Cu^{2+} are the most active, Cu being used for low temperature (180-350 °C), while Fe for higher temperature applications (300-600°C) [101–104]. The Fe and Cu can be introduced in the zeolite cages by different techniques of impregnation, wet ion-exchange and solid-state ion exchange. Practically, the exchange of Fe is more difficult to perform since in aqueous solution the Fe^{3+} has high hydration diameter and requires 3 Al sites thereby obtaining low exchange ratio. The ion exchange has to be performed using Fe^{2+} precursor in oxygen free solution/atmosphere to avoid oxidation to Fe^{3+}. Compared to impregnation methods, the ion exchange achieves higher dispersion and stabilization of the metal ions which translate into better SCR activity. The optimal zeolite loading of Cu is between 2-3.5 wt%, while for Fe 1-2 wt% depending on the zeolite type and SiO_2/Al_2O_3 ratio. The interaction between the zeolite and the exchanged metal influences the NO_x-SCR activity. The performance of Fe is enhanced by larger pore and lower acid strength zeolites, such as BEA or ZSM-5 zeolites, while for Cu smaller pore zeolites and higher Brønsted strength zeolites, such as chabazite structured SSZ-13 or SAPO-34, are more favourable [51,101–104].

During the SCR reaction the NH_3 activation on zeolite, its interaction with the metal site and the activated NO has to be optimal. Since the zeolites have high NH_3 and NO_x adsorption capacity, the performance can be very different in the transient dynamic conditions when compared to results obtained in steady state conditions. For example, the conclusion that the low temperature (<300 °C) activity of Fe zeolite is much lower compared to Cu is true only when comparing steady state data. In transient conditions however, the NO_x-SCR performance of Fe zeolite is nearly the same as that of Cu zeolite [102]. This is the result of the poisoning effect of NH_3 adsorbed on the zeolite, since too high coverage with NH_3 results in the inhibition of the SCR reaction over Fe, while over Cu such phenomena are not observed. For this reason, the BEA zeolite, where the adsorption of NH_3 is weaker, is more suitable zeolite for Fe exchange and its performance when exchanged in SSZ-13 is inhibited [51,102,105,106]. Another correlation between the zeolite-metal interaction has been observed regarding the

formation nitrates. The NO_x conversion activity observed for different Cu exchanged zeolites followed the trend BEA<ZSM-5<SSZ-13.

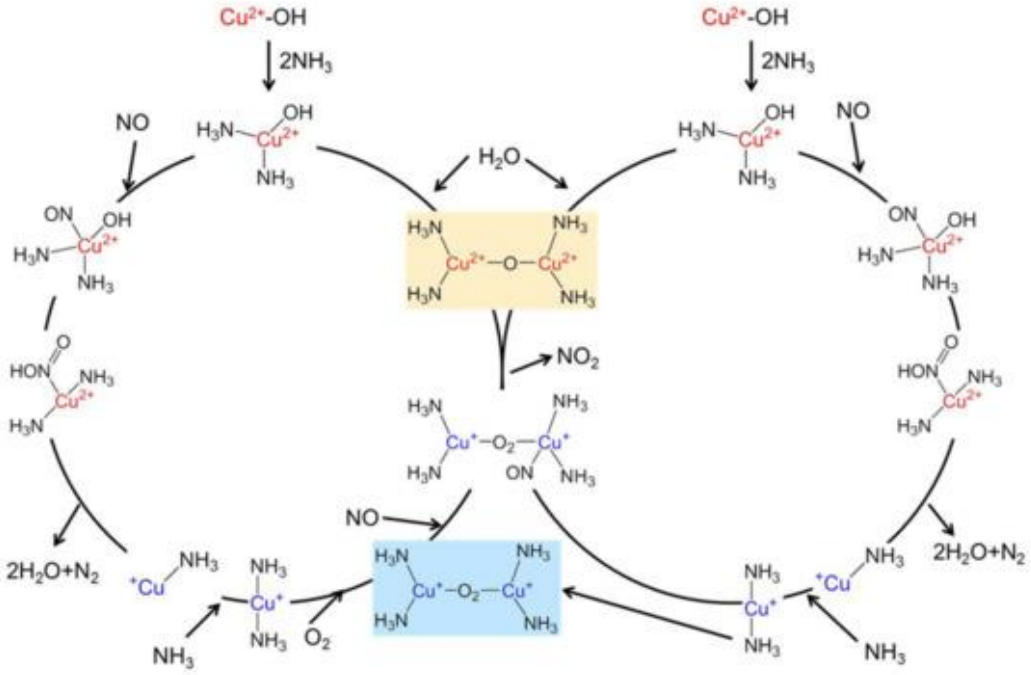

Figure 1.4. The latest NH_3 mediated NO_x SCR cycle proposed over Cu-SSZ-13. Adapted from [93].

The current state-of-the-art zeolite-based SCR catalysis used in the automotive aftertreatment systems are Cu exchanged chabazite type SSZ-13. Until recently SAPO-34 was favoured due to slightly better resistance to high temperature deactivation. However, surprisingly the SAPO-34 deactivates quickly at low temperature (200 °C) in hydrothermal conditions, the underlying cause is still under investigation, most likely hydrolysis. The small pores of SSZ-13 offer very high hydrothermal stability, up to 800 °C, and partial resistance to hydrocarbon poisoning due to size exclusion and diffusional effects. The high amount of acid sites in the zeolite contributes to the high ammonia storage capacity and consequently the catalyst is resistant to sudden changes in the exhaust NO_x concentration or the urea dosing. From the described urea-based SCR catalysts, the zeolite-based catalysts offer the best NO_x conversion, lowest ammonia overoxidation and N_2O production and high NO_x conversion in a wide temperature range [52,93,107,108].

The disadvantages of the zeolite catalysts compared to V based catalysts are higher susceptibility to chemical deactivation. The highly dispersed Cu in the zeolite cage, that is behind its high NH_3-SCR activity, also makes it susceptible to chemical deactivation when compared to V_2O_5-WO_3/TiO_2 catalysts. In the presence of SO_2, copper sulphates form and they slowly but irreversibly deactivate the SCR reaction [99]. Potassium, sodium, magnesium and calcium originating from the fuel and lubricants also cause strong poison for the NH_3-SCR catalysts in general. Alkali and alkali earth elements are strongly alkaline, and

they strongly adsorb and deactivate acid sites that are required for the NH_3 activation. Such processes and the deactivation are obviously irreversible and can be avoided only by excluding them from the diesel fuel and lubricant [109–111].
Hydrocarbons, when present in the exhaust, suddenly and strongly deactivates the catalyst. The hydrocarbons oxidation and the NO_x SCR are competitive for the same active site and due to the strong adsorption of hydrocarbons, the NH_3-NO_x SCR pathway is inhibited. Due to high acid strength and isolated metal sites, the hydrocarbons tend to polymerize and form coke deposits that plug the zeolite pores and further reduce the NO_x conversion. The hydrocarbon poisoning is fully reversible and most of the activity can be recovered once the hydrocarbons are absent in the exhaust stream and full recovery of the original NO_x conversion when the coke deposits are burnt off [105,107,112].
Highly dispersed metal and low metal loadings in the Cu-zeolites are sensitive to reducing conditions that can be occasionally found in certain configurations such as SCRoF or LNT + SCR. In reducing conditions, the Cu is displaced from its ion exchanged positions and becomes inactive. This loss in activity is partially reversible and repeated exposure to reducing conditions leads to progressive deactivation [113,114].
From financial standpoint, the zeolite-based catalysts have ca. 30 % higher capital costs than the V based SCR catalyst. However, if we consider that the proportion of the catalyst is a small portion (10-20% of total) of the total capital costs, it is clear that the final choice is dependent of the technological requirements.

3. Mixed metal oxide-based catalysts

Different metal mixed oxides have been proposed as alternatives to the previous two types of catalysts. The two most promising types are doped and supported MnO_2-based catalysts for low temperature NO_x-SCR and doped CeO_2-ZrO_2 for the mid-temperature range.
The main perspective of MnO_2-based SCR catalysts is for low temperature (<300 °C) NH_3-SCR applications. MnO_2 can be supported over a zeolite, TiO_2 or used as bulk oxide with the introduction of dopants. The high conversions at low temperature can be attributed to the high NO oxidation and nitrate formation rate of Mn oxides and simultaneous presence of acid sites that enable ammonia activation. The highly oxidative nature of MnO_2 however contributes to high NH_3 oxidation during which N_2O can form. When the NH_3 oxidation rate becomes high, the NO_x conversion decreases due to the lack of reductant. The selectivity can be improved by optimizing the Mn loading and by dopants. The main issue of the N_2O formation can be mitigated by doping with other metals, most notably Fe, W, Ce and Sn [115–117].
The other metal oxide based SCR catalysts are the doped CeO_2-ZrO_2, most promisingly with Nb_2O_5, WO_3, MoO_3 or SnO_2. CeO_2-ZrO_2 by itself has no significant SCR activity and upon the introduction of dopants high NO_x conversion in the temperature range 250-450 °C can be achieved with very little N_2O production. The dopants introduce several changes that are hypothesised to enhance the SCR activity: the type and number of acid sites increase, which enable NH_3 activation, and the partial insertion of the dopant into the parent

crystal, that enhance the redox ability. The most promising dopant appears to be 5-15 wt% WO_3 impregnated on the CeO_2-ZrO_2 support. Several optimization and mechanistic studies as well as patents can be found in the recent literature. These SCR catalysts present an interesting alternative and a compromise between the toxic and thermally unstable V_2O_5-WO_3/TiO_2 and the chemical poisoning sensitive metal-zeolite based catalysts [97,118–120].

1.3.5. Hydrocarbon mediated NO_x SCR catalysts

An alternative to the urea SCR and LNT NO_x reduction catalysts are continuous NO_x reduction by hydrocarbons (mainly alkanes and alkenes) in lean condition. The most active catalysts used are Ag/Al_2O_3, Sn/Al_2O_3 and zeolites (ferrierite, mordenite and ZSM-5) containing transition metals (Co, Ce, Cu, Ag, Fe) with loadings typically ranging from 2 to 5 wt%. The catalyst must have high NO to NO_2 oxidation activity and ability to activate the hydrocarbons. It was shown in spectroscopic studies that the hydrocarbons adsorbed are transformed into partially oxygenated intermediates, notably enolates, acetates and formates are observed. Simultaneously to the introduction of the hydrocarbons, the nitrates are consumed and -NCO intermediates are observed [57,121–123].
The advantage of such catalysts is that the fuel can be used as a reductant, without additional space and reservoirs (such as with the urea) or additional reformer and special injector (as can be found in LNT). Hydrocarbon-mediated NO_x-SCR has the disadvantage of low NO_x conversion, especially at low temperatures, and only above 350 °C NO_x conversions are achieved that can be considered practical. Furthermore, the activity is highly dependent on the NO_2 concentration in the reaction stream. When NO_2/NO_x is equal to 1 the best NO_x conversion can be achieved and it is proportionally decreasing with NO_2/NO_x ratio. Co-feeding methanol, ethanol and/or H_2 can improve the low temperature activity, however the increased complexity and additional reforming unit would make such systsem unfeasable [57,121–123].

1.3.6. Integrated NO_x aftertreatment configurations

The aftertreatment units described in the previous section are composed of numerous sections and are voluminous, which presents a problem where the space is limited. Integrating several components into a single unit can reduce the space requirements, reduce the complexity and cost and better performance can be achieved due to close-coupling. Among the several integrations proposed, the most interesting are: integration of DOC and cDPF into a single unit, integration of LNT catalyst in the DPF (the so called DPNR), combination of LNT and NH_3 SCR, and SCR on Filter (SCRoF) from the integration of SCR and DPF.
The DPNR involves the addition of a LNT catalyst on the DPF for simultaneous NO_x reduction and soot oxidation. Pt-K/Al_2O_3 formulation is preferred over Ba

since K enhances the soot oxidation in loose contact, while over Ba is less active for soot oxidation. The nitrates that are adsorbed over potassium during the lean phase can oxidize the accumulated soot according to the reaction R3. This means that in the presence of soot the NO_x adsorption capacity is apparently reduced. Another disadvantage of DPNR is related to the relative lower stability of K compared to Ba [54,68].

2. LNT + SCR: it has been observed under certain conditions that LNT can form high amounts of NH_3 during the reduction phase. Instead of oxidation, it was proposed that an SCR catalyst (mainly Cu zeolite) could be placed downstream of LNT to capture the NH_3 and reduce the emitted NO_x slip. The LNT and SCR catalysts can be either physically mixed, deposited in dual layer or alternating patches along the monolith length or dual brick system whereby the SCR component is downstream of LNT. Several studies have shown slight improvement in the NO_x conversion in such combined system, as well as reduced NH_3 slip. Another advantage of such system is the reduced cost due to partial substitution of expensive PGM-based LNT catalysts.

The main disadvantages of such system are mostly related to the incompatibility of the SCR catalyst related to the cyclic lean/rich operating conditions. Cu zeolites deactivate strongly when exposed to reducing conditions and hydrocarbons for prolonged periods that can be found during LNT operation. Another issue is the migration of PGM metals from the LNT and depositing over the SCR catalyst that results in lowered selectivity and N_2O production during the NH_3 SCR reaction [86,114,124].

1.3.7. In-situ technologies and modifications for preventing emissions.

Besides aftertreatment of the exhaust gases, several methods have been developed for the emission reduction during the combustion process. The main methods are:

1. Fuel additives: oxygenated hydrocarbon additives can lead to the suppression of the particulate matter formation. Methanol, ethanol, MTBE and DME have all been noted as successful additives. By mixing 5-10 wt% additives with diesel fuel, 30-60% of soot and NO_x reduction can be achieved [125,126].

2. Metallic fuel additives: Diesel additives in the form of emulsions containing metals of Ce, Fe, Sr, Mg, Mn have been shown to reduce the soot emission during the combustion and exhibit catalytic post-combustion activity. The metals combusted together with the fuel exit the cylinder in tight contact with the soot and are deposited on the filter. The deposited metals exhibit catalytic activity for soot oxidation. While seemingly an elegant solution, the disadvantages are accumulation of metals plugging the filter, potential poisoning of the downstream catalysts and damage to the fuel injection system and cylinder [127].

3. Modified combustion cycle: modified combustion methods can lead to lowered emission and higher engine efficiency. Most notably, the homogeneous charge compression ignition (HCCI) is subject to research as promising

alternative to current diesel engines. They have significantly reduced NO_x emissions albeit at a cost of slightly elevated hydrocarbon and CO emission. The ignition control and combustion timing that results in engine knock is still an issue that prevented the large-scale commercialization of HCCI and its derivatives [128].

1.4. SCR on Filter (SCRoF)

1.4.1. Overview of some recent trends in the diesel aftertreatment

Decades of active research have been dedicated to the abatement of the pollutants due to challenging issues and socio-economic impact [129]. Despite this, there are still challenging issues to be addressed and the catalytic research is still very active with new solutions being produced. The current trends in the catalytic aftertreatment of diesel pollutants are oriented towards:

1. Enhancing the NO_x conversion at low temperature that is challenging under 200 °C.
2. Reducing the N_2O emissions that are currently not regulated but expected to be in the future.
3. Optimizing the NH_3 economy since currently urea is typically dosed in higher amounts for better performance.
4. Enhanced durability for longer lifetime
5. Lowering the size, complexity and costs of the system. Most notably by integrating several aftertreatment functionalities in a single device and reducing the PGM use.
6. Reducing the cold-start NO_x and hydrocarbon emissions by Pd-based Passive NO_x Adsorption (PNA) or close coupling the SCR functionality for shorter heat up.

Some of the currently used and explored alternatives of the NO_x aftertreatment system are shown in Figure 1.5.

SCRoF is one of the main technologies with successful implementation. Today they are considered state-of-the-art and in widespread use, however there are several unsolved issues.

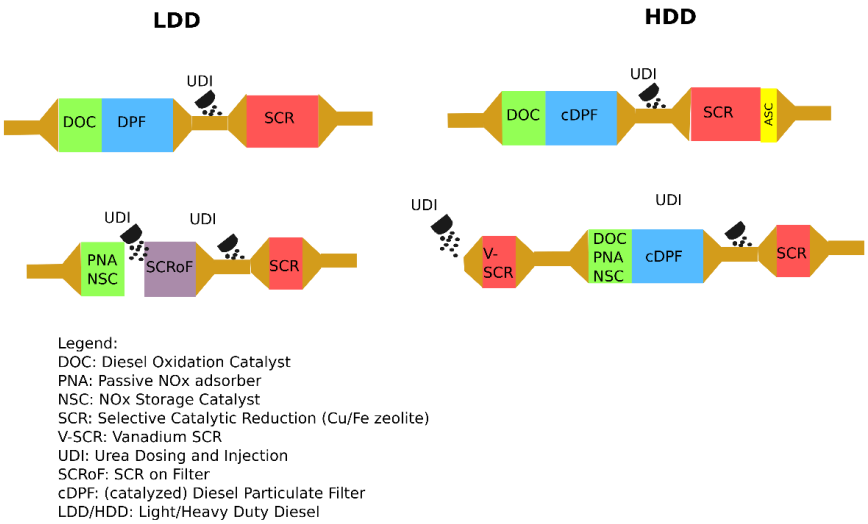

Figure 1.5. Some of the currently used and proposed for the NH_3 mediated SCR and soot filtration system configurations.

1.4.2. General structure and practical challenges of SCRoF

The SCRoF involves the addition of the SCR catalyst inside the pores of the filter for simultaneous NO_x removal and soot filtration. The monolith ends are plugged in alternating checkerboard pattern and the exhaust gas is forced through the porous monolith wall during which the filtration of the particulate matter occurs (Figure 1.6). As a result of integrating two devices into one, the size of the aftertreatment system is nearly halved presenting obvious advantage for saving space. Better NO_x reduction can be achieved due to the close-coupling the SCR to the exhaust point which results in higher operating temperature and shortens the heat-up time.

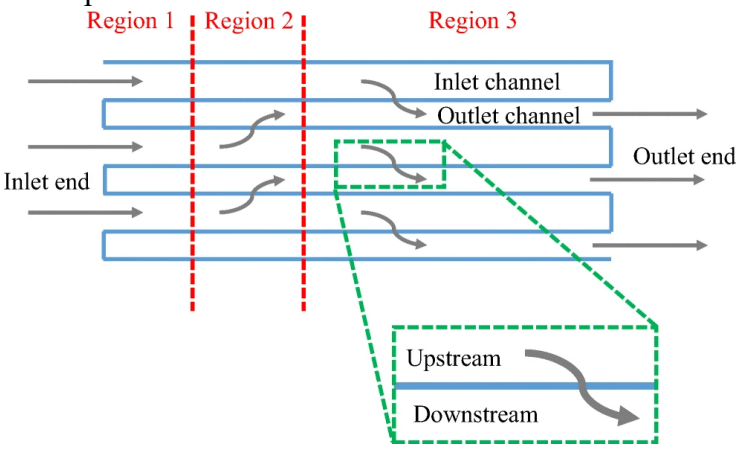

Figure 1.6. Operational principle and coating of the SCRoF. Adapted from [130].

The main issue with SCRoF is the management of the soot accumulation. It has been shown in numerous experimental, real world and simulation studies that the SCR reaction is inhibiting the soot oxidation on the SCRoF. This can be better seen by summarizing the parallel reactions that occur on the SCRoF:

$2\ NO + 2\ NO_2 + 4NH_3 \rightarrow 2N_2 + 6H_2O$ Fast SCR

$C + (2x+y)\ NO_2 \rightarrow x\ CO_2 + y\ CO + (2x+y)\ NO$ NO_2 assisted soot oxidation

It can be observed that the Fast SCR reaction and the NO_2-assisted soot oxidation are competitive for the same NO_2 reactant. Taking into consideration that the Fast SCR reaction is kinetically much faster than the NO_2-mediated soot oxidation and that the wall flow velocities in the monolith are low, with Peclet number typically under 1 (meaning that the diffusional transport of the reactants is predominant), it is clear that the NO_x cannot be relied on as soot oxidants for passive regeneration as in the cDPF. Rappe [131] showed (Figure 1.7) that when NH_3 is included in the reaction stream over SCRoF, meaning the NO_x SCR reaction is taking place, the regeneration temperature was delayed by 70 °C compared to the case when NH_3 was excluded. Other studies [132–135] have also shown that the contribution of NO_2 to the soot oxidation in the simultaneous presence of the SCR reaction is negligible and that the soot oxidation by O_2 is predominant and occurs only above 450 °C. This means that there is a mismatch between the temperature range typical of diesel exhaust (200-400 °C) and temperature required for soot oxidation by O_2 (> 450 °C) over the SCRoF. The influence of soot on the SCR reaction is considered negligible: slight reduction in NO_x conversion was observed over SCRoF that is considered a consequence of diffusional limitations and slower NO_x transport to the SCR catalyst [132–135].

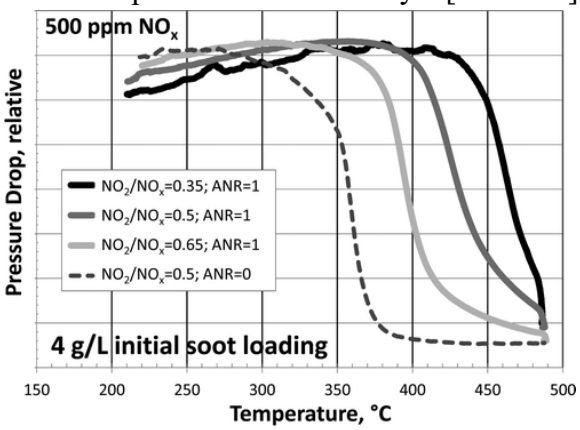

Figure 1.7. Influence of the NO_2/NO_x ratio and the presence of NH_3 on the backpressure and regeneration of SCRoF. Adapted from [131].

Because of the soot accumulation, the corresponding rise backpressure takes place faster when compared to cDPF. Most of the soot (ca. 90%) is present as accumulated soot filter cake while the rest is located inside the filter pores. Both contribute to the rise in backpressure, however the soot that is trapped inside the SCRoF pores is the main cause of the rise since it blocks the exhaust gas flow and changes the flow pattern (Figure 1.8). This is the reason why the correlation

between the pressure rise and the amount of accumulated soot is not linear and the backpressure rises slower once the filtration transitions to cake filtration [131]. Because of this, the SCRoF monolith has to be made of material that is highly porous (50-60% porosity) to accommodate the SCR catalyst inside the pores. The washcoating of the SCR catalyst inside the monolith pores is a complicated process. A common process is the mixing of binder (e.g. boehmite) and catalyst and circulating the slurry through the filter until the desired loading is achieved. Several process parameters during the washcoating are regulated, (the evaporation rate, slurry viscosity, solid load in the slurry, etc.), with the aim to achieve the optimal distribution with the lowest pore obstruction that is associated with pressure drop. High heat tolerance, low heat expansion and conductivity for rapid heat dispersion are also necessary to avoid local hot spots. For these reasons, SiC is used as monolith material with different modification, most commonly with Al and Mg [136].

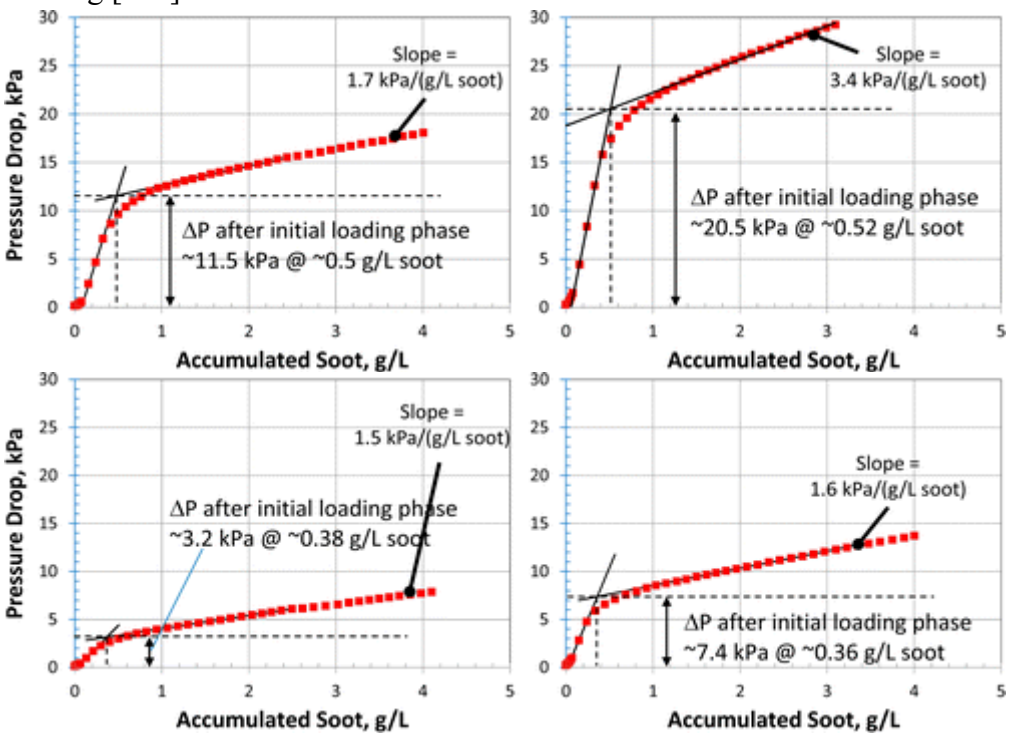

Figure 1.8. Soot-loading characteristics of 90 g/L (left) and 150 g/L (right) SCRoF samples configured such that catalyst was present predominantly on the downstream (up) and upstream (down) portion of the filter microstructure and on the outlet channel wall (150 g/L sample). Adapted from [131]

When the backpressure increases above a certain threshold, the SCRoF is actively regenerated during which fuel is injected and combusted over the DOC to raise the temperature of the SCRoF unit and induce soot oxidation. The temperatures easily reach over 600 °C during the regeneration and the heat released from the soot oxidation can trigger further temperature rise. During the soot oxidation very high exotherms are generated and local hotspots can form that can irreversibly damage the SCR catalyst and the filter [46,137]. This commonly occurs also when the engine load is suddenly decreased during the regeneration process. The low

gas flowrate cannot transport the soot generated heat from the SCRoF rapidly enough that triggers further temperature rise. This is shown in Figure 1.9B, following a stepwise input of high flowrate and temperature (e.g. acceleration of the vehicle) there was a sudden decrease in load. The heat originating from the soot caused a rapid increase in the temperature and after 300 s there was a 300 °C exotherm at the outlet [137]. The current state-of-the-art SCR catalyst for SCRoF is Cu-SSZ-13, owing to its small pores and chabazite zeolite structure can, to some extent, withstand such temperatures. Deactivation is still an issue due to high thermal stress, as well as due to the reducing conditions encountered during the regeneration that can deactivate the Cu active sites and induce dealumination and loss of acid sites.

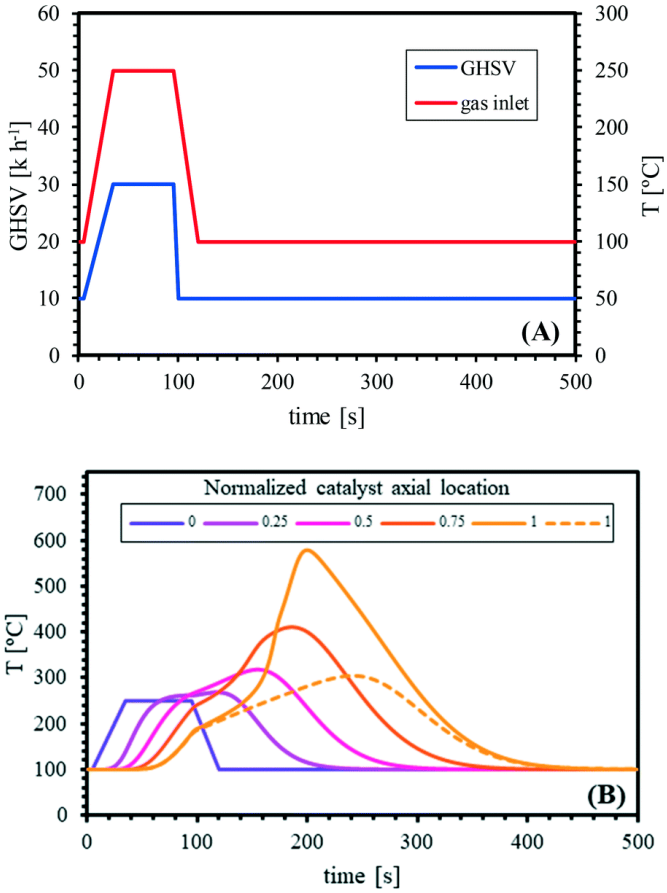

Figure 1.9. Simulated exotherm and thermal front over SCRoF during triggered soot oxidation followed by drop to idle. Adapted from [138]

Methods to partially mitigate the soot build-up have been proposed. One method is to raise the NO_2/NO_x ratio well above the 0.5 that is optimal for the NH_3-mediated SCR reaction. The rationale is that the excess NO_2 will be available for the soot oxidation and thereby automatically regulate the NO_2/NO_x ratio back to the optimal 0.5. In such case slight improvement of soot oxidation was observed, however since the NO_x was present in low concentration soot build up still occurred (see Figure 1.7) [131].

Another solution proposed, complementary to the previous, is that the SCR catalyst should be more concentrated in the downstream section. For example,

Rappe compared a SCRoF with uniform distribution of 120 g/L catalyst to the dual zone whereby on the inlet half the SCR catalyst loading was 90 g/L while on the downstream half 150 g/L with significantly lower pressure drop in the case of zoned catalyst and comparable NO_x conversion [131]. Multidimensional simulation of SCRoF was performed by Karamitros et al. [134] for in depth understanding of the effects of zoning on the NO_x distribution along the SCRoF and soot oxidation. As reproduced in Figure 1.10, the zoning had significant effect as more NO_x was available along the filter when the inlet portion was lightly coated compared to uniform coating. Thus, the NO_x involvement in the soot oxidation is slightly improved.

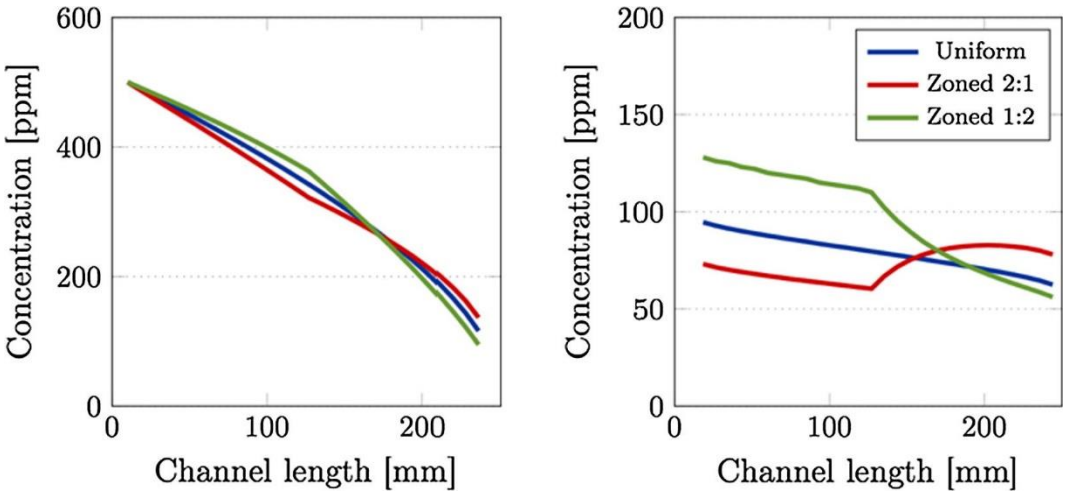

Figure 1.10. Comparison of (a) inlet and (b) outlet channel NO_x concentration profiles, at 250 °C and in presence of 4 g/l of soot, between uniformly- and zone-coated SCRoF. Reproduced from [134].

Stewart et al. [130] analysed an industrial SCRoF and the distribution of the SCR catalyst. They found 3 zone distribution (Figure 1.11) whereby the 20% of the inlet length was lightly coated, followed by 20 % of high-density coating and the rest of the SCRoF length was medium coated. No numerical densities were reported, only qualitative analysis. In this way the same overall NO_x conversion was achieved with improved soot oxidation since there was more NO_2 available in

the inlet side of the monolith.

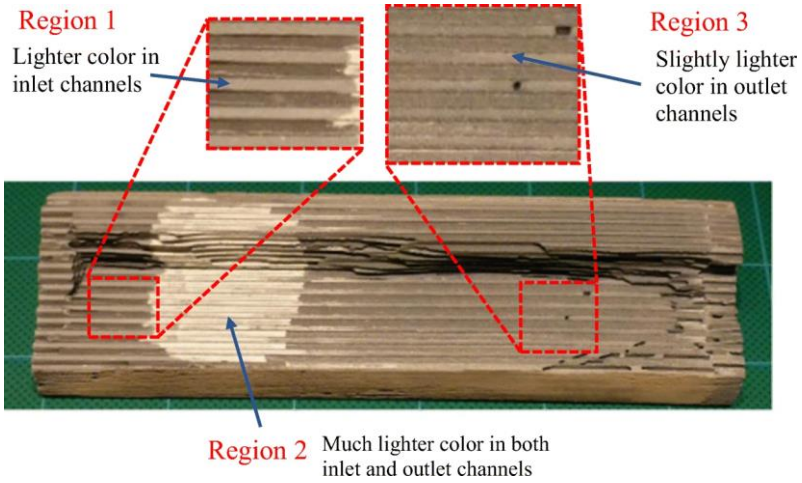

Figure 1.11. Catalyst distribution in along the SCRoF. Lighter color corresponds to higher catalyst loading. Reproduced from [130].

These methods however do not decrease the regeneration temperature nor solve the problem of soot build up merely delaying it and active regeneration would still be required. Furthermore, the concept assumes high NO_2/NO_x ratio that can be achieved only with high performing and expensive DOC preceding the SCRoF.

1.4.3. Content of the thesis

The aim of this thesis has been the improvement of the SCRoF from the issues previously mentioned. Chapter 2 deals with finding a suitable soot oxidation catalyst that does not interfere with the SCR reaction. The focus was on soot oxidation and little attention was paid to the SCR catalyst itself. Chapter 3 builds on the previous and the interaction between the soot oxidation catalyst and the SCR catalyst was explored in detail by changing the NO_2/NO_x ratio and the SCR and soot oxidation catalysts. In both chapters the approach taken was, to combine two catalysts, one specific for the NH_3-mediated SCR reaction and the other highly active for soot oxidation. As SCR catalyst, Cu and Fe zeolites were used since they are well characterized and investigated in literature and they are of most practical relevance. For the design and selection of the soot oxidation catalysts, several initial assumptions were made, based on the previous publications and the conceptual analysis of the reaction scheme. These were:

- The NO_x-mediated soot oxidation is inhibited by the SCR reaction; hence the soot oxidation catalyst has to be active for the O_2-soot reaction
- The catalytic activity for the soot oxidation is dependent from the catalyst ability to generate active oxygen and the same oxygen can typically oxidize the NH_3 that is the reductant for the SCR reaction. The overoxidation of NH_3 must be avoided to avoid the potential corresponding decrease in NO_x conversion, due to the lack of NH_3, or high N_2O production.

-NO to NO_2 oxidation over the soot oxidation would be favourable since the NO_2/NO_x ratio higher than 0.5 can enhance the NO_x conversion by providing Fast SCR conditions.
-The SCR activity and NO_x conversion should not be compromised.
In order to simultaneously avoid the NH_3 oxidation and improve the soot oxidation, the impregnation of the soot oxidation catalyst with alkaline metal was investigated. The poisoning of the NH_3 adsorption sites can deactivate the NH_3 oxidation while retaining the NO and soot oxidation activity. In Chapter 3 it is demonstrated that if the soot oxidation catalyst has NO oxidation activity, the NO_x conversion can be improved by partially transforming the reaction from standard to fast SCR. In all cases, it was evident that the contribution of NO_2 towards soot oxidation was very small since it participated in the kinetically faster SCR reaction and the main oxidant available was O_2. In the physical mixture the soot oxidation temperature was reduced by 150 °C, while to NO_x conversion simultaneously improved as much as 20%.
Due to the lack of cDPF as well as the injection of hydrocarbons during the active regeneration, the SCR catalyst over the SCRoF must be also resistant to hydrocarbon poisoning. Diesel soot also contains soluble organic fraction (typically 10-20 wt%) composed of complex PAH that evaporate in the temperature region 250-350 °C. Since Cu and Fe zeolites exhibit high Brønsted acidity and metal dispersion, the NO_x conversion decreases significantly due to the competitive SCR-hydrocarbon oxidation reactions. In Chapter 4 the hydrocarbon deactivation was studied, and novel solution proposed for its mitigation. The Cu-SSZ-13 SCR catalyst was mixed with a CeO_2-SnO_2 catalyst in 4:1 ratio. The CeO_2-SnO_2 catalyst did not deactivate in the presence of hydrocarbons and it had high activity for hydrocarbon oxidation. A complex interaction was found between the principal active sites (zeolite exchanged Cu and CeO_2-SnO_2) and demonstrated that the resistance of SCR reaction towards hydrocarbon poisoning was due to the migration of nitrate intermediates between the components.
Chapters 5 and 6 involve the investigation of $LaCoO_3$ perovskite as NO to NO_2 oxidation catalyst and its activity for soot oxidation. Although no SCR reaction was involved, $LaCoO_3$ was investigated since it has been reported as one of the best candidates for replacing PGM catalysts. In the previous section the importance of the NO_2/NO_x ratio for the SCRoF operation and how in the SCRoF this ratio should be much higher than the ideal 0.5 for the Fast SCR and optimal NO_x conversion were discussed. This would mean that the DOC preceding the SCRoF would have to feature high PGM loading to ensure high activity. To reduce the costs associated with the use of PGM metals, perovskites were investigated as alternative catalysts for NO oxidation. In chapter 5 the $LaCoO_3$ was doped with Al to enhance the NO and soot oxidation activity. The effect of introducing Al in the perovskite structure was investigated by different characterization techniques in detail. The $LaCo_{0.75}Al_{0.25}O_3$ had very high NO oxidation activity could achieve NO_2/NO_x ratio of 0.8 at 300 °C. In Chapter 6 the effect of SO_2 poisoning, a common issue associated with DOC, of $LaCoO_3$ was

investigated from mechanistic point of view as well as several regeneration techniques were suggested. In the first step of the SO_2 deactivation, the sulphates strongly adsorbed and poisoned the active site involved in the NO oxidation, while in the second stage sulphate salts grew on the perovskite surface. It was found that washing the catalyst with distilled water and reacting with soot can release the accumulated sulphates and regenerate the catalytic activity. The effect of poisoning can be reduced by the addition of guard bed ($Ca(OH)_2$) that absorbs the sulphates.

1.4. Conclusions

The aftertreatment of diesel exhaust to remove pollutants, mainly NO_x and soot, is required to meet the emission standards and improve air quality. The aftertreatment system is complex, expensive and consists of several units with different functionalities. Since the diesel engine is used in a variety of applications with different power rating, modifications and dynamic operation, there is no unique "best" solution for the aftertreatment configuration and it has to be adapted for each case. In the DOC unit the main catalysts used are PGM metals with the aim to increase the NO_2/NO_x ratio and achieve the full oxidation of hydrocarbons and CO. Following the DOC, the soot is accumulated over monolith filter where it is regenerated by oxidation to CO_2. The filter can be regenerated (cDPF) either with NO_x by catalytically raising the NO_2/NO_x ratio, or, when NO_x is not available, the soot oxidation with O_2 is promoted. The most active catalysts for the O_2-soot oxidation reaction are Ag, K and doped CeO_2.

Following the cDPF, the NO_x is removed catalytically with different reductants. In LNT hydrocarbons are injected in alternating lean/rich regimes whereby the NO_x are trapped in the lean regime and reduced in the rich regime. The advantage is the resistance of the system towards sudden change in NO_x concentration and better performance at cold start owing to the trapping component. The LNT catalyst, based primarily on Pt-Rh/Ba-K/CeO_2-Al_2O_3 formulation, is however susceptible to thermal and chemical deactivation and have higher fuel penalty when compared to urea-based NO_x reduction.

For the urea-based NOx reduction, there are different catalysts available with their respective advantages and disadvantages. V_2O_5-WO_3/TiO_2 based formulations are resistant to chemical poisons such as SO_2, As, Hg and hydrocarbons. They are susceptible however to thermal deactivation and high NO_x conversion can be obtained in a relatively narrow temperature range of 300-450 °C. For these reasons, their application is limited to stationary applications where stable and constant operational parameters can be maintained such as industrial boilers or power plants.

The high hydrothermal stability of Cu and Fe exchanged zeolites makes them the preferred catalyst for the NH_3-mediated NO_x SCR in the automotive applications. Several issues are still unsolved, such as deactivation in the presence

of K or SO_2 and high sensitivity of NO_x conversion to the presence of hydrocarbons or reducing conditions. Thus, the zeolites are limited to applications when relatively clean fuel and combustion can be ensured. Table 1 summarizes the general characteristics and most important features of the different NO_x reduction catalysts.

Table 1.1. Summary of the main NOx reduction technologies and characteristics

HC-SCR (Ag/Al_2O_3, Co-mordente)	DPNR (Pt-K/Al_2O_3)	LNT (Pt-BaO/Al_2O_3)	Mixed oxides (WO_3/CeO_2-ZrO_2	Vanadium based (V_2O_5-	Cu-zeolite (Cu-SSZ-13)	Fe-zeolite (Fe-β)
350-600 °C	250-600 °C	250-450 °C	250-450 °C	300-450 °C	200-450 °C	300-650 °C
Hydrocarbons, Ethanol, H_2	H_2, CO, Hydrocarbons (periodic)	H_2, CO, Hyrocarbons (periodic)	Urea (NH_3)	Urea (NH_3)	Urea(NH_3)	Urea (NH_3)
--	-	+	+	+	++	+
+	-	-	o	+	o	++
+	--	--	+	++	o	+
+	-	o	+	--	++	++
+	--	--	+	+	o	o

Catalyst	Temperature range	Reductant	NO_x SCR activity	N_2O formation	S-tolerance	Temperature tolerance	Cost

Legend: ++ very good, + good, o neutral, - bad, --very bad

References

[1] R.D. Brook, S. Rajagopalan, C.A. Pope, J.R. Brook, A. Bhatnagar, A. V. Diez-Roux, F. Holguin, Y. Hong, R. V. Luepker, M.A. Mittleman, A. Peters, D. Siscovick, S.C. Smith, L. Whitsel, J.D. Kaufman, Circulation 121 (2010) 2331–2378.

[2] B.A. Franklin, R. Brook, C. Arden Pope, Curr. Probl. Cardiol. 40 (2015) 207–238.

[3] B.J. Lee, B. Kim, K. Lee, Toxicol. Res. 30 (2014) 71–75.

[4] B. Brunekreef, S.T. Holgate, Lancet 360 (2002) 1233–1242.

[5] J. Fenger, Atmos. Environ. 43 (2009) 13–22.

[6] L. Han, W. Zhou, W. Li, Y. Qian, W. Wang, Phys. Chem. Earth 111 (2019) 100–104.

[7] S.X. Wang, B. Zhao, S.Y. Cai, Z. Klimont, C.P. Nielsen, T. Morikawa, J.H. Woo, Y. Kim, X. Fu, J.Y. Xu, J.M. Hao, K.B. He, Atmos. Chem. Phys. 14 (2014) 6571–6603.

[8] https://www.who.int/airpollution/data/cities/en/. Retrieved 01.04.2020.

[9] D. Yang, C. Ye, X. Wang, D. Lu, J. Xu, H. Yang, Atmos. Environ. 182 (2018) 171–178.

[10] A. Auld, A. Ward, K. Mustafa, B. Hansen, SAE Int. J. Engines 10 (2017).

[11] N. Hooftman, M. Messagie, J. Van Mierlo, T. Coosemans, Renew. Sustain. Energy Rev. 86 (2018) 1–21.

[12] T. V. Johnson, SAE Int. J. Engines 8 (2015).

[13] M. Rexeis, S. Hausberger, Atmos. Environ. 43 (2009) 4689–4698.

[14] P. Bielaczyc, J. Woodburn, Emiss. Control Sci. Technol. 5 (2019) 86–98.

[15] D. Bianco-Rodriguez, G. Vagnoni, B. Holderbaum, IFAC-PapersOnLine 49 (2016) 649–656.

[16] A.P. Mock, J. Kühlwein, U. Tietge, V. Franco, A. Bandivadekar, ICCT White Pap. (2014) 1–24.

[17] J. Pavlovic, B. Ciuffo, G. Fontaras, V. Valverde, A. Marotta, Transp. Res. Part A Policy Pract. 111 (2018) 136–147.

[18] A. Marotta, J. Pavlovic, B. Ciuffo, S. Serra, G. Fontaras, Environ. Sci. Technol. 49 (2015) 8315–8322.

[19] C. Brand, Energy Policy 97 (2016) 1–12.

[20] A.M. Mellor, J.P. Mello, K.P. Duffy, W.L. Easley, J.C. Faulkner, in: SAE Tech. Pap., 1998.

[21] C.T. Goralski, W.F. Schneider, Appl. Catal. B Environ. 37 (2002) 263–277.

[22] Z. Han, A. Uludogan, G.J. Hampson, R.D. Reitz, in: SAE Tech. Pap., 1996.

[23] J. Arrègle, J.J. López, C. Guardiola, C. Monin, Lect. Notes Control Inf. Sci. 402 (2010) 25–36.

[24] M.P.B. Musculus, in: SAE Tech. Pap., 2004.

[25] J.A. Last, W.-M. Sun, H. Witschi, in: Environ. Health Perspect., 1994, p. 179.

[26] F. Payri, J. Arrègle, J. Javier López, E. Mocholí, in: SAE Tech. Pap., 2008.

[27] J. Jang, Y. Lee, O. Kwon, Int. J. Automot. Technol. 18 (2017) 751–758.

[28] T.R. Dallmann, S.J. Demartini, T.W. Kirchstetter, S.C. Herndon, T.B. Onasch, E.C. Wood, R.A. Harley, Environ. Sci. Technol. 46 (2012) 8511–8518.

[29] G. Corro, React. Kinet. Catal. Lett. 75 (2002) 89–106.

[30] Y. Osaka, K. Yamada, T. Tsujiguchi, A. Kodama, H. Huang, Z. He, in: J. Chem. Eng. Japan, 2014, pp. 555–560.

[31] M.A. Patterson, S.C. Kong, G.J. Hampson, R.D. Reitz, in: SAE Tech. Pap., 1994.

[32] C.A. Idicheria, L.M. Pickett, in: SAE Tech. Pap., 2005.

[33] A.B. Dempsey, S.J. Curran, R.M. Wagner, Int. J. Engine Res. 17 (2016) 897–917.

[34] S. Curran, R. Hanson, R. Wagner, R. Reitz, in: SAE Tech. Pap., 2013.

[35] G.A. Stratakis, G.S. Konstantas, A.M. Stamatelos, in: Proc. Inst. Mech. Eng. Part D J. Automob. Eng., 2003, pp. 307–317.

[36] H.S. Chong, S.K. Aggarwal, K.O. Lee, S.Y. Yang, H. Seong, Combust. Sci. Technol. 185 (2013) 95–121.

[37] I. Atribak, A. Bueno-López, A. García-García, Combust. Flame 157 (2010) 2086–

2094.
[38] N. Pérez, J. Pey, M. Cusack, C. Reche, X. Querol, A. Alastuey, M. Viana, in: Aerosol Sci. Technol., 2010, pp. 487–499.
[39] S. Iavarone, A. Parente, Front. Mech. Eng. 6 (2020).
[40] B. Guan, R. Zhan, H. Lin, Z. Huang, J. Environ. Manage. 154 (2015) 225–258.
[41] P. Stobbe, H.G. Petersen, J.W. Hoj, S.C. Sorenson, in: SAE Tech. Pap., 1993.
[42] M. Václavík, P. Kočí, V. Novák, D. Thompsett, Chem. Eng. J. 329 (2017) 128–134.
[43] C. Zhou, Z. Feng, Y. Zhang, L. Hu, R. Chen, B. Shan, H. Yin, W.G. Wang, A. Huang, RSC Adv. 5 (2015) 28054–28059.
[44] Z. Nazarpoor, S. Golden, R.F. Liu, SAE Int. J. Mater. Manuf. 10 (2017) 72–77.
[45] T. Watanabe, K. Kawashima, Y. Tagawa, K. Tashiro, H. Anoda, K. Ichioka, S. Sumiya, G. Zhang, in: SAE Tech. Pap., 2007.
[46] K. Chen, K.S. Martirosyan, D. Luss, Chem. Eng. J. 176–177 (2011) 144–150.
[47] M. Schejbal, J. Štěpánek, M. Marek, P. Kočí, M. Kubíček, Fuel 89 (2010) 2365–2375.
[48] R. Zhan, Y. Huang, M. Khair, SAE Tech. Pap. (2006).
[49] Y. Liu, C. Su, J. Clerc, A. Harinath, L. Rogoski, SAE Int. J. Engines 8 (2015).
[50] A.P.E. York, T.C. Watling, M. Ahmadinejad, D. Bergeal, P.R. Phillips, D. Swallow, in: SAE Tech. Pap., 2009, pp. 578–589.
[51] D. Zhang, R.T. Yang, Energy and Fuels 32 (2018) 2170–2182.
[52] J. Wang, H. Zhao, G. Haller, Y. Li, Appl. Catal. B Environ. 202 (2017) 346–354.
[53] W. Tang, D. Youngren, M.M. Santa, S. Kumar, SAE Int. J. Engines 6 (2013) 862–872.
[54] L. Castoldi, N. Artioli, R. Matarrese, L. Lietti, P. Forzatti, Catal. Today 157 (2010) 384–389.
[55] Z. Liu, J. Hao, L. Fu, T. Zhu, J. Li, X. Cui, Chem. Eng. Technol. 27 (2004) 77–79.
[56] N. Serhan, A. Tsolakis, A. Wahbi, F.J. Martos, S. Golunski, Appl. Catal. B Environ. 241 (2019) 471–482.
[57] A. Sultana, M. Sasaki, K. Suzuki, H. Hamada, Appl. Catal. A Gen. 466 (2013) 179–184.
[58] M. Devarakonda, G. Parker, J.H. Johnson, V. Strots, S. Santhanam, SAE Int. J. Fuels Lubr. 1 (2009) 646–661.
[59] D.Y. Wang, S. Yao, M. Shost, J.H. Yoo, D. Cabush, D. Racine, R. Cloudt, F. Willems, in: SAE Tech. Pap., 2008.
[60] C.M. Schär, C.H. Onder, H.P. Geering, IEEE Trans. Control Syst. Technol. 14 (2006) 641–653.
[61] F. Birkhold, U. Meingast, P. Wassermann, O. Deutschmann, Appl. Catal. B Environ. 70 (2007) 119–127.
[62] L. Tan, P. Feng, S. Yang, Y. Guo, S. Liu, Z. Li, Chem. Eng. Process. Process Intensif. 123 (2018) 82–88.
[63] T. Andana, M. Piumetti, S. Bensaid, L. Veyre, C. Thieuleux, N. Russo, D. Fino, E.A. Quadrelli, R. Pirone, Appl. Catal. B Environ. 226 (2018) 147–161.
[64] Q.N. Tran, F. Martinovic, M. Ceretti, S. Esposito, B. Bonelli, W. Paulus, F. Di Renzo, F.A. Deorsola, S. Bensaid, R. Pirone, Appl. Catal. A Gen. 589 (2020).
[65] F. Martinovic, Q.N. Tran, F.A. Deorsola, S. Bensaid, R. Palkovits, W. Paulus, B. Bonelli, F. Di Renzo, R. Pirone, Catal. Sci. Technol. 10 (2020) 2193–2202.
[66] H. Shimokawa, Y. Kurihara, H. Kusaba, H. Einaga, Y. Teraoka, in: Catal. Today, 2012, pp. 99–103.
[67] F. Martinovic, T. Andana, F.A. Deorsola, S. Bensaid, R. Pirone, Catal. Letters 150 (2020) 573–585.
[68] R. Matarrese, L. Lietti, L. Castoldi, G. Busca, P. Forzatti, in: Top. Catal., 2013, pp. 477–482.
[69] I.S. Pieta, M. García-Diéguez, C. Herrera, M.A. Larrubia, L.J. Alemany, J. Catal. 270 (2010) 256–267.

[70] K. Yamazaki, Y. Sakakibara, F. Dong, H. Shinjoh, Appl. Catal. A Gen. 476 (2014) 113–120.
[71] M. Kikugawa, K. Yamazaki, A. Kato, T. Uyama, N. Takahashi, H. Shinjoh, Appl. Catal. A Gen. 576 (2019) 32–38.
[72] K. ichi Shimizu, M. Katagiri, S. Satokawa, A. Satsuma, Appl. Catal. B Environ. 108–109 (2011) 39–46.
[73] J.H. Lee, S.H. Lee, J.W. Choung, C.H. Kim, K.Y. Lee, Appl. Catal. B Environ. 246 (2019) 356–366.
[74] C.A. Neyertz, E.E. Miró, C.A. Querini, Chem. Eng. J. 181–182 (2012) 93–102.
[75] R. Jiménez, X. García, C. Cellier, P. Ruiz, A.L. Gordon, Appl. Catal. A Gen. 297 (2006) 125–134.
[76] M. Ogura, R. Kimura, H. Ushiyama, F. Nikaido, K. Yamashita, T. Okubo, ChemCatChem 6 (2014) 479–484.
[77] B.S. Sánchez, C.A. Querini, E.E. Miró, Appl. Catal. A Gen. 392 (2011) 158–165.
[78] R. Matarrese, E. Aneggi, L. Castoldi, J. Llorca, A. Trovarelli, L. Lietti, Catal. Today 267 (2016) 119–129.
[79] R. Kimura, J. Wakabayashi, S.P. Elangovan, M. Ogura, T. Okubo, J. Am. Chem. Soc. 130 (2008) 12844–12845.
[80] J. Zokoe, C. Su, P.J. McGinn, Ind. Eng. Chem. Res. 58 (2019) 11891–11901.
[81] J. Zokoe, P.J. McGinn, Chem. Eng. J. 262 (2015) 68–77.
[82] S. Bensaid, N. Russo, D. Fino, in: Catal. Today, 2013, pp. 57–63.
[83] P. Miceli, S. Bensaid, N. Russo, D. Fino, Nanoscale Res. Lett. 9 (2014) 1–10.
[84] Focus Catal. 2018 (2018) 7.
[85] Y. Bisaiji, K. Yoshida, M. Inoue, K. Umemoto, T. Fukuma, SAE Int. J. Fuels Lubr. 5 (2012) 380–388.
[86] Y. Zheng, M. Li, M. Harold, D. Luss, SAE Int. J. Engines 8 (2015).
[87] C. Lambert, R. Hammerle, R. McGill, M. Khair, C. Sharp, in: SAE Tech. Pap., 2004.
[88] A.M. Bernhard, D. Peitz, M. Elsener, T. Schildhauer, O. Kröcher, Catal. Sci. Technol. 3 (2013) 942–951.
[89] Y. Ma, X. Wu, J. Zhang, R. Ran, D. Weng, Appl. Catal. B Environ. 227 (2018) 198–208.
[90] M. Seneque, X. Courtois, F. Can, D. Duprez, Top. Catal. 59 (2016) 938–944.
[91] M. Bendrich, A. Scheuer, R.E. Hayes, M. Votsmeier, Appl. Catal. B Environ. 270 (2020).
[92] A. Burkardt, W. Weisweiler, J.A.A. Van Den Tillaart, A. Schäfer-Sindlinger, E.S. Lox, Top. Catal. 16–17 (2001) 369–375.
[93] F. Gao, C.H.F. Peden, Catalysts 8 (2018).
[94] A.R. Fahami, T. Günter, D.E. Doronkin, M. Casapu, D. Zengel, T.H. Vuong, M. Simon, F. Breher, A. V. Kucherov, A. Brückner, J.D. Grunwaldt, React. Chem. Eng. 4 (2019) 1000–1018.
[95] S.M. Maier, A. Jentys, E. Metwalli, P. Müller-Buschbaum, J.A. Lercher, J. Phys. Chem. Lett. 2 (2011) 950–955.
[96] C. Li, M. Shen, J. Wang, J. Wang, Y. Zhai, Ind. Eng. Chem. Res. 57 (2018) 8424–8435.
[97] H. Chen, Y. Xia, R. Fang, H. Huang, Y. Gan, C. Liang, J. Zhang, W. Zhang, X. Liu, Appl. Surf. Sci. 459 (2018) 639–646.
[98] D.W. Kwon, K.H. Park, S.C. Hong, Appl. Catal. A Gen. 499 (2015) 1–12.
[99] J.W. Girard, C. Montreuil, J. Kim, G. Cavataio, C. Lambert, SAE Int. J. Fuels Lubr. 1 (2009) 488–494.
[100] L. Zheng, M. Casapu, M. Stehle, O. Deutschmann, J.D. Grunwaldt, Top. Catal. 62 (2019) 129–139.
[101] P.S. Metkar, M.P. Harold, V. Balakotaiah, Appl. Catal. B Environ. 111–112 (2012) 67–80.
[102] K. Kamasamudram, N. Currier, T. Szailer, A. Yezerets, SAE Int. J. Fuels Lubr. 3 (2010) 664–672.

[103] J. Wang, Y. Ji, Z. He, M. Crocker, M. Dearth, R.W. McCabe, Appl. Catal. B Environ. 111–112 (2012) 562–570.
[104] M. Iwasaki, H. Shinjoh, Appl. Catal. A Gen. 390 (2010) 71–77.
[105] I. Heo, S. Sung, M.B. Park, T.S. Chang, Y.J. Kim, B.K. Cho, S.B. Hong, J.W. Choung, I.S. Nam, ACS Catal. 9 (2019) 9800–9812.
[106] J.Y. Luo, A. Yezerets, C. Henry, H. Hess, K. Kamasamudram, H.Y. Chen, W.S. Epling, in: SAE Tech. Pap., 2012.
[107] Q. Ye, L. Wang, R.T. Yang, Appl. Catal. A Gen. 427–428 (2012) 24–34.
[108] A. Wang, Y. Chen, E.D. Walter, N.M. Washton, D. Mei, T. Varga, Y. Wang, J. Szanyi, Y. Wang, C.H.F. Peden, F. Gao, Nat. Commun. 10 (2019) 1–10.
[109] Y. Peng, J. Li, X. Huang, X. Li, W. Su, X. Sun, D. Wang, J. Hao, Environ. Sci. Technol. 48 (2014) 4515–4520.
[110] S. Dahlin, J. Englund, H. Malm, M. Feigel, B. Westerberg, F. Regali, M. Skoglundh, L.J. Pettersson, Catal. Today (2020).
[111] F. Gao, Y. Wang, N.M. Washton, M. Kollár, J. Szanyi, C.H.F. Peden, ACS Catal. 5 (2015) 6780–6791.
[112] L. Ma, J. Li, Y. Cheng, C.K. Lambert, L. Fu, Environ. Sci. Technol. 46 (2012) 1747–1754.
[113] R. Villamaina, I. Nova, E. Tronconi, T. Maunula, M. Keenan, Appl. Catal. A Gen. 580 (2019) 11–16.
[114] Y.J. Kim, P.S. Kim, C.H. Kim, Appl. Catal. A Gen. 569 (2019) 175–180.
[115] S. Zhang, B. Zhang, B. Liu, S. Sun, RSC Adv. 7 (2017) 26226–26242.
[116] J. Li, H. Chang, L. Ma, J. Hao, R.T. Yang, in: Catal. Today, 2011, pp. 147–156.
[117] M. Fu, C. Li, P. Lu, L. Qu, M. Zhang, Y. Zhou, M. Yu, Y. Fang, Catal. Sci. Technol. 4 (2014) 14–25.
[118] S. Ding, F. Liu, X. Shi, H. He, Appl. Catal. B Environ. 180 (2016) 766–774.
[119] Z. Ma, X. Wu, Z. Si, D. Weng, J. Ma, T. Xu, Appl. Catal. B Environ. 179 (2015) 380–394.
[120] M. Iwasaki, K. Dohmae, Y. Nagai, E. Sudo, T. Tanaka, J. Catal. 359 (2018) 55–67.
[121] A. Satsuma, J. Shibata, K.I. Shimizu, T. Hattori, Catal. Surv. from Asia 9 (2005) 75–85.
[122] A. Shichi, A. Satsuma, T. Hattori, Appl. Catal. B Environ. 30 (2001) 25–33.
[123] S.G. Aspromonte, E.E. Miró, A. V. Boix, Catal. Commun. 28 (2012) 105–110.
[124] T. Wittka, B. Holderbaum, P. Dittmann, S. Pischinger, Emiss. Control Sci. Technol. 1 (2015) 167–182.
[125] G. Karavalakis, S. Stournas, E. Bakeas, Atmos. Environ. 43 (2009) 1745–1752.
[126] H.G. Roh, D. Lee, C.S. Lee, J. Energy Inst. 88 (2015) 376–385.
[127] A. Keskin, M. Gürü, D. Altiparmak, in: Energy Convers. Manag., 2011, pp. 60–65.
[128] X. Lu, Y. Qian, Z. Yang, D. Han, J. Ji, X. Zhou, Z. Huang, Energy 64 (2014) 707–718.
[129] M. V. Twigg, Appl. Catal. B Environ. 70 (2007) 2–15.
[130] M.L. Stewart, C.J. Kamp, F. Gao, Y. Wang, M.H. Engelhard, Emiss. Control Sci. Technol. 4 (2018) 260–270.
[131] K.G. Rappé, Ind. Eng. Chem. Res. 53 (2014) 17547–17557.
[132] T.C. Watling, M.R. Ravenscroft, G. Avery, in: Catal. Today, 2012, pp. 32–41.
[133] S. Bensaid, V. Balakotaiah, D. Luss, AIChE J. 63 (2017) 238–248.
[134] D. Karamitros, G. Koltsakis, Chem. Eng. Sci. 173 (2017) 514–524.
[135] F. Marchitti, I. Nova, E. Tronconi, Catal. Today 267 (2016) 110–118.
[136] T. Wolff, R. Deinlein, H. Christensen, L. Larsen, SAE Int. J. Mater. Manuf. 7 (2014).
[137] Y. Xi, N.A. Ottinger, Z.G. Liu, React. Chem. Eng. 4 (2019) 1090–1102.

Chapter 2

2. On-Filter Integration of Soot Oxidation and Selective Catalytic Reduction of NO_x with NH_3 by Selective Two Component Catalysts

Chapter summary

In this chapter the enhancement of the soot oxidation over the SCRoF was investigated. The focus was on developing a soot oxidation catalyst compatible with the SCR reaction, meaning that no significant NH_3 oxidation is taking place over the soot oxidation catalyst. The SCR reaction was included in the integrated reaction, however it was assumed to be „ideal" Fast SCR. From the screened soot oxidation catalysts, 20 wt% K_2CO_3 impregnated over CeO_2-ZrO_2 (KCZ) catalyst was found to have the best performance with strong synergy between the potassium and support. When KCZ was mixed with Fe-ZSM5 high NO_x conversion and selectivity was achieved in the whole temperature range investigated while the soot oxidation temperature was lowered by 200 °C. Although KCZ catalyzed the NO_2-soot reaction the SCR reaction was kinetically much faster and consumed the NO_2 before it could react with the soot. The soot oxidation was mainly through catalyzed O_2 oxidation over KCZ.

Adapted from publication Catalysis Letters (2020) 150:573–585
https://doi.org/10.1007/s10562-019-03012-1

2.1. Introduction

Diesel engines have higher net efficiency than gasoline ones, for which their use is widespread in long haul transport, heavy work machines and passenger vehicles. The emission of NO_x and soot however remains problematic and, with more stringent regulation, the aftertreatment devices become more complex and expensive. Soot abatement remains especially challenging since oxidation with oxygen starts only at temperatures above 500 °C [1–4]. Typical exhaust temperatures, however, are in the range of 200-400 °C, and exceeding 500 °C only under maximum load or artificial conditions like active regeneration by fuel injection [1–4]. The soot oxidation temperature can be reduced by the use of the soot oxidation catalysts or through the NO_x present in the exhaust gas, NO_2 being a much stronger oxidant for soot than O_2 [1,5,6]. In the latter case, catalytic systems usually involve an active component (in most applications Pt) for NO to NO_2 oxidation, in the so called continuously regenerating trap (CRT or cDPF) [1], which is practically effective only if both NO_x levels and exhaust temperatures are within appropriate ranges, as happens for heavy duty diesel engines. However, in passenger vehicles, NO_2 is present in concentrations which are insufficient to induce appreciable soot oxidation by passive regeneration [1,4]. For this reason, active regeneration is the preferred mechanism to restore the functionality of the DPF after reaching its limit of soot loading, which is determined by pressured drop constraints as well as the need to avoid the risk for an excessive temperature rise inside the filter [4,7,8]. It is preferable to reduce the active regeneration

temperature on the DPF to avoid filter damage as well as additional high fuel consumption. For this, the filter is usually coated with a catalyst, that is capable of catalyzing soot oxidation relying mainly on oxygen. These catalysts are necessarily stable and usually based on doped cerium oxides, perovskites, Ag or alkali salt [9–12].

To achieve the latest Euro 6 regulations a section for NO_x reduction in the aftertreatment system has to be included. There are generally 2 main types of NO_x reduction systems:

1. NO_x reduction by NH_3 from decomposition of urea solution. The catalysts are mainly based on Fe or Cu zeolites or titania-supported vanadia [13,14], according to the preferred temperature ranges of application.
2. LNT catalysts which operate in alternating rich-lean regimes for NO_x capture and reduction [14].

Between these two systems, the urea-based system is preferred in some applications for the real driving emission treatment as it presents higher conversion, wider operational temperature window, considerably better stability and much lower fuel penalty (0.5% vs 2%) [14,15].

The typical aftertreatment system consists of several bricks, as well as a dedicated urea solution reservoir, with different functionalities and their integration in vehicles is highly complex and limited by space requirements (especially in LDD). One way to reduce the size of the aftertreatment is to integrate diesel particulate filter (DPF) and urea-mediated selective catalytic reduction (SCR) of NO_x into the same device, named Selective Catalytic Reduction on Filter (SCRoF) [4,5,8,16,17]. With this, the complexity and size are reduced and, due to close coupling, higher temperatures can be achieved enabling more efficient operation. For the SCRoF, a monolith is used with channels plugged on alternating ends, thus forcing the exhaust gas through the monolith wall, with the SCR catalyst which is located inside the filter pores. Soot is filtered and retained inside and on the wall, most of it (>80%) present on the top as soot cake. The current state-of-the-art of the SCR catalyst in the commercial SCRoF system is Cu-zeolite, more specifically Cu-chabazite, deposited inside the pores of SCRoF by BASF [4]. Cu-chabazite offers high SCR activity and hydrothermal stability however it lacks any soot oxidation capability [7,8,16,18–20]. For SCRoF, it has been shown that soot oxidation and regeneration is inhibited by the much faster SCR reaction which quickly consumes the NO_2 leaving none for soot oxidation. This leads to much faster pore clogging with soot and higher backpressure [7,8,16,18–20]. This can be presented as competing reactions R1-R3:

$2NH_3 + NO + NO_2 \rightarrow 2N_2 + 3H_2O$	R1 Fast SCR reaction
$C + NO_2 + O_2 \rightarrow CO + NO$	R2Soot oxidation by NO_2
$2C + O_2 + 2NO_2 \rightarrow CO_2 + 2NO$	R3

Rappe [8] showed that on SCRoF the soot conversion profile was shifted upwards 70 °C in the presence of the SCR reaction compared to the case without SCR, under the same conditions. As a solution, non-uniform SCR catalyst distribution in the monolith was suggested, with the SCR catalyst concentrated in the

downstream portion and a NO_2/NO_x ratio higher than 0.5. Watling, Marchitti and Kolstakis [5,7,18] also showed for SCRoF that under 450 °C the soot oxidation and filter regeneration was significantly inhibited due to NO_2 consumption and only above 450 °C the oxidation by O_2 was prevalent. It was further suggested that concentrating the catalyst in the downstream portion of the filter improved the soot oxidation activity due to smaller NO_x conversion at the inlet. As will be shown later, the NO to NO_2 oxidation and soot oxidation by NO_2 reactions cannot be used on SCRoF since the NO_2 is consumed quickly by the SCR reaction [8]. SCRoF is usually regenerated by raising the temperature above 600 °C by injecting hydrocarbons. This is undesirable since excess fuel is consumed and elevated temperatures can irreversibly damage the filter or accelerate the ageing of the SCR catalyst [4,8].

To introduce soot oxidation function on SCRoF, and to reduce the regeneration temperature and time, a novel dual layer reactor configuration is proposed here for the first time. Dual layer monoliths have been used in diesel aftertreatment monoliths such as LNT+SCR combination [14], for widening operational window by the combination of Fe and Cu zeolite [13] and for stabilizing SCRoF with silica [21]. In the proposed novel dual layer configuration, a soot oxidation catalyst layer is situated on the top of the filter on the inlet side, in contact with the soot cake. The SCR catalyst is deposited inside the monolith like in conventional SCRoF system. Such dual layer configuration could perform both the NO_x reduction and achieve significant reduction of the soot regeneration temperature, thus reducing the associated fuel penalty, as well as mitigate the conditions that might lead to catalyst and filter damage during active regeneration. Since the ammonia passes through the top layer first, any ammonia oxidation would be detrimental for the SCR reaction. The challenge was to find a catalyst that is highly active for soot oxidation in loose contact, however completely inactive for ammonia oxidation. It has been found that catalysts with alkali carbonates impregnated on supports with neutral or basic surface (e.g. MgO, sodalite, MgAlO, CeO_2, ZrO_2, etc.) are suitable for such purpose. In this chapter, the interaction between a suitable catalyst with high soot oxidation activity and a conventional SCR catalyst (Fe-ZSM5) are also explored in a laboratory setup.

2.2. Experimental

2.2.1. Catalysts' preparation

For the soot oxidation catalyst, CeO_2-ZrO_2 (labelled CZ) with Zr:Ce atomic ratio 9:1 (Alfa-Aesar, product number 39216) was impregnated with 20 wt.% K_2CO_3 by wet impregnation: CZ was placed in a 0.03 M aqueous solution of K_2CO_3 and stirred for 24 h and then water was evaporated at 80 °C. The obtained 20 wt.% K_2CO_3/CeO_2-ZrO_2 (KCZ) had K:Zr:Ce bulk atomic ratio 3:9:1 determined by EDS, or 8 wt.% K. CZ was chosen as the support, as after screening of several different types of potential supports (MgO, MgAlO, nepheline, CeO_2-CuO) the

CZ had the best performance for soot oxidation and low ammonia oxidation. The powder was dried overnight at 100 °C and calcined at 800 °C for 5 h with a heating rate of 10 °C/min.

To demonstrate the effect of excessive NH_3 oxidation on the SCR reaction in the SCR and soot oxidation coupled reaction CZ was impregnated with 10 %wt $AgNO_3$ (Ag/CZ). Ag/CZ was chosen because of soot oxidation characteristics comparable to KCZ (see Table 2.1 and [12,22,23]). Other catalysts were also prepared by using different supports synthetized with different methods (MgAlO, MgO, nepheline, CeO_2-CuO) wet impregnated with 20 wt.% K_2CO_3 by employing the same procedure described previously for the KCZ catalyst. These supports were chosen after literature review and screening of several potential catalysts. The preparation of these materials are given in the supplementary material and in references [24–27].

To achieve stable performance and high NO_x conversion in a wide temperature range and because of its widespread industrial use, for the SCR reaction Fe-ZSM5 was prepared by ion exchange. First NH_4-ZSM5 (Alfa Aesar, SiO_2: Al_2O_3 = 23) was calcined at 500 °C for 3 h to transform it into H-ZSM5. H-ZSM5 was placed in a 50 mM aqueous solution of $Fe(NO_3)_3$, stirred at 50 °C for 24 hours. The slurry was then washed and dried overnight at 100 °C and calcined at 700 °C for 6 h with a heating rate of 10 °C/min. Final Fe content in the Fe-ZSM5 was determined by EDS and ICP to be 0.5 wt.%.

The soot used in the reactivity tests was a commercial Printex U carbon black from Degussa, commonly used as model soot in the scientific literature. The soot had an average particle size 25 nm (supplier specification), specific surface area 88 m^2/g and cumulative pore volume 0.31 mL/g obtained from BET measurement.

2.2.2. Catalyst characterization

XRD was conducted for phase verification with X'Pert Philips PW3040 diffractometer equipped with Pixel detector using a Cu Kα radiation. The diffractograms were obtained in the 2θ range 20-80° with 0.013° step size.

H_2-TPR was conducted on TRPDO-1100 equipment (Thermo Scientific) with 5% H_2 in Ar as reaction gas. Before the test, the samples were pretreated in N_2 at 550 °C and cooled to room temperature. After that, reduction was performed with 5 °C/min ramp until 850 °C. Soot-TPR was performed in the reactor setup (see below) by mixing the catalyst and the soot and ball milled for 15 minutes to achieve tight contact. The temperature was increased with 5 °C/min rate in N_2 gas without oxygen.

Specific surface area was determined on Tristar II 3020 instrument (Micrometrics) by N_2 physisorption of the catalyst pretreated at 200 °C for 2 hours. The reported values (S_{BET}) were calculated according to the BET method.

Morphology and elemental composition were determined by field emission scanning electron microscopy (FE-SEM) using Zeiss MERLIN Gemini II equipped with EDS at 3 keV accelerating voltage and different magnifications.
NO_x temperature programmed desorption-oxidation (TPDO) was performed in the reactor (see below) on the KCZ sample to determine the NO_x adsorption capacity and reactivity. The catalyst was fully saturated with 250 ppm NO, 250 ppm NO_2, 4% O_2 in N_2 at 200 °C and desorbed with a heating rate of 5 °C/min in 4% O_2 in N_2 atmosphere with w/f 0.027 g_{cat}·s/mL. To determine the soot-NO_x-O_2 reactivity and interaction, the desorption-reaction was done in the presence and absence of soot.
NH_3-TPD was performed in the reactor (see below) by saturating the catalyst with 500 ppm NH_3 in N_2 at 100 °C and desorbed in N_2 with a 5 °C/min temperature ramp with w/f 0.027 g_{cat}·s/mL.

2.2.3. Catalytic tests

Catalytic tests were conducted in a 10 mm i.d. quartz tube reactor typically with 270 mg of powdered (<100 μm fraction) and/or pelletized (<300 μm fraction) catalyst placed on a porous sintered glass membrane inside the tube. The quartz reactor containing the catalyst bed was placed inside a PID-controlled vertical oven. A thermocouple was vertically put on the top of the catalytic bed in order to track and measure the reaction temperature. In all tests, a temperature ramp of 2 °C/min was used, starting after the outlet composition stabilized at initial temperature of 200 °C (waiting time c.a. 15 minutes). Such slow ramp ensured that the NO_x and NH_3 composition was similar as in isothermal test in the observed range.
A 4-way valve was placed upstream the reactor allowing it to bypass and enabling the analysis of both inlet and outlet gas mixture through a single device. The NO, NO_2, N_2O, NH_3, CO and CO_2 species were continuously analyzed with UV (Limas 11, ABB) and NDIR (Uras 14, ABB) analyzers. The volumetric flowrate was 600 mL/min in all cases which is typically equivalent to 80 000 h^{-1} GHSV or *w/f* of 0.027 g·s/mL.
Depending on the test, different gas mixture combinations were used. In soot oxidation tests with oxygen, 270 mg of catalyst and 30 mg of soot were mixed gently with spatula to obtain loose contact and oxidized in a 4% O_2 in N_2 gas flow. Soot oxidation in the presence of NO_x was also performed, in which case 250 ppm NO and 250 ppm NO_2 was also added to the oxidizing gas. In some cases, the KCZ was saturated with NO_x (labeled KCZ-sat) at 200 °C before the reaction to reproduce steady state conditions and avoid interference between NO_x adsorption and soot reactivity.
To demonstrate the catalytic effect of KCZ on the soot-NO_x-O_2 reaction, comparative soot oxidation tests were conducted on Fe-ZSM5 and KCZ-sat in a gas mixture containing 500 ppm NO_x with initial ratio NO_2/NO_x=0.5. The non-catalytic test was performed by mixing SiC with soot under the same conditions. The SCR reaction over Fe-ZSM5 was conducted by feeding 4% O_2, 250 ppm NO,

250 ppm NO_2, 500 ppm NH_3 in N_2 over 270 mg of catalyst with and without 30 mg of soot.

The SCR conversion was calculated according to the following formula:

$$X_{NOx} = \frac{[NO_x]_{in} - [NO_x]_{out}}{[NO_x]_{in}}$$

while for the N_2 selectivity the following one was employed:

$$S_{N_2} = 1 - \frac{2[N_2O]_{out}}{[NO_x]_{in} - [NO_x]_{out} + [NH_3]_{in} - [NH_3]_{out}}$$

The temperatures when 10% 50%, 90% of soot was converted and the CO_x concentration achieved maximum conversion (T_{10}, T_{50}, T_{90}, T_{max}) were used for comparison of different catalysts and configurations and reference to non-catalytic tests. T_{10} and T_{90} are especially useful for the comparison of the onset of the soot oxidation and to evaluate the temperature at which the soot is fully oxidized. The turnover frequency of the soot oxidation was calculated according to the formula for the specific soot oxidation rate proposed in [28,29]. It was evaluated at 400 °C and expressed as normalized soot oxidation rate with the unit s $\mu g_{oxidized\ soot} \cdot s^{-1} \times g_{initial\ soot} \cdot g^{-2}_{catalyst}$. The soot oxidation reproducibility can be low in loose contact as uncertainty is involved with the mixing mode. Soot oxidation was repeated in triplets over several catalysts and the maximum change in T_{max} observed was always within ± 5 °C.

The integrated soot oxidation and NO_x SCR reactions were performed by employing 270 mg of KCZ, 270 mg of Fe-ZSM5 and 30 mg of soot with different contact and granulation modes. The flowrate of the gaseous reaction mixture was 600 mL/min and consisted of 250 ppm NO, 250 ppm NO_2, 500 ppm NH_3 and 4% O_2 in N_2.

The relative positioning of the soot oxidation and SCR catalyst was evaluated by dimensional analysis to compare the catalyst positioning in the laboratory reactor with the real-life monolith and experiments were conducted to demonstrate the importance of the contact mode and occlusion between the soot oxidation and SCR catalyst and soot. Two cases were compared in the dimensional analysis:

1. Physical mixture where the SCR and soot oxidation catalyst powders were physically mixed.
2. Dual-bed configuration with soot catalyst on top and separated with glass wool from the SCR catalyst on the bottom.

To compare the diffusive and convective fluxes, the Peclet number was evaluated. The assumptions and equations used are given in the supplementary material. At 300°C the estimated Pe number was 0.35 in the monolith, meaning that the diffusional fluxes are the main transport form of the reactant species. For the dual bed reactor configuration, with the catalyst separated in layers, the estimated Pe number 28.32 which means that the SCR reactions in the bottom layer had no effect on the soot oxidation in the upper layer and the soot oxidation reactions were not influenced by diffusion and the SCR reaction. This drastic difference is because the wall flow velocity in the monolith is almost 7 times lower than the

flow velocity in the tubular reactor [8,16]. The Pe number for the physical mixture of the two catalyst in the reactor was 0.95, slightly higher than in the monolith, but the characteristic lengths (~100 µm) and the transport mode was still in the diffusional regime and approximated the monolith quite well (see e.g. [16,18]). The lower distance between the particles in the physical mixture compared to the distance between the dual bed configuration (100 µm compared to 3 mm) enabled the diffusional operating regime in the reactor and approximated the monolithic configuration closely.

Different configurations were tested to demonstrate the influence of different contact modes, the importance of the soot catalyst-soot contact, the impact of the SCR catalyst acting as a barrier as well as the influence of diffusion and NO_x adsorption (also shown schematically on Figure 2.1). To do this, different granulations of the used catalysts were implemented, the "powdered" catalysts refer to finely crushed catalyst, which was easily sieved through the 100 µm sieve, while the "pelletized" fraction refer to the fraction between 300-500 µm :

1. 270 mg of pelletized KCZ mixed in loose contact with 30 mg of soot and with powdered 270 mg Fe-ZSM5 also in loose contact.
2. 270 mg of powdered KCZ and 30 mg of soot in loose contact, mixed with pelletized 270 mg of the SCR catalyst in loose contact
3. To determine the worst-case scenario for the SCR reaction, powdered 270 mg of KCZ-Sat was mixed with 30 mg of soot in loose contact and with powdered 270 mg of the SCR catalyst.
4. 270 mg of KCZ and 270 mg of Fe-ZSM5 catalyst pelletized together in tight contact and mixed with 30 mg of soot in loose contact.
5. In the dual bed reactor system, the 270 mg of Fe-ZSM5 was placed on the bottom and sealed with glass wool. In the upper layer 270 mg of KCZ-sat was mixed in loose contact with 30 mg of soot.
6. To demonstrate the negative effect of ammonia oxidation, powdered 270 mg of Ag/CZ was used as soot oxidation catalyst mixed with 30 mg of soot and 270 mg of Fe-ZSM5.

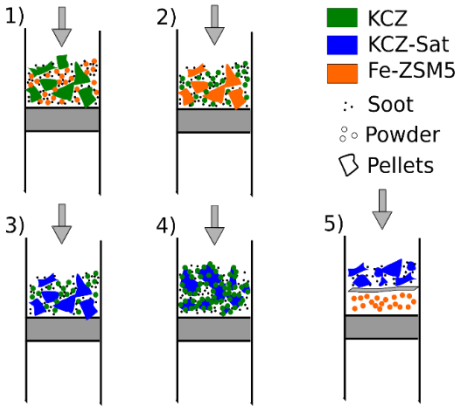

Figure 2.1. Schematics of different reactor configurations used for the physical mixture experiments.

While there is a lot of research reports and patents concerning the use of K in aftertreatment devices (LNT, DPNR, CRT) [9,30,31], the main issue that have prevented their wide-spread use is the low stability. To check the stability of the KCZ catalyst, the following tests were conducted:

1. Low temperature stability: repeated tests of soot combustion with O_2 were performed with the same catalyst. During each test, the temperature was allowed to reach 650°C regardless if the soot was burned completely.
2. High temperature stability in wet atmosphere: the KCZ catalyst was hydrothermally treated at 700°C for 7 h in 4 % O_2 and 5 % H_2O in N_2. This accelerated ageing is equivalent to c.a. 30 000 km of normal operation [31].

2.3. Results and discussion:

2.3.1. Characterization results

The diffractograms of the CZ and KCZ catalysts, reported in Figure S2.1, are practically equal suggesting that no phase transformation occurred. The potassium carbonate phase was not detected as it was uniformly distributed on the CZ support surface and likely because of the overlapping of the main diffraction peaks of the K_2CO_3 with CZ [32]. Indeed, for potassium insertion to occur in the zirconia lattice prolonged calcination at temperatures above 900 °C is required [33]. Characteristic peaks revealed the tetragonal structure of Ce-stabilized ZrO_2 ($Zr_{0.88}Ce_{0.12}O_2$-t) as the dominant phase with smaller amount of monoclinic phase zirconia (ZrO_2-m). The average crystallite size, calculated according to the Scherrer equation, was 22.5 nm.

The FE-SEM images, shown in Figure S2, reveal uniform coating of CZ with the K_2CO_3 on the KCZ sample. After impregnation, the particle size slightly increased and the edges of the CZ became rounder as they were covered with potassium (see Figure S2.2A and S2.2B). After hydrothermal ageing, aggregates of recrystallized potassium salts were found in several spots, indicating that the hydrothermally aged catalyst had lower potassium dispersion (Figure S2.2C). These crystals were likely formed by the excess potassium that is not adhering strongly to the support surface.

The BET surface area and microporosity for both the CZ and KCZ samples were low, 8.51 m^2/g and 9.42 m^2/g respectively. The addition of potassium did not change significantly the surface area.

The ammonia TPD profile, reported in Figure 2.2A, indicates the presence of small amount of acid sites on the CZ support. However, after adding potassium on the CZ support, all the acid sites disappeared and there was no NH_3 adsorption/desorption on the sample. From this, we can infer that the acid sites (both Lewis and Bronsted) are poisoned and/or blocked by the potassium that prevents any ammonia reactivity [35]. In contrast, by adding Ag on CZ, the

number of acid sites increased. In fact, a pronounced peak can be observed in the low temperature region, while the NH_3 signal quickly decreases, most likely because the adsorbed ammonia was oxidized by the Ag.

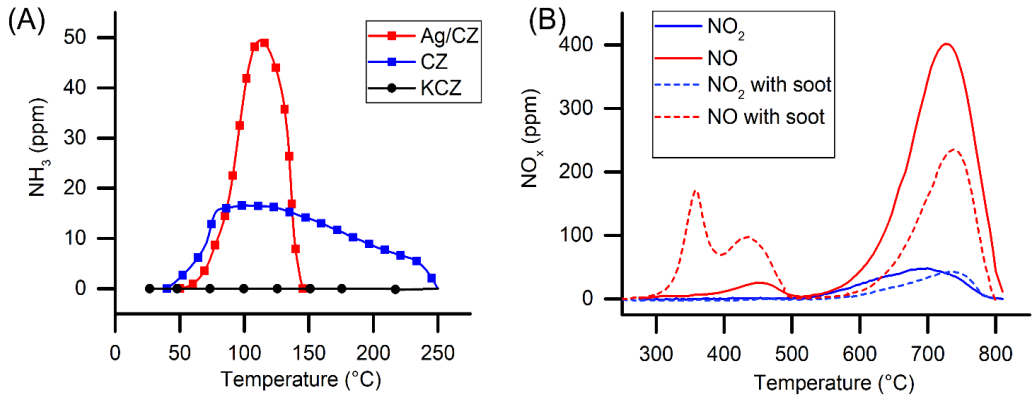

Figure 2.2. (A) NH_3-TPD of CZ, KCZ and Ag/CZ samples; (B) NO_x TPDO of the KCZ sample in absence (full lines) and presence (dashed lines) of soot.

In Figure 2.2B the NO_x TPDO of the KCZ catalyst is shown. During saturation, both NO and NO_2 were adsorbed on the sample with simultaneous evolution of CO_2, suggesting that the following reaction occurred:

$K_2CO_3 + 2\ NO_2 \rightarrow 2\ KNO_3 + CO_2$ R4

$KNO_3 \rightarrow KNO_2 + 1/2O_2$ R5

$2\ KNO_2 \rightarrow K_2O + 2NO + 1/2O_2$ R6

$2K_2NO_3 + C \rightarrow 2K_2O + CO_2 + 2NO$ R7

During NO_x-TPDO, 2 peaks were identified on the KCZ-sat samples: a small peak at 450 °C of the chemisorbed nitrites, and another at 740 °C of the reactively adsorbed nitrite and nitrated potassium salts (Figure 2.2B) [35,36]. Complete decomposition occurred slightly above 800 °C (R6). During adsorption most of the adsorbed species on the catalyst were NO_2, forming nitrates (R4) and the adsorption of NO was minimal. While most of the adsorbed species were NO_2, NO was the main component observed during desorption. This was likely because of the nitrate decomposition into nitrite above 500 °C according to R5 [37]. When soot was added to the saturated KCZ in loose contact, the NO_x adsorption and desorption dynamics during the TPDO changed significantly, and NO_x was released at significantly lower temperatures. Additional peak was observed at much lower temperature (at 360 °C), simultaneously accompanied with significantly higher soot combustion rates (see Figure 2.2B). This indicates that the NO_2 adsorbed on K has higher reactivity with soot and KCZ catalyzes not only the oxidation of soot with O_2 but also the soot-NO_2-O_2 reaction (see Figure 2.4 for corresponding the soot oxidation). Similar phenomena were investigated in more detail on Pt-K/Al_2O_3 [35–39], however in our case higher desorption temperature and no platinum group metal was used. The total amount of NO_x adsorbed-desorbed on the catalyst was 1.24 mmol NO_x/g_{cat} in both cases, meaning about 65% of K was present in the nitrate/nitrite form. The rest of the K is

possibly in the form -O-K on the surface or covered and inaccessible for NO_x adsorption [32].

In Figure 2.3 the soot-TPR and H_2-TPR are shown. CZ in tight contact with soot showed small ability to generate reactive oxidizing species during soot-TPR, i.e. the oxygen mobility was low. K_2CO_3 alone, however, could oxidize higher amount of soot. The mechanism for this, suggested in [27], is:

$$C + K_2CO_3 \rightarrow CO_2 + K_2O \qquad R8$$

In [27] it was also investigated in detail the reason why K_2CO_3 impregnated on ZrO_2 and CeO_2 could oxidize higher amount of soot. The support, coupled with potassium (K^+) with high electron positivity, could destabilize the oxygen on the surface in the form of O-K bonds [35–37]. This increased the surface oxygen mobility of the support and facilitated oxygen spillover to activate the soot oxidation.

Furthermore, the activity for the Boudouard reaction or incomplete soot oxidation (R9) on potassium-containing samples was increased at temperatures above 600°C as high CO production was observed.

$$C + CO_2 \rightarrow 2CO \qquad R9$$

The enhanced reducibility of the support by potassium was further confirmed by H_2-TPR. The H_2 reduction of CZ had a single peak at 610 °C, which corresponds to the reduction of the CeO_2 to Ce_2O_3 in the sample. According to the stoichiometric calculations, the total amount of H_2 uptake (465 µmol/g) on CZ corresponded to the Ce^{4+} to Ce^{3+} reduction. While K_2CO_3 by itself was not reducible by H_2, the KCZ sample had higher H_2 uptake (761 µmol/g), nearly double the amount of the CZ sample. It is hypothesized that the addition of K enhanced the reducibility of ZrO_2, which is not reducible by itself [38]. Visually the same color change was observed, the fresh KCZ was transformed from pale yellow to dark brown after H_2-TPR.

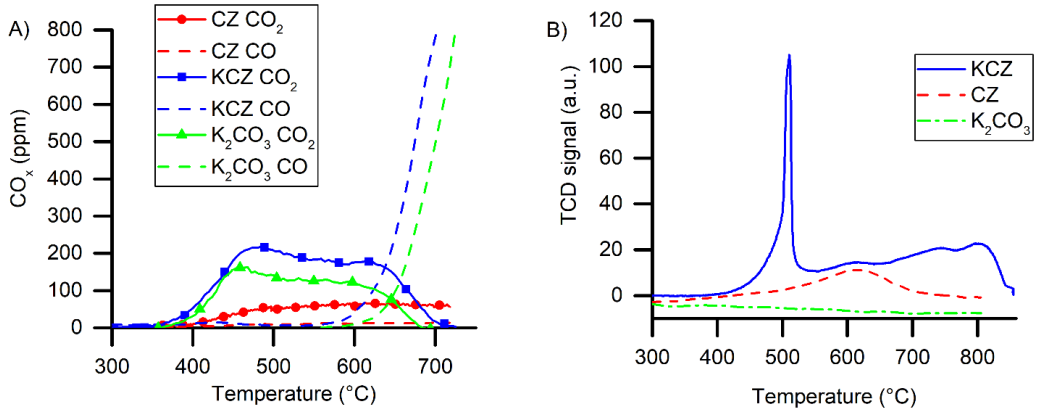

Figure 2.3. Soot (A) and H_2 -TPR (B) of K_2CO_3, CZ and KCZ samples.

2.3.2. Catalytic activity of the soot oxidation catalyst

In Figure 2.4 and Table 2.1 the effect of different supports impregnated with K_2CO_3 on the oxidation of soot is compared. The CZ support demonstrated superior performance with respect to the other supports and it was chosen for further testing. Supports with redox capability (e.g. CeO_2-CuO, CeO_2-ZrO_2) had some synergistic effect with potassium, while neutral supports (e.g. MgO, MgAlO) always had worse performance than pure K_2CO_3 (see Table 2.1). As illustrated in Figure S2.3, the optimal loading was found to be 20 wt.% K_2CO_3 on CZ, while above this loading the conversion decreased. The optimal K loading amount found matches closely the reported values in literature as optimal [10,22,24,25,39,40]. As can be seen from Table 2.1 and Figure 2.4, the CZ support alone had no effect on soot oxidation in loose contact and it was practically the same as the blank test with SiC. The K_2CO_3 powder had lower soot oxidation activity than KCZ, suggesting strong interaction and synergy between the CZ support and potassium. In fact, the KCZ catalyst in loose contact had much better soot oxidation activity than the CZ support in tight contact with soot (Figure 2.4), i.e. the improvement of the soot oxidation activity cannot be attributed simply to enhanced contact.

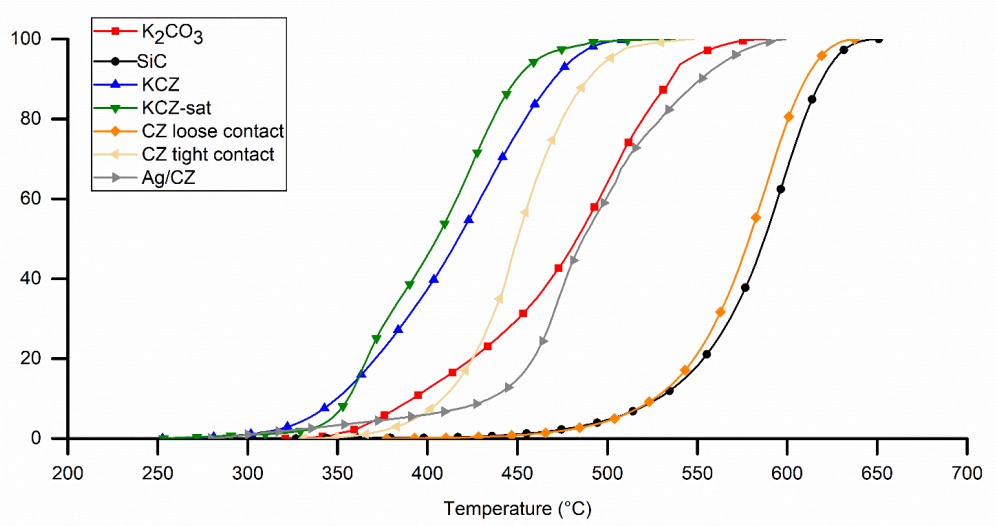

Figure 2.4. Soot-TPO activity comparison of potassium carbonate, CZ support, KCZ and KCZ-Sat on soot oxidation. Reaction conditions: *w/f* 0.027 g_{cat}·s/mL, 4% O_2 in N_2, 9:1 catalyst:soot mass ratio, loose contact, 2 °C/min heating ramp.

Table 2.1. Soot oxidation characteristics of the screened catalyst active for soot oxidation with O_2. Reaction conditions same as in Fig.2.4.

Catalyst	T_{10} [°C]	T_{50} [°C]	T_{max} [°C]	T_{90} [°C]	CO_2 selectivity[a]	Specific soot
SiC	528	587	594	620	51	0
CZ loose contact	526	579	586	610	63	0
CZ tight contact	408	450	443	489	91	1.25
K_2CO_3	391	483	497	536	88	1.13
KCZ-Sat	355	405	425	448	95	2.83
KCZ-Sat[b]	354	391	356	433	95	3.2
10% K_2CO_3/CZ	407	470	472	526	92	1.53
20% K_2CO_3/CZ (KCZ)	348	417	429	470	93	2.91
30% K_2CO_3/CZ	412	475	478	534	93	1.99
40% K_2CO_3/CZ	418	488	498	540	91	0.71
20% K_2CO_3/MgAlO	473	524	526	570	92	0.14
20% K_2CO_3/MgO	471	537	544	571	78	0.12
20%K_2CO_3/Nepheline	475	536	544	569	79	0.17
20% K_2CO_3/CeO_2-CuO	430	448	494	540	98	0.40
Ag/CZ	434	485	469	552	99	0.28

[a]CO_2 selectivity at T_{max}, selectivity changes little (±2%) during the reaction.
[b]In this case the reaction gas also contained 250 ppm NO and 250 ppm NO_2.
[c]The specific soot oxidation rate was calculated at 400 °C and expressed as $[\mu g_{oxidized\ soot} \cdot s^{-1} \times g_{initial\ soot} \cdot g^{-2}_{catalyst}] \times 1000$

KCZ-Sat had higher activity than KCZ, however this was due to the effect of NO_x present on the catalyst. The KCZ catalyzes the reaction between the adsorbed NO_x and soot since the presence of soot improved the release of NO_x on KCZ-Sat (see Figure 2.2B), which is accompanied by high soot oxidation rates (Figure 2.4). The mechanism of the soot oxidation over cerium and doped cerium oxides was investigate extensively in literature by different methods. It is generally accepted that the oxidation of the soot and NO is initiated with the activation and adsorption of gas phase oxygen on the surface, which is subsequently transferred to the reacting species [11,28,29,41]. The promoting effect of potassium on this catalytic cycle is still disputed, however the evidence points for the electron transfer mechanism (e.g. [9,25,27]), proved by UPS and FTIR. Potassium, due to its high electron positivity, enhances the electron transfer between the support surface and the molecule receiving it. In the case of potassium doping it is still disputed if oxygen receives the electron forming reactive gaseous oxidative radicals (e.g. CO_3^{2-}, O_2^{2-}) or it is directly transferred to soot [9, 22, 25-27, 35]. To demonstrate the catalytic effect of KCZ on the soot-NO_x-O_2 reaction, comparative soot oxidation tests were conducted on Fe-ZSM5 and KCZ-sat in a gas mixture containing 500 ppm NO_x with initial ratio of NO_2/NO_x 0.5. The difference in the NO_2/NO_x ratio on Fe-ZSM5 and KCZ indicates the rate and efficiency of NO_2 utilization for soot oxidation. This is illustrated in Figure S2.4, where the NO_2/NO_x ratio during the soot oxidation with NO_x is much lower in the presence of KCZ than on Fe-ZSM5. Fe-ZSM5 has no catalytic effect for soot oxidation with NO_2 (see e.g. [18] and Figure S2.5) meaning that the NO_2 is reacting with the soot from the gas phase and the NO_2/NO_x ratio during the soot oxidation remains always higher than 0.25. NO_2 however, becomes more reactive with soot in presence of KCZ and during the reaction almost all the NO_2 is effectively utilized for soot oxidation. With potassium the NO_2 is adsorbed and activated becoming more reactive with soot. This was also confirmed with the NO_x TPDO in the presence of soot, as illustrated in Figure 2.2B.

For the application of the dual layer, it is necessary that the soot oxidation catalyst is not oxidative towards ammonia and allows the SCR reaction to proceed. Over the KCZ and over catalysts described in Table 2.1, neither ammonia adsorption nor oxidation in O_2 and O_2 + NO_x atmosphere was observed. The NH_3 oxidation started at temperatures higher than 500 °C and it was practically the same as the non-catalytic oxidation (Figure S2.5). This was achieved by tailoring the catalyst surface properties as the potassium poisoned the acid sites on the catalyst and prevented ammonia adsorption and activation thereby reaction (see Figures S2.2 and S2.5 and [34]). In contrast, the CZ support and the Ag/CZ catalyst had high ammonia conversion and NO production.

2.3.3. Catalytic activity of SCR catalyst

For the SCR catalyst the Fe-ZSM5 catalyst was chosen because of high NO_x conversion in wide operational temperature range, as it has been investigated in

detail in the scientific literature and because of its widespread commercial use [13,42–44]. Cu zeolite was not used as at higher temperatures the NO_x conversion decreased and ammonia oxidation was more pronounced [8,13,17,18,44]. As illustrated in Figure 2.5A, Fe-ZSM5 had no catalytic effect on the soot oxidation in oxygen and was the same as the non-catalytic oxidation. In the presence of NO_x, the soot oxidation by the gas phase NO_2 started already at low temperatures (T_{10} = 384 °C) however the soot oxidation rate was rather slow due to limited NO_x availability. However, using the same reaction conditions and in the presence of NH_3, the oxidizing effect of NO_2 was lost due to much faster NO_2 consumption by the fast SCR and the soot conversion showed the same profile as the soot oxidation in only O_2. This finding is important, since it indicates that soot oxidation mediated by NO_2 cannot be applied on SCRoF and for the proposed dual layer configuration, as NO_x is consumed in the SCR reaction and not available for soot oxidation.

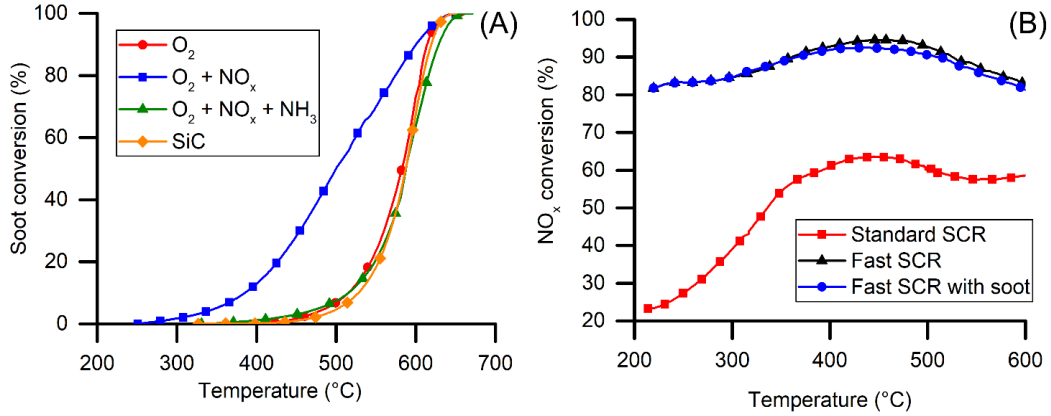

Figure 2.5. (A) Soot TPO on Fe-ZSM catalyst with different gas composition. Reaction conditions: *w/f* 0.027 g_{cat}·s/mL, 4% O_2 in N_2, 9: 1 catalyst: soot mass ratio, loose contact, 2 °C/min heating ramp. When indicated, 250 ppm NO, 250 ppm NO_2 and 500 ppm NH_3 was also added; (B) SCR activity of Fe-ZSM5. Reaction conditions: *w/f* 0.027 g_{cat}·s/mL, 500 ppm NO_x (NO_2/NO_x = 0 for standard SCR and 0.5 for fast SCR), 500 ppm NH_3, 4% O_2 in N_2, 9:1 Fe-ZSM5:soot mass ratio, loose contact, 2 °C/min heating ramp.

Table 2.2. Soot oxidation on Fe-ZSM5 in different gas compositions. Reaction conditions same as in Figure S2.5.

Gas composition	T_{10} [°C]	T_{50} [°C]	T_{max} [°C]	T_{90} [°C]	CO_2 selectivity[a] [%]
O_2	515	583	594	613	52
O_2+NO+NO_2	384	500	516	600	72
O_2+NO+NO_2+NH_3	517	584	605	629	48

SiC	528	587	594	620	51

[a]CO_2 selectivity at T_{max}

Fe-ZSM5 had very good fast-SCR performance in the observed temperature region, always keeping NO_x conversion around 90% even with the high value of GHSV used in this study (Figure 2.5B). The Fe-ZSM5 was however very sensitive to standard SCR conditions [42] and NO_x conversion significantly decreased when the NO_2/NO_x ratio was lower than 0.5. The NO_x conversion activity and the obtained trends over Fe-ZSM5 are comparable to the ones reported in literature under similar reaction conditions [13,16,42-44] and are compared in Table S2.1. The presence of soot was not significant for the SCR reaction due to the fact that the SCR reaction was kinetically much faster compared to the soot oxidation. Slightly lower NO_x conversions were obtained due to slightly lowered NO_2 concentration which was used for the soot oxidation. The N_2 selectivity was also high in the whole range (>95%) and N_2O production was always lower than 10 ppm (Figures 2.5B and S2.6).

2.3.4. Catalytic activity of the integrated soot oxidation and NO_x SCR reactions

2.3.4.1. Soot oxidation activity of the integrated soot oxidation and NO_x SCR reactions

By mixing our soot oxidation catalyst (KCZ) with the SCR catalyst (Fe-ZSM5), the soot oxidation was significantly improved (Figure 2.6A). However, the contact mode between the SCR and soot oxidation catalyst played a major role. The best soot oxidation activity was obtained when the KCZ catalyst was in powdered form and the SCR in pellets, as the best contact between the soot oxidation catalyst and soot was achieved. In this case, the soot oxidation profile was comparable to the profile of soot oxidation in only O_2, since NO_2 was converted by the SCR catalyst. A small portion was however still segregated from the KCZ. This is indicated through T_{10} and T_{50} which were practically the same as with soot oxidation on KCZ in O_2. T_{90} was however much higher in the physical mixture configuration, i.e. it was more difficult to completely burn all the soot. This also confirmed that in the physical mixture configuration, without strong NO to NO_2 oxidation, the NO_x played no significant role in soot oxidation since it was consumed by the SCR reaction. In contrast, when the KCZ catalyst was in pellets and Fe-ZSM5 in powdered form only a small initial catalytic activity was observed. Since Fe-ZSM5 acted like a physical barrier there was little contact between KCZ and soot and most of the soot was burned by non-catalytic thermal oxidation. The worst result was obtained by co-pelletizing the Fe-ZSM5 and KCZ; by this way the catalytic soot oxidation was significantly inhibited. From the above results, we can conclude that when soot is mixed in loose contact with

both KCZ and Fe-ZSM5 the effective range of KCZ is not higher than few μms [45] and if the soot oxidation catalyst is not powdered (well dispersed) soot is physically segregated from KCZ by the SCR catalyst. In general the catalytic soot oxidation activity is related more to the external morphology of the catalyst while the specific surface area has little influence [11, 28,29,39]. Catalyst morphology with shapes that contribute to formation of active oxygen and increased contact points with soot, e.g. nanocubes, nanorods, etc, have better soot oxidation performance [11,28,29,39]. As can be seen on the SEM images on figure S2.2 the CZ surface was coated with the potassium compounds (carbonates, hydroxides and nitrates). In several studies it was highlighted that these salts can form melts on the surface which in turn improves the soot-catalyst contact [9,26,27]. In the physical mixture the granulation was more important as the SCR catalyst, when in powdered form (diameter <100 μm), presented a barrier and prevented the soot-soot oxidation catalyst contact. When KCZ was saturated and used in pellets and Fe-ZSM5 in powder, the release and increased reactivity of NO_x on KCZ-sat enabled high initial soot oxidation rate. However, once the nitrates were depleted from the catalyst, the oxidation rate dropped significantly, and the second portion of soot was oxidized without significant enhancement deriving from the NO_x.

In the dual-bed reactor configuration, the SCR reaction had no effect on soot oxidation since the distance between the two layers (c.a. 3 mm) was too large and diffusion played no role (see above the Pe number). During soot oxidation NO_x could be utilized and the best results were obtained for this type of setup. Considering however the distances between the two layers on the monolith (in the range of few μms) the dual bed reactor setup is not representative, and it more closely resembles a separate two-unit system.

From these findings, we can infer that the monolith coating method with the soot oxidation catalyst would be a key factor. A thin uniform KCZ layer coated on the top of the monolith wall would provide the best contact with soot. Deposition inside the pores with the SCR catalyst would likely have negative effect since it would only increase the pressure drop, while the contact with soot would be minimal [8].

During the soot oxidation by employing only Fe-ZSM5, the selectivity towards CO_2 was low (only 52%) and the CO concentration was high. For this reason, in commercial systems SCRoF must be followed by an oxidation catalyst. In contrast, with the physical mixture configuration, the CO_2 selectivity remained high during the reaction (>90%) and this would eliminate the need for another oxidation aftertreatment unit.

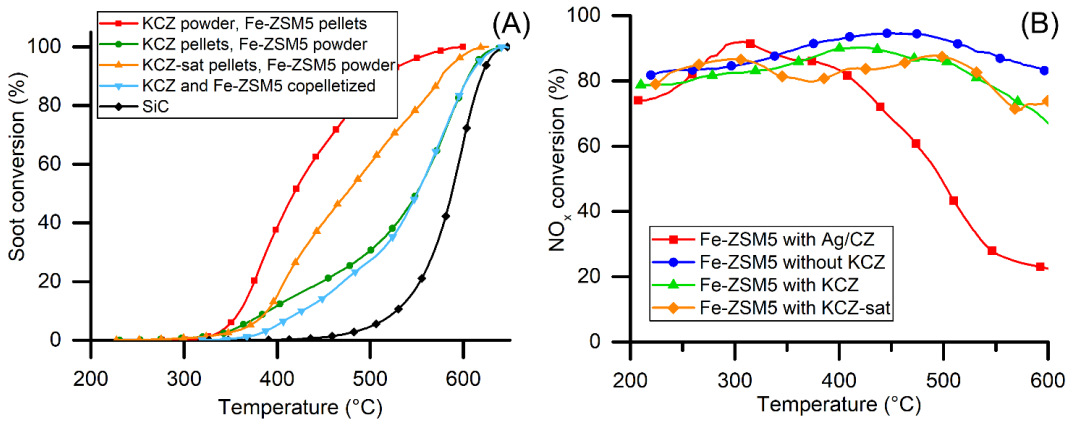

Figure 2.6. A) Soot oxidation in the physical mixture configuration. B) Corresponding SCR activity in the physical mixture configuration. Reaction conditions: *w/f* 0.054 g_{cat}·s/mL, 250 ppm NO, 250 ppm NO_2 and/or 500 ppm NH_3 4% O_2 in N_2, 9:9:1 KCZ: Fe-ZSM5: soot mass ratio, loose contact, 2 °C/min heating ramp.

Table 2.3. Soot oxidation on Fe-ZSM5 and KCZ physical mixture configuration with different granulation. Reaction conditions same as in Fig 6.

Configuration	T_{10} [°C]	T_{50} [°C]	T_{max} [°C]	T_{90} [°C]	CO_2 selectivity[a] [%]	Specific soot oxidation rate[b]
Fe-ZSM5 powder, KCZ pellet	390	550	585	605	89	0.59
Fe-ZSM5 pellet, KCZ powder	360	418	377	510	94	2.90
Fe-ZSM5 powder, KCZ-sat pellet	390	402	474	575	93	2.89
Fe-ZSM and KCZ pelletized together	426	550	590	604	84	0.67
Dual bed reactor configuration	354	398	355	445	94	3.79
Fe-ZSM5 with Ag/CZ	375	446	454	513	99	1.69
SiC	528	587	594	620	51	0

[a]CO_2 selectivity at T_{max}
[b]The specific soot oxidation rate was calculated at 400 °C and expressed as $[\mu g_{oxidized\ soot} \cdot s^{-1} \times g_{initial\ soot} \cdot g^{-2}_{catalyst}] \times 1000$

2.3.4.2. SCR activity of the integrated soot oxidation and NO_x SCR reactions

Figure 2.6B illustrates the NO_x conversion in the physical mixture configuration. The addition of powdered KCZ to the mixture slightly decreased the NO_x conversion by ca. 3-5% compared to the case of Fe-ZSM5 without KCZ. This was most likely because the KCZ was catalytically active for the soot-NO_2 reaction rate and slightly lowered the NO_2/NO_x ratio. As shown in Figure S4.4, the NO_2/NO_x ratio during soot oxidation on KCZ decreased which in turn had negative influence on the SCR reaction. This deviation in NO_2/NO_x ratio from the ideal 0.5 means that the fast SCR was partially inhibited. Only at temperatures above 550 °C there was a significant decrease in NO_x conversion, however this was only due to the desorption of NO (see NO_x-TPDO in Figure 2.2B).
In order to reproduce the "worst-case scenario" for the NO_x conversion, the KCZ soot oxidation catalyst was saturated with NO_x before the test. With KCZ-Sat the pre-adsorbed NO_x was released during the continuous temperature increase. A drop in the NO_x conversion was observed at temperatures corresponding to the peaks in the NO_x TPDO at 360 °C and 440 °C (see Figure 2.2B). This temporary decrease in the NO_x conversion was modest (ca. 12%) and it was never lower than 70%. After the release of all the NO_x from the KCZ-sat, the conversion returned to the original value. In real application, the NO_x adsorption on the potassium could have positive effect in dynamic conditions since it would store NO_x at high concentration and low temperatures when the SCR catalyst is less active and releasing it during higher temperatures when NO_x conversion and soot oxidation rate is higher. The addition of basic component to induce inertia in NO_x emission was shown recently by [49] for physical mixture of Ba/Al_2O_3 and Cu-zeolite to be highly beneficial for reducing cold start emissions. In the dual bed reactor configuration, the KCZ-sat in the upper layer had no significant effect on the subsequent SCR reaction and the NO_x conversion was the same as in the physical mixture of Fe-ZSM5 with KCZ-sat.
By using the Ag/CZ catalyst the SCR reaction could not proceed because ammonia was oxidized (Figure 2.6B). At lower temperature, when there was excess NH_3, high N_2O production was observed, and the selectivity was lowered (Figure S2.6). At higher temperatures, the NO_x conversion decreased significantly, because the ammonia oxidation on Ag/CZ was competitive with SCR. This highlights the importance that the soot oxidation catalyst used in the proposed dual layer catalyst configuration should be inert towards ammonia.

2.3.5. Stability of KCZ catalyst

The catalyst showed satisfactory low-temperature stability in the repeated soot combustion and after 6 cycles the T_{50} was increased by only 23 °C (see Table 2.4). The difference in the onset of the soot oxidation was however more pronounced, T_{10} increasing by 42 °C.
The high temperature and harsh hydrothermal ageing lowered the soot oxidation rate compared to fresh KCZ and T_{50} increased by 115 °C. The FE-SEM analysis revealed that, under hydrothermal conditions, the potassium tends to recrystallize and form aggregates. This causes the loss of contact between the support and the potassium and the positive synergistic effect is lost. However, the activity remaining after the harsh treatment was still significant and comparable to soot oxidation catalysts in the literature (Table 2.1 or e.g. [47]).

Table 2.4. Stability of the KCZ catalyst under different conditions

Configuration	T_{10} [°C]	T_{50} [°C]	T_{max} [°C]	T_{90} [°C]	CO_2 selectivity[a] [%]	Specific soot oxidation rate[b]
CZ	526	579	586	610	63	0
Fresh KCZ	348	417	429	470	93	2.91
Hydrothermally aged KCZ	454	532	560	580	93	1.37
KCZ 3rd run	368	426	432	481	92	2.51
KCZ 6th run	390	440	440	497	92	2.38

[a]CO_2 selectivity at T_{max}
[b]The specific soot oxidation rate was calculated at 400 °C and expressed as $[\mu g_{oxidized\ soot} \cdot s^{-1} \times g_{initial\ soot} \cdot g^{-2}_{catalyst}] \times 1000$

2.4. Conclusions

It has been demonstrated that soot oxidation can be integrated on SCRoF by using specifically tailored soot oxidation catalyst, which is inactive towards ammonia oxidation. When only Fe-ZSM5 (an SCR catalyst) was used, the soot oxidation was inhibited by the SCR reaction because NO_2 was not available. In general, in SCRoF the strategy of soot oxidation by NO_x cannot be exploited because of the fast SCR reaction is consuming most of the NO_2.

The soot oxidation catalyst used in this study was potassium based. 20 wt.% potassium carbonate impregnated on CeO_2-ZrO_2 had strong synergistic effect with the support and high activity for soot oxidation with O_2. Furthermore, the addition of potassium poisoned the acid sites of the support and inhibited any ammonia reactivity. By physically mixing the SCR catalyst (Fe-ZSM5) and the soot oxidation catalyst (KCZ), activity of soot oxidation was successfully coupled with ammonia-mediated NO_x reduction. In the physical mixture, KCZ had no negative effect for NO_x reduction, while the Ag/CZ, employed for comparison, inhibited the SCR reaction by oxidizing ammonia, thereby lowering selectivity and conversion.

In the physical mixture the contact and granulation mode played a significant role for the soot oxidation activity and the best results were obtained when KCZ was powdered and Fe-ZSM5 pelletized. In the reversed case, powdered Fe-ZSM5 acted as a barrier between soot and KCZ and the soot oxidation was inhibited. This has further implication for the monolith coating method, i.e. the contact between soot oxidation catalyst with soot should be maximized and that with the SCR catalyst minimized.

It should be noted that in this study the catalytic activities and interactions were studied on powdered catalysts. While the length-scales (order of magnitude ~100 μm) and diffusion phenomena are similar as in a monolith, the interaction described are mainly of chemical nature, i.e. the reactivity, adsorption-desorption phenomena etc. Further studies on real monolith will be performed to describe the macroscopic physical phenomena since the addition of a soot oxidation coating layer on the monolith would most likely have significant effect on the diffusion rate of the reacting species and the pressure drop through the monolith wall.

References

[1] M. Schejbal, J. Štěpánek, M. Marek, P. Kočí, M. Kubíček, Fuel 89 (2010) 2365–2375.

[2] M.D. Tomić, L.D. Savin, R.D. Mićić, M.D. Simikić, T.F. Furman, Therm. Sci. 17 (2013) 263–278.

[3] A. Shigapov, A. Dubkov, R. Ukropec, B. Carberry, G. Graham, W. Chun, R. McCabe, Kinet. Catal. 49 (2008) 756–764.

[4] W. Tang, D. Youngren, M. SantaMaria, S. Kumar, SAE Int. J. Engines 6 (2013) 862–872.

[5] T.C. Watling, M.R. Ravenscroft, G. Avery, in: Catal. Today, 2012, pp. 32–41.

[6] M. Lapuerta, F. Oliva, J.R. Agudelo, A.L. Boehman, Combust. Flame 159 (2012) 844–853.

[7] D. Karamitros, G. Koltsakis, Chem. Eng. Sci. 173 (2017) 514–524.

[8] K.G. Rappé, Ind. Eng. Chem. Res. 53 (2014) 17547–17557.

[9] C.A. Neyertz, E.E. Miró, C.A. Querini, Chem. Eng. J. 181–182 (2012) 93–102.

[10] D. Weng, J. Li, X. Wu, Z. Si, J. Environ. Sci. 23 (2011) 145–150.

[11] P.A. Kumar, M.D. Tanwar, S. Bensaid, N. Russo, D. Fino, Chem. Eng. J. 207–208 (2012) 258–266.

[12] G. Corro, A. Flores, F. Pacheco-Aguirre, U. Pal, F. Bañuelos, A. Ramirez, A. Zehe, Fuel 250 (2019) 17–26.
[13] P.S. Metkar, M.P. Harold, V. Balakotaiah, Appl. Catal. B Environ. (2012).
[14] T. Wittka, B. Holderbaum, P. Dittmann, S. Pischinger, Emiss. Control Sci. Technol. 1 (2015) 167–182.
[15] C.L. Myung, W. Jang, S. Kwon, J. Ko, D. Jin, S. Park, Energy 132 (2017) 356–369.
[16] S. Bensaid, V. Balakotaiah, D. Luss, AIChE J. 63 (2017) 238–248.
[17] O. Mihai, S. Tamm, M. Stenfeldt, L. Olsson, Philos. Trans. R. Soc. A Math. Phys. Eng. Sci. 374 (2016) 20150086.
[18] F. Marchitti, I. Nova, E. Tronconi, Catal. Today 267 (2016) 110–118.
[19] J. Czerwinski, Y. Zimmerli, A. Mayer, G. D'Urbano, D. Zürcher, Emiss. Control Sci. Technol. 1 (2015) 152–166.
[20] S.Y. Park, K. Narayanaswamy, S.J. Schmieg, C.J. Rutland, Ind. Eng. Chem. Res. 51 (2012) 15582–15592.
[21] T. Wolff, R. Deinlein, H. Christensen, L. Larsen, SAE Int. J. Mater. Manuf. (2014).
[22] H. Shimokawa, Y. Kurihara, H. Kusaba, H. Einaga, Y. Teraoka, in: Catal. Today, 2012, pp. 99–103.
[23] C. Davies, K. Thompson, A. Cooper, S. Golunski, S.H. Taylor, M. Bogarra Macias, O. Doustdar, A. Tsolakis, Appl. Catal. B Environ. 239 (2018) 10–15.
[24] R. Jiménez, X. García, C. Cellier, P. Ruiz, A.L. Gordon, Appl. Catal. A Gen. 297 (2006) 125–134.
[25] Y. Zhang, Q. Su, Q. Li, Z. Wang, X. Gao, Z. Zhang, Chem. Eng. Technol. 34 (2011) 1864–1868.
[26] M. Ogura, R. Kimura, H. Ushiyama, F. Nikaido, K. Yamashita, T. Okubo, ChemCatChem 6 (2014) 479–484.
[27] Q. Li, X. Wang, Y. Xin, Z. Zhang, Y. Zhang, C. Hao, M. Meng, L. Zheng, L. Zheng, Sci. Rep. 4 (2014) 4725.
[28] Y. Liu, Q. Lai, Y. Sun, X. Xu, X. Fang, Y. Liu, C. Rao, X. Wang, Catal. Today 337 (2019) 171–181.
[29] R. Matarrese, E. Aneggi, L. Castoldi, J. Llorca, A. Trovarelli, L. Lietti, Catal. Today 267 (2016) 119–129.
[30] K. Mizutani, K. Takizawa, H. Shimokawa, T. Suzawa, N. Ohyama, Top. Catal. 56 (2013) 473–476.
[31] Y. Bisaiji, K. Yoshida, M. Inoue, K. Umemoto, T. Fukuma, SAE Int. J. Fuels Lubr. 5 (2011) 380–388.
[32] N. Hou, Y. Zhang, M. Meng, J. Phys. Chem. C 117 (2013) 4089–4097.
[33] Q. Wang, J.H. Sohn, S.Y. Park, J.S. Choi, J.Y. Lee, J.S. Chung, J. Ind. Eng. Chem. 16 (2010) 68–73.
[34] Y. Peng, J. Li, X. Huang, X. Li, W. Su, X. Sun, D. Wang, J. Hao, Environ. Sci. Technol. 48 (2014) 4515–4520.
[35] B.S. Sánchez, C.A. Querini, E.E. Miró, Appl. Catal. A Gen. 392 (2011) 158–165.
[36] L. Castoldi, N. Artioli, R. Matarrese, L. Lietti, P. Forzatti, Catal. Today 157 (2010) 384–389.
[37] A. Sinhamahapatra, J.P. Jeon, J. Kang, B. Han, J.S. Yu, Sci. Rep. 6 (2016) 27218.
[38] I. Atribak, A. Bueno-López, A. García-García, Combust. Flame 157 (2010) 2086–2094.

[39] L. Castoldi, R. Matarrese, L. Lietti, P. Forzatti, Appl. Catal. B Environ. 64 (2006) 25–34.
[40] M.A. Peralta, M.S. Zanuttini, M.A. Ulla, C.A. Querini, Appl. Catal. A Gen. 399 (2011) 161–171.
[41] M. Iwasaki, H. Shinjoh, Appl. Catal. A Gen. (2010).
[42] P.S. Metkar, M.P. Harold, V. Balakotaiah, Chem. Eng. Sci. 87 (2013) 51–66.
[43] K. Kamasamudram, N. Currier, T. Szailer, A. Yezerets, SAE Int. J. Fuels Lubr. 3 (2010) 664–672.
[44] K. Kamatani, K. Higuchi, Y. Yamamoto, S. Arai, N. Tanaka, M. Ogura, Sci. Rep. 5 (2015) 10161.
[45] T. Selleri, F. Gramigni, I. Nova, E. Tronconi, S. Dieterich, M. Weibel, V. Schmeisser, Catal. Sci. Technol. 8 (2018) 2467–2476.
[46] D. Fino, S. Bensaid, M. Piumetti, N. Russo, Appl. Catal. A Gen. 509 (2016) 75–96.

2.5. Supplementary material for Chapter 2

1. Support and catalyst preparation:

MgAlO was prepared by coprecipation. $Mg(NO_3)_2$ and $Al(NO_3)_3$ solution with Mg:Al ratio 3:1 was slowly dripped in a solution of NH_4OH. During the precipitation the pH was kept between 9.5-10.5 by adding NH_4OH solution. The precipitate was aged at room temperature for 24 hours and after that centrifuged and washed until neutral pH. The slurry was dried at 100°C for 24 hours and calcined at 500°C for 5 hours. The obtained powder was impregnated with 20 wt.% K_2CO_3 and calcined at 800°C for 6 hours.

Nepheline was prepared according to [26]. A solution with SiO_2: 0.5 Al_2O_3: 10 Na_2O: 41 H_2O was prepared by dissolving $NaAlO_2$, Na_2SiO_3, NaOH in water in appropriate ratio. The solution was aged for 24 hours in a Teflon autoclave at 100°C. The obtained crystals were separated by centrifugation and washed until pH 7 and dried at 100°C for 24 hours. The obtained powder was impregnated with 20 wt.% K_2CO_3 and calcined at 800°C for 6 hours. After calcination the potassium doped nepheline was suspended in water, centrifuged, washed and dried. This means that this type of catalyst does not lose the potassium and activity upon contact with water.

MgO was prepared by making a solution of $Mg(NO_3)_2$ and citric acid in molar ratio 1:1. The solution was evaporated until a yellow gel was obtained. The gel was dried at 100°C for 24 hours and crushed to powder. The powder was combusted at 250°C and calcined at 500°C for 5 hours. The obtained MgO was impregnated with 20wt.% K_2CO_3 and calcined at 800°C for 6 hours.

CeO_2-CuO was prepared by coprecipitation. A solution was prepared from $Ce(NO_3)_3$ and $Cu(NO_3)_2$ with Ce:Cu molar ratio 9:1. This solution was slowly dripped in a buffer solution of Na_2CO_3-NaOH and pH maintained at 10. The obtained slurry was aged, centrifuged, washed, dried and calcined at 500°C for 5 hours. The obtained powder was impregnated with 20 wt.% K_2CO_3 and calcined at 800°C for 6 hours.

2. Equations and assumptions used for the Peclet number calculation

$$Pe = \frac{w \times d}{D_{eff}}$$

$$D_{eff} = D\frac{\varepsilon}{\tau}$$

$$D = 7.9236 \cdot 10^{-10}\, T^{1.7297}$$

$$\tau = \frac{\varepsilon}{1-(1-\varepsilon)^{2/3}}$$

Where:

w- gas flow velocity

d- characteristic length

D_{eff}- effective diffusivity, the diffusivity D of NO_2 corrected for the tortuosity and void fraction

τ- tortuosity

ε- void fraction

	Monolith	Physical mixture	Dual-bed
w (m/s)	0.02	0.127	0.127
d (m)	$300 \cdot 10^{-6}$	$3 \cdot 10^{-3}$	$100 \cdot 10^{-6}$
ε	0.5	0.4	0.4
τ	1.35	1.39	1.39
D_{eff} (m^2/s)	$1.73 \cdot 10^{-5}$	$1.69 \cdot 10^{-5}$	$1.69 \cdot 10^{-5}$
Pe	0.35	28.32	0.94

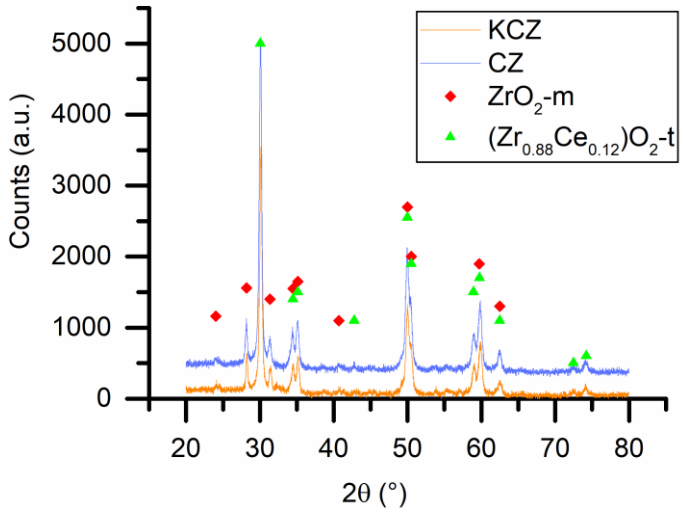

Figure S2.1. Diffractogram of the KCZ and CZ samples. Monoclinic zirconia (ZrO2-m) and tetragonal ceria stabilized zirconia ($Zr_{0.88}Ce_{0.12}O_2$-t) as main phases

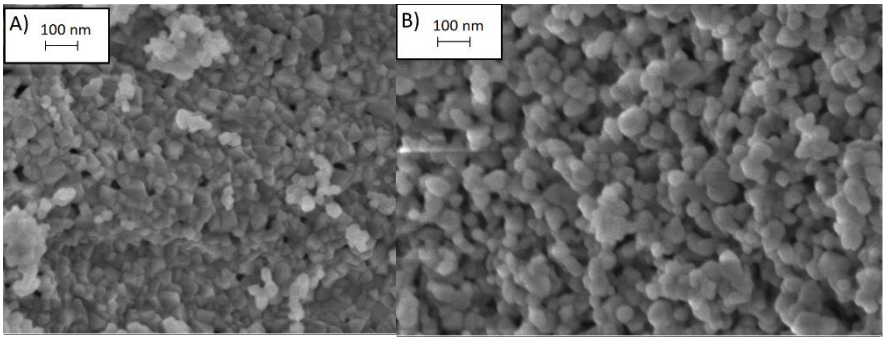

Figure S2.2. FE-SEM images of CZ (A), KCZ (B)

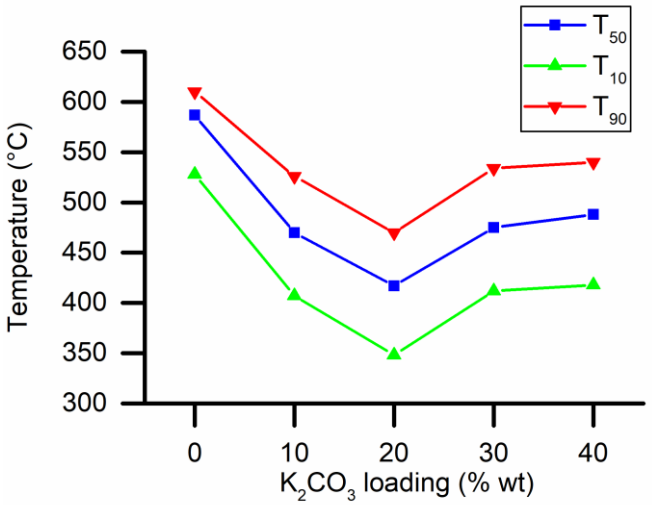

Figure S2.3. Effect of CZ potassium carbonate loading on soot oxidation lowering. Reaction conditions: w/f 0.027 g_{cat}·s/mL, 4% O_2 in N_2, 9:1 catalyst:soot mass ratio, loose contact, 2 °C/min heating ramp

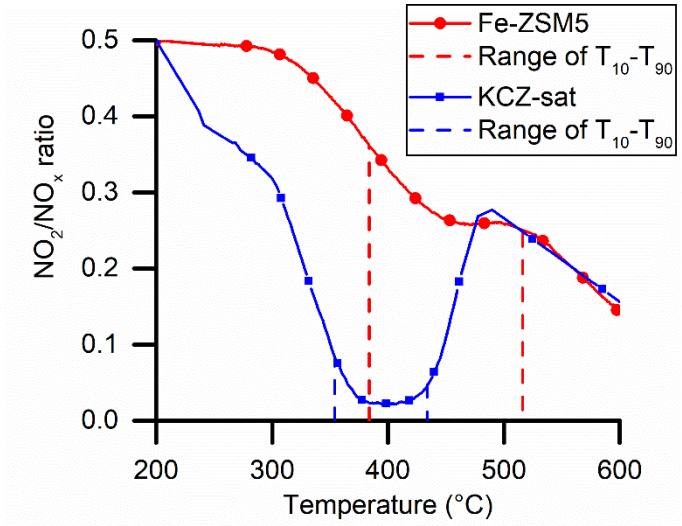

Figure S2.4. NO_2/NO_x ratio during soot combustion on Fe-ZSM5 and KCZ-sat. Reaction conditions: w/f 0.027 g_{cat}·s/mL, 250 ppm NO, 250 ppm NO_2, 4% O_2 in N_2, 9:1 catalyst:soot mass ratio, loose contact, 2 °C/min heating ramp. T_{10} and T_{90} are marked with dashed lines to indicate the soot oxidation range.

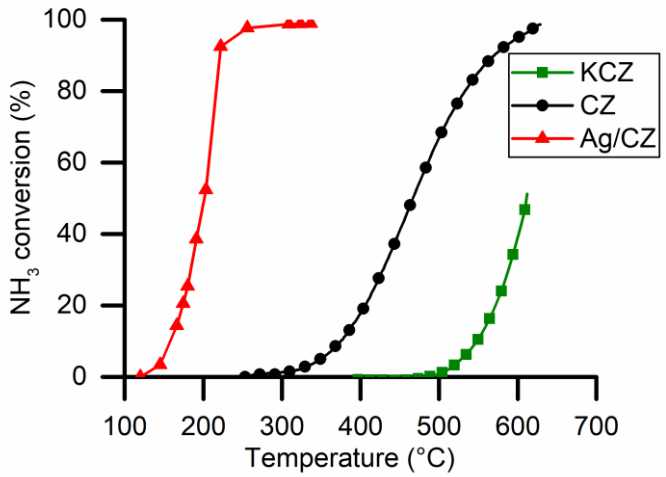

Figure S2.5. Ammonia oxidation on Ag/CZ, KCZ, CZ samples. Reaction conditions: w/f 0.027 g_{cat}·s/mL, 500 ppm NH_3, 4% O_2 in N_2, 2 °C/min heating ramp.

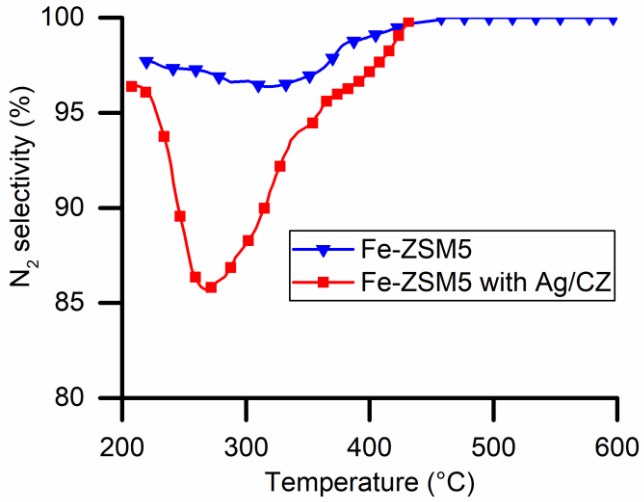

Figure S2.6. N_2 selectivity in the physical mixture configuration with Ag/CZ and Fe-ZSM5. Reaction conditions: w/f 0.054 g_{cat}·s/mL, 250 ppm NO, 250 ppm NO_2 and/or 500 ppm NH_3 , 4% O_2 in N_2, 9:9:1 KCZ:Fe-ZSM5:soot mass ratio, loose contact, 2°C/min heating ramp.

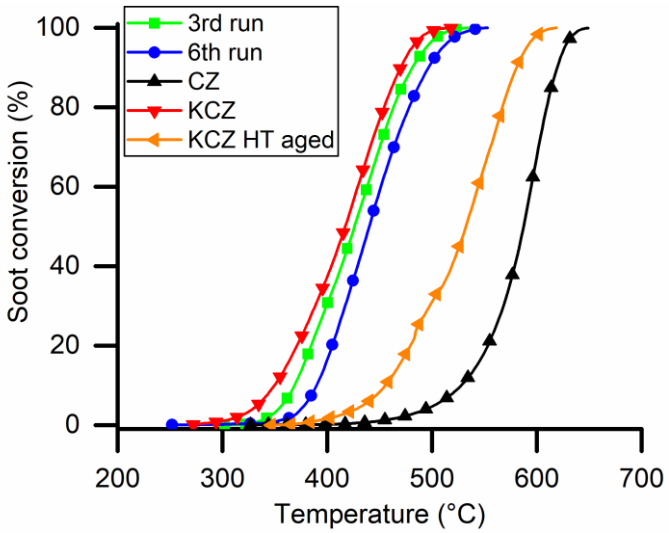

Figure S2.7. Soot TPO on hydrothermally aged KCZ, fresh KCZ, after 3rd and 6th repeat, and CZ. Reaction conditions: w/f 0.027 g_{cat}·s/mL, 4% O_2 in N2, 9:1 catalyst:soot mass ratio, loose contact, 2°C/min heating ramp.

Chapter 3

3. Simultaneous improvement of ammonia mediated NO_x SCR and soot oxidation for enhanced SCR-on-Filter application

Chapter summary

This chapter investigates in more depth the interaction between the soot oxidation and SCR catalyst in physical mixture by changing the catalyst mass ratio, gas composition and type of catalysts. The soot oxidation in the physical mixture was improved as the temperature was decreased by ca. 150 °C and it was alike to the catalytic soot oxidation by O_2 as the participation of NO_x was limited by the SCR reaction. Even when adjusting the inlet NO_2/NO_x ratio to 0.5 and the soot oxidation catalyst active for NO oxidation only minor contribution of NO_2 towards soot oxidation was observed. The ratio of the SCR and soot oxidation catalyst needs to be optimized relative to the characteristics of the SCR catalyst, most important parameter being the sensitivity of NO_x conversion towards the NO_2/NO_x ratio. In standard SCR conditions the NO_x conversion could be improved by the NO oxidation over the soot oxidation catalyts. In this manner the NO_x conversion for the mixture with Fe-ZSM5 could be improved by 20%, while for the Cu-ZSM5 only 5% due to its low dependency towards NO_2/NO_x ratio. If the feed contained fast SCR mixture (NO_2/NO_x = 0.5) the NO_x conversion was in all cases slightly lower in the physical mixture due to lower amount of the SCR catalyst.

Adapted from publication in Applied Catalysis A: General (2020) 596:117538 https://doi.org/10.1016/j.apcata.2020.117538

3.1. Introduction

Diesel engines inherently have higher thermodynamic efficiency due to lean operation, and because of this it is the preferred choice over petrol based internal combustion engines in long haul transport, locomotives, work machines etc. However, diesel engines have higher NO_x and soot emissions, that are difficult to remove from the exhaust due to low temperature and net oxidizing conditions [1–3]. Due to the harmfulness of the exhaust gases ever more stringent emission limits are implemented with the latest Euro 6d, which is expected to come into force in 2020. To stay below the threshold limits, especially regarding NO_x and particulate matter (PM) emissions, aftertreatment of the exhaust gasses is necessary [4,5]. The current aftertreatment systems are usually complex, expensive and require several successive reaction steps and monolith bricks. The main components are typically, the diesel oxidation catalyst (DOC) for the NO

and hydrocarbon oxidation, catalyzed or non-catalyzed diesel particulate filter (DPF) for the PM removal and a component for the selective catalytic reduction (SCR) of NO_x [5–8]. The NO_x SCR is mediated by a reductant, with the urea-based NH_3 reduction using Cu or Fe zeolites being the most efficient [9–13]. The main reactions occurring in the aftertreatment system are:

$2NO + 2NH_3 + 1/2O_2 \rightarrow 2N_2 + 3H_2O$	Standard SCR (R1)
$NO + NO_2 + 2NH_3 \rightarrow 2N_2 + 3H_2O$	Fast SCR (R2)
$6NO_2 + 8NH_3 \rightarrow 7N_2 + 12H_2O$	NO_2 SCR (R3)
$NO + 1/2O_2 \rightarrow NO_2$	NO oxidation (R4)
$NH_3 + O_2 \rightarrow xN_2O + xNO + xN_2$	Non selective ammonia oxidation (R5)
$C + O2 \rightarrow xCO + xCO_2$	Soot oxidation with oxygen (R6)
$C + NO_2 + O_2 \rightarrow xCO + xCO_2 + NO$	NO_x assisted soot oxidation (R7)

One method to reduce complexity and cost and to improve efficiency of the aftertreatment system is to integrate the DPF and NO_x SCR into a single device, a so-called SCR on Filter (SCRoF) device. In the SCRoF, the SCR catalyst is washcoated into the pores of the monolith and the channels are plugged on alternating ends to force the exhaust gasses through the wall, thereby performing simultaneously the SCR reaction and the filtration of soot. With this, the size and cost is reduced and, if it is in close-coupled position, higher operating temperatures and more efficient performance can be achieved [11,13–19]. It has been proven in several experimental and modeling studies that on SCRoF the passive soot oxidation is inhibited as the fast SCR reaction (R2) is consuming the NO_2, leaving none for soot oxidation [11,13–19]. As the soot accumulates during filtration, the resistance to the flow and pressure drop increases and the filter has to be regenerated by an active method whereby fuel is injected to increase the temperature above 600 °C to oxidize all the soot [11,13–19]. This regeneration is usually performed less frequently, or completely avoided, in the DPF as they are typically coated with Pt-based NO oxidation catalyst, as NO_2 can passively oxidize soot at much lower temperatures (< 400 °C) compared to O_2 [1]. The high temperatures reached during the regeneration can easily damage the filter and deactivate the SCR catalyst. For this reason, typically Fe and Cu zeolites are used for SCRoF application, as they present high hydrothermal stability and, to some extent, they resist the harsh conditions reached during regeneration [11,13–19].

To decrease the frequency of the filter regeneration, it is suggested that the NO_2/NO_x ratio should be adjusted above the ideal 0.5 required for the SCR. The rationale is that a portion of the excess NO_2 will be consumed by the accumulated soot and the NO_2/NO_x ratio self-regulates back to 0.5 [11,13,14]. Another proposal is to concentrate the SCR catalyst in the downstream part of the monolith, so in the inlet side NO_x is available for soot oxidation [11,18]. These partial solutions, however, do not solve the problem of the soot accumulation and regeneration, merely delaying it.

As a solution for the soot accumulation problem, a novel physical mixture of an SCR catalyst and soot oxidation catalyst is proposed. The physical mixture of quite different catalysts was applied for NO_x reduction in various and quite innovative settings, such as Ag/Al_2O_3 combined with Sn/Al_2O_3 or Zn-ZSM5 for HC-SCR [20,21], combined Pt/Al_2O_3 and Cu-Zn-Al water-gas shift to generate in-situ hydrogen for the reduction [22], the combination of Fe and Cu zeolites to widen the SCR window [12,23] and the combination of LNT and SCR catalysts for in-situ ammonia generation and utilization in the so-called "urealess passive SCR" [24,25]. Another concept introduced as early as 1997 by Misono et al [26] is to combine a catalyst for NO oxidation (R4) and transform the reaction pathway from standard SCR (R1) to fast SCR (R2) whereby higher NO_x conversion can be achieved. Similar concept was investigated later in more detail by two different research groups of Stakheev et al.[27–29] and Salazar et. al. [30,31], where mainly Mn was used as the NO oxidation catalyst. One important finding, emphasized even in the references, was that NO_x conversion was enhanced at only low temperatures, and decreased significantly as the temperature increased above 300 °C. The reason was that the oxidative component oxidized not only NO but also the reductant NH_3, producing high amounts of N_2O and, as ammonia was depleted, the SCR reaction could not proceed [26–31]. For this reason, we tailored the soot oxidation catalyst specifically to be selectively oxidative towards soot and NO, to simultaneously improve the soot oxidation and NO_x conversion by transforming the reaction pathway from standard to fast SCR. An innovative solution was found to prevent ammonia oxidation, whereby the catalyst was impregnated with small amount of potassium [32]. The potassium selectively poisoned the acid sites and the catalyst became passive towards ammonia oxidation, while simultaneously the soot oxidation was improved.

The novel solution proposed here is a physical mixture of two different catalysts, one for the SCR and one for enhancing the soot oxidation to achieve the combined effect. For the SCR catalyst, Fe- or Cu-ZSM5 are used as they are also widely utilized in the practical applications and they are well characterized from both chemical and engineering point of view. For the soot oxidation catalyst CeO_2-PrO_2 was impregnated with potassium to tailor its reactivity to the various components as will be described later. The aim of this report is to investigate the integration of soot oxidation and NO_x SCR by a two-component selective catalytic system and to investigate the interaction between them.

3.2. Materials and methods

3.2.1 Catalysts preparation

As SCR catalyst, Fe- and Cu-ZSM5 were used as they are the reference catalyst chosen for the SCRoF in commercial applications and they have been

investigated and characterized in detail in the scientific literature [10,23]. In a typical synthesis, 1 g of H-ZSM5 (Alfa-aesar) with SiO_2:Al_2O_3 ratio 23:1 and surface area 425 m^2 was placed in a 50 mM solution of iron nitrate or copper acetate to obtain Fe-ZSM5 and Cu-ZSM5 respectively. The suspension was stirred at room temperature for 24 h to conduct ion exchange of metal ions into the zeolite structure. After stirring, the slurry was separated by centrifugation and washed 4 times. The washed zeolites were dried for 12 hours at 120 °C and calcined at 700 °C for 5 h. Fe content in the Fe-ZSM5 was 0.4 wt% while the Cu content in Cu-ZSM5 was 4.1 wt% as determined by ICP-AES analyses. The soot utilized in the reactivity tests was Printex-U supplied by Degussa. The soot had average particle size 25 nm (supplier specifications) and specific surface area 88 m^2/g and high porosity. Printex-U is established as a model soot in scientific literature and it should be noted that it is generally less reactive that real diesel soot, as a consequence the results obtained can be considered conservative [33].

Concerning the soot and selective NO oxidation catalyst, CeO_2-PrO_2 was prepared by hydrothermal synthesis described and characterized in detail elsewhere [34]. In short, an equimolar solution of $Ce(NO_3)_3 \cdot 6H_2O$ and $Pr(NO_3)_3 \cdot H_2O$ was added dropwise to an 8 M NaOH solution under stirring. The obtained precipitate was aged for 1 hour and transferred into a Teflon autoclave. The crystallization was performed under hydrothermal conditions at 180 °C for 24 h. After cooling, the precipitate was centrifuged and washed several times until neutral pH. The slurry was then dried for 12 hours at 120 °C and calcined at 700 °C for 5 h with a heating rate of 5 °C/min. K/CeO_2-PrO_2 was prepared by wet impregnation with the theoretical loading of 3 wt% of potassium carbonate. The previously prepared CeO_2-PrO_2 was placed in an appropriate amount of 0.03 M K_2CO_3 solution. The water was evaporated at 80 °C under constant stirring, dried for 12 h at 100 °C and calcined for 3 h at 700 °C with a heating rate of 5 °C/min. For the demonstration of ammonia over-oxidation, a Pt/Al_2O3 catalyst with 5 wt% of Pt loading (Sigma-Aldrich) was used as the soot oxidation catalyst in the physical mixture.

3.2.2. Catalysts characterization

The XRD diffractograms were recorded by a X'Pert Philips PW3040 diffractometer equipped with Pixel detector using a Cu Kα radiation in the 2θ range 20-80° with 0.013° stepsize.

The specific surface area was determined by a Tristar II 3020 instrument (Micrometrics) by N_2 physisorption and condensation. The catalyst was pretreated at 200 °C for 2 h to remove any adsorbed species that could interfere with the analysis. The reported values for the specific surface area (S_{BET}) are calculated according to the BET method.

FT-IR spectra was obtained for the KCP and NO_x saturated KCP catalyst to investigate the adsorbed species. The catalyst powder was pressed in thin pellets, loaded into quartz cell with KBr window and outgassed for 30 min at 100 °C. The

transmitted spectra was collected on BRUKER EQUINOX-55 spectrometer equipped with a mercury cadmium telluride (MCT) cryodetector with 2 cm^{-1} and 32 scan resolution.

To characterize the acid/base sites of the catalyst surface and the relevant adsorption/desorption kinetics, NO_x temperature programmed desorption-oxidation (TPDO) and NH_3 temperature programmed desorption (TPD) on the CP and KCP catalysts were conducted on the experimental setup described below. Before the NO_x TPDO, the KCP catalyst was pre-saturated with 250 ppm NO and 250 ppm NO_2 at 250 °C. To observe the catalytic reactivity of the adsorbed NO_x with soot, the NO_x was desorbed in the presence and absence of soot with a heating rate of 2 °C/min in the temperature range 200-800 °C. The sweep gas during desorption was 4% O_2 in N_2 to avoid potential NO_x decomposition at high temperatures [32].

NH_3 adsorption and oxidation was performed to describe the NH_3 reactivity, which is important in connection with the SCR reactivity. Before the NH_3 adsorption, the catalyst was pretreated at 400 °C to remove any adsorbed species (H_2O, CO_2) and saturated by flowing a gas containing 1000 ppm NH_3 in N_2 at 50 °C. After adsorption and cooling down to room temperature, the adsorbed NH_3 was desorbed by flowing inert N_2 gas and increasing temperature up to 600 °C with a 5 °C/min heating rate.

The impregnation with potassium did not significantly change the other physico-chemical characteristics of the CP catalyst. For detailed characterization (XPS, TPR) the reader can refer to the previous works on the same catalyst [34].

3.2.3. Catalytic activity test

Catalytic activity tests were conducted in a 10 mm internal diameter tubular glass reactor, heated by an isolated vertical tube furnace programmable with the desired heating rate. The investigated catalyst (or mixture of catalysts), pelletized to 250 μm, was placed in the reactor to create a fixed bed. The thermocouple was inserted on the top layer of the catalytic bed for continuous thermal measurements of the reaction temperature. The desired reaction gas mixtures were controlled by mass flow controllers. The typical gas concentrations used were 4% O_2, 500 ppm NO_x ($NO+NO_2$) with different NO_2/NO_x ratios, 500 ppm NH_3 and balanced with N_2. The reaction species continuously monitored were NO, NO_2, CO_2, CO, NH_3 and N_2O by NDIR and UV analyzers with the appropriate filters (ABB AO2020 Uras and Limas). A bypass valve was installed before the reactor and the concentrations were monitored before and after passing through the catalytic bed.

The soot oxidation by O_2 was conducted by gently mixing 270 mg of the indicated catalyst with 30 mg of soot with a spatula for 30 seconds to obtain a loose contact, while tight contact was achieved by ball-milling the catalyst-soot mixture for 15 minutes. The reaction was initiated at 200 °C with a 2 °C/min heating rate and a 600 mL/min flow of a gas mixture containing 4% O_2 in N_2. The

NO_x-assisted soot oxidation was conducted with the same parameters, just with the addition of 500 ppm of NO in the gaseous reacting mixture. To compare the efficiency of NO_2 utilization for soot oxidation, NO oxidation was performed under the same conditions without soot and the NO_2/NO_x was contrasted.

NH_3 oxidation was also performed over CP and KCP in order to explain the observed SCR activities and interaction between the soot oxidation catalyst and the SCR catalyst. NH_3 was oxidized by flowing 600 mL/min of 500 ppm NH_3, 4% O_2 in N_2 over 270 mg of catalyst. As NO_x is a stronger oxidant than O_2 alone, NH_3 oxidation was also performed with the same reaction conditions as before in the presence of 500 ppm NO. The temperature was increased stepwise in 40 °C increments and the reported values are obtained after stabilization in isothermal conditions.

The combined soot oxidation and NO_x SCR was conducted by flowing 600 mL/min of 4% O_2, 500 ppm NO_x and 500 ppm NH_3 in N_2 over 270 mg of catalyst with or without 30 mg of soot. Usually, standard SCR was conducted with the NO_2/NO_x ratio adjusted to 0 or, when indicated, fast SCR with NO_2/NO_x ratio 0.5. The catalysts used were Fe-ZSM5, Cu-ZSM5, CP and KCP individually, as well as their physical mixtures.

To investigate the soot and NO oxidation and SCR reaction interactions, the developed KCP soot oxidation catalyst was physically mixed with the Fe-ZSM5 and Cu-ZSM5 SCR catalyst in different mass ratios. Different reaction conditions and configurations were also examined, to demonstrate that the proposed integrated soot oxidation-SCR system is not limited only to specific types of SCR catalysts and reaction conditions but can be extended and applicable to general cases. Different reaction conditions and physical mixtures were used and the system performance in the soot and NO_x abatement was compared with the results obtained for the individual catalysts. Combined soot oxidation and standard and fast SCR was conducted always keeping a total catalyst mass of 270 mg with 30 mg of soot and a gas flow of 600 mL/min, maintaining the *w/f* always constant. In the physical mixture, the combined soot oxidation-SCR reaction, the inlet gas concentration was 500 ppm NO, 500 ppm NH_3, 4% O_2 in N_2. A temperature increase of 2 °C/min was used starting at 200 °C, and, after burning the soot, the NO_x conversion was observed under the same conditions without soot to quantify the interaction of soot and the SCR reaction. When a significant difference (>2%) of NO_x conversion was observed, in the presence and absence of soot, the deviation was marked on the figures with dots. To quantify the interaction between the two different SCR and soot oxidation catalysts, they were mixed in different mass ratios keeping the total mass in all the experiments always constant at 270 mg. The following cases for the physical mixture with Fe-ZSM5 were considered:

1. Case I: Fe-ZSM5:KCP:soot mixed loosely in mass ratio 6:3:1 respectively.
2. Case II: Fe-ZSM5:KCP:soot mixed in mass ratio 3:6:1.
3. Case III: Fe-ZSM5:KCP:soot mixed in mass ratio 4.5:4.5:1.
5. Case IV: Fe-ZSM5:KCP:soot mixed in mass ratio 6:3:1 with NO_2/NO_x ratio 0.5 (fast SCR).

For the low temperature applications, soot integration was examined over Cu-ZSM5. In this case, as will be shown later, low NO_2 concentration is not limiting the SCR reaction as much as on Fe-ZSM5 [10,12] and lower amount of the soot oxidation catalyst is preferable. The following physical mixtures were examined:

1. Case I: Cu-ZSM5:KCP:soot mixed loosely in mass ratio 6:3:1.
2. Case II: Cu-ZSM5:KCP:soot mixed in mass ratio 7.6:1.6:1.
3. Case IV: Cu-ZSM5:KCP:soot mixed in mass ratio 7.6:1.6:1 with NO_2/NO_x ratio 0.5.
4. Case V: To demonstrate the effect of the reductant over-oxidation, the Cu-ZSM5 was mixed with Pt/Al_2O_3 and soot in mass ratio 7.6:1.6:1.

The sensitivity of CP and KCP towards sulphur poisoning was tested as NO oxidation catalysts are typically deactivated in the presence of SO_2. The deactivation tests were performed at constant 350 °C temperature under the same reaction conditions as in the NO oxidation tests. After reaching stability of NO_x concentration, 60 ppm of SO_2 was introduced in the reaction stream and the decrease of the NO_2/NO_x ratio over time was observed. The thermal stability and repeatability of KCP was tested by cyclic soot oxidation in O_2, in total five repetitions were performed.

3.3. Results and discussion

3.3.1. Characterization results

The diffractograms presented in Figure S3.1 of KCP and CP are the same, indicating that the potassium concentration is low and present in a highly dispersed state on the surface. The characteristic diffraction peaks of CP correspond to fluorite cubic ceria structure, meaning that the Ce and Pr create a well-mixed solution without the insertion of potassium in the crystal lattice. Crystallite size, calculated according to the Scherrer equation, was 28 nm for both CP and KCP.

The SEM images of CP and KCP, illustrated in Figure S3.2, show that the KCP particles are slightly enlarged and more rounded than CP, indicating uniform deposition of K_2CO_3. Furthermore, the BET surface area of KCP is somewhat lower than CP (9 vs. 24 m^2/g) meaning that the deposited K_2CO_3 was evenly distributed on the surface and plugged the pore channels during impregnation. The rod structure was the result of the hydrothermal synthesis method for which was shown to have superior soot oxidation activity [34].

The FE-SEM images of the Fe-ZSM5 and Cu-ZSM5 physical mixture with KCP are shown in Figure 3.1. The samples used for the analysis and presented were the ones recovered after 2 tests. The different zeolite and KCP particulates were separated with significant distance (μm order of magnitude) and coalescence or melting phenomena did not occur even after the subjected to the high temperatures reached (700 °C) during the combined soot oxidation-SCR reaction.

It is worth to notice that this provided evidence demonstrates that the two reactions and phenomena on the two catalysts in loose contant are separate and no direct spillover of the reaction species are occuring. In contrast, when two catalysts are in tight contact, direct transport of the intermediates is possible as shown by [26–31].

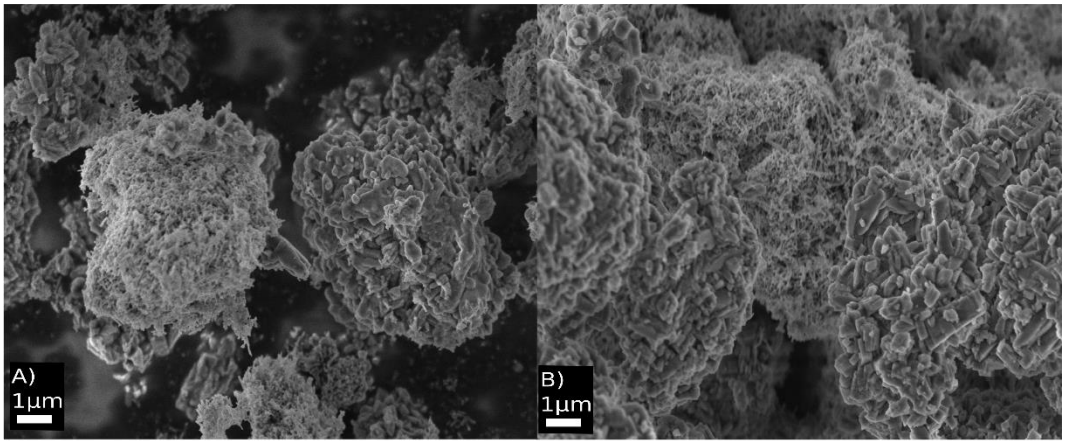

Figure 3.1**.** FE-SEM images of the physical mixture of KCP and Cu-ZSM-5 and Fe-ZSM-5 zeolites after reaction.

In Figure 3.2 the Temperature programmed desorption-oxidation (TPDO) of NO_x on the samples CP and KCP is shown. In the absence of soot, the adsorbed nitrates on KCP are stable and the desorption initiated only above 450 °C, finishing with the complete depletion above 750 °C. In contrast, when the NO_x-saturated KCP is mixed with soot in loose contact, the NO_x present on the catalyst is destabilized as oxygen is transferred to the soot and desorbed at significantly lower temperatures. Concurrently, NO_2 is reduced to NO and soot oxidation is enhanced (see Figure 3.2 below). NO is released already at 350 °C, however a portion of NO_x remains adsorbed and releases at high temperatures. The total amount of NO_x released was 0.74 mmol/g in both the presence and absence of soot, meaning that in oxidizing atmosphere the NO_2 reduces to NO and not to N_2. This proves that the potassium is catalytically active not only towards the soot-O_2 reaction but also for the soot-NO_2-O_2 reaction. It can be hypothesized that the soot acts as an oxygen acceptor and destabilizes the adsorbed NO_2, however the exact mechanism and reaction intermediates are still largely unknown [35–37]. Due to the lack of alkali metals, CP presented much lower NO_x adsorption capacity and a very heterogeneous surface. Several adsorption sites were observed; however, the strength of adsorption is much less than in the case when potassium is present on the surface, and NO_x is released at much lower temperatures compared to KCP. There was no notable difference in the desorption profile when soot was present with the CP sample, meaning that it is not active for the soot-NO_2-O_2 reaction but the NO_2 is desorbed and reacts from the gas phase.

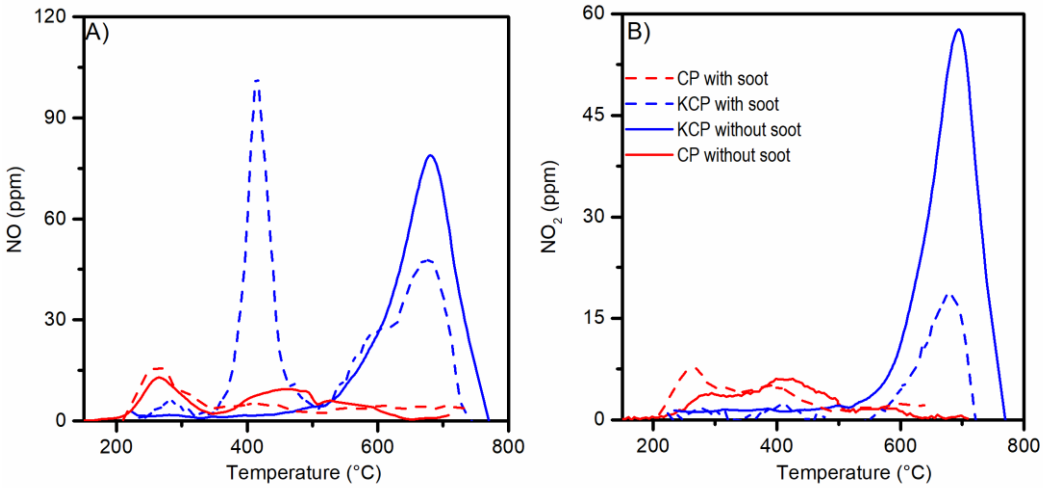

Figure 3.2. NO_x TPDO on the CP and KCP samples with and without soot.

In Figure 3.3, the ammonia TPD on the CP and KCP samples is shown. The CP sample showed a moderate amount of acid sites that can adsorb and activate ammonia, while, in contrast, on KCP, after the addition of small amount of potassium, no ammonia adsorption or desorption was observed. It is well known that gaseous ammonia adsorption and activation is readily occurring on both Lewis and Bronsted acid sites producing various intermediates and that the acid sites are essential for the NH_3-mediated SCR [38,39]. Here, the strategy to avoid ammonia over-oxidation involved the addition of potassium, as it effectively poisons the acid sites which are responsible for the activation of NH_3. For similar reasons, potassium is used as a promoter on ammonia synthesis catalysts, where it has been shown that potassium facilitates ammonia desorption [39]. By tailoring the surface properties and acidity, the NH_3 and oxidation can be prevented, without negative effects for the soot oxidation. The number of acid sites over CP was 3.65 $\mu mol/g_{cat}$ as calculated from the integration of the desorption curve in Figure 3.3. This amount is much lower from the amount of total K loaded (1 %wt or 250 $\mu mol/g_{cat}$), which ensured that all the acid sites are deactivated. As has been shown by [26–31] and will be shown later, the over-oxidation of the reductant, in this case NH_3, would be detrimental for the SCR reaction.

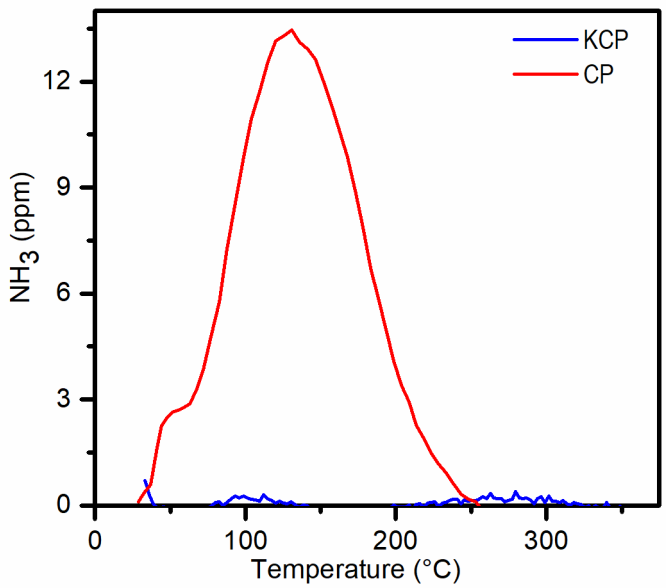

Figure 3.3. Ammonia TPD over the CP and KCP samples.

3.3.2. Catalytic activity of individual catalysts

As described in equations R1-5, the oxidation of ammonia is competitive with the SCR reactions (both standard and fast) and the relative amount of NH_3 used as a NO_x reductant or wasted in the oxidation is crucial for the SCR performance. The addition of small amounts of potassium poisoned the acid sites on the soot oxidation catalyst and correspondingly the NH_3 oxidation activity decreased significantly (see Figure 3.3 and 3.4). The NH_3 oxidation was delayed by more than 150 °C in both O_2 and O_2 + NO_x reaction mixtures. While on CP almost full NH_3 conversion was observed at 400 °C, on KCP the NH_3 oxidation just initiated at that temperature and full conversion was reached only above 550 °C. In the presence of 500 ppm NO, the NH_3 oxidation started earlier, partially also due to some NO_x SCR occurring, however full conversion was reached approximately at the same temperature as without NO_x.

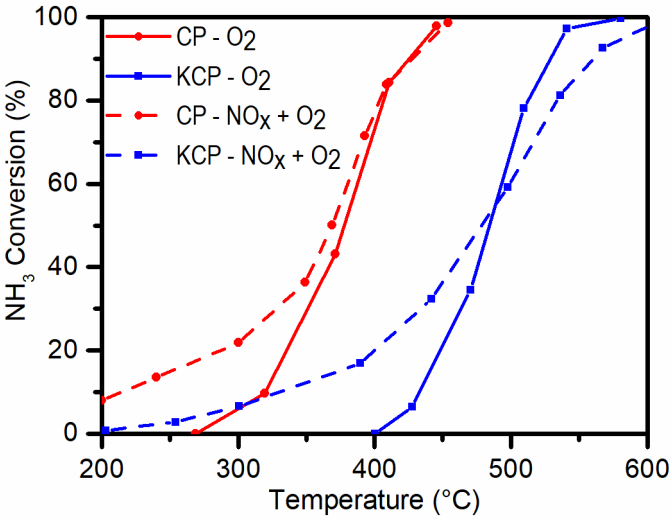

Figure 3.4. Ammonia oxidation over CP and KCP catalysts. Reaction conditions: 500 ppm NH_3, 4% O_2 in N_2; *w/f* 27 g_{cat}·s /L. The dashed line case also contained 500 ppm NO_x.

The soot oxidation mediated by O_2 on CP and KCP improved significantly in respect to the non-catalyzed soot oxidation, as illustrated in Figure 3.5. The CP sample lowered the soot oxidation temperature by 50 °C and the addition of 3 wt% of potassium carbonate further lowered it by 100 °C. However, the most significant improvement was observed in the presence of NO, as CP and KCP both can oxidize NO to NO_2. In the presence of NO_x, the soot oxidation proceeded at much lower temperatures in comparison with O_2 alone. The soot oxidation rates were similar over CP and KCP, and soot oxidation initiated as low as 250 °C and reached a maximum already at 450 °C. KCP presented a double peak, as the dynamic NO_x adsorption-reaction due to potassium played a significant role in the reaction: when NO was re-oxidized and desorbed a sudden increase in the soot oxidation rate occurred and a smaller second peak appeared. In tight contact of soot-KCP soot oxidation in O_2 was shifted by 50 °C to lower temperatures, while in the NO_x + O_2 reaction mixture soot oxidation exhibited a pronounced rapid increase in oxidation and the soot was oxidized in a shorter period relative to loose contact. The peak of soot oxidation was accompanied by a rapid increase in NO concentration, suggesting the dominant contribution of R7 and the enhanced contribution of surface nitrates to soot oxidation.

When the KCP catalyst was saturated with NO_x before the reaction, it performed the soot oxidation without NO_x in the inlet gas as good as with NO_x in the reaction gas mixture. The stored nitrates on the potassium participated in the reaction (see NO_x TPDO in Figure 3.2) and enhanced the soot oxidation significantly. The NO_2 stored on the potassium could participate in the soot oxidation and it was released as NO starting at 350 °C. However, the improvement was temporary, and it could be replicated only if the catalyst was saturated with NO_x again before the oxidation.

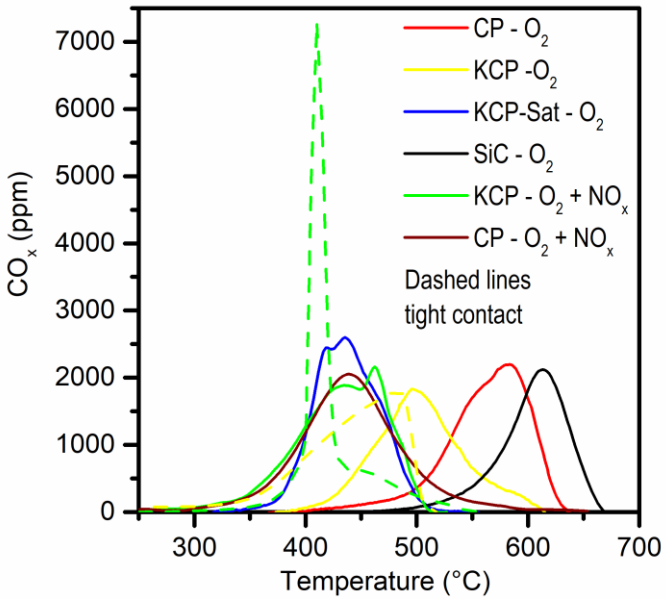

Figure 3.5. Soot oxidation and NO_x assisted oxidation on CP and KCP. Reaction conditions: 4% O_2 in N_2 and 500 ppm NO when indicated, *w/f* 27 g_{cat}·s/L, catalyst: soot mass ratio 9:1 in loose contact.

On the CP and KCP samples, the NO oxidation started at 250 °C and reached a maximum NO_2/NO_x ratio of c.a. 0.45 at 350 °C (Figure 3.6). There was no significant difference in the NO oxidation activity between CP and KCP despite the much lower surface area of KCP (24 vs 9 m^2/g). During the NO_x-assisted soot oxidation, the NO_2/NO_x ratio was significantly lowered. In both the KCP and CP catalysts, the ratio was lowered by almost 0.2 as the NO_2 was being consumed for soot oxidation and producing NO, according to equation R7. This is even more obvious on the KCP, as the adsorption/desorption dynamics during soot oxidation produced high variations in the NO_x. This has an implication for the SCR, as the presence of soot can somewhat lower the NO_2/NO_x ratio, and in some cases have negative effect on the NO_x conversion as it is lower than 0.5. Only in the case when the NO_2/NO_x ratio is higher than 0.5 the presence of soot has a positive effect on NO_x conversion as it consumes the NO_2 and adjusts the ratio to the fast SCR regime [11,18].

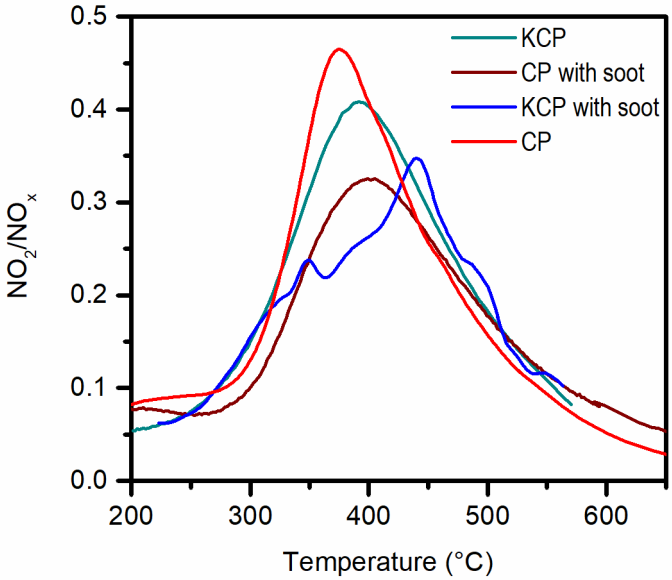

Figure 3.6. NO_2/NO_x ratio during NO oxidation and NO_x assisted soot oxidation. Reaction conditions: 500 ppm NO. 4% O_2 in N_2 and when indicated soot is present, *w/f* 27 g_{cat}·s/L, catalyst: soot mass ratio 9:1 in loose contact.

As SCR catalysts, Fe-ZSM5 and Cu-ZSM5 were used as they have superior stability, high NO_x conversion and selectivity and wide operational temperature range. For these reasons, in the majority of practical applications, metal-exchanged zeolites are used as SCR catalysts [10,19,40]. As can be seen in Figure 3.7, the Fe-exchanged zeolite had superior performance in the high temperature region, while the Cu exchanged one in the low temperature region. For this reason, Fe zeolites are mainly used for the aftertreatment in HDD, while Cu zeolites for LDD applications [10,19,40]. Fe-ZSM5 is much more sensitive to excessive ammonia adsorption and coverage, and, accordingly, there is a large difference between the Fast and Standard SCR. It is generally accepted that Fe zeolites are more sensitive to NO_2/NO_x ratio than their Cu counterparts (Figure

3.7) [10,41]. With the Fast SCR gas mixture, high NO_x conversions are reached for both catalysts, even with the high flowrates used in this study. On the other hand, the Standard SCR is limited at low temperatures for Fe-ZSM5. At higher temperatures (>400 ˚C), Fe-ZSM5 can oxidize NO and the ammonia coverage is lower and NO_x conversion rises. In contrast, Cu-ZSM5 is not as sensitive to the NO_2/NO_x ratio at lower temperature, and accordingly there is a much smaller difference between the Fast and Standard SCR. Due to the over-oxidation of the ammonia a steady decrease in NO_x conversion initiates already at 300 ˚C. The selectivity was much better on Fe-ZSM5 compared to Cu-ZSM5 (Figure 3.11), which is in accordance with other reports [41]. While on the Fe zeolite very little N_2O was observed, and selectivity was always above 95%, over Cu zeolite, at its peak, 50 ppm N_2O was produced. The selection between Fe- or Cu-zeolites for the SCRoF application depends on a variety of factors, such as the expected working exhaust temperature, the DOC performance and the NO_2/NO_x ratio, the stability requirements, etc.

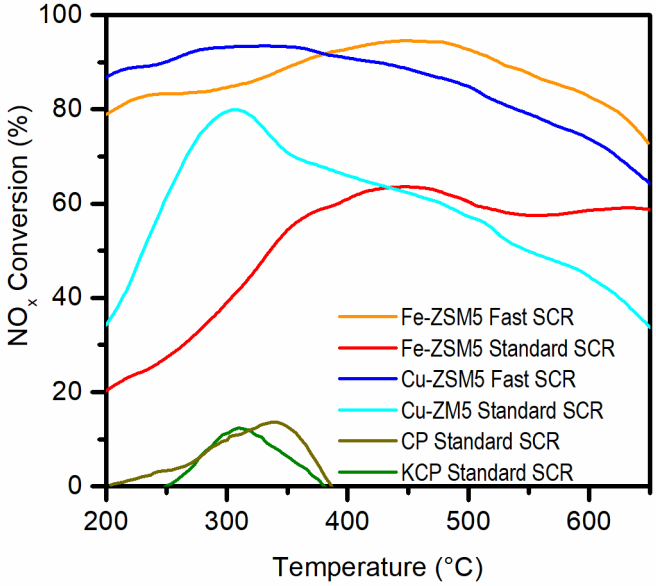

Figure 3.7. SCR activity of individual catalysts Fe and Cu-ZSM-5, CP and KCP. Reaction conditions: 500 ppm NO_x, 500 ppm NH_3, 4% O_2 in N_2; $NO_2/NO_x = 0$ for Standard SCR and 0.5 for Fast SCR; *w/f* 27 g_{cat}·s/L; catalyst: soot mass ratio 9:1 in loose contact; 2 °C/min heating rate.

The soot oxidation catalysts, CP and KCP, individually presented negligible SCR activity in the range 250-350 ˚C, as the NO_x conversion never exceeded 15%. Above 350 ˚C, the NOx conversion was “negative” over CP and KCP as ammonia was non-selectively oxidized to NO. From this, we can infer that any improvements observed due to the mixing of the soot oxidation with an SCR catalyst is due to phenomena other than simply their linear combination.

The biggest issue of the SCRoF is that the soot oxidation is inhibited as the NO_2 is consumed in the much faster SCR reaction, leaving none NO_2 for soot oxidation. This was demonstrated in detail in several reports [11,13,19,42] and, in Figure 3.8, for both the Cu- and Fe-ZSM5 catalysts. Without dosing NH_3, and

hence without the occurrence of the SCR reaction, the soot oxidation initiates as low as 300 ˚C and reaches a plateau due to limited availability of NO_2. However, with the addition of NH_3 in the reaction gas, the NO_x is converted by the much faster SCR reaction, and the soot oxidation profiles are practically the same as for the non-catalytic soot oxidation. In the SCRoF system, the main oxidant available is O_2 and the contribution of NO_2 to the oxidation of soot is inhibited by the kinetically much faster SCR reaction. For this reason, very high regeneration temperatures are necessary, which can damage the filter or the catalyst. The only condition where NO_2 could participate in the soot oxidation on SCRoF would be if the soot-O_2-NO_2 reaction was catalyzed and significant amount of NO_2 was present (i.e. NO_2/NO_x ratio higher than 0.5). This is of course not practical, as the NO_x conversion should not be compromised on the SCRoF systems.

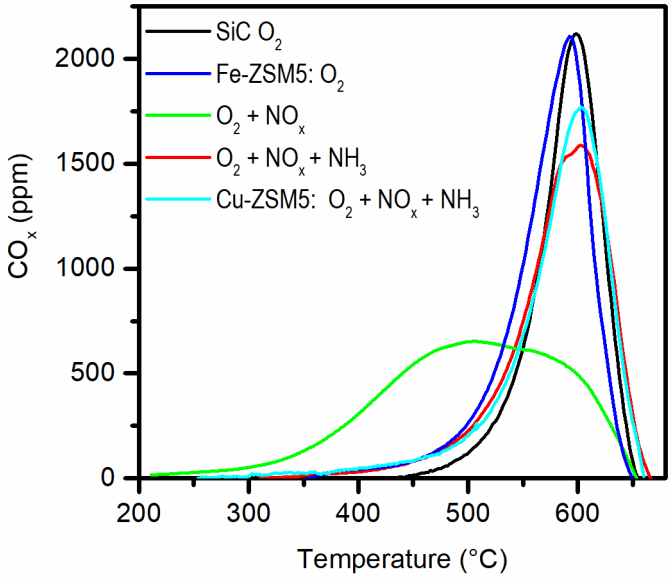

Figure 3.8. Inhibition of soot oxidation by SCR reaction on Cu-ZSM-5 and Fe-ZSM-5. Reaction conditions: 4% O_2 in N_2 and 500 ppm NO_x, NO_2/NO_x ratio 0.5, 500 ppm NH_3 added when indicated; *w/f* 27 g_{cat}·s/L; catalyst: soot mass ratio 9:1 in loose contact; 2 °C/min heating rate.

3.3.3. Catalytic activity of the dual component system

Figures 3.9 and 3.10 show the catalytic activities for NO_x reduction and soot oxidation of the physical mixtures of KCP and Fe and Cu zeolites in different mass fractions. Both standard and fast SCR were measured, coupled with soot oxidation and benchmarked to the cases when Fe and Cu zeolites were used without soot oxidation catalysts, while the soot oxidation performance was compared to that of soot oxidation on KCP in O_2 and $NO_x + O_2$.

For the system based on Fe-zeolite, different Fe-ZSM5: KCP ratios were tested in standard SCR conditions: 1:2, 1:1 and 2:1, as well as the optimal 2:1 ratio mixture in the fast SCR conditions. From the NO_x-SCR viewpoint, the worst results were obtained when the least amount of the Fe-ZSM5 catalyst was used

(1:2 ratio), as there was not enough catalyst to perform the NO_x reduction. Furthermore, above 500 ˚C, there was a sharp decline in NO_x conversion, as ammonia started to be oxidized. Due to low NO_x conversion, there was plenty of NO_2 available and the soot oxidation profile was shifted to the lowest temperature amongst the three mixtures.

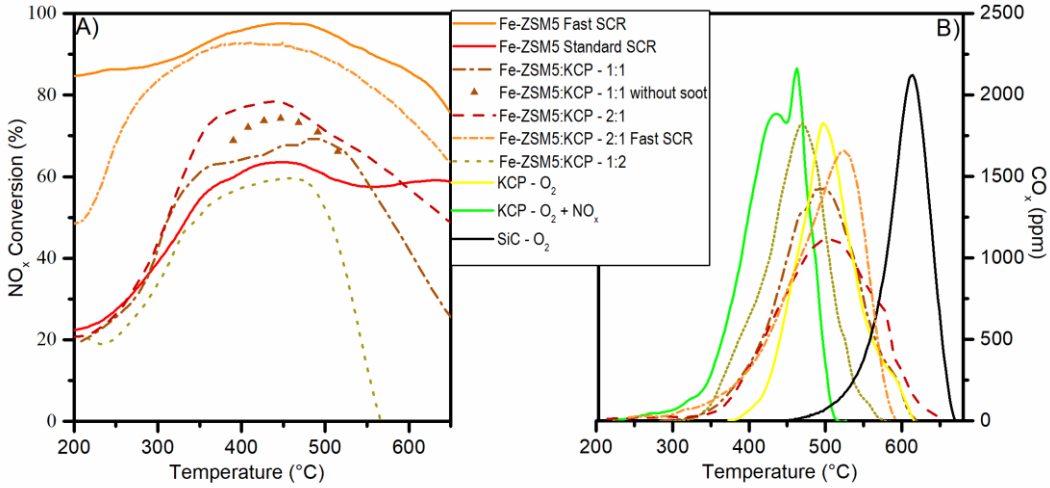

Figure 3.9. Combined soot oxidation and NO_x SCR in the physical mixture of KCP and Fe-ZSM-5. Reaction conditions: 500 ppm NO_x, 500 ppm NH_3, 4% O_2 in N_2; $NO_2/NO_x = 0$ for standard SCR and 0.5 for fast SCR; *w/f* 27 g_{cat}·s/L; catalyst: soot mass ratio 9:1 in loose contact; 2 °C/min heating rate.

Regarding the NO_x conversion, the mixture with mass ratio 2:1 showed the best performance. At low temperatures the same performance was observed as with 270 mg of Fe-ZSM5, however above 300 ˚C the NO_x conversion was significantly increased with the physical mixture, presenting nearly 20% improved conversion in wide temperature range compared to Fe-ZSM5 only. This can be explained with the partial transformation of the NO_x reaction pathway from standard to fast SCR. As can be seen in Figure 3.7, significant NO oxidation initiates at 300 ˚C on the KCP catalyst and the largest difference was observed at 450 ˚C where NO oxidation is not kinetically limited. As lower amount of KCP was used in the mixture, ammonia oxidation was not pronounced and, compared to Fe-ZSM5 alone, slightly inferior SCR performance was observed only above 600 ˚C due to ammonia over-oxidation. In this physical mixture the soot oxidation was also significantly improved compared to the case of Fe-ZSM5 alone. However as high NO_x conversions are achieved in the combined SCR and soot oxidation, NO_2 could not participate significantly in the soot oxidation and the CO_x profile was more similar to soot oxidation on KCP with only O_2 (Figures 3.9 and 3.10). This confirms previous studies [11,13–19] that in the simultaneous presence of soot oxidation and NO_x SCR reaction the NO_2 reduction is kinetically much faster and its contribution to soot oxidation is inhibited. Soot oxidation was initiated at lower temperatures, indicating at least a partial contribution of NO_2 to the soot oxidation. It also took more time to reach the complete soot oxidation,

due to inferior contact of KCP and soot as the SCR catalyst presented a physical barrier, indicating that a portion of the soot was non-catalytically oxidized.

When the KCP and Fe-ZSM5 were mixed in equal amounts, the NO_x SCR performance was better than on pure Fe-ZSM5, however worse than the mixture with a 2:1 ratio. As the relative amount of the soot oxidation catalyst was higher, the NH_3 oxidation was more pronounced and the NO_x conversion decreased significantly at temperatures above 550 ˚C. For the same reason, the soot oxidation was slightly better than the previous case, however it still approached the soot oxidation curve of the test with only O_2 over KCP. Among the three mixtures, only for the one with a 1:1 ratio a significant difference in the NO_x conversion (~10%) in the presence and absence of soot was observed in the initial temperature range of the soot oxidation. As KCP catalyzed the NO_2-soot oxidation (see Figure 3.2 and 3.6), it also decreased the NO_2/NO_x ratio in the presence of soot consequently lowering the contribution of the Fast SCR. In the other two cases this was not observed, since the relative amount of Fe-ZSM5 was high, thus the NO_2 was depleted for the fast SCR and there was not enough KCP for the NO_2-soot reaction to proceed. In contrast, when the relative Fe-ZSM5 content was low, the NO oxidation could proceed and plenty of NO_2 was produced, hence the SCR reaction was not limited by the NO_2-soot reaction.

With the inlet NO_2/NO_x ratio adjusted to 0.5, the combined soot oxidation and fast SCR was performed for the mixture with a Fe-ZSM5:KCP ratio of 2:1. Due to the lower amount of the SCR catalyst (180 mg vs. 270 mg) in the catalytic system, the NO_x conversion was much lower in the low temperature range (c.a. 20% less) if compared to the pure Fe-ZSM5 catalyst. However, as the temperature increased above 300 ˚C, it approached the profile of the pure Fe-ZSM5. As such, in terms of NO_x conversion, no improvement was observed for the physical mixture since the SCR regime was already in the Fast SCR regime and no transformation of standard-to-fast SCR occurred. The soot oxidation was slightly improved in the Fast SCR regime compared to the Standard SCR under the same conditions, most likely due to the improved NO oxidation and slight NO_2 contribution at higher temperatures. The same principle applies however, as in the previous case, i.e. NO_2 did not contribute significantly to soot oxidation due to the simultaneously occurring faster SCR reactions.

To extend and generalize the concept of simultaneous improvement of NO_x and soot removal, the same concept was tested with the Cu-ZSM5 catalyst. Cu-zeolites are, in general, less sensitive to the NO_2/NO_x ratio and they have better NO_x performance at low temperatures. This, however, comes at a cost of ammonia over-oxidation at higher temperatures and higher N_2O production compared to Fe zeolites [41]. In Figure 3.10 the behavior of a soot oxidation catalyst mixed with Cu-ZSM5 is shown. As SCR on Cu-ZSM5 is not as sensitive to the NO_2/NO_x ratio as Fe-ZSM5, a lower amount of the soot oxidation catalyst was used in the physical mixture. Below 300 ˚C, as there was no significant NO oxidation on KCP, there was a decrease in conversion proportional to the amount of the Cu-ZSM5 present. However, there was also a small improvement (~5%) in

the NO_x conversion in the range 300-400 ˚C for the Cu-ZSM5:KCP 4.5:1 mixture when the NO oxidation became significant.

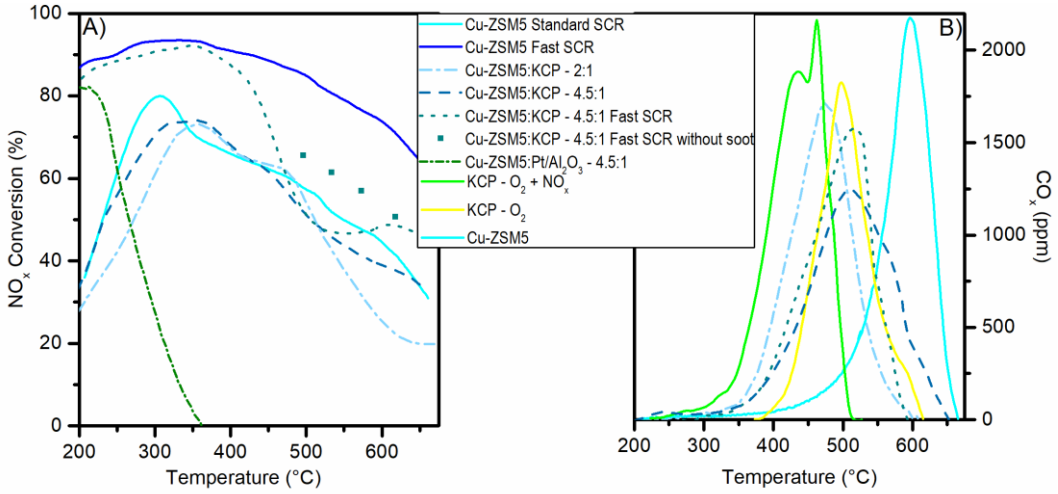

Figure 3.10. Combined soot oxidation and NO_x SCR in the physical mixture of KCP and Cu-ZSM-5. Reaction conditions: 500 ppm NO_x, 500 ppm NH_3, 4% O_2 in N_2; $NO_2/NO_x = 0$ for standard SCR and 0.5 for fast SCR; *w/f* 27 g_{cat}·s/L; catalyst: soot mass ratio 9:1 in loose contact; 2 °C/min heating rate.

Fast SCR was also performed for the physical mixture with a Cu-ZSM5:KCP ratio of 4.5:1. Below 400 ˚C the performance was the same as pure Cu-ZSM5, whereas at higher temperatures the NO_x conversion decreased by ~15% as ammonia was non-selectively oxidized. From this, it can be inferred that for Cu-zeolites only small improvements are possible in exploiting the pathway of transformation of standard to fast SCR the reaction system, and they are more sensitive to ammonia over-oxidation compared to Fe-zeolites. Over the Cu-ZSM5: KCP physical mixture the NO_x conversion in the Fast SCR differed in the presence and absence of soot. In the presence of soot the NO_x conversion was lowered by 15% between 450-550 °C, corresponding to the soot oxidation temperature range. Since the conversion in the presence of soot approached that of obtained under Standard SCR conditions it is most likely that the KCP enhanced NO_2 utilization decreased the participation of the Fast SCR in the reaction scheme.

The soot oxidation was significantly improved in the physical mixture compared to the pure Cu-ZSM5. As in the case with the Fe-ZSM5 catalyst, the soot oxidation in the mixture was more similar to the soot oxidation with O_2 on KCP. It is important to note that, while the peak of maximum soot oxidation almost matched, the oxidation initiated at a c.a. 50 ˚C temperature lower, indicating at least the partial involvement of NO_2. As the SCR catalyst presented a physical barrier to the soot oxidation catalyst, the soot oxidation needed more time and higher temperatures to complete the soot oxidation, implying that at least a portion of the soot was non-catalytically burned. From this, it can be inferred that the washcoating of the monolith with the soot oxidation catalyst would be an important parameter and should be done on the inlet side as to maximize the

catalyst-soot contact. The CO emission in the case of physical mixture was also significantly lowered and remained always under 100 ppm (Figure S3.4) as with catalytic soot oxidation higher selectivity towards CO_2 was achieved. While in the case of the Cu-ZSM5 catalyst alone the selectivity towards CO was as high as 30%, in all the physical mixture cases remained under 5%.

The N_2O production in the physical mixture mimicked the cases with the pure SCR catalyst, so only those for the optimal mixture are shown. Cu-ZSM5 had much higher N_2O production than its Fe counterpart and its concentration reached almost 50 ppm in the fast SCR.

To demonstrate the effect of the ammonia oxidation on the SCR reactions, Cu-ZSM5 was mixed with Pt/Al_2O_3 in 4.5:1 ratio and simultaneous SCR and soot oxidation was performed. As can be seen in figures 3.10a and 3.11, NO_x conversion quickly decreased and, due to the non-selective oxidation of ammonia, almost 250 ppm of N_2O was present in the outlet. This highlights the importance that the soot and NO oxidation catalyst must not be oxidative towards ammonia as it decreases the amount of the reductant available for the NO_x SCR and can produce unwanted reaction products.

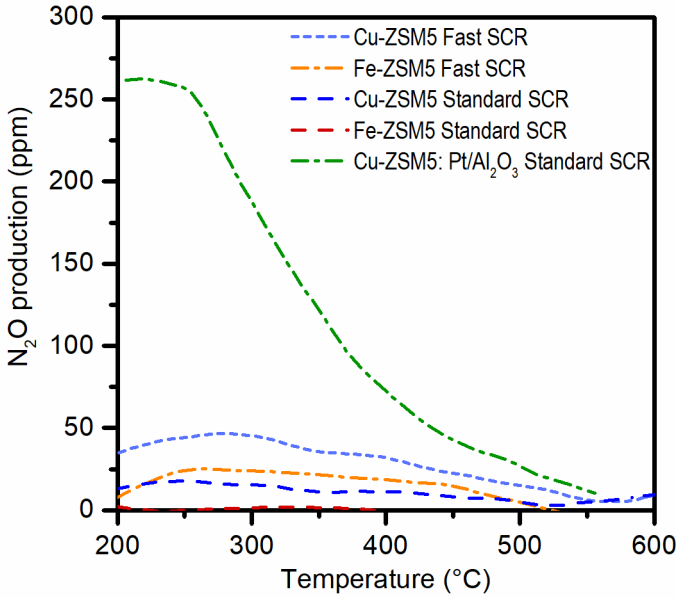

Figure 3.11. N_2O production during the combined soot oxidation and NO_x SCR in the physical mixture of soot oxidation and SCR catalysts. Reaction conditions: 500 ppm NO_x, 500 ppm NH_3, 4% O_2 in N_2; $NO_2/NO_x = 0$ for standard SCR and 0.5 for fast SCR; *w/f* 27 g_{cat}·s/L; catalyst: soot mass ratio 9:1 in loose contact; 2 °C/min heating rate.

3.3.4. Stability of the soot oxidation catalyst

SO_2 is a known poison for the NO oxidation catalysts as it can adsorb on the active sites and form stable sulfates, thereby inhibiting NO oxidation. When exposed to SO_2, CP underwent sever deactivation, and after c.a. 150 minutes complete deactivation was observed (Figure S3.5A). KCP on the other hand had abundant basic sites (Figure 3.2) that could adsorb and passivize the sulfates, essentially acting as a guard bed. After 150 min, the NO_2/NO_x ratio decrease only

by 0.1 and the catalyst retained significant NO oxidation activity even after 6 hours of exposure.

The thermal stability of KCP was demonstrated through repeated soot oxidation (Figure S3.5B). Potassium as soot oxidation catalyst is known to have low stability under certain conditions [32,43], however several methods are known for its stabilization [44,45]. The stability of potassium in KCP was ensured by low loading and high calcination temperature which enabled strong anchoring on the support and steady performance. As shown in Figure 3.11b, after 5 repeated soot oxidation cycles the soot oxidation temperature decreased the conversion curves only by 15 ˚C, confirming the thermal stability of KCP during soot oxidation.

3.4. Conclusions

The soot oxidation on SCRoF was successfully enhanced to address the problem of soot accumulation by the combination of a common SCR catalyst and a soot and NO oxidation catalyst. The soot oxidation on the single component Cu- or Fe-ZSM5 was significantly inhibited by the NO_2 consumption in the kinetically much faster SCR reaction and temperatures above 600 °C were required to oxidize all the soot. However, by mixing a soot oxidation catalyst and a common SCR catalyst, the temperature of soot oxidation was lowered by more than 150 °C while at the same time maintaining high NO_x conversion. In the physical mixture the soot was oxidized mainly by O_2 as the contribution of NO_2 was limited as it reacted in the kinetically much faster SCR reaction leaving little for the soot oxidation. Avoiding the ammonia oxidation by the soot oxidation catalyst was crucial as the consumption of the reductant inhibited the performance of the SCR reaction. This was achieved by targeted poisoning of the acid sites on the soot oxidation catalyst through its impregnation with small amounts of potassium.

The K/CeO_2-PrO_2 soot oxidation catalyst was also selectively active for NO oxidation that offered simultaneous improvement in the NO_x conversion by transforming the SCR reaction pathway from standard to fast SCR. As SCR catalyst, Cu-ZSM5 offered better performance at low temperatures and Fe-ZSM5 in the higher temperature range, while in fast SCR regime both catalysts offered high activity in a wide temperature range. By varying the relative amounts of the soot oxidation and SCR catalysts, several characteristic phenomena were observed. In the physical mixture, for the optimal Fe-ZSM5:KCP ratio of 2:1, almost 20% improvement in NO_x conversion was observed relative to the same amount of pure Fe-ZSM5 (1:0 “ratio”). In contrast, as Cu-ZSM5 was not as sensitive to the NO_2/NO_x inlet ratio, the improvement in the physical mixture was modest (c.a. 5%) and observed only above 300 °C. Cu-ZSM5 was however more sensitive to ammonia oxidation and thereby the optimal ratio of the Cu-ZSM5:KCP was 4.5:1, much lower than in the case of Fe-ZSM5. Lower SCR catalyst: KCP ratio was beneficial for the soot oxidation however it lowered the NO_x conversion as less SCR catalyst was available.

Finally, it should be emphasized that the tests were conducted in a laboratory setup and the main aim was to provide a detailed study between the interaction of a soot oxidation catalyst and the SCR reactions. Besides the chemical interactions, on the real monolith other important parameters should also be considered. The fluid dynamics and pressure drop are important variables, as well as the catalyst loading and distribution. Furthermore, the effect of the soot oxidation catalyst and soot contact should be evaluated as different contact length with the filtered soot cake can limit the effective range.

References

[1] M. Schejbal, J. Štěpánek, M. Marek, P. Kočí, M. Kubíček, Fuel 89 (2010) 2365–2375.
[2] M.D. Tomić, L.D. Savin, R.D. Mićić, M.D. Simikić, T.F. Furman, Therm. Sci. (2013).
[3] S.M. Platt, I. El Haddad, S.M. Pieber, A.A. Zardini, R. Suarez-Bertoa, M. Clairotte, K.R. Daellenbach, R.J. Huang, J.G. Slowik, S. Hellebust, B. Temime-Roussel, N. Marchand, J. De Gouw, J.L. Jimenez, P.L. Hayes, A.L. Robinson, U. Baltensperger, C. Astorga, A.S.H. Prévôt, Sci. Rep. (2017).
[4] C.L. Myung, W. Jang, S. Kwon, J. Ko, D. Jin, S. Park, Energy (2017).
[5] N. Hooftman, M. Messagie, J. Van Mierlo, T. Coosemans, Renew. Sustain. Energy Rev. (2018).
[6] T.R. Dallmann, R.A. Harley, T.W. Kirchstetter, Environ. Sci. Technol. (2011).
[7] T.R. Dallmann, S.J. Demartini, T.W. Kirchstetter, S.C. Herndon, T.B. Onasch, E.C. Wood, R.A. Harley, Environ. Sci. Technol. (2012).
[8] D. Fino, S. Bensaid, M. Piumetti, N. Russo, Appl. Catal. A Gen. 509 (2016) 75–96.
[9] G.J. Bartley, in: SAE Tech. Pap. Ser., 2015.
[10] K. Kamasamudram, N. Currier, T. Szailer, A. Yezerets, SAE Int. J. Fuels Lubr. (2010).
[11] K.G. Rappé, Ind. Eng. Chem. Res. 53 (2014) 17547–17557.
[12] P.S. Metkar, M.P. Harold, V. Balakotaiah, Chem. Eng. Sci. (2013).
[13] S. Bensaid, V. Balakotaiah, D. Luss, AIChE J. 63 (2017) 238–248.
[14] F. Marchitti, I. Nova, E. Tronconi, Catal. Today 267 (2016) 110–118.
[15] T. Wolff, R. Deinlein, H. Christensen, L. Larsen, SAE Int. J. Mater. Manuf. (2014).
[16] A.Y. Stakheev, G.N. Baeva, G.O. Bragina, N.S. Teleguina, A.L. Kustov, M. Grill, J.R. Thøgersen, in: Top. Catal., 2013.
[17] S.Y. Park, K. Narayanaswamy, S.J. Schmieg, C.J. Rutland, Ind. Eng. Chem. Res. (2012).
[18] D. Karamitros, G. Koltsakis, Chem. Eng. Sci. (2017).
[19] W. Tang, D. Youngren, M. SantaMaria, S. Kumar, SAE Int. J. Engines (2013).
[20] A. Sultana, M. Sasaki, K. Suzuki, H. Hamada, Appl. Catal. A Gen. (2013).
[21] Z. Liu, J. Hao, L. Fu, T. Zhu, J. Li, X. Cui, Chem. Eng. Technol. (2004).
[22] Y.K. Hong, D.W. Lee, Y.C. Ko, L. Yinghua, H.S. Han, K.Y. Lee, Catal. Letters (2010).
[23] P.S. Metkar, M.P. Harold, V. Balakotaiah, Appl. Catal. B Environ. (2012).
[24] T. Wittka, B. Holderbaum, P. Dittmann, S. Pischinger, Emiss. Control Sci. Technol. (2015).
[25] M. Václavík, P. Kočí, V. Novák, D. Thompsett, Chem. Eng. J. (2017).
[26] M. Misono, Y. Hirao, C. Yokoyama, Catal. Today (1997).
[27] A.I. Mytareva, D.A. Bokarev, G.N. Baeva, D.S. Krivoruchenko, A.Y. Belyankin, A.Y. Stakheev, Pet. Chem. 56 (2016) 211–216.
[28] A.I. Mytareva, D.A. Bokarev, G.N. Baeva, A.Y. Belyankin, A.Y. Stakheev, Top.

Catal. 0 (2018) 0.
[29] D.S. Krivoruchenko, N.S. Telegina, D.A. Bokarev, A.Y. Stakheev, Kinet. Catal. 56 (2015) 741–746.
[30] M. Salazar, R. Becker, W. Grünert, Appl. Catal. B Environ. (2015).
[31] M. Salazar, S. Hoffmann, O.P. Tkachenko, R. Becker, W. Grünert, Appl. Catal. B Environ. (2016).
[32] F. Martinovic, T. Andana, F.A. Deorsola, B. Samir, P. Raffaele, Catal. Letters (2019).
[33] I. Atribak, A. Bueno-López, A. García-García, Combust. Flame (2010).
[34] T. Andana, M. Piumetti, S. Bensaid, L. Veyre, C. Thieuleux, N. Russo, D. Fino, E.A. Quadrelli, R. Pirone, Appl. Catal. B Environ. (2018).
[35] L. Castoldi, N. Artioli, R. Matarrese, L. Lietti, P. Forzatti, in: Catal. Today, 2010.
[36] B.S. Sánchez, C.A. Querini, E.E. Miró, Appl. Catal. A Gen. 392 (2011) 158–165.
[37] Q. Li, X. Wang, Y. Xin, Z. Zhang, Y. Zhang, C. Hao, M. Meng, L. Zheng, L. Zheng, Sci. Rep. 4 (2014).
[38] Y. Peng, J. Li, X. Huang, X. Li, W. Su, X. Sun, D. Wang, J. Hao, Environ. Sci. Technol. (2014).
[39] K. Tanaka, Dynamic Chemical Processes on Solid Surfaces, 2017.
[40] W. Tang, B. Chen, K. Hallstrom, A. Wille, SAE Int. J. Engines (2016).
[41] D. Zhang, R.T. Yang, Energy and Fuels (2018).
[42] O. Mihai, S. Tamm, M. Stenfeldt, L. Olsson, Philos. Trans. R. Soc. A Math. Phys. Eng. Sci. 374 (2016) 20150086.
[43] R. Matarrese, E. Aneggi, L. Castoldi, J. Llorca, A. Trovarelli, L. Lietti, Catal. Today (2016).
[44] R. Kimura, J. Wakabayashi, S.P. Elangovan, M. Ogura, T. Okubo, J. Am. Chem. Soc. (2008).
[45] M. Ogura, R. Kimura, H. Ushiyama, F. Nikaido, K. Yamashita, T. Okubo, ChemCatChem 6 (2014) 479–484.

Supplementary material for Chapter 3

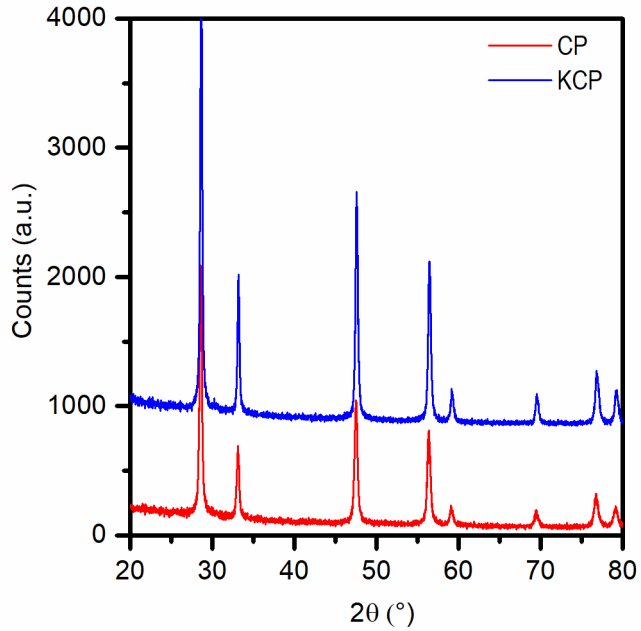

Figure S3.1. XRD diffractogram of the CP and KCP samples.

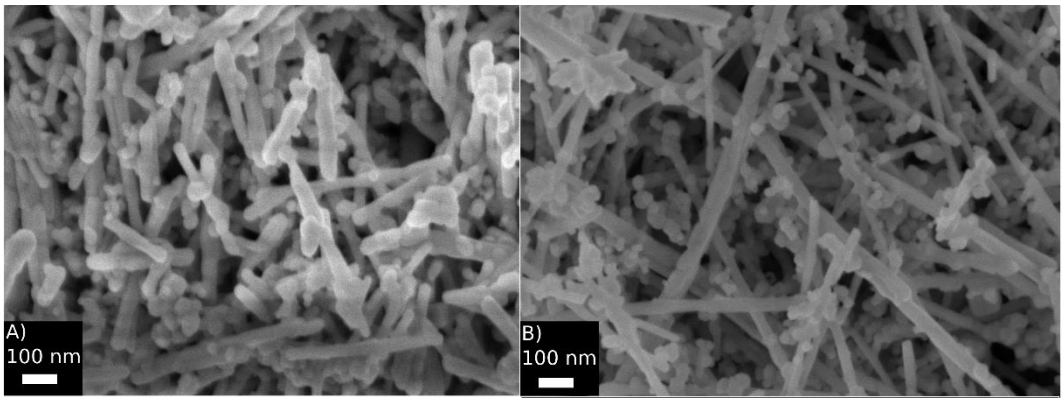

Figure S3.2. FE-SEM images of the CP and KCP samples.

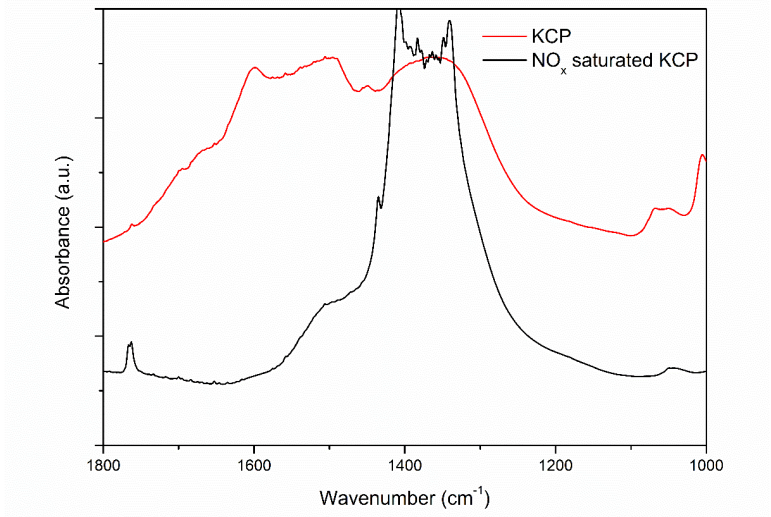

Figure S3.3. FT-IR spectra of the CP and NO_x saturated KCP samples.

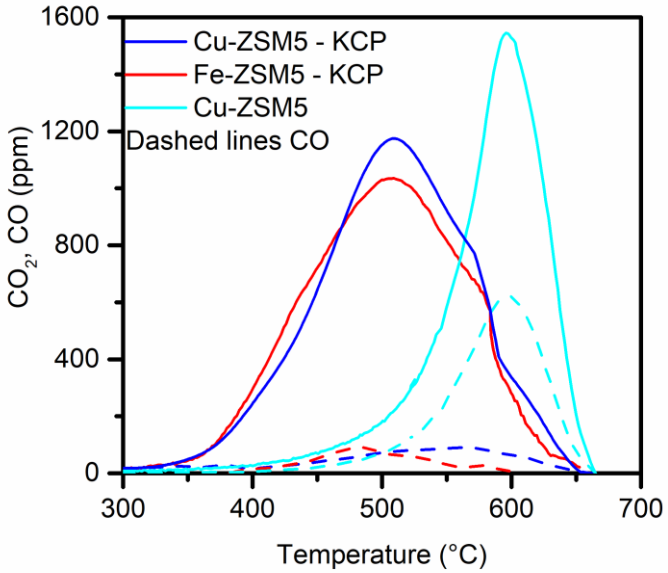

Figure S3.4. . CO_2 and CO evolution during combined soot oxidation-SCR reactions over Cu-ZSM5 and physical mixtures of KCP and Fe- and Cu-ZSM5 catalysts.

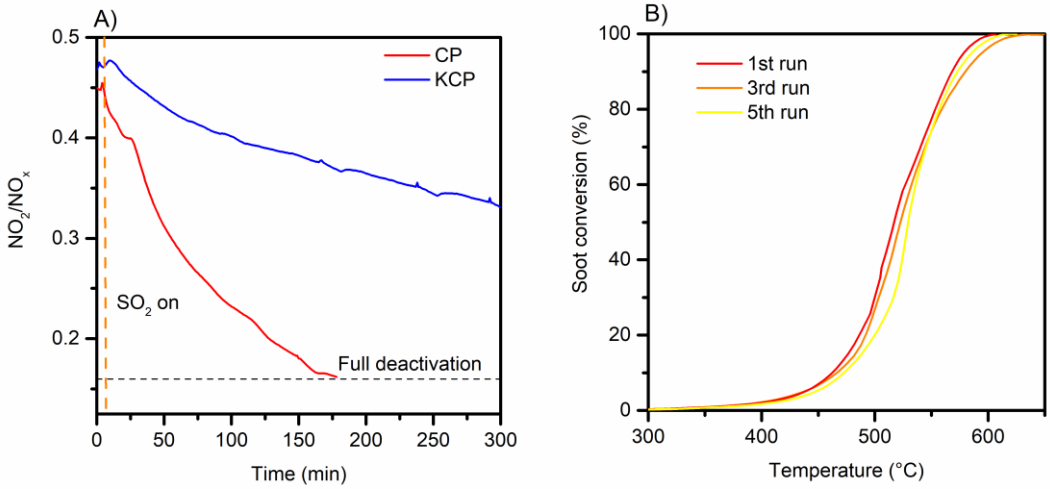

Figure S3.5. . Deactivation of CP and KCP upon A) exposure to 60 ppm of SO_2 and B) repeated soot oxidation over KCP.

Chapter 4

4. Composite Cu-SSZ-13 and CeO_2-SnO_2 for enhanced NH_3-SCR resistance towards hydrocarbon deactivation

Chapter summary

The active soot regeneration of the SCRoF necessitates SCR catalyst that is resistant towards thermal sintering and for that reason the current state-of-the-art catalyst used is the Cu-SSZ-13. The Cu zeolites are however highly susceptible towards poisoning by hydrocarbons due to highly dispersed metal sites and strong acidity. Over the SCRoF the poisoning by the hydrocarbons is more pronounced due to the close coupling, presence of soot and hydrocarbon injection during regeneration. To overcome this problem a Composite catalyst was prepared by ball milling Cu-SSZ-13 and CeO_2-SnO_2 in 4: 1 mass ratio. The as prepared catalyst exhibited excellent resistance towards hydrocarbon and SO_2 poisoning. By transient and specific reactivity tests a strong synergy and direct interaction was found between the principal active sites (Cu-protonic sites-CeO_2-SnO_2) participating in the SCR reaction. It is suggested that the resistance towards hydrocarbon poisoning is due to the migration of reaction intermediate, possibly nitrate, from the CeO_2-SnO_2 towards Cu-SSZ-13 thereby reactivating the SCR catalytic cycle.

Adapted from the publication in Applied Catalysis B: Environmental (2021) 282: 119536

https://doi.org/10.1016/j.apcatb.2020.119536

4.1. Introduction

Due to the toxic effect of NO_x gases and particulate matter (PM), stringent regulations are implemented worldwide for automotive exhaust treatment (e.g. Euro 6d went in effect in January 2020). In the vast majority of cases, for the abatement of NO_x in the exhaust gases urea-based systems are used in which the ammonia generated from the injected urea decomposition acts as a reductant. The state-of-the-art catalyst used in NH_3-SCR (Selective Catalytic Reduction) systems is copper-exchanged chabazite zeolite, mainly Cu-SSZ-13 [1,2]. Diesel engines typically operate in lean (oxygen-rich) conditions, however hydrocarbon (HC) slip often occurs, especially at cold start, during sudden changes in engine load, as a consequence of degradation of diesel oxidation catalyst (DOC), etc. Furthermore, in certain aftertreatment configurations, the SCR catalyst is regularly exposed to HC and to reducing conditions. For example, in the combination of NH_3-SCR with lean NO_x traps (LNT), where the in situ generated ammonia is used on the downstream SCR catalyst, the SCR system is often exposed, at regular intervals, to high concentrations of HC and to reducing conditions. Several reports have noticed in that such a HC exposure results in severe poisoning and subsequent deactivation of the SCR catalyst [3,4]. Another configuration where HC poisoning of SCR catalyst is a common issue is SCR on Filter (SCRoF) systems, as they are more exposed to HC due to close coupling and forced regenerations where HC is

injected to increase temperature and trigger soot oxidation [5,6]. Furthermore, the filtered soot accumulated on the SCRoF typically contains a significant fraction of soluble organic compounds in the form of naphtalenes that can migrate and poison the SCR catalyst [2,7,8].

SSZ-13 zeolite is a small pore zeolite that offers enhanced hydrothermal stability, activity and, resistance to HC poisoning as compared to other (larger pore) zeolites such as ZSM-5 or BEA. The enhanced resistance of SSZ-13 towards HC poisoning originates from its (small) 8-membered rings pore structure, since the pore diameter of 3.8 Å inhibits the diffusion of HC, which typically have larger kinetic diameters, e.g. 4.3 Å for straight chain alkanes and alkenes, such as propene or dodecane. At elevated temperatures (>250 °C), however, the zeolite pores widen, HC diffusivity increases, and significant poisoning still occurs over the SSZ-13 [1,9,10]. The reason why metal-exchanged zeolites are highly susceptible to HC poisoning is the simultaneous presence of strong Brønsted acid sites and highly dispersed metals, typically Cu and Fe. Their combination favors the formation of carbenium and carbonium intermediates and the polymerization is catalyzed by the same active sites, resulting in coke deposition and consequent zeolite deactivation. Both HC and NO adsorb on the same metal sites and the competition for the same redox sites prevents nitrates formation in the SCR cycle. Mechanistic studies indicate that coke forms selectively on zeolite metal sites, preventing the oxidation of NO to NO_2, which is a key reaction step in the NH_3-mediated SCR of NO_x. NH_3 activation and interaction with HC, which mainly occurs on the zeolite acidic sites, is not considered an important factor in the poisoning mechanism [1,8–12].

The approach for the control of HC poisoning suggested in this chapter involves the combination of two different catalysts. The former is a common SCR catalyst used in automotive aftertreatment systems (Cu-SSZ-13), while the latter is a mixed CeO_2-SnO_2 oxide. One of the earliest examples regarding this kind of approach is the combination of ZSM-5, SnO_2 and/or MnO_2 for enhanced HC-SCR, where different roles in the reaction cycle were assigned to the different components [13]. Another example is the combination of Zn-ZSM-5 and Ag/Al_2O_3 for improved SCR of NO_x with octane [14]. In the previous cases, the primary role of SnO_2 or Zn-ZSM-5 was the transformation of HC into more reactive oxygenated compounds, while MnO_2 and Ag/Al_2O_3 catalyzed the oxidation of NO to nitrate. Another combination suggested in the literature is that between Fe-zeolites and doped MnO_2 oxides. The aim was to enhance the NO oxidation and thereby transform the reaction system from standard to fast SCR, also improving NO_x conversion. In those cases, the NO_x conversion was significantly improved at lower temperature, however high amount of N_2O was observed and, above 300 °C, detrimental NH_3 oxidation prevented the occurrence of SCR reaction. The above considerations highlight the importance that the two components must be compatible, i.e. the non-selective overoxidation of NH_3 (the SCR reductant) over the added metal oxide must be prevented [15–20].

Despite numerous detailed mechanistic investigations of HC poisoning of zeolite-based SCR catalysts [1,8–12,21], only few solutions have been proposed in literature. One of them was the coating of the SCR catalyst with a layer of small pore mordenite zeolite to capture and filter HC to prevent them from reaching the SCR catalyst with moderate success [22,23]. Another suggested solution was the combination of the SCR catalyst with MnO_2, which increases the HC and the NO to NO_2 oxidation, thereby minimizing the poisoning effect. Although HC poisoning was prevented, NH_3 overoxidation was also observed, leading to high N_2O production and lowering NO_x conversion [15,18,19,24].
The aim of this chapter is to produce a catalyst that, by offering a different catalytic pathway, retains the high SCR activity of Cu-SSZ-13 without the negative effects of NH_3 overoxidation and decrease of selectivity. Such a goal was achieved by mixing in tight contact the Cu-SSZ-13 and CeO_2-SnO_2 catalysts and demonstrating the resistance to HC poisoning, without overoxidation of NH_3, N_2O production and the corresponding decrease in the SCR activity and selectivity. An alternative pathway is suggested, where HC poisoning is inhibited by the interaction between the mixed oxide and the ion exchanged Cu zeolite through the intermediates formed during the SCR reaction.

4.2. Materials and methods

4.2.1. Catalyst preparation

The Cu-SSZ-13 catalyst was prepared by ion exchange from a NH_4-SSZ-13 zeolite (SiO_2/Al_2O_3 ratio of 18, ACS Materials) that was previously calcined at 500 °C for 4 h to get the H-SSZ-13 form. The ion exchange was performed by placing the so-obtained H-SSZ-13 zeolite in a 50 mM solution of copper(II) acetate (Sigma-Aldrich) and stirring for 24 h at room temperature (25°C). The ion exchanged zeolite was separated by centrifugation and washed with distilled water until neutral pH was reached in the resulting liquid. The powder was subsequently dried at 110 °C for 12 h and calcined at 700 °C for 5 h. The resulting Cu-SSZ-13 catalyst had a 3.4 wt.% Cu content, as determined by EDX, and a final Al/Cu ratio of 2.6 that is equal to ca. 77 % of the maximum exchange capacity.
Besides Cu-SSZ-13, also a Fe-BEA zeolite was explored as a different type of catalyst. Iron having less affinity than copper towards HC and BEA being a larger pore zeolite (12 member rings) than SSZ-13. Fe-BEA zeolite is more sensitive to HC poisoning than Cu-SSZ-13 due to absence of diffusion limitations [23]. The Fe-BEA catalyst was prepared by ion exchange under protective N_2 atmosphere to prevent Fe(III) formation. After degassing deionized water in N_2 flow, ascorbic acid (Sigma-Aldrich) was added as oxygen scavenger followed by addition of iron(II) acetate (Sigma-Aldrich) to obtain a 50 mM Fe^{2+} solution. Subsequent washing and thermal treatments were the same of the Cu-SSZ-13 catalyst and the iron loading in the product was 1.4 wt%.
CeO_2-SnO_2 was used as second catalyst since it is a proven catalyst for both HC-SCR and NH_3-SCR ([25–29], also *vide infra*). CeO_2-SnO_2 (Ce:Sn atomic ratio

1:1) was prepared by coprecipitation whereby $Ce(NO_3)_3 \cdot 6H_2O$ and $SnCl_4 \cdot 5H_2O$ (Sigma-Aldrich) were used as precursors. Proper amounts of the two precursors were dissolved in distilled water and precipitated by addition of NH_4OH aqueous solution and raising the pH to 9.5 under stirring. The precipitate was aged for 24 h at room temperature, separated by centrifugation and thoroughly washed with distilled water. The catalyst was dried at 110 °C for 12 h and calcined at 700 °C for 5 h (5 °C/min heating rate). For comparison, another mixed MnO_2-CeO_2 oxide with Mn:Ce ratio equal to 1:9 was prepared by using the same procedure adopted for the CeO_2-SnO_2 catalyst using $Mn(NO_3)_2 \cdot 6H_2O$ as precursor.
The Composite catalyst was prepared by mixing the Cu-SSZ-13 catalyst with the CeO_2-SnO_2 catalyst in mass ratio 4:1, which was determined as the optimal ratio in a preliminary screening stage. The mixture was ball-milled in a planetary colloidal mill for 30 minutes to achieve tight contact between the two catalysts. The color of the as obtained Composite catalyst became light green as a consequence of the mixing of the light blue Cu-SSZ-13 powder and the yellow CeO_2-SnO_2 powder. The H-Composite catalyst was prepared by an analogous method, except for the fact that the CeO_2-SnO_2 catalyst was mixed with H-SSZ-13 instead of Cu-SSZ-13. The composite of Fe-BEA and CeO_2-SnO_2 (BEA-Composite) as well as the composite of MnO_2-CeO_2 and Cu-SSZ-13 (Mn-Composite) were prepared in a similar fashion as described before. Due to the comparison purpose of these preparations, not all the physico-chemical characterizations as well as the catalytic ones were performed on these catalysts. The most relevant ones to the results discussion are illustrated in the Supplementary material.

4.2.2. Catalyst characterization

The superficial properties of the as-prepared and poisoned catalysts were determined on a Tristar 3020 (Micrometrics) by N_2 physisorption at -196 °C and the specific surface area of the powders was calculated according to the BET (Brunauer-Emmett-Teller) method. Prior analysis, the samples were treated at 150 °C for 2 h under He flow to remove adsorbed water and other contaminants.
The morphological characterization was performed by field emission scanning electron microscopy (FE-SEM) on a Zeiss MERLIN Gemini II equipped with EDS (Electron Dispersive X-ray Spectroscopy) probe at 3 keV accelerating voltage and at different magnification.
X-ray diffraction (XRD) was performed on a Panalytical PW 3040 X'Pert equipped with a Cu anode for the Kα radiation generation at 40 kV operating voltage. The pixel array detector enabled continuous data acquisition in the 2θ range of 20-80 ° with a step of 0.013 °.
The catalyst reducibility was determined by H_2-TPR (Temperature Programmed Reduction) in a TPDRO (Temperature Programmed Desorption Oxidation Reduction,) 1100 instrument (Thermo-Scientific) equipped a with TCD (Thermal Conductivity Detector) and appropriate filters. Typically, 60 mg sample was

pretreated in Ar flow for 6 h at 500 °C to remove moisture and other adsorbed contaminants. After cooling down, the reactive gas consisting of a 5 vol.% H_2 in Ar mixture was introduced and the catalyst was reduced with a heating ramp of 5 °C/min in the 50 - 850 °C temperature range.
The number and change in acid sites of the Composite was evaluated by NH_3-TPD experiments before and after coking on the same experimental setup used in reactivity studies (*vide infra*). The Composite was saturated with 1000 ppm NH_3 in N_2 at 120 °C for 1 h at a 600 mL/min flowrate. After saturation, the sample was cooled down to 50 °C and a 5 °C/min temperature ramp was initiated for NH_3 desorption in a 300 mL/min N_2 flow.
The FT-IR (Fourier Transform Infra Red) spectra were collected in home-made quartz cell equipped with (IR transparent) KBr windows on a Bruker EQUINOX 55 instrument. Before analysis, the Cu-SSZ-13 and the Composite catalysts were exposed to $C_3H_6 + O_2$ and $C_3H_6 + NO + O_2$ gas mixtures at 300 °C for 30 min, upon which the samples turned dark brown evidencing coke deposition. Such a temperature was chosen since high degree of deactivation was observed, with low C_3H_6 oxidation activity. The catalyst samples were then pressed into thin uniform self-supporting pellets and outgassed at 100 °C and the IR spectra collected in transmittance mode at 2 cm^{-1} resolution. The reported difference IR spectra were obtained by subtracting the spectra of the pristine samples.

4.2.3. Reactivity studies

Reactivity studies were performed in a tubular quartz reactor with 10 mm internal diameter. The powdered catalyst was placed on a porous glass frit inside the reactor which was heated in a vertical furnace with a programmable temperature. A thermocouple was placed in the catalyst bed to record the reaction temperature. The gaseous reaction products continuously analyzed with dedicated ND-IR and ND-UV analyzers (ABB AO2000 Uras and Limas) were: NO, NO_2, N_2O, NH_3, CO_2 and CO.
In a typical experiment, 200 mg catalyst was employed, while the total gas flowrate was 600 mL/min giving a catalyst weight per flowrate (*w/f)* of 0.02 g_{cat}/mL·s. The GHSV through the powdered catalytic bed was 60 000 h^{-1}. Considering the practical perspective of this study for the SCR on Filter application and assuming a catalyst loading of on the monolith 120 g/L, the corresponding monolith GHSV would be almost 22 000 h^{-1}. The typical concentrations utilized for the standard SCR mixture were: 500 ppm NO, 500 ppm NH_3, 4% O_2 with N_2 as carrier gas. When indicated, 4 vol.% H_2O and/or 700 ppm of C_3H_6 as model HC were added in the reaction stream. Standard SCR with and without propylene were performed in the 175-600 °C temperature range by collecting data every 50 °C. The reported conversions were obtained after 20 min waiting time at each temperature, since, in some cases, steady state conditions could not be achieved as the catalyst progressively deactivated with time.
The stability of the Composite catalyst was evaluated by performing accelerated hydrothermal and SO_2 ageing. Hydrothermal ageing was conducted at 700 °C for

6 h in a 4% H_2O, 4% O_2 in N_2 flow, with the flowrate and catalyst loading as in the SCR tests. Additionally, a severe hydrothermal ageing was also performed at 800 °C for 80 h with the same flow composition in order to investigate the extent of the deactivation for both the Composite and the Cu-SSZ-13 under these harsh conditions. The SO_2 poisoning was performed by exposing the catalyst to a 50 ppm SO_2, 4% O_2 in N_2 flow for 3 h, resulting in a cumulative SO_2 flowed of 10 mmol SO_2/g_{cat}. If a 6 kg/100 km consumption of fuel containing 10 ppm S (Euro 5 fuel upper limit, EN 590:2009) and a total 200 g of SCR catalyst in the aftertreatment system are assumed, the equivalent SO_2 poisoning would be reached after ca. 25 000 km. Both the hydrothermal and SO_2 aged Composite were tested for the SCR reaction using the same conditions as described above and the potential loss in the resistance towards hydrocarbon poisoning was investigated.

Transient HC poisoning studies were performed at a constant temperature of 350 °C, since at that temperature the most severe deactivation was observed over the Cu-SSZ-13 catalyst (vide infra). After the NO_x concentration stabilized under standard SCR conditions, 700 ppm of C_3H_6 was introduced for 30 min and simultaneously the decrease in NO_x conversion as well as the CO_2 and CO produced from the C_3H_6 oxidation were recorded. After 30 minutes of poisoning, the C_3H_6 flow was turned off and the extent of recovery of the SCR activity was observed.

The impact of contact mode between Cu-SSZ-13 and CeO_2-SnO_2 was evaluated in a similar fashion at 350 °C. Besides the tight contact mode of the Composite catalyst, loose contact mode was obtained by gently mixing the two catalyst powders with a spatula: in this case, the powder mixture did not change color and, instead, distinct blue or yellow particles/patches could be distinguished. A dual-zone configuration was obtained by placing a layer of 40 mg CeO_2-SnO_2 on top of 160 mg Cu-SSZ-13 that was located downstream.

Further reactivity studies were conducted under dynamic conditions with the reaction gas containing C_3H_6 + O_2 and C_3H_6 + NO + O_2 (i.e. HC-mediated SCR). A temperature ramp of 5 °C/min was used, as steady state conditions could not be achieved due to continuous coking and gradual deactivation over time. Furthermore, dynamic conditions enabled the assessment of some additional features, e.g. the T_{max} (indicating the burn-off temperature of the accumulated coke), the CO/CO_x ratio, etc.

Coke-TPO (Temperature Programmed Oxidation) was performed by saturating the catalyst in C_3H_6 + O_2 gas for 30 min at 250 °C. The reactor was cooled down and a 5 °C/min heating ramp was set, starting at 100 °C. The so-accumulated coke on the catalyst was oxidized in a 4 vol.% O_2 in N_2 flow to provide information about the nature and reactivity of the built-up coke.

For evidencing the direct transfer of intermediates, the CeO_2-SnO_2 was presaturated in a 600 mL/min flow of 500 ppm NO, 4% O_2 in N_2 for 30 minutes at 250 °C. The Cu-SSZ-13 was exposed to 700 ppm C_3H_6, 4 % O_2 in N_2 for 30 minutes to form coke deposits. The as-saturated catalysts were then placed in dual

layer configuration, whereby 160 mg of coked Cu-SSZ-13 was downstream of 40 mg of NO_x saturated CeO_2-SnO_2, with the two layers physically separated by a 2 mm thick layer of quartz wool. The saturated catalysts were also ball-milled in the same mass ratio to achieve tight contact analogously to the Composite synthesis. The two configurations were then exposed to a 300 mL/min flowrate of N_2 with 5 °C/min heating rate to observe the desorption, reaction and interaction of the adsorbed species.

4.3. Results

4.3.1. Catalysts characterization

In Figure 4.1, a representative FE-SEM micrograph of the Composite catalyst is shown, while further images coupled with EDS maps can be found in Supplementary material (Figure S4.1). The simultaneous ball-milling of the Cu-SSZ-13 and CeO_2-SnO_2 catalysts induced a high dispersion of the CeO_2-SnO_2 particles over the zeolite catalyst. CeO_2-SnO_2 could be found uniformly through the whole Composite sample, however the particle size of the oxide varied in a broad range, from ca. 50 nm (Figure 4.1A) to several μm (Figure 4.1B). The CeO_2-SnO_2 particles adhered to the zeolite particles, without obstructing the zeolite pores (*vide infra*) or changing the zeolite morphology, since cubic-like particles are observed.

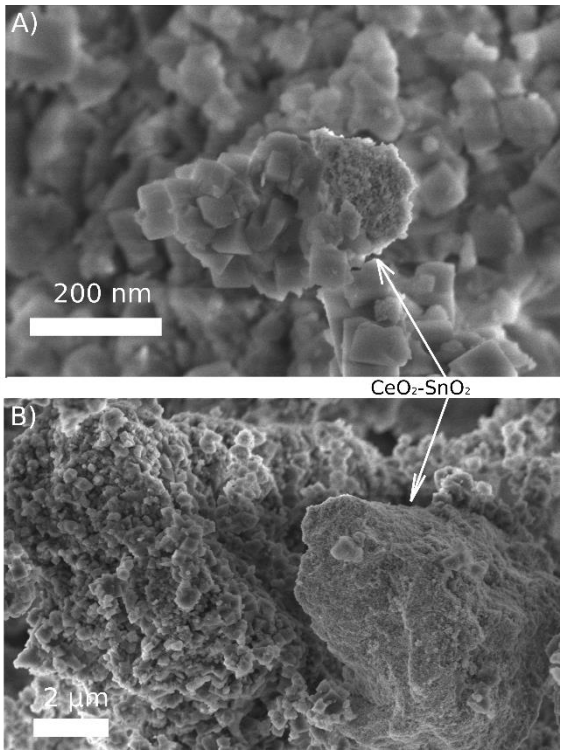

Figure 4.1. FE-SEM micrographs of the Composite catalyst at two different magnifications.

N_2 isotherms (Figure 4.2) at-196 °C of CeO_2-SnO_2 showed a type IV shape, with type H1 hysteresis loop due to inter-particle mesoporosity (with average pore size of 13.6 nm), the corresponding specific surface area (SSA) being 50 m^2/g. The H-SSZ-13 zeolite showed a type I isotherm, typical of microporous materials with a SSA of 540 m^2/g and specific pore volume of 0.25 cm^3/g. Although being basically a type I isotherm, the H-SSZ-13 catalyt isotherm also show a limited hysteresis loop due to inter-particle mesopores reflecting the occurrence of some aggregation phenomena. The SSA of Cu-SSZ-13 was lower, i.e. to 472 m^2/g, likely due to the ion-exchange procedure and the subsequent thermal treatment. The Composite and H-Composite catalysts had SSA values of 411 m^2/g and 461 m^2/g, respectively, and showed "composite" isotherms, due to the co-presence of both a microporous adsorbent (i.e. the zeolite) and a mesoporous adsorbent (i.e. the oxide phase with aggregated spherical particles): the two isotherms showed indeed a steep increase at low relative pressure (due to adsorption within micropores) and a hysteresis loop at higher relative pressure (due to adsorption within inter-particle mesopores). The shape of the isotherms was the result of the linear combination of CeO_2-SnO_2 contributing for 20% and Cu- and H-SSZ-13 contributing for 80%.

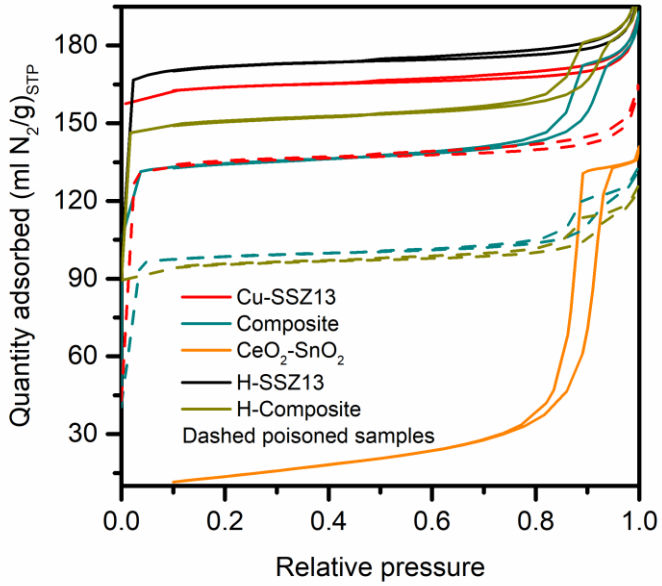

Figure 4.2. N_2 physisorption isotherms at -196 °C as obtained with the Composite, Cu-SSZ-13, CeO_2-SnO_2, H-Composite catalysts and the parent H-SSZ-13 zeolite and the corresponding poisoned samples: Cu-SSZ-13; Composite and H-Composite. The isotherms have been shifted long the Y-direction to facilitate understanding the graph.

The HC poisoned Cu-SSZ-13, Composite and H-Composite powders had markedly lowered SSA of 411 m^2/g, 303 m^2/g and 279 m^2/g respectively. Such relevant reduction in both SSA and pore volume (Table 4.1) can be attributed to the coke deposition and blocking of the small pores of zeolites. The importance of

this result is that the CeO_2-SnO_2 does not prevent coke formation and deposition within the zeolite pores and, in fact, the relative SSA reduction of the H-Composite catalyst was higher than that of Cu-SSZ-13. The worst deactivation observed with H-Composite (in terms of loss of SSA) might be the consequence of the highest concentration and strength of protonic acid sites, which promoted coke formation within the pores. Indeed, no reduction or change in both the SSA and morphology was observed after the poisoning on CeO_2-SnO_2.

Figure 4.3A reports the H_2-TPR curves of the investigated samples. The Cu-SSZ-13 featured a H_2-TPR curve characteristical for the ion-exchanged Cu-SSZ-13 with the sequential reduction steps $Cu^{2+}/Cu^{+}/Cu$ that started as low as 170 °C and the first peak appeared at 210 °C. In the XRD pattern of Cu-SSZ-13 (Figure S4.2), only the SSZ-13 zeolite phase could be detected and CuO was missing, evidencing the predominant ion-exchange state of Cu. The CeO_2-SnO_2 catalyst presented a complex TPR profile as a result of the variety of oxides with different Ce:Sn ratios occurring in the catalyst, as shown in the corresponding XRD pattern reported in Figure S4.2. A reduction onset is seen at ca. 200 °C and then, in the 250 – 500 °C range, several peaks are seen, which can be attributed to highly reducible species. The mixed oxide system reducibility is regulated by the Ce:Sn ratio in the -Ce^{4+}-O-Sn^{4+}- crystal lattice [25,26] and the mutual doping and insertion of Sn in CeO_2 and of Ce in SnO_2 can promote the formation of the Ce^{4+} / Ce^{3+} and Sn^{4+} /Sn^{2+} redox pairs. The reduction peak at the highest temperature (ca. 600 °C) can be attributed to the reduction of (unpromoted) SnO_2 (single peak at 515 °C) and CeO_2 (650 °C) [25,26]. The presence of mixed oxides as well as of separate CeO_2 and SnO_2 was observed by XRD analysis (see Figure S4.2 in Supplementary material). The XRD pattern of CeO_2-SnO_2 presented two phases: the tetragonal rutile SnO_2 and cubic fluorite crystal structure arising from CeO_2. Partial insertion of Ce into the rutile SnO_2 and Sn into CeO_2 crystal structure can easily take place, without changing significantly the peak position [32]. The total H_2 consumed during the reduction of the Composite catalyst corresponded to the value calculated as the linear combination of the proportional contribution of CeO_2-SnO_2 (20 wt.%) and of Cu-SSZ-13 (80 wt.%). Indeed, the TPR curve of Composite showed the first main H_2 consumption peak at ca. 210 °C, which also occurs in the Cu-SSZ-13 catalyst at the same temperature, indicating that the zeolite is almost unperturbed in the mixture. The low temperature TPR profile was very close to that of the CeO_2-SnO_2 catalyst; however, interestingly, the highest temperature reduction peak was markedly shifted downward to 560 °C from the original 600 °C with both the Composite and H-Composite catalyst. The increased reducibility of the two composites can be attributed to a smaller particle size, as a result of the ball-milling procedure. Such mechano-chemical activation and interaction has been already observed and investigated for other catalytic systems, involving, for example CeO_2-Cu-ZSM5 [13] and discussed in the review [29].

Figure 4.3B presents the NH_3-TPD of the Composite catalyst with the changes in its acidity induced by the C_3H_6 exposure and coking. The NH_3-TPD curve of

zeolites can be generally classified into three temperature regions: the 100-200 °C range is associated with the physisorbed or weakly chemisorbed NH_3, the 200-400 °C one is related to the NH_3 adsorbed on the zeolite hydroxyl groups and the region over 600 °C identifies the NH_3 adsorbed on the dehydroxylated strong Brønsted and Lewis acid sites. The total NH_3 adsorption capacity of the coked Composite was calculated, by estimation of the area under the NH_3-TPD curves, to be lowered by 18% if compared to the fresh Composite. However, this decrease was limited only to temperatures lower than 200 °C. Considering that the NH_3 desorbed below 200 °C is attributable to the physisorbed NH_3, this decrease could be ascribed to the pore blocking by coke and to the consequent decrease in the surface area and pore volume, as evidenced in Table 4.1. The areas under the curve of the deconvoluted first region (peak at 175 °C in Figure 3B) of the coked and fresh samples presented a ratio of 0.54, which well correlates to the ratio of the SSA after/before coking of 0.6. The NH_3 desorption profiles above 200 °C were practically identical of both the coked and fresh samples, suggesting that coke does not interfere with the NH_3 adsorption on the active sites that are involved in the NH_3 storage and that participate in the SCR reaction [1,9].
During the NH_3-TPD of the coked sample, CO and CO_2 could be detected deriving from the oxidation of the coke deposited on the Composite. In this process the Cu was reduced considering that there was no O_2 in the sweep gas.

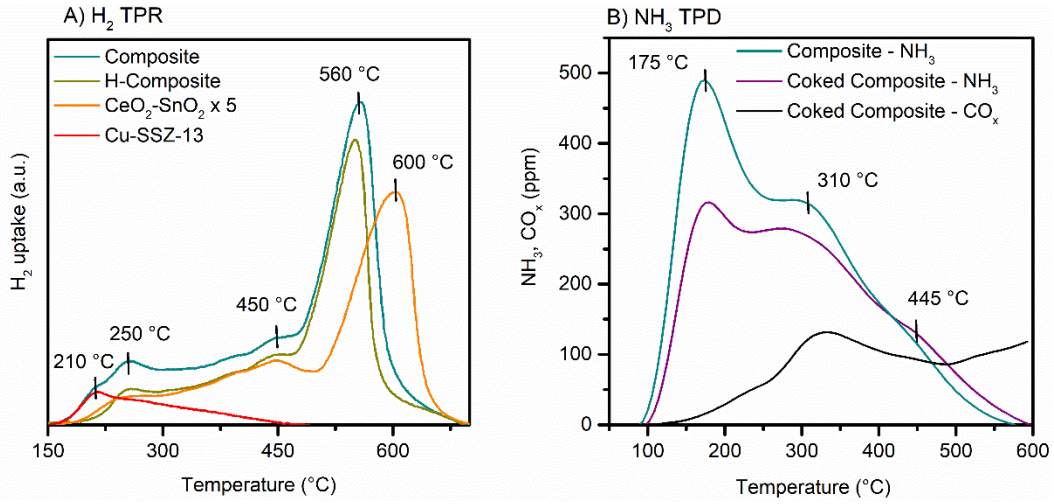

Figure 4.3. (A) H_2-TPR curves as obtained with the investigated samples, with the exception of H-SSZ-13 zeolite, for which no H_2 consumption is expected. To allow comparison, the CeO_2-SnO_2 TPR curve has been reduced by a factor of 5, as detailed in the legend. (B) NH_3-TPD of Composite before and after coking.

Table 4.1. Values of the SSA (m^2/g) and specific pore volume (cm^3/g) before and after coking, in order to show their decrease as a result of poisoning.

Catalyst	SSA (m^2/g)		Specific pore volume (cm^3/g)	
	Before coking	After coking	Before coking	After coking
Cu-SSZ-13	472	411	0.241	0.194
Composite	411	303	0.195	0.143
H-Composite	461	279	0.224	0.137
CeO_2-SnO_2	50	n.a.	0.211	n.a.

4.3.2. Reactivity studies

4.3.2.1. SCR activity

The steady-state SCR activities of the four investigated catalysts (CeO_2-SnO_2, Cu-SSZ-13, Composite and H-Composite) under different reaction conditions are shown in Figure 4.4. Without HC in the reaction stream, under both dry and humid conditions, the Composite catalyst had the same NO_x conversion as the Cu-SSZ-13 over the whole temperature range. CeO_2-SnO_2 had high NO_x conversion in the temperature range 300-450 °C, however above 450 °C the NO_x conversion decreased due to the competitive reaction of ammonia oxidation and NO production. Such a decrease was not observed in the Composite catalyst, as the SCR reaction over the Cu-SSZ-13 is kinetically faster, thereby consuming the NH_3 before it can react over the CeO_2-SnO_2. With the addition of C_3H_6 as model HC in the reaction stream the highest decrease in the NO_x conversion was observed over the Cu-SSZ-13, with the largest difference at 350 °C. The inhibition of the SCR reaction was more pronounced in dry conditions, where a decrease in conversion of 40% was observed in contrast to 24% when H_2O was also present in the reaction stream. Conversely, CeO_2-SnO_2 did not undergo significant deactivation when C_3H_6 was included in the reaction stream and above 350 °C the NO_x conversion was even improved, because C_3H_6 acted as additional reductant cooperatively with NH_3. The resistance of CeO_2-SnO_2 to HC poisoning can be attributed to the lack of Brønsted acid sites and, as a result, there was no interaction and coking of the active sites (*vide infra* the coke-TPO). The combination of CeO_2-SnO_2 and Cu-SSZ-13 conferred resistance towards HC inhibition to the Composite catalyst, where the highest difference observed in the NO_x conversion was 9%, with the performance improving in humid conditions as compared to dry conditions (Figure 4.4C). Furthermore, over the Composite catalyst, the NO_x conversion improved above 400 °C in the presence of C_3H_6 as a result of the additional reductant available. Unexpectedly and in contrast to the Composite catalyst, the H-Composite also underwent significant deactivation (decrease of 10-15%) and showed low C_3H_6 oxidation activity, from which it was hypothesised that the HC resistance was not simply due to the oxidation of the

HC, but also to the interaction between CeO_2-SnO_2 and Cu-SSZ-13, which was further investigated and it is presented in the following sections. The H-Composite retained the bell-shaped curve of the NO_x conversion in contrast to Cu-SSZ-13 that showed a large decrease of conversion between 300 and 400 °C and a sudden recovery at higher temperatures, with a behavior that has been widely observed in the literature [1,8–12,21]. Since the CeO_2-SnO_2 is the SCR component mainly active towards NO oxidation while the NH_3 adsorption occurred over the H-SSZ-13, the H-Composite did not exhibit the same behavior of the Cu-SSZ-13. The Cu-SSZ-13, and to lesser extent the Composite, presented a seagull-shaped curve of the NO_x conversion with a minimum at 350 °C when C_3H_6 was included in the reaction stream. This kind of response to HC poisoning is peculiar and it has been observed only for the small pore CHA type zeolites (e.g. SSZ-13 or SAPO-34), in contrast to ZSM-5 or BEA zeolites where deactivation is more pronounced at lower temperatures. The absence of low-temperature (< 250 °C) deactivation can be attributed to the effect of size exclusion due to the small pores of the zeolite structure that isolates the Cu active sites from the hydrocarbons. Subsequently, with the temperature increase, the pores of the zeolite widen as well as the rate of diffusion and reactivity of the C_3H_6 increase and interferes with the SCR reaction. At higher temperatures (> 450 °C), the rate of the oxidation of C_3H_6 by molecular oxygen becomes more apparent and the inhibition of the NH_3-SCR reaction is avoided when full oxidation is achieved [1-3, 21, 23].

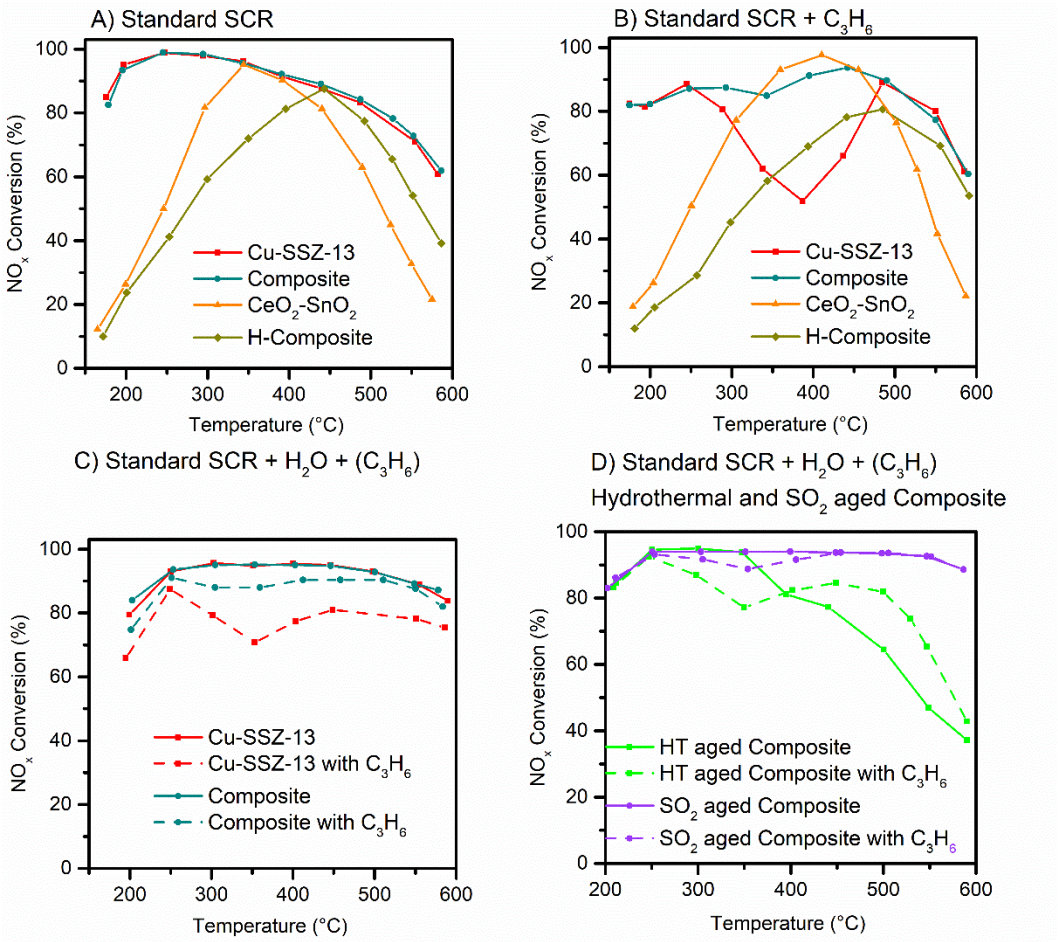

Figure 4.4. Comparison of NO_x SCR activity of the investigated catalysts: Standard SCR (A), Standard SCR with HC (B) and Standard SCR with H_2O and C_3H_6 added (C) and the stability of the Composite catalyst (D).

The current widespread use of Cu-SSZ-13 is due to its high resistance to hydrothermal ageing and SO_2 poisoning, both phenomena well investigated in the literature. Since the Composite is composed of 80% Cu-SSZ-13, the same degradation behavior could be assumed. The stability of the second component (CeO_2-SnO_2) and the interaction in the physical mixture are unknown and its deactivation could lead to the loss of the HC resistance in the Composite catalyst. In Figure 4.4D the SCR activity and the resistance to hydrocarbon poisoning of the Composite are shown after different deactivation treatments. The hydrothermally aged Composite had the same SCR activity as before the ageing at low temperatures, however above 450 °C the NO_x conversion decreased. This phenomenon is well investigated in the literature and usually ascribed to the formation of extraframework CuO as a result of Cu migration from the Cu-SSZ-13. The extraframework CuO induces NH_3 non-selective overoxidation towards NO that reduces NO_x conversion at higher temperature [4,30,31]. After undergoing hydrothermal ageing, the HC resistance of the Composite was partially degraded but not fully lost. The highest decrease in the NO_x conversion, upon the C_3H_6 inclusion, was at 350 °C hence this temperature was considered for

the description of the extent of deactivation. The NO_x conversion was 88% and 70% over the fresh Composite and Cu-SSZ-13, while the hydrothermally aged Composite had 78% NO_x conversion in the presence of HC, still higher than the unmodified Cu-SSZ-13. Above 400 °C, the inclusion of hydrocarbons was highly beneficial for the SCR activity of the hydrothermally aged Composite since the C_3H_6 acted as additional reductant, thereby limiting the NH_3 overoxidation that was pronounced on the aged Composite. Upon a severe hydrothermal ageing (800 °C for 80 h), both Composite and Cu-SSZ-13 underwent the same extent of deactivation as the NO_x conversion decreased ca. 20-30 % for the standard SCR reaction conditions in the whole temperature range (Figure S4.3). The most significant reduction in the activity was observed at low temperature since the NO_x conversion at 200 °C decreased from 95% to only 60%. The resistance to C_3H_6 poisoning was reduced as the severely aged Composite had only ca. 5% higher NO_x conversion than the Cu-SSZ-13. Such effects are not surprising considering that above 700 °C the SSZ-13 zeolite structure undergoes severe dealumination, loss of Brønsted acid sites, collapse of the structure and the Cu sites can form CuO or $CuAl_2O_4$ spinel that is inactive for the SCR reaction [3-5, 30, 31].

SO_2 ageing did not have any effect on the SCR activity since the NO_x conversion, with and without HC, over the Composite exposed to SO_2 was practically the same as the fresh Composite. It has been reported in the literature that similar SO_2 ageing of Cu-SSZ-13 results in a decrease of conversion of ca. 20% [32,33], however this was not the case with the Composite. The resistance to SO_2 poisoning in hybrid Cu-SSZ-13 + $ZnTi_{10}O_x$ was investigated in [33], where it was demonstrated that the addition of a mixed oxide can serve as a guard bed and reduce the effects of SO_2 .

N_2O production (not shown) was in all cases low (<10 ppm), except in the case of the Mn-Composite where a maximum of 40 ppm N_2O was observed at 350 °C .

4.3.2.2. Transient HC poisoning

In Figure 4.5, the transient deactivation and the recovery of NO_x conversion activity after adding/removing C_3H_6 in the reaction mixture are shown. The tests were performed at constant 350 °C, since at that temperature the highest SCR deactivation was observed (Figure 4.4) and therefore it was the most useful choice for the observation of the build-up and depletion of the reaction intermediates. Cu-SSZ-13 underwent significant deactivation, as the NO_x conversion decreased by 40% upon the introduction of C_3H_6 and underwent further gradual deactivation with time. The CO/CO_x ratio, when C_3H_6 was present in the reaction stream, was 0.41 over the Cu-SSZ-13 and even higher over Fe-BEA zeolite (0.63 Figure S4.4) resulting in high CO emission. When the C_3H_6 was turned off, the SCR activity progressively recovered, however low concentration of CO_x (ca. 150 ppm for Cu-SSZ-13 and 50 ppm for Fe-BEA) was detected in the outlet, suggesting the buildup and slow oxidation of the coke polymerized and deposited on the active

sites. Interestingly, the CO/CO_x ratio was markedly lower when the C_3H_6 was turned off and the coke oxidized, being 0.13 for the Cu-SSZ-13 and 0.25 for the Fe-BEA. This suggests a different oxidation mechanism involved in the oxidation of C_3H_6 and coke, with the HC oxidation involving concurrent reactions of protolytic cracking. The NO_x conversion over the coked Cu-SSZ-13, however, remained 10 % lower than at the beginning of the experiment and the initial SCR activity could be recovered only after burning off the coke deposits and reactivating the catalyst by calcination at 650 °C. The CeO_2-SnO_2, in turn, did not exhibit significant deactivation in the presence of HC and the NO_x conversion decreased only by 7 %, most likely due to the consumption of surface nitrates. Since the CeO_2-SnO_2 surface is characterized by the predominant presence of Lewis type acid sites [25–27], there was no coking (*vide infra*, Figure 4.8) and the initial SCR activity could be recovered immediately when the C_3H_6 flow was turned off. The Composite catalyst displayed a similar resistance to HC poisoning, as the degree and the recovery from deactivation followed the same pattern as CeO_2-SnO_2. Both CeO_2-SnO_2 and the Composite oxidized nearly 90% of the C_3H_6 from the gas stream with high selectivity towards CO_2. In stark contrast, with the H-Composite the NO_x conversion decreased by more than 15 % and only 25 % of the C_3H_6 was oxidized to CO_x. This provides evidence for the interaction and synergy between the ion-exchanged Cu-SSZ-13 zeolite and the CeO_2-SnO_2 as the addition of CeO_2-SnO_2 to the H form of the SSZ-13 zeolite led to much worse performance towards HC oxidation and poisoning prevention, as compared to the Composite catalyst, due to the occurrence of Brønsted acid sites in the H-SSZ-13 zeolite, which catalyse coke deposition. Furthermore, from these results we can infer that one of the main causes of the coke formation is due to the HC polymerization over the protonic acid sites of the zeolite. The decrease in the SCR activity is attributable mainly to the competitive oxidation reaction between the NO_x SCR reaction cycle and the C_3H_6 oxidation. As shown in Figure 4.5, after stopping the C_3H_6 flow, the deposited coke also contributed to the decrease of the NO_x conversion, though to a much less extent than the inclusion of C_3H_6 in the gas stream. The lower reactivity of the coke relative to C_3H_6 means that its interference with the SCR reaction is much less pronounced.

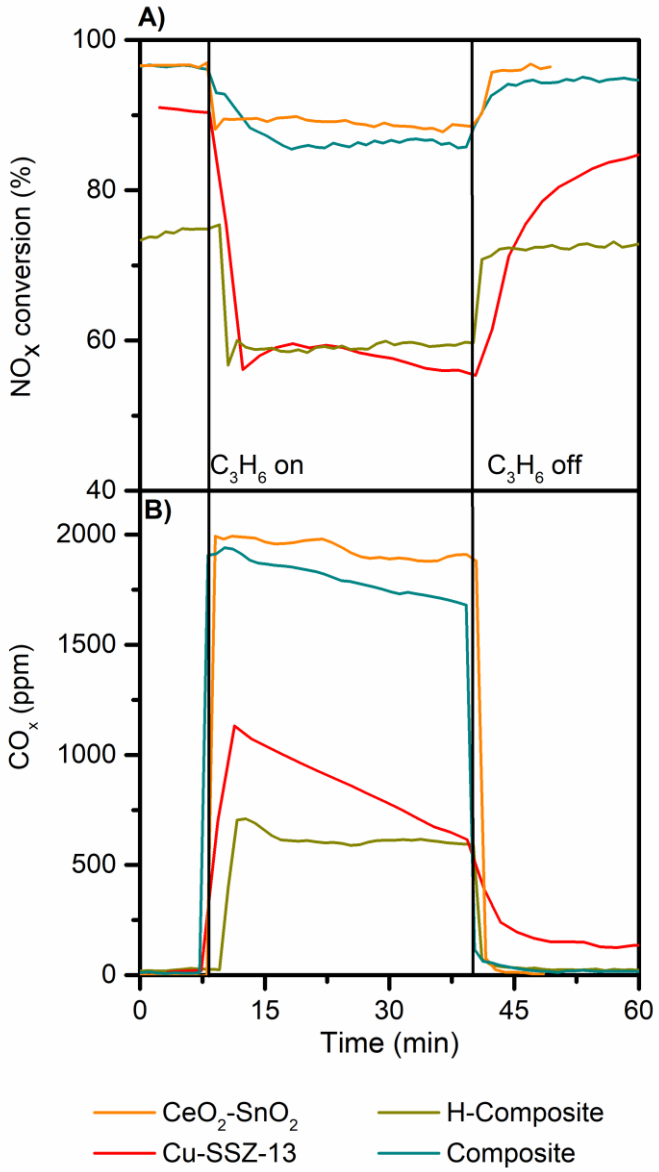

Figure 4.5. Transient HC poisoning under standard SCR conditions. Reaction conditions: 200 mg catalyst, 600 mL/min flowrate of 500 ppm NO and NH_3, 4% O_2 in N_2, 700 ppm C_3H_6 added when indicated, T = 350 °C.

The summary and comparison of the key results (relative decrease in NO_x conversion, CO/CO_x ratio and C_3H_6 conversion) obtained for the catalysts used are presented in Table 4.2.

Table 4.2. Comparison of key parameters during the transient test. Reaction conditions as in Figure 5.

Catalyst used	Decrease in NO_x conversion after C_3H_6 introduction (%)	C_3H_6 Conversion (%)	CO/CO_x ratio
Cu-SSZ-13	40	35	0.41
Composite	9	91	0.07
H-Composite	15	25	0.05
CeO_2-SnO_2	7	90	0.01
Fe-BEA	40	29	0.63
BEA-Composite	20	60	0.07
Mn-Composite	30	65	0.07

4.3.2.3. Influence of the contact mode

Figure 4.6 shows the influence of the contact mode by using the Composite catalyst. The best performance was observed in tight contact mode, as in both loose contact and dual-zone configuration the NO_x conversion was 5 % and 10 % lower in the presence of C_3H_6, respectively. Furthermore, in both cases the conversion of C_3H_6 was lower and the production of CO higher, as compared to the tight contact, which is indicative of the higher contribution of the Cu sites towards the C_3H_6 oxidation. Thus, the resistance of the Cu-SSZ-13 catalyst in the Composite system to HC poisoning could not be attributed solely to kinetic effects, meaning that the resistance is not simply due to the C_3H_6 oxidation on CeO_2-SnO_2, since it would imply the achievement of the same NO_x conversion and C_3H_6 oxidation activity in both loose contact and dual-layer configuration as in tight contact. This would suggest a strong interaction and reactant spillover between Cu-SSZ-13 and CeO_2-SnO_2 catalyst as in other similar combined systems, (e.g. in Cu-ZSM-5 or Fe-ZSM-5 + Ba/Al_2O_3 [34,35], Nb/TiO_2 + Mn_2O_3 [36], Zn-ZSM-5 + Ag/Al_2O_3 [14], Pt/CeO_2 + BaO [37], Fe-ZSM-5 + MnO_2 [15,24], K/CeO_2-soot [38,39]), where it has been extensively shown that nitrite or nitrate intermediates can migrate between the different components in tight contact and sometimes even in loose contact.

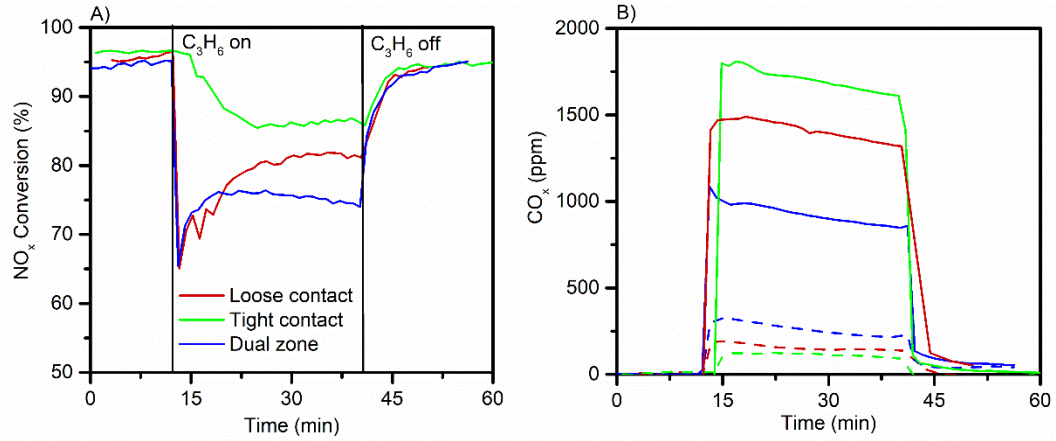

Figure 4.6. Influence of the contact mode with the Composite catalyst on the NO_x conversion (A) and C_3H_6 oxidation (B), along with selectivity to CO (dashed lines) and to CO_2 (full lines). The reaction conditions were the same as reported in Figure 4.5.

4.3.2.4. Influence of the gas composition on HC oxidation

To further elucidate the NO_x and C_3H_6 interaction, C_3H_6 was oxidized under dynamic conditions with a programmed temperature ramp (Figure 4.7 and Table 4.3). The most important finding was that over the Cu-SSZ-13 catalyst the C_3H_6 oxidation was significantly inhibited by the simultaneous presence of NO, as the whole C_3H_6 oxidation curve was delayed by more than 50 °C, with respect to the test where C_3H_6 was oxidized with only O_2. On the contrary, the Composite, CeO_2-SnO_2 and even the H-Composite catalysts did not exhibit such interaction and the presence of NO did not inhibit C_3H_6 oxidation. Surprisingly, the H-Composite had a bad performance for C_3H_6 oxidation, i.e. worse than Cu-SSZ-13 in the presence of a C_3H_6 + O_2 mixture and the same in a C_3H_6 + O_2 + NO atmosphere (Table 4.3). Such a drastic improvement in the performance of C_3H_6 oxidation with the Composite relative to the H-Composite catalysts when NO was included suggests a complex interaction and strong synergy between all the three (CeO_2-SnO_2 , copper, protonic sites) principal active sites involved in the catalytic cycle. The fed C_3H_6 was oxidized to CO_2 and CO, however a portion was also deposited as carbonaceous coke and an estimation of the total amount based on the coke TPO is given in Table 4.3. This can be also seen in Figure 4.7 from the part of the CO_x curve that overcomes the stoichiometric value of CO_x deriving from total oxidation of C_3H_6 (2100 ppm, dashed line) which is originated from the coke oxidation. The integration of the curve above the dashed line yields the estimate of the coke deposits that was found to be constant, ca. 20 mg C/g_{cat}, in all the three zeolite-containing samples and in both NO + O_2 and O_2 containing atmosphere. This would suggest that the coke deposition on the zeolite occurs rapidly in the initial stages of the reaction and reaches a constant value that is temperature dependent and influenced by the equilibrium between the coke

deposition and oxidation reaction rate. The coke burn-off temperature (represented as T_{max} in Table 4.3 i.e. the peak of the overshoot originating form the coke oxidation in Figure 4.7) had reverse trend on Cu-SSZ-13 as compared to the H-Composite. On Cu-SSZ-13, the coke oxidation was delayed by almost 50 °C in the presence of NO, while in contrast on the H-Composite the coke was oxidized at a lower temperature. This further implies that on Cu-SSZ-13 the oxidation of NO and C_3H_6 are competitive reactions on the isolated Cu^{2+} sites, whereas on CeO_2-SnO_2 the same interaction is beneficial, as the nitrite/nitrate formation and transfer was enhancing the HC and coke oxidation.

In the H-Composite, the CeO_2-SnO_2 did not enhance the coke burn-off temperature when only O_2 was used as oxidant (vide infra in Figure 4.8 coke-TPO) as the coke was deposited inside the zeolite pores and was not in contact with the CeO_2-SnO_2. Further confirmation that the ion exchanged Cu are the main active site in the Composite catalyst for the C_3H_6 oxidation can be inferred from the selectivity towards CO (reported as CO/CO_x) ratio, which is indicative of the oxidation mechanism. The Cu-exchanged zeolite had high CO production during the C_3H_6 oxidation with the CO/CO_x ratio reaching 0.41 (CO/CO_x ratio = 0.63 over the Fe-BEA catalyst, Figure S4.4), with higher CO production under C_3H_6 + NO + O_2 with respect to the C_3H_6 + O_2 gas composition (Figure 4.7 and Table 4.3). The CO/CO_x ratio had reverse trend over the Composite catalyst as it was lowered from 0.2 to 0.15 when NO was included. The CO/CO_x ratio for the Composite was markedly higher than the ratio observed for the H-Composite (0.1) or for the CeO_2-SnO_2 (near 0). It is hypothesized that the main catalytically active site involved in the C_3H_6 oxidation remains the zeolite Cu sites, while the role of CeO_2-SnO_2 is to supply the reactive nitrite/nitrate intermediates, thereby improving the coke reactivity and decomposition and re-activating the catalytic SCR cycle.

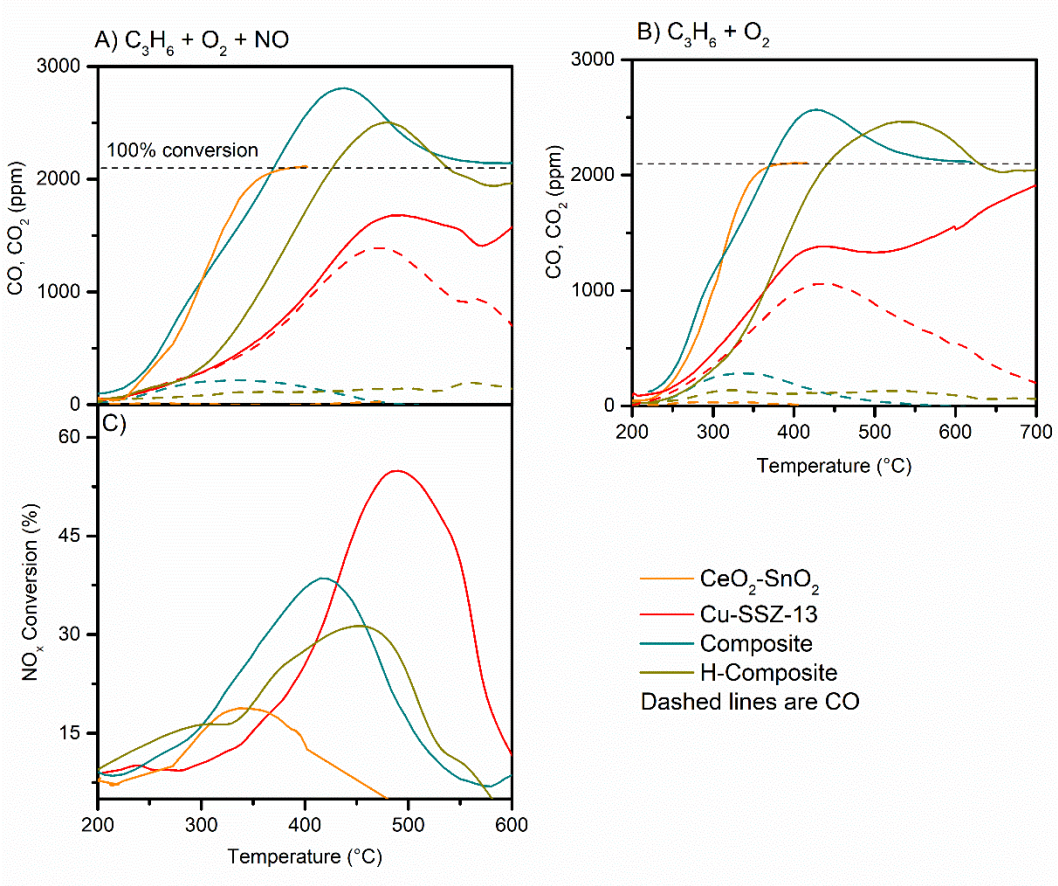

Figure 4.7. Dynamic C_3H_6 oxidation and HC-SCR under A) C_3H_6 + O_2 + NO and B) C_3H_6 + O_2 conditions and C) NO_x conversion under HC SCR conditions. Reaction conditions: 200 mg catalyst, 600 mL/min flowrate of 700 ppm C_3H_6, 500 ppm NO, 4% O_2 in N_2 5 °C/min heating rate.

Table 4.3. Comparison of the key parameters in C_3H_6 oxidation under O_2 and NO + O_2 atmosphere.

Parameter	T_{50} (°C)[a]		CO/CO_x (% at T_{50})		T_{max} (°C)[b]		Total amount of coke (mg C/g_{cat})
Gas composition	C_3H_6 + O_2	C_3H_6 + O_2 + NO	C_3H_6 + O_2	C_3H_6 + O_2 + NO	C_3H_6 + O_2	C_3H_6 + O_2 + NO	TPO after C_3H_6 + O_2 saturation for 30 min
H-Composite	361	354	10.6	9.6	**534**	**482**	20.5
Composite	**286**	**287**	**19.4**	**15.8**	425	433	28.65
CeO_2-SnO_2	301	294	0.8	0.9	-	-	0.9
Cu-SSZ-13	**322**	**363**	41	41	**436**	**480**	41.22

[a]Temperature of 50% C_3H_6 conversion.
[b]Peak temperature of the CO_x overshoot resulting from the coke oxidation.

Figure 4.8 illustrates the results of coke-TPO that was performed by saturating the catalyst in a C_3H_6 + O_2 flow for 30 min and by subsequently oxidizing the deposits formed under oxygen flow with a temperature ramp. The coke formation is the result of cracking, polymerization and partial oxidation processes over the copper Lewis sites and the protonic Brønsted sites of zeolite [1,8,9,11,12,21,40]. Over CeO_2-SnO_2 very small coke formation was observed, confirming the assumption that the mixed phase has poor interaction with the HC and does not favour significantly polymerization and formation of coke deposits. The addition of CeO_2-SnO_2 to the Cu-SSZ-13 zeolite did not prevent coke formation, as the total amount of coke deposited over the Composite catalyst was 70 % if compared to the Cu-SSZ-13, therefore almost proportional to the fraction of the Cu-SSZ-13 in the Composite catalyst. The coke reactivity was also the same, since the oxidation temperature and peak oxidation temperature (366 °C) coincided with both catalysts. The only major difference was that the CO production on the Cu-SSZ-13 was higher compared to the Composite catalyst (32% vs 8.6%). Significant coke formation was also observed over the H-Composite catalyst, in agreement with the role of Brønsted acid sites in coking mechanism. The coke oxidation profile over the H-SSZ-13 was the same as the one over the H-Composite, with the only exception that over H-Composite the CO production was low, while over H-SSZ-13 the selectivity towards CO was favoured. This provides further evidence that the addition of CeO_2-SnO_2 did not prevent coke formation nor enhance its oxidation, but it promotes the interaction occurring between the reaction products/intermediates such as nitrites/nitrates. The addition of CeO_2-SnO_2 did not improve the coke burnoff and in the absence of the ion exchanged Cu, the coke over H-Composite required the highest temperature for oxidation.

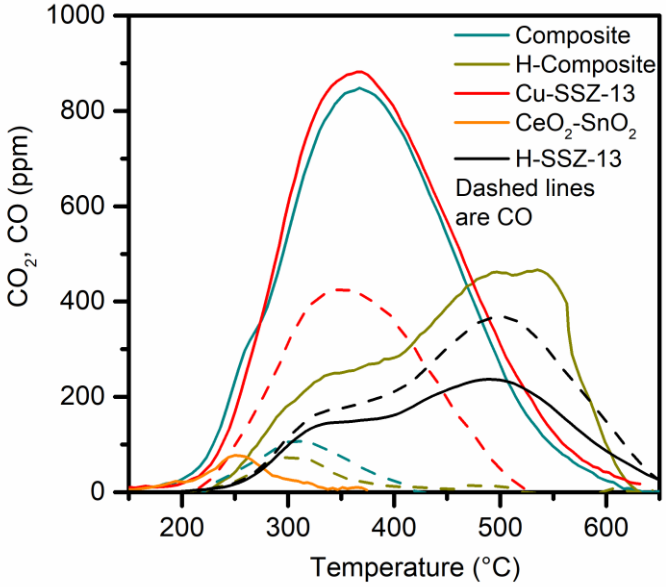

Figure 4.8. Coke-TPO over the investigated catalysts.

4.3.3. IR spectroscopy study

The IR spectra of the Cu-SSZ-13 and the Composite catalysts (Figure 4.9A) after exposure to the $C_3H_6 + O_2$ mixture are very similar, in that they differ only in their relative intensity: the IR bands occurring at *ca.* 1750, 1650, 1590 (with a shoulder at ca. 1550 cm^{-1}) and 1460 cm^{-1} are more intense with the zeolite alone, in agreement with the lower content of Cu-SSZ-13 in the Composite. Although the observed bands cannot be assigned unambiguously, the 1750 cm^{-1} band may be due to C=C double bonds of unsaturated C chains, the 1650 cm^{-1} to the stretching mode of C=O bonds in partially oxidized C chains or to C=C double bonds conjugated with either C=C or C=O bonds and the 1590, 1550 and 1460 cm^{-1} bands to carboxylate (likely acetate) groups. The weak bands at ca. 1480 and 1465 cm^{-1} can be due to the bending vibrations of CH_x groups in ethers, alcohols and enolic compounds, i.e. partially oxygenated carbon compounds [1, 41-43].

The IR spectra of the catalysts exposed to the $C_3H_6 + O_2 + NO$ mixture (Figure 4.9B) present significant differences, and in particular the relative intensity of the 1460 cm-1 band is is higher with the Cu-SSZ-13 sample, suggesting the prevalence of carboxylate ($-COO^-$) species in the partially oxidized deposits. The Composite showed a complex band envelope between 1500-1700 cm^{-1} likely due to the occurrence of different (partially) oxidized species, especially the carbonyl C=O functional group. When the Cu-SSZ-13 and the Composite were exposed to an $NO + O_2$ gas mixture the evolution of band at 1620 cm^{-1} that corresponds to the N=O group i surface adsorbed nitrate species (Figure S4.6 in supplementary material) was detected. On the $C_3H_6 + NO + O_2$ saturated Composite, the relatively stronger signal in the 1600– 1650 cm^{-1} range could be attributed to a more abundant presence of nitrate species, when compared to the Cu-SSZ-13 alone meaning that nitrates formation is not inhibited over the Composite. This result is in agreement with the reactivity tests where NO had an inhibitory effect over Cu-SSZ-13, whereas over the Composite it enhanced the HC reactivity.

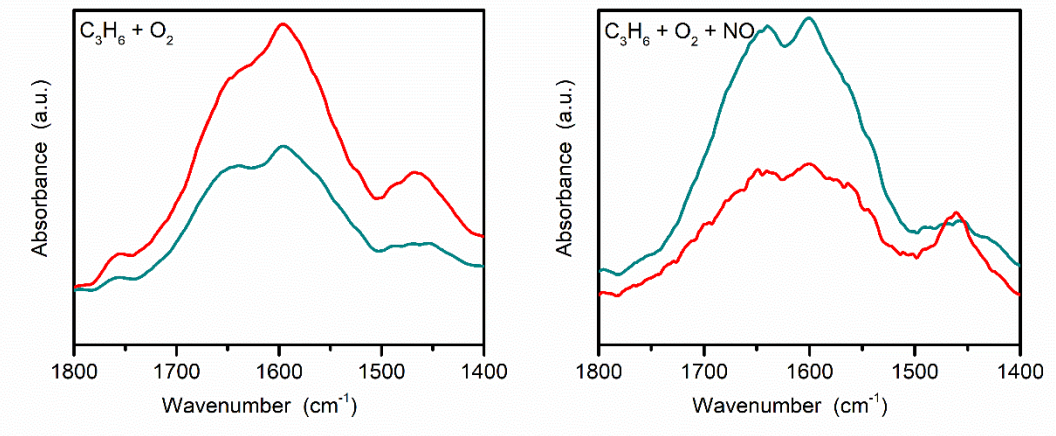

Figure 4. 9. Difference IR spectra of the Composite and the Cu-SSZ-13 catalysts after 30 min exposure to different reaction mixtures. Spectra have been normalized to sample unit specific weight to allow comparison.

4.3.4. Proposed deactivation and poisoning mechanism

The NH_3-mediated NO_x SCR mechanism in Cu-SSZ-13 is still debated and several theories have been proposed. Mechanistic consideration is further complicated by the fact that the SCR reaction appears to involve the interaction of multiple sites (metal-protonic sites), as well as the fact that different mechanisms seem to take place at low temperature (<300 °C) with respect to higher temperatures [44–46]. In the mechanistic considerations, the latest catalytic cycle proposed was slightly modified and expanded to involve the C_3H_6 poisoning and the poisoning prevention by the CeO_2-SnO_2 and it is shown in Figure 4.11. The challenge was to identify which is the critical step in the catalytic cycle that undergoes deactivation, and how deactivation is prevented. From transient and dynamic reactivity tests, the most prominent result was the interaction between NO and C_3H_6, namely the addition of NO in the reaction stream inhibited the NO to NO_2 oxidation as well as the C_3H_6 oxidation over Cu-SSZ-13, while with the addition of CeO_2-SnO_2 the reverse effect was observed, i.e. the presence of NO promoted the C_3H_6 oxidation. Another important consideration is that the H-Composite, obtained by the addition of CeO_2-SnO_2 to the H-SSZ-13 zeolite, had considerably poor performance for NO_x SCR, poisoning resistance, coke and C_3H_6 oxidation. As the performance was also worse in loose contact and dual-zone configuration relative to tight contact used in the Composite catalyst, it could be concluded that the synergy and a reaction intermediate spillover between the CeO_2-SnO_2-Cu^{2+}-zeolite was partially behind the resistance to poisoning.

The presence of C_3H_6 in the reaction stream resulted in the inhibition of NO_2 formation over Cu-SSZ-13, and instantly upon its introduction, no NO_2 could be observed even after removing C_3H_6 from the reaction stream and until the coke was completely oxidized. The consumption and inhibition of the formation of nitrites/nitrates by the HC is well evidenced [1,8–12,21]. As nitrates are key

intermediate in the NH_3 mediated SCR cycle, its depletion would lead to decreased activity, dependent on the kinetic ratio of the nitrate involvement in SCR and HC oxidation reaction. From the catalytic point of view, the Cu^+ / Cu^{2+} redox pair is considered the active site for O_2 capture and activation for the oxidation of NO to nitrate. In the presence of HC, the copper reoxidation through Cu^+-O_2-Cu^+ and Cu^{2+}-OH sites is reduced and the Cu^{2+} /Cu^+ redox cycle is inhibited as the HC consume oxygen and the formation of oxygenates, coke polymer deposits as well as CO and CO_2 is favoured. Indeed, for both ZSM-5 and BEA zeolites (where there are no diffusional limitations as in SSZ-13) it has been shown that the NO_x conversion matches the one of HC-SCR in the presence of NH_3, NO_x and HC, indicating the complete inhibition of the NH_3-SCR cycle [1,3,9,11,23].

The mobility and exchange of ions in zeolites is well evidenced. For example, in the physical mixture of CuO/H-SSZ13 above 250 °C the Cu becomes mobile in the zeolite to occupy the ion-exchanged position [47,48]. The mobility and spillover of nitrites/nitrates between mixtures of oxides and zeolites have also been extensively investigated. Salazar et. al investigated the SCR activity of the physical mixture of different mixed oxides (Ce, Cu and Mn oxides f) and SCR catalysts (V_2O_5-WO_3/TiO_2 and Fe-ZSM5) [15,17] by different contact modes of the two components and found that in tight contact and multilayered configuration, different NO_x conversions could be achieved, from which it was hypothesized that the reactive intermediate was directly transferred between the components and not indirectly through the gas phase. Similar hypothesis was obtained by Ruggeri et al. [34], who used a mixture of Fe-ZSM-5 and Ba/Al_2O_3, whereby Ba acted as trapping site for the intermediate. In both cases, the role of nitrites in the form of HONO was emphasized and considered a key mobile intermediate, although NO_2 was also detected in the product stream. On the other hand, Weiss et al. [35] found both nitrite and nitrate intermediates formed by N_2O_4 dispropotionation ($[NO]^+[NO_3]^-$), however the key role was placed on the nitrates, since the adsorbed nitrites were unstable and could be easily displaced by carbonates. Yu et al. [49] investigated the nitrite/nitrate transfer under NH_3-SCR reaction between Fe-SSZ-13 and $Fe_{0.2}Mn_{0.4}TiZr_{0.03}O_x$ in 7:1 mass ratio where the mobility of nitrates between the components was extensively demonstrated by TPD and DRIFTS measurements.

To experimentally highlight whether the interaction was indirect through the gas phase or direct interaction was involved in the spillover of the nitrates between the CeO_2-SnO_2 and the Cu-SSZ-13, the CeO_2-SnO_2 was saturated only with NO_x and the Cu-SSZ-13 coked by C_3H_6 prior the experiments and different contact modes were investigated. Comparison was made between the dual layer configuration, whereby the coked Cu-SSZ-13 was placed downstream of the NO_x saturated CeO_2-SnO_2, and the tight contact (i.e. the Composite configuration), whereby the saturated CeO_2-SnO_2 and Cu-SSZ-13 were ball milled. The rationale was that if the interaction is indirect, that is through the gas phase, the NO_x and CO_x profiles of the two configurations would be identical since the dual layer

configuration interacts only indirectly. This would involve the desorption of the NO_2 from the CeO_2-SnO_2 (R1) and subsequent reaction from the gas phase with the coke deposited over the Cu-SSZ-13 active site (R2).

CeO_2-SnO_2 -NO_3 → CeO_2-SnO_2 + NO_2 + ½ O_2 R1

Cu-SSZ-13-Coke + NO_2 + ½ O_2 → Cu-SSZ-13 + NO + CO_2 R2

Direct interaction involving the migration of the nitrates (present only on CeO_2-SnO_2) towards Cu-SSZ-13 (R3) would result in fundamentally different NO and CO_x when the dual layer and tight contact configurations are compared.

CeO_2-SnO_2 -NO_3 + Cu-SSZ-13-Coke →

→ Cu-SSZ-13 + CeO_2-SnO_2 + NO + CO_2 R3

Besides R1-3, CO_x could also form from the coke oxidation involving the Cu-SSZ-13 and NO_x reduction that can be represented as overall reactions R4-5.

Cu^{2+}-SSZ-13-Coke → Cu^0-SSZ-13 + CO_x R4

Cu-SSZ-13-Coke + NO + NO_2 → Cu-SSZ-13 + N_2 + CO_x R5

As shown in Figure 4.10, the NO and CO_x profiles differed significantly. In the tight contact (i.e. Composite), a markedly shorter and higher burst of NO was detected at lower temperatures, that resulted from the rapid reaction involving coke oxidation by adsorbed nitrates (per R3). In fact, an increase in CO_x was also detected simultaneously to the NO evolution. The interaction initiated at temperatures as low as 180 °C suggesting that a synergy between the two components was present in the whole temperature range of the investigated HC poisoning. In the dual layer configuration, the interaction was exclusively through the gas phase and more prolonged NO release and CO_x evolution could be observed, involving R1-2. The NO_x in the tight contact was quickly depleted through the reaction R3 as compared to the longer release in the dual layer through R1-2. In neither case NO_2 was detected at the outlet since it is a strong oxidant that easily reacts with coke and reduces to NO or N_2 while producing CO_x.

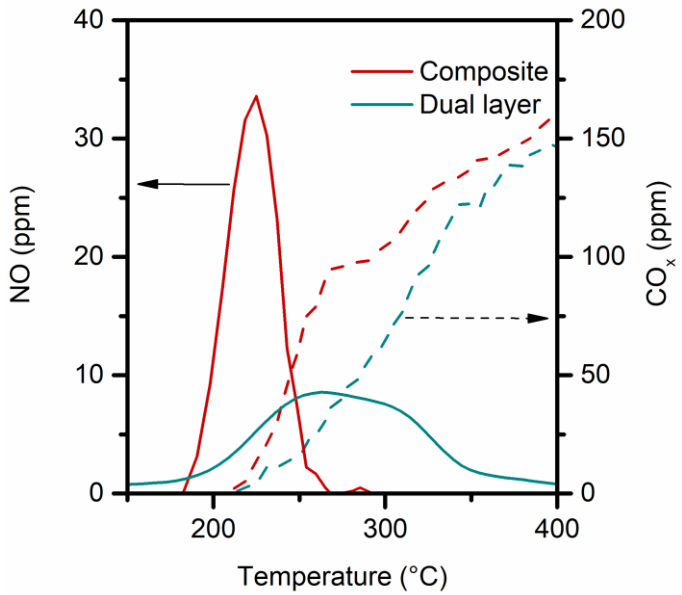

Figure 4.10. TPD profiles of NO (solid lines) and CO_x (dashed lines) of tight contact and dual layer configurations of CeO_2-SnO_2 presaturated with NO_x and Cu-SSZ-13 with C_3H_6.

The role of nitrates was further investigated here by using an alternative mixed oxide MnO_2-CeO_2 that has higher NO to NO_2 oxidation activity than CeO_2 -SnO_2 (Figure S4.5B in Supplementary material). Despite such a higher NO oxidation activity, the deactivation of the Mn-Composite was much more pronounced than over the Composite catalyst, the decreases in NO_x conversion upon the introduction of C_3H_6 being 40 %, 30 % and 9 % over Cu-SSZ-13, Mn-Composite and Composite, respectively. Furthermore, the conversion of C_3H_6 was much lower over the Mn-Composite reaching 65 % at 350 °C versus 90 % over the Composite.

The addition of CeO_2-SnO_2 to the zeolite did not prevent coke formation, or significantly affect its properties or reactivity. Instead, the reactivity studies allude that the role of CeO_2-SnO_2 in the prevention of the poisoning is the re-activation of the Cu active site for the SCR reaction by supplying active intermediates, hypothesized to be in the form of HONO, NO_3^- or OH^- species. The markedly lower deactivation of Cu-SSZ-13 in humid conditions relative to the dry gas mixture further points out the important process of copper redox regeneration, since the Cu^{2+}-OH formation is enhanced in the presence of water.

A complementary hypothesis to the previous one could be constructed with the aim to explain the synergy between the Cu^{2+} and the CeO_2-SnO_2 component and the drastic difference of performance between H-Composite and Composite based on the pathways proposed in the literature for the role of SnO_2 in HC-mediated NO_x SCR. While HC-mediated SCR catalysts based on Ag, Co and Mn oxide rely largely on the high NO to NO_2 oxidation [13,48,49], for SnO_2-based catalysts a different pathway has been demonstrated, whereby Sn activates the HC intermediates and produces more reactive oxygenates (such as acetates and acrolein) considering its low NO oxidation activity [13, 50]. In the case of the Composite catalyst, this would mean that the Cu sites in the zeolite can oxidize more easily the reactive intermediates that, consequently, will not interfere with the SCR reaction. The catalytic cycles and the proposed deactivation prevention mechanisms are summarized in Figure 4.11.

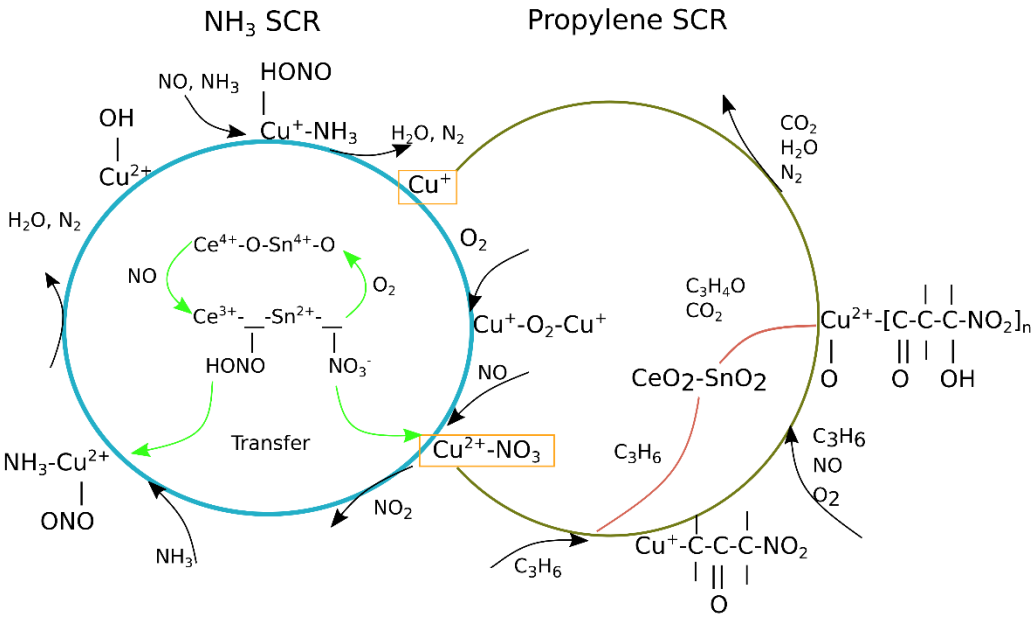

Figure 4.11. Proposed reaction scheme of the propylene poisoning prevention over the Composite catalyst.

4.4. Conclusions

The HC deactivation of the Cu-SSZ-13, the state of the art NH_3-SCR catalyst, was investigated and a potential method for its mitigation proposed. A facile preparation method of a Composite catalyst involved mixing a mixed CeO_2-SnO_2 oxide and Cu-SSZ-13 in tight contact, whereby the optimal mass ratio of the two catalysts was found to be 4: 1. The relative decrease in NO_x conversion was lowered from 40 % over the Cu-SSZ-13 catalyst to 9 % over the Composite catalyst. The composite of Fe-BEA and CeO_2-SnO_2 also demonstrated similar resistance to C_3H_6 poisoning (Figure S4.4), thus extending the concept to different types of SCR catalyst. Dynamic and transient reactivity studies revealed the build-up and interaction between the reaction intermediates and the catalyst components. Over Cu-SSZ-13, the C_3H_6 and NO were competing for the same active sites and, as a result, the C_3H_6 oxidation was delayed and nitrate formation inhibited when both were present in the reaction stream. Over CeO_2-SnO_2 no such C_3H_6-NO_x interaction and coking were observed. On the other hand, the Composite catalyst had a reverse trend, as the addition of NO slightly improved C_3H_6 oxidation. Investigation of the influence of the contact mode, CO and CO_2 selectivity and the low activity of the H-Composite points out the predominant role of Cu species in C_3H_6 oxidation as well as its principal role in the SCR cycle. Interestingly, the addition of the CeO_2-SnO_2 did not inhibit (or even significantly decrease) the formation of coke originating from the polymerization of C_3H_6 partial oxidation products. The role of CeO_2-SnO_2 was suggested to be a combination of oxidation of HC to more reactive intermediates and supply of nitrite/nitrate intermediates to the SCR cycle since their formation was not inhibited by the presence of HC.

From the presented results the main general features that the mixed oxide used as additive to the Cu-SSZ-13 (or other zeolite based SCR catalyst) should posess can be summarized as follows:

Minimizing both HC adsorption and coking, which can be accomplished by avoiding Brønsted acid sites that induce cracking and polymerization in protonic zeolites.

Avoiding the interaction and competition of the NO and C_3H_6 oxidation for the same active sites.

HC oxidation should be selective since the NH_3 oxidation must be avoided. The over-oxidation of NH_3 (as is the case of MnO_2 additives) leads to the decrease of the NO_x conversion and N_2 selectivity due to the lack of reductant and high N_2O generation.

References

[1] L. Ma, W. Su, Z. Li, J. Li, L. Fu, J. Hao, Catal. Today. 245 (2015) 16-21.
[2] W. Tang, D. Youngren, M. SantaMaria, S. Kumar, SAE Int. J. Engines. 6 (2013) 862-872.
[3] Q. Ye, L. Wang, R.T. Yang, Appl. Catal. A Gen. 427 (2012) 24-34.
[4] J. Wang, Y. Ji, G. Jacobs, S. Jones, D.J. Kim, M. Crocker, Appl. Catal. B Environ. 148 (2014) 51-61.
[5] Y.J. Kim, P.S. Kim, C.H. Kim, Appl. Catal. A Gen. 569 (2019) 175–180.
[6] R. Villamaina, I. Nova, E. Tronconi, T. Maunula, M. Keenan, Appl. Catal. A Gen. 580 (2019) 11–16.
[7] N. Serhan, A. Tsolakis, A. Wahbi, F.J. Martos, S. Golunski, Appl. Catal. B Environ. 241 (2019) 471-482.
[8] G. Cavataio, J.R. Warner, J.W. Girard, J. Ura, D. Dobson, C.K. Lambert, SAE Int. J. Fuels Lubr. 2 (2009) 342-368.
[9] I. Heo, S. Sung, M.B. Park, T.S. Chang, Y.J. Kim, B.K. Cho, S.B. Hong, J.W. Choung, I.-S.S. Nam, ACS Catal. 9 (2019) 9800-9812.
[10] R. Raj, M.P. Harold, V. Balakotaiah, , Chem. Eng. J. 254 (2014) 452–462.
[11] J.Y. Luo, A. Yezerets, C. Henry, H. Hess, K. Kamasamudram, H.Y. Chen, W.S. Epling, SAE Tech. Pap. (2012).
[12] T. Nanba, A. Sultana, S. Masukawa, M. Haneda, J. Uchisawa, A. Obuchi, H. Hamada, Top. Catal. 52 (2009) 1766-1770.
[13] M. Misono, Y. Hirao, C. Yokoyama, Catal. Today. 38 (1997) 157-162.
[14] A. Sultana, M. Sasaki, K. Suzuki, H. Hamada, Appl. Catal. A Gen. 466 (2013) 179-184.
[15] M. Salazar, S. Hoffmann, O.P. Tkachenko, R. Becker, W. Grünert, Appl. Catal. B Environ. 182 (2016) 213-219.
[16] D.S. Krivoruchenko, N.S. Telegina, D.A. Bokarev, A.Y. Stakheev, Kinet. Catal. 56 (2015) 741–746.
[17] M. Salazar, R. Becker, W. Grünert, Appl. Catal. B Environ. 165 (2015) 316-327.
[18] A.I. Mytareva, D.A. Bokarev, G.N. Baeva, A.Y. Belyankin, A.Y. Stakheev, Top. Catal. 62 (2019) 192–197.
[19] Q. Zhao, B. Chen, Z. Bai, L. Yu, M. Crocker, C. Shi, Appl. Catal. B Environ. 242 (2019) 161–170.
[20] Y.J. Kim, H.J. Kwon, I. Heo, I.S. Nam, B.K. Cho, J.W. Choung, M.S. Cha, G.K. Yeo, Appl. Catal. B Environ. 126 (2012) 9–21.
[21] Y. Zheng, M.P. Harold, D. Luss, Catal. Today. 264 (2016) 44-54.
[22] N. Soeger, K. Adelmann, M. Seyler, T. R. Pauly, G. Jeske, United States Patent

8926925 (2015).
[23] L. Ma, J. Li, Y. Cheng, C.K. Lambert, L. Fu, Environ. Sci. Technol. 46 (2012) 1747-1754.
[24] A.I. Mytareva, D.A. Bokarev, G.N. Baeva, D.S. Krivoruchenko, A.Y. Belyankin, A.Y. Stakheev, Pet. Chem. 56 (2016) 211–216.
[25] X. Li, Y. Li, S. Deng, T. A. Rong, A Ce-Sn-O_x catalyst for the selective catalytic reduction of NO_x with NH_3, Catal. Commun. 40 (2013) 47-50.
[26] Z. Liu, X. Feng, Z. Zhou, Y. Feng, J. Li, Appl. Surf. Sci. 428 (2018) 526–533.
[27] Z. Liu, K.S. Oh, S.I. Woo, Catal. Letters. 106 (2006) 35-40.
[28] J. Zhang, Y. Liu, Y. Sun, H. Peng, X. Xu, X. Fang, W. Liu, J. Liu, X. Wang, Ind. Eng. Chem. Res. 57 (2018) 10315-10326.
[29] M. Manzoli, B. Bonelli, Catalysts. 8 (2018) 262.
[30] D. Wang, Y. Jangjou, Y. Liu, M.K. Sharma, J. Luo, J. Li, K. Kamasamudram, W.S. Epling, Appl. Catal. B Environ. 165 (2015) 438-445.
[31] R. Daya, S.Y. Joshi, J. Luo, R.K. Dadi, N.W. Currier, A. Yezerets, Appl. Catal. B Environ. 263 (2020) 118368.
[32] K. Wijayanti, K. Xie, A. Kumar, K. Kamasamudram, L. Olsson, Appl. Catal. B Environ. 219 (2017) 142-154.
[33] R. Yu, Z. Zhao, S. Huang, W. Zhang, Appl. Catal. B Environ. 269 (2020) 118825.
[34] M.P. Ruggeri, T. Selleri, M. Colombo, I. Nova, E. Tronconi, J. Catal. 311 (2014) 266-270.
[35] B.M. Weiss, K.B. Caldwell, E. Iglesia, J. Phys. Chem. C. 115 (2011) 6561-6570.
[36] H. Kawai, H. Hinode, React. Kinet. Catal. Lett. 93 (2008) 67−73.
[37] S.J. Castillo Marcano, S. Bensaid, F.A. Deorsola, N. Russo, D. Fino, Fuel. 149 (2015) 78-84.
[38] F. Martinovic, T. Andana, F.A. Deorsola, S. Bensaid, R. Pirone, Catal. Letters. 150 (2020) 573–585.
[39] R. Matarrese, L. Lietti, L. Castoldi, G. Busca, P. Forzatti, Top. Catal., 56 (2013) 477–482 .
[40] A. Kumar, K. Kamasamudram, A. Yezerets, SAE Int. J. Engines. 6 (2013) 680-687.
[41] L. Li, N. Guan, Microporous Mesoporous Mater. 117 (2009) 450-457.
[42] A. Shichi, A. Satsuma, T. Hattori, Appl. Catal. B Environ. 30 (2001) 25-33.
[43] S.A. Beloshapkin, V.A. Matyshak, E.A. Paukshtis, V.A. Sadykov, A.N. Ilyichev, A.A. Ukharskii, V. V. Lunin, React. Kinet. Catal. Lett. 66 (1999) 297–304.
[44] J. Wang, H. Zhao, G. Haller, Y. Li, Appl. Catal. B Environ. 202 (2017) 346-354.
[45] F. Gao, C.H.F. Peden, Catalysts. 8 (2018) 140.
[46] A.R. Fahami, T. Günter, D.E. Doronkin, M. Casapu, D. Zengel, T.H. Vuong, M. Simon, F. Breher, A. V. Kucherov, A. Brückner, J.D. Grunwaldt, React. Chem. Eng. 4 (2019) 1000-1018.
[47] P.N.R. Vennestrøm, L.F. Lundegaard, C. Tyrsted, D.A. Bokarev, A.I. Mytareva, G.N. Baeva, A.Y. Stakheev, T.V.W. Janssens, Top. Catal. 62 (2019) 100–107.
[48] T. Usui, Z. Liu, S. Ibe, J. Zhu, C. Anand, H. Igarashi, N. Onaya, Y. Sasaki, Y. Shiramata, T. Kusamoto, T. Wakihara, ACS Catal. 59 (2018) 6416-6423.
[49] R. Yu, Z. Zhao, C. Shi, W. Zhang, J. Phys. Chem. C. 123 (2019) 2216-2227.
[50] A.E. Palomares, J.G. Prato, F.E. Imbert, A. Corma, Appl. Catal. B Environ. 75 (2007) 88-94 .

Supplementary material to Chapter 4

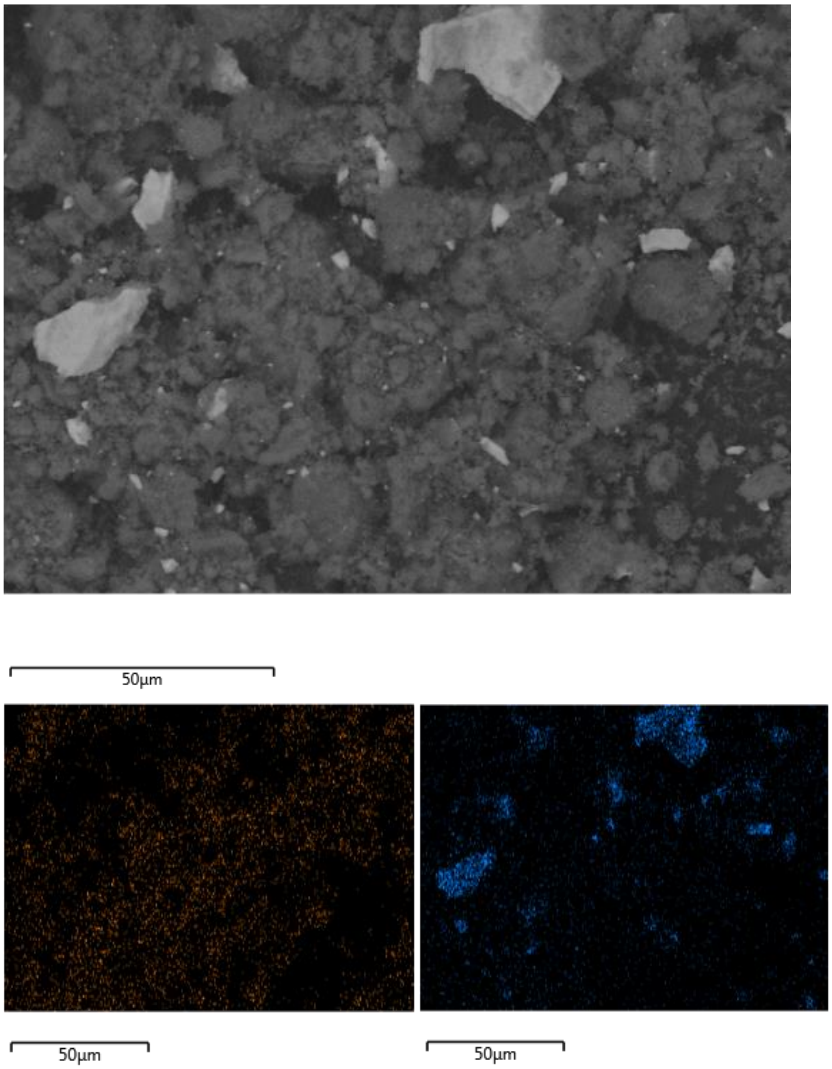

Figure S4.1. Low magnification FE-SEM backscatter image (A) and corresponding elemental EDX maps of Cu (orange) originating from the zeolite and Sn (blue) from CeO_2-SnO_2.

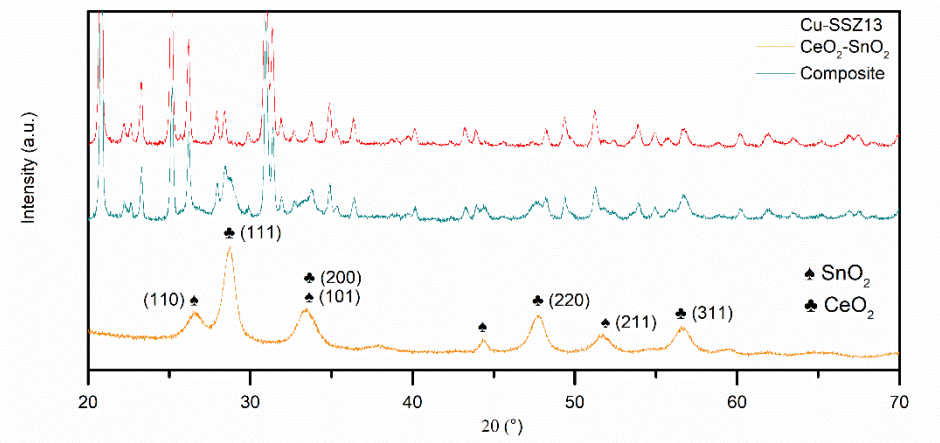

Figure S4.2. XRD of Cu-SSZ13, Composite and CeO_2-SnO_2 catalysts

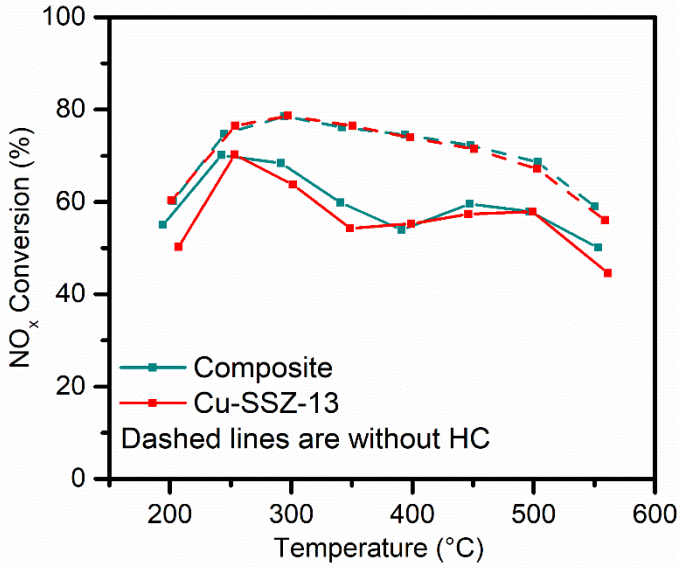

Figure S4.3. SCR activity and HC poisoning resistance of Composite and Cu-SSZ-13 upon severe ageing (800 °C for 80 h). Reaction conditions same as in Figure 4.4.

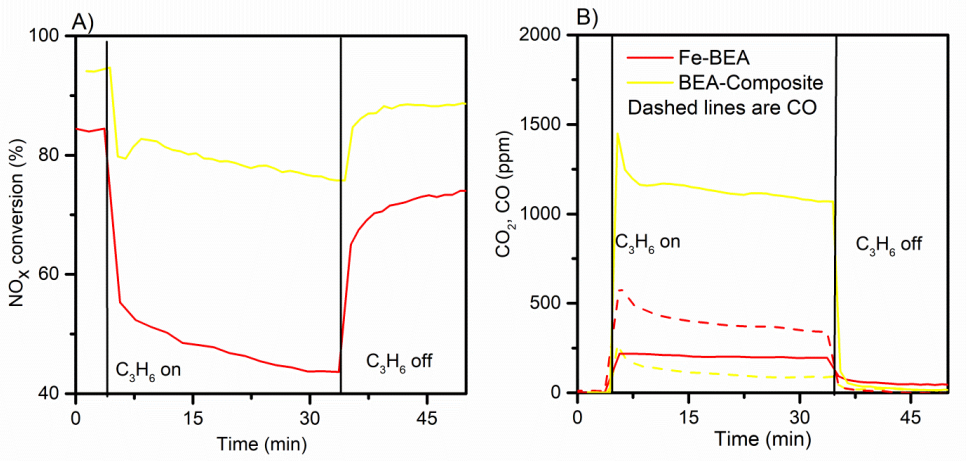

Figure S4.4. Transient propylene deactivation of SCR reaction over Fe-BEA and BEA-Composite. Reaction conditions as in Figure 4.5.

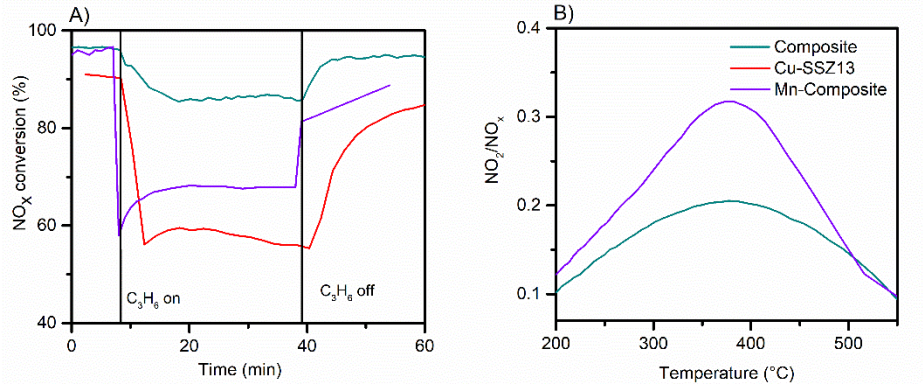

Figure S4.5. Transient propylene deactivation of SCR reaction over Composite, Cu-SSZ13 and Mn-Composite (A) and NO oxidation (B). Reaction conditions as in Figure 4.5.

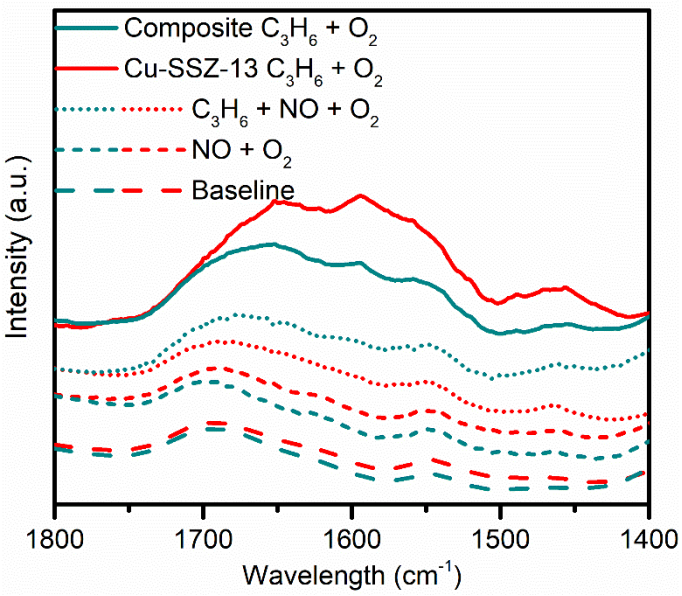

Figure S4.6. FT-IR spectra of the Composite and Cu-SSZ-13 after saturation with different gas compositions.

Table S4.1. Band assignments of the FT-IR spectra [45,46]

Wavenumber (cm^{-1})	Assignment
1716, 1668	νCO of -C=O
1625	νONO of bridged Cu^{2+}-NO_3
1598	νNO of bridged Cu^{2+}-NO_3
1587, 1547	Asymmetric νCO of CH_3-COO
1568	νNO of chelating Cu^{2+}-NO_3

1507	Asymmetric νCO of H-COO
1457	Symmetric νCO of CH_3-COO

Chapter 5

5. Co-doped $LaAlO_3$ perovskite oxide for NO_x-assisted soot oxidation

Chapter summary

In this chapter the La(Al, Co)O_3 perovskite was investigated as catalyst for NO and soot oxidation as low cost substitute for Pt based oxidation catalysts. The catalysts were synthesised via citrate complexation method and the impact of Al doping and the calcination temperature on the peroskite structure investigated by XRD, XPS and programmed thermal methods. Increasing the calcination temperature improved the crystallinity of the perovskite, however above 700 °C drastic loss in the specific surface area was observed. Doping of $LaCoO_3$ with Al enhanced the oxygen mobility and the redox processes of the catalyst that resulted in superior NO oxidation performance. Indeed the $LaCo_{0.75}Al_{0.25}O_3$ could reach NO_2/NO_x ratio of 0.8 at 300°C, comparable to Pt based catalysts. This catalyst was developed not intending to be used directly over the SCRoF brick but as a overall improvement of aftertreatment configuration that includes a SCRoF, considering the need for SCRoF to have NO_2/NO_x ratio as high as possible. In that case the partial subsititution of Pt in the DOC could lead to lower overall costs.

Adapted from the publication in Applied Catalysts A:General (2020) 589: 117304

https://doi.org/10.1016/j.apcata.2019.117304

5.1. Introduction

Perovskite oxides have general formula ABO_3, where the 12-fold cubo-octahedral A site is usually occupied by alkaline earth/alkaline or larger cations and the octahedral B-site by smaller cations [1]. The ideal structure of perovskite is cubic with tolerance factor t (so-called Goldschmidt factor) of 1 (t = $(r_A + r_O)/\sqrt{2(r_B + r_O)}$, where r_A , r_B and r_O are ionic radii of A, B, and oxygen, respectively) [2]. A t parameter between 0.75 and 1 is necessary to form perovskite structures, with decreasing symmetry for t < 1 [1]. Thanks to the wide range of metals able to adapting in the perovskite structures (about 90 % of metallic elements in the periodic table), the physicochemical properties of perovskite oxides can be finely tuned and they find enormous applications in catalysis for, *e. g.*, steam reforming of toluene [3–5], ethanol [6,7], CH_4 [8–10] and bioglycerol [11]; valorization of bio-oil [12–15], biomass [16] and HMF [17], lignin partial oxidation [18] [19] and environmental treatments [20–24].

Particulate matter (PM), which is normally referred as soot (although the latter strictly refers only to its carbonaceous fraction), is a noxious emission of diesel engines, which find enormous applications thanks to their high energy efficiency in fuel consumption [25]. PMs can cause a number of respiratory diseases [26] and deactivation of post-treatment's catalysts for the NO_x (NO and NO_2) reduction processes [27]. Thus, the control of PM's emission is necessary for diesel engine future developments. Generally, there are two steps of PM's treatment: filtration and regeneration [28]. Filtration consists of capturing soot in a Diesel Particulate Filter (DPF), followed by the regeneration which refers to combustion soot at relatively high temperature (around 600 °C [29]) to avoid backpressure across the filter [25]. Alternatively, the Continuously Regenerating Trap (CRT) is able to continuously oxidize soot at lower temperature by using NO_2 as a stronger oxidant instead of O_2 [30,31]. On the other hand, NO_x gases, which are also included in diesel exhaust in extremely small quantity, are highly toxic pollutants. NO_x elimination is a technical problem because of mandatory requirements to add extra elements to aftertreatment systems, leading to an increase in overall cost of vehicles. A conventional diesel aftertreatment system combines both oxidation catalysts to oxidize trace substances (unburnt hydrocarbon, soot, CO, NO) and a consecutive NO_x reduction catalyst. Many efforts have been made to reduce NO_x in lean-rich exhaust cycles such as using lean NO_x trap (LNT) or NO_x storage/reduction (NSR) catalysts. An alternative way is to employ Selective Catalytic Reduction (SCR) by using extra reductants such as NH_3 from injected urea solution or itself as NO_2 [32]. These treatments are only productive in case of a large proportion of NO_2 present in the exhaust gases [25,33,34]. Therefore, finding catalysts for soot combustion at low temperature while maintaining a high proportion of NO_2 for further reduction processes is highly desirable.

NO_x-assisted soot oxidation is a simultaneous approach which involves NO to NO_2 conversion and subsequent soot oxidation by the formed NO_2 from the gas phase, at relatively low temperature [28]. Many works have investigated this reaction using noble metal catalysts, which are able to reduce the ignition temperature of soot oxidation ($T_{10\%}$ - temperature when 10% of soot is combusted) down to 370 °C, depending on the operating conditions [28,35–38]. However, no high NO_2 yields of the soot oxidation reaction have been reported whereas a high proportion of NO_2 is beneficial for further NO_x elimination processes (for instance, NH_3-SCR) . Obviously, the applications of noble metals are limited by their prohibitively expensive cost and strategic limitations of availability. Recently, Kim et al. suggested that perovskite $La_{0.9}Sr_{0.1}CoO_3$ can be reasonably priced alternative since it can oxidize about 86 % of NO at lower temperature (300 °C) than noble metal rival Pt/Al_2O_3[39]. The study has been followed by other works on doped perovskites for low temperature soot oxidation such as $LaMn_{0.9}Co_{0.1}O_3$ [40] , $BaMn_{0.7}Cu_{0.3}O_3$ [41], $La_{0.9}ACoO_3$ (A=Na, K and Rb)[23], $La_{1-x}B_xO_3$ (B=Ce and Sr)[27] and $BaCoO_{3-\lambda}$[42] , focusing on the substitution of A- or B-sites to promote redox properties of perovskite oxides by generating either defective structure or multiple oxidation state cations.

Furthermore, modified $LaCoO_3$ is generally accepted as a highly active catalyst for NO oxidation [20,43,44], whereas Al_2O_3 supported oxides are reportedly able to catalyze NO_x-assisted soot oxidation at relatively low temperature [45]. The combination of Al and Co in La-based perovskite oxides may be a promising approach for the NO_x-assisted soot oxidation at low temperature. The present work investigates Co-doped $LaAlO_3$ perovskite oxides for soot oxidation in the presence of NO_x gases to correlate the catalytic activity with crystallinity, redox properties and the role of lattice oxygen.

5.2. Experimental Section

5.2.1 Catalyst preparation

$LaAl_{1-x}Co_xO_3$ were prepared by the sol–gel method with citric acid. $La(NO_3)_3 \cdot 6H_2O$ (Sigma-Aldrich,99%), $Al(NO_3)_3 \cdot 9H_2O$ (Sigma-Aldrich, 99%), $Co(NO_3)_2 \cdot 6H_2O$ (Sigma-Aldrich,99%) were used as metal precursors and citric acid $C_6H_8O_7 \cdot H_2O$ as a gel-forming agent. Stoichiometric amounts of nitrate salts were dissolved in deionized water. A suitable amount of citric acid (citric acid:metal = 2 mol/mol) was added to the solution where the pH was kept at 7.5 ± 0.5 by dropwise addition of ammonia. The solution was stirred and evaporated at 80 °C until the gel was formed. The gel was then kept at 150 °C for 3 h and at calcination temperature (500, 600 and 700 °C) for 5 h with ramp-up of 5 °C. min^{-1}.

5.2.2 Catalyst Characterization

The BET surface area was determined by N_2 adsorption at -196 °C using a Micrometrics Tristar instrument with improved vacuum system. Samples were previously degassed at 250 °C until stable 10 Pa pressure was reached. XRD diffractograms were recorded using Cu K_α (λ = 0.15418 nm) radiation in a Bruker D8-Advance device.

The reducibility of perovskite oxides was studied by H_2-temperature programmed reduction (H_2-TPR) using ThermoQuest TPDRO 1100 equipment equipped with TCD detector. The quartz tube reactor was loaded with about 50 mg of sample and pretreated with 10 mL min^{-1} N_2 at 500 °C for 30 min and then cooled down to 50 °C. Samples were then heated from room temperature to 950 °C with 5 °C min^{-1} heating rate under 20 mL min^{-1} 5 % H_2/Ar. O_2-Temperature Programmed Desorption (O_2-TPD) was conducted in the same instrument. The samples were previously treated under pure O_2 flow (40 mL min^{-1}) at 600 °C for 30 min before cooling down to ambient temperature under O_2 flow. The desorption was performed from room temperature to 950 °C under He flow (20 mL min^{-1}) with heating rate of 5 °C min^{-1}.

The NO_x-TPD experiments were conducted in a flow-gas reactor system equipped with ABB Limas and Uras UV and NDIR analyzers to detect NO, NO_2, N_2O, CO, and CO_2 gases separately. Catalysts were placed at the middle position of a 10 mm i.d. tubular reactor with thermocouple inserted into the catalytic bed to measure the reaction temperature. In a typical experiment, 200 mg of sample was used. For the NO_x desorption tests, NO_x (250 ppm NO; 250 ppm NO_2, balance N_2; total flow 300 mL min^{-1}) was adsorbed at 250 °C until stable concentration of NO_x and cooled down to room temperature under N_2 flow. The sample was then heated under N_2 flow (300 mL min^{-1}) from room temperature to about 600 °C at 5 °C min^{-1}.

The XPS experiments were done as reported elsewhere [46]. Briefly, XPS analysis was carried out on an XPS PHI 5000 Versa probe apparatus, using the band-pass energy of 187.85 eV, a 45° take off angle and a 100.0 µm diameter X-ray spot size for survey spectra. High-resolution XP spectra were recorded in the following conditions: pass energy of 23.5 eV, resolution of 0.1 eV, and a step of 0.2 eV. Sample charging effects were eliminated by referring to the spectral line shift of the C 1 s binding energy (BE) value at 284.5 eV.

5.2.3 Activity Tests

The NO oxidation tests were conducted in isothermal mode in the same system for NO_x-TPD experiments mentioned above. The feed gas contained 650 ppm NO and 5 % O_2 in N_2 (total flow 254 mL min^{-1}) and 200 mg of catalyst was used. The temperature range for the oxidation was 150-400 °C. At each temperature, the stabilization time was about 20 -30 min for reaching the steady state reaction in order to avoid the adsorption/desorption effect of NO_x on catalysts. NO oxidation was also performed in the temperature ramping mode, in this case the reaction conditions matched those of the NO_x assisted soot oxidation: the feed gas contained 500 ppm NO and 4 % O_2 in N_2 with total flow 600 mL min^{-1} and 200 mg of catalyst with ramping rate 5 °C min^{-1}. Besides the $LaAl_{1-x}Co_xO_3$ catalysts Pt/Al_2O_3 with 5% Pt loading (Sigma-Aldrich 205974) was used as commercial reference.

The activity of the catalysts in NO_x-assisted soot oxidation tests was determined by Temperature Programmed Reaction (TPR) with heating rate of 5 °C min^{-1}. The soot oxidation was studied by mixing 20 mg of soot (Printex U, a carbon black used as model soot) with 180 mg of catalyst or SiC for the reference non-catalytic test (catalyst:soot = 9:1) in loose contact. Feed gas contained 500 ppm of NO and 4 % oxygen in a flow of N_2 as balance gas, the total flow being 600 mL min^{-1}. The tests were conducted between 200 °C and 700 °C with a ramp of 5 °C min^{-1}. The soot conversion and CO_2 selectivity were calculated as followed:

$$\text{Soot conversion (\%)} = \frac{\sum_0^t (co_2 + co)}{(co_2 + co)_{total}} 100$$

$$CO_2 \text{ selectivity } (\%) = \frac{\Sigma_0^t (co_2)}{(co_2 + co)_{total}} 100$$

5.3. Results and discussion

5.3.1 Characterization

5.3.1.1 Structural Properties

X-ray diffraction patterns of all catalysts $LaAl_{1-x}Co_xO_3$ (x = 0, 0.25, 0.5, 0.75 and 1) calcined at 700 °C are shown in Figure 5.1. All catalysts exhibit a well-crystallized perovskite phase, which is the only phase present from x = 0 to 0.5 and is accompanied in $LaAl_{0.25}Co_{0.75}O_3$ and $LaCoO_3$ by two minor peaks at 2θ of about 36.7 and 28.1°, which belong respectively to Co_3O_4 and La_2O_3. The perovskite phase presents symmetric diffraction peaks in the case of $LaAlO_3$, whereas peak splitting is observed with increasing cobalt. Rietveld analysis has been conducted on all catalysts calcined at 700 °C to understand the lowering of symmetry with Co-doping. The refinement was done with the Thompson-Cox-Hastings pseudo-Voigt peak profile and two space groups: rhombohedral R-3c and cubic Pm-3m. The refinement data, reported in Table. 5.1, confirm the change of perovskite symmetry with the composition, $LaAlO_3$ being cubic and all other samples being rhombohedral. Interestingly, all samples would be expected presenting R-3c space group at room temperature [47]. Rhombohedral perovskite normally evolves towards cubic structure when the octahedral tilting is reduced at higher temperature. $LaAlO_3$ is normally rhombohedral at room temperature, reaching space group Pm-3m at nearly 530 °C [47,48]. The presence of cubic phase at room temperature is probably due to a metastability effect. Substituted LaAl perovskites remain rhombohedral also at very high temperature and, in the case of $LaCoO_3$, the rhombohedral structure is also stable above 970 °C [48,49]. In the case of solid solutions intermediate between $LaAlO_3$ and $LaCoO_3$, Aswin *et al.* observed that the rhombohedral phase was accompanied by a secondary monoclinic perovskite phase [50] and no monoclinic phase was observed in our samples.

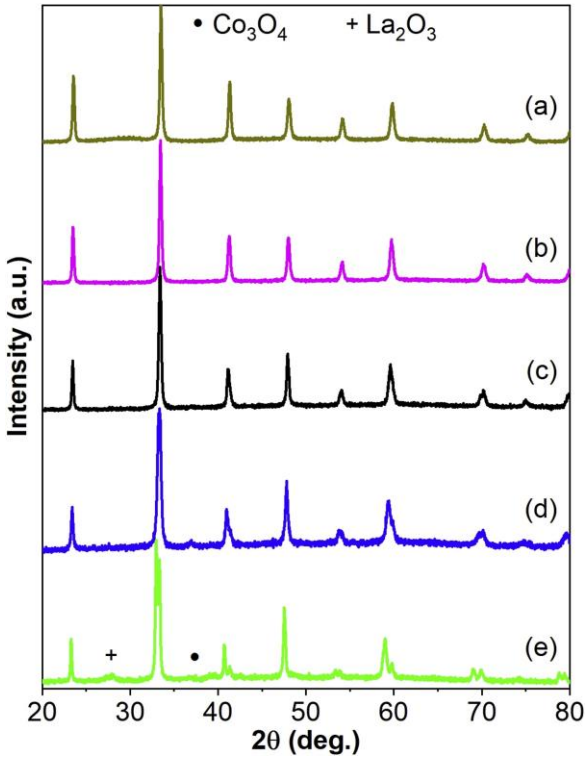

Figure 5.1. X-Ray diffractions of $LaAl_{1-x}Co_xO_3$ calcined at 700 °C: (a) x = 0; (b) x = 0.5; (c) x = 0.5; (d) x = 0.75; (e) x = 1.

The volume of the formula units $LaAl_{1-x}Co_xO_3$ calculated from the cell parameters, taking into account Z = 1 for Pm-3m and Z = 6 for R-3c space groups, are reported in Tab 5.1 and highlighted in Figure 5.2A. They show a systematic increase of volume from $LaAlO_3$ to $LaCoO_3$ once the R-3c symmetry is established, indicating that Co is well incorporated inside the perovskite framework. In fact, trivalent Co is larger than Al^{3+} [51], so the substitution of Al by Co tends to expand the unit cell.

The effect of calcination temperature on the formation of the perovskite phase is highlighted in Figure 5.2B, in which the diffraction patterns of $LaAl_{0.25}Co_{0.75}O_3$ calcined at 500, 600 and 700 °C are shown. The diffraction pattern at 500°C present no perovskite peaks but exhibits broad bands of Co_3O_4 and La_2O_3 phases. Evaluation of the peaks of these phases by the Scherrer method suggests sizes of 27 nm for Co_3O_4 and 2.6 nm for La_2O_3, a signature of nano-crystalline form for this last phase. At 600 °C, the perovskite structure emerges beside traces of La_2O_3 phase, better crystallized than at 500°C. La_2O_3 disappears altogether at a calcination temperature of 700 °C, leaving perovskite as the only crystalline phase.

Table 5.1. Refinement parameters of $LaAl_{1-x}Co_xO_3$ calcined at 700 °C

$LaAl_{1-x}Co_x-O_3$ (x)	Space group	a (Å)	c (Å)	formula unit volume (Å^3)
0	**Pm-3m**	3.7927(1)	-	54.556(2)
0.25	**R-3c**	5.3673(2)	13.117(1)	54.542(3)
0.5	**R-3c**	5.3772(2)	13.101(1)	54.882(1)
0.75	**R-3c**	5.4046(2)	13.108(1)	55.263(3)
1	**R-3c**	5.4427(2)	13.126(1)	56.122(3)

The textural properties of $LaAl_{1-x}Co_xO_3$ calcined at 700 °C are listed in Table 5.2. The average crystallite size of $LaAl_{1-x}Co_xO_3$ is calculated from the Rietveld refinement by the Williamson-Hall method. Crystallite size d_c slightly varies around 30 nm for x=0 to 0.75, before jumping up for the total introduction of cobalt. The surface areas of all samples, measured by N_2 sorption, are between 10 – 15 m^2 g^{-1}, as expected for samples annealed at high temperature [52]. It can be observed that the observed variation in crystallite size does not correspond to any equivalent change in surface area. Indeed, taking into account the density of the perovskite, the observed surface areas correspond to grain size between 60 and 80 nm, in good agreement only with the crystallite size of $LaCoO_3$. It is tempting to advance the hypothesis that, in the case of all other samples, the 30 nm crystallites are the result of splitting of larger grains during the thermal treatment.

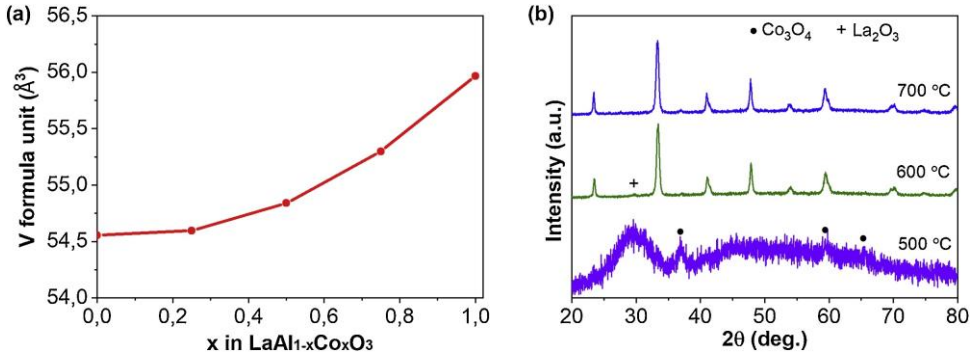

Figure 5.2. (a) Volume of the formula units $LaAl_{1-x}Co_xO_3$ as a function of the cobalt fraction; (b) diffraction patterns of $LaAl_{0.25}Co_{0.75}O_3$ calcined at different temperatures.

Table 5.2. Textural properties of $LaAl_{1-x}Co_xO_3$ calcined at 700 °C.

$LaAl_{1-x}Co_xO_3$(x)	d_c (nm)	S_{BET} (m^2 g^{-1})	V_p (cm^3 g^{-1})
0	30.5	14.4	0.10
0.25	32.1	11.4	0.09
0.50	36.8	11.6	0.09
0.75	28.7	13.1	0.08
1.0	73.7	12.3	0.08

5.3.1.2 Redox properties

Figure 5.3 summarizes the H_2-TPR profiles of $LaAl_{1-x}Co_xO_3$ (x =0, 0.25, 0.5, 0.75, 1) calcined at 700 °C and $LaAl_{0.25}Co_{0.75}O_3$ calcined at 500, 600 and 700 °C. In the literature, the reduction of Co^{3+} in $LaCoO_3$ was generally proposed by two different pathways, implying one or two steps. In the two-steps route, Co^{3+} is converted to Co^0 via Co^{2+} in two distinguished temperature regions at around 420 °C for Co^{3+} to Co^{2+} and 550 °C for Co^{2+} to Co^0 with the formation of intermediate brownmillerite $LaCoO_{2.5}$ [16,53–57]. This two-steps mechanism should be confirmed by the area ratio of the first peak to the second one of 1:2 [58]. However, the H_2 consumption in the high-temperature reduction region is usually found lower than expected [44,55,59], suggesting that Co^0 might be partially formed in the first stage at lower temperature [55,60]. Indeed, the Co^{3+} reduction was also proposed as one-step mechanism, in which Co^0 can be produced directly from Co^{3+} with the formation of oxygen-deficient compound $LaCoO_{3-y}$, bypassing the Co^{2+} species [60], and splitting of the reduction peak can be attributed to different structural Co^{3+} species related to the distortion of perovskite structure and oxygen defects [61].

The TPR profile of the as-prepared $LaCoO_3$ reveals two separate peaks with maxima at ca. 395 and 580 °C (Figure 5.3A). The H_2-consumption, reported in Table 5.3, corresponds to a 1.5 H_2/Co ratio, indicating that all Co^{3+} has been reduced to Co^0. The H_2-consumption ratio between the first and second reduction peaks is 1.04/1, indicating that the first peak does not correspond only to the reduction of Co^{3+} to Co^{2+} but includes some further reduction of Co^{2+}. The mechanism of reduction seems hence to be a mixed one-step and two-steps process. The first reduction peak presents several components: the small shoulder located at 310 °C can be ascribed to microcrystalline part or chemisorbed oxygen in the catalyst surface [20]. The two overlapping components at 391 and 418 °C probably include the formation of Co^0 at relatively low temperature [55,60].

When Al partially replaces Co in $LaCoO_3$, the H_2-TPR profiles of $LaAl_{1-x}Co_xO_3$ follow the one–step reduction mechanism from around 210 °C to 600 °C. The H_2/Co ratio (Table 5.3) is close to the values of total reduction for $LaAl_{0.25}Co_{0.75}O_3$, indicating that Co^{3+} is completely reduced to Co^0 up to around 600 °C. This suggests that, in bimetallic Al-Co perovskites, Co^{3+} can be reduced to metallic species at low temperature without any clear intermediate formation of Co^{2+}, and the asymmetry of peak shape may be due to variously distinct Co^{3+} species in perovskite lattice [61]. $LaAl_{0.5}Co_{0.5}O_3$ and $LaAl_{0.75}Co_{0.25}O_3$, the most Al-rich mixed samples, present a H_2-consumption lower than the value expected for complete reduction of Co^{3+} (Table 5.3). This effect could be attributed to a lower than expected average oxidation state of cobalt, probably related to cation vacancies. In the case of the Co-free $LaAlO_3$, a small peak observed above 800 °C is not related to reduction phenomena but corresponds to CO_2 release from decomposition of carbonate species from the surface of this highly basic solid.

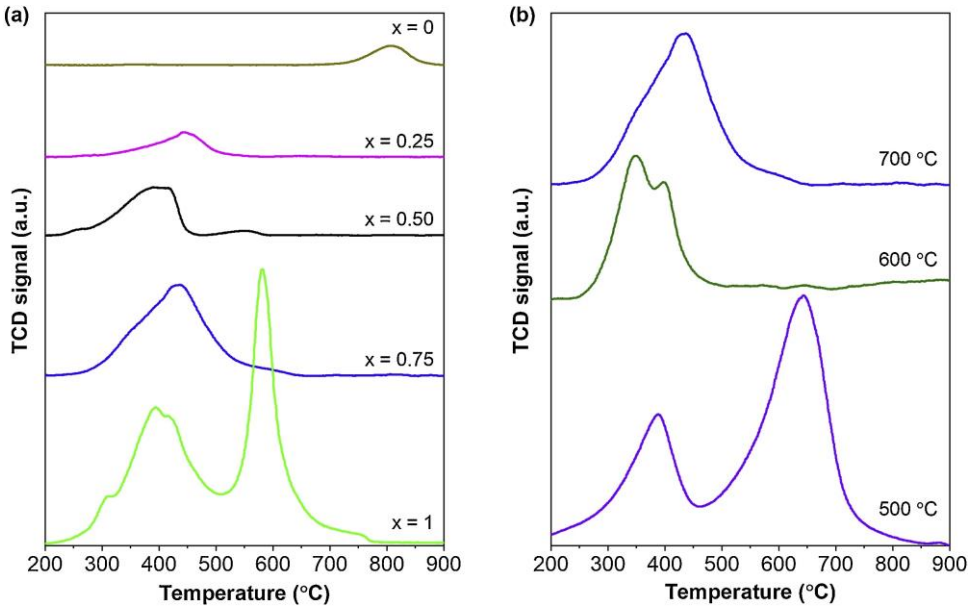

Figure 5.3. H_2-TPR profiles of the samples $LaAl_{1-x}Co_xO_3$ calcined at 700 °C (a); $LaAl_{0.25}Co_{0.75}O_3$ calcined at different temperatures (b).

Figure 5.3B shows H_2-TPR profiles of $LaAl_{0.25}Co_{0.75}O_3$ calcined at 500, 600 and 700 °C. The sample annealed at 500 °C exhibits two peaks at 388 and 646 °C. The first peak closely correspond to the expected temperature for reduction of the Co_3O_4 phase observed in the sample [62]. The second peak does not correspond to a reduction peak but it is at the temperature expected for the decarbonation of the carbonate species at the surface of the extremely dispersed La_2O_3 evidenced by the XRD pattern [63]. $LaAl_{0.25}Co_{0.75}O_3$ calcined at 600 °C reveals two overlapped peaks at 350 and 398 °C. This corresponds to the formation of Co^0 by reduction of perovskite $LaAl_{0.25}Co_{0.75}O_3$ at a temperature nearly 90 °C lower than in the case of the same material calcined at 700 °C. This may be linked with lower surface area, narrower crystal size distribution and higher crystal size with higher calcination temperature, which leads to more diffusional resistance [24].

Table 5.3. H_2-consumption of $LaAl_{1-x}Co_xO_3$ with different composition.

Catalysts	X	Peak temperature (°C)	H_2-consumption (μmol g^{-1})	H_2/Co mol/mol
$LaAlO_3$	0.00	-	-	-
$LaAl_{0.75}Co_{0.25}O_3$	0.25	445	1202	1.07
$LaAl_{0.50}Co_{0.50}O_3$	0.50	394	2909	1.34
$LaAl_{0.25}Co_{0.75}O_3$	0.75	437	4909	1.56
$LaCoO_3$	1.00	395, 580	6379	1.57

It is generally accepted that perovskite $LaCoO_3$ exhibits two type of desorbed oxygen. The α-oxygen, which is desorbed below 750 °C, is usually ascribed to oxygen weakly bound to perovskite surface. β-oxygen is lattice oxygen which diffuses from bulk and it is considered as an indicator of oxygen mobility in the structure [54,59,64,65]. The latter species can come from inner bulk oxygen vacancies or can be directly associated with the B-site cation reduction in the

perovskite oxide framework [56]. $LaCoO_3$ shows two desorption peaks at around 650 °C and 827 °C, probably corresponding to α- and β-oxygen, respectively (Figure 5.4). $LaCoO_3$ releases 77.5 μmol g^{-1} of β-oxygen (nearly 2% of bulk oxygen), as a result of Co^{3+} to Co^{2+} reduction and anion vacancy generation [20,64]. The amount of β-oxygen release from $LaCoO_3$ and the desorption temperature are comparable with the results of other groups [66] [67]. Decreasing the cobalt fraction x from 1 to 0.75 significantly raises the quantity of β-oxygen, $LaAl_{0.25}Co_{0.75}O_3$ releasing 158.1 μmol g^{-1} at a lower desorption temperature of 849 °C. The oxygen species in $LaAl_{0.25}Co_{0.75}O_3$ occupies almost 3.7 % of total oxygen anion in perovskite, revealing the highest oxygen mobility among the studied samples. It should be noticed that Royer et al. suggested that β-oxygen is likely to originate from grain boundaries between two neighbor crystal domains due to higher oxygen diffusivity within boundaries than bulk, and the feature was significantly enhanced by substituting 20 % of Co by Fe to form $LaCo_{0.8}Fe_{0.2}O_3$ [66]. Therefore, the highest amount of lattice oxygen for $LaAl_{0.25}Co_{0.75}O_3$ may be related to the smallest crystallite size among the studied samples. For further decrease of cobalt content, the oxygen evolution dramatically drops to 9.1 μmol g^{-1} when 50 % of Co is replaced by Al and no β-oxygen is measured when only 25 % cobalt is left (Table 5.4). $LaAl_{0.75}Co_{0.25}O_3$ exhibits no oxygen evolution during the experiment, as it is the case for $LaAlO_3$ due to non-reducibility of aluminum cations. The decrease of β-oxygen with the increase of cobalt content closely matches the decrease of H_2-consumption in H_2-TPR and confirms that the cobalt-richest samples present abundant cation vacancies and a lower than expected cobalt oxidation state.

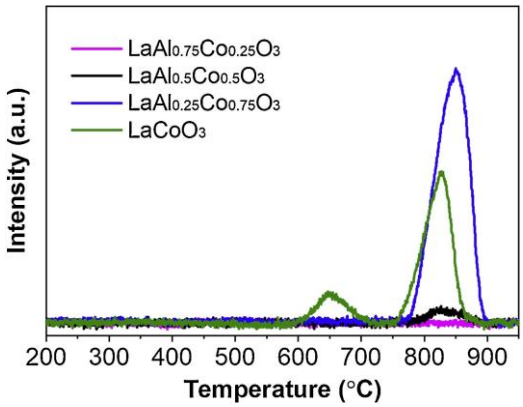

Figure 5.4. O_2-TPD profiles of $LaCo_{1-x}Al_xO_3$ samples calcined at 700 °C.

Table 5.4. Calculated quantity of desorbed oxygen of $LaAl_{1-x}Co_xO_3$ obtained by integration of O_2-TPD profiles.

Samples	β-O_2-desorption (μmol g^{-1})	O-percentage (mol.%)	Temperature (°C)
$LaAl_{0.75}Co_{0.25}O_3$	-	-	-
$LaAl_{0.50}Co_{0.50}O_3$	9.1	0.2	827
$LaAl_{0.25}Co_{0.75}O_3$	158.1	3.7	849
$LaCoO_3$	77.5	1.9	827

5.3.1.3 Surface properties

The Figure 5.5A shows XPS profiles of $LaAl_{1-x}Co_xO_3$ (x =0, 0.25, 0.5 and 0.75) with Co $2p_{3/2}$ and $2p_{1/2}$ binding energy at 780-780.4 eV and 795.4 eV respectively, both ascribed to Co^{3+} species [67,68]. Moreover, distorted $2p_{3/2}$ Co pattern is distinctive for Co^{3+} species [69], with a similar gap between $2p_{1/2}$ - $2p_{3/2}$ of 15.4 eV [70] and no Co^{2+} shake up peaks at 785-788 eV [69] [71], suggesting that mainly Co^{3+} species can be detected at the surface of the prepared samples. However, the satellite signal at 790.2 eV and broadening region at about 805 eV can be seen in $LaAl_{0.5}Co_{0.5}O_3$, and more pronounced in the sample with more cobalt: $LaAl_{0.25}Co_{0.75}O_3$. This profile is reported for Co_3O_4 [72], indicating that there may be some cobalt oxides not incorporated in perovskite structure when more than 50 % of Al is replaced by Co, which is in agreement with XRD profiles. Table 5.5 listed the ratios of surface Co/Al which increase from 0.4 for $LaAl_{0.75}Co_{0.25}O_3$ to 3.2 for $LaAl_{0.25}Co_{0.75}O_3$. This ratio for $LaAl_{0.75}Co_{0.25}O_3$ is higher than its bulk composition (0.33) by around 20 % and the surface is slightly enriched with Co. By contrast, $LaAl_{0.5}Co_{0.5}O_3$ has surface Co lower than in the bulk composition: 0.6 in comparison with theoretical 1.0.

The O 1s XPS spectra are deconvoluted to two oxygen species: peaks at 529.1-529.3 eV are characteristic of surface lattice oxygen (denoted as O_{lat}) and signals at 531.1-531.3 eV can be ascribed to oxygen adsorbed on perovskite surface (denoted as O_{ads})[73,74] (Figure 5.5B). The ratios O_{ads}/O_{lat} of $LaAl_{1-x}Co_xO_3$ with x = 0, 0.25, 0.5 and 0.75 are 0.77, 0.80, 0.65 and 0.75, respectively (Table 5.5). These four samples, with similar surface area, show O_{ads}/O_{lat} ratios in the same range, whereas the $LaCoO_3$ sample, with much lower surface area, shows a much higher O_{ads}/O_{lat} surface ratio. These data clearly indicate that the oxygen distribution at the surface in non-reactive conditions poorly reflects the bulk mobility of oxygen as revealed by H_2-TPR or O_2-desorption experiments. The quantity of O_{ads} is relatively correlated to surface area values which are similar for $LaAlO_3$,

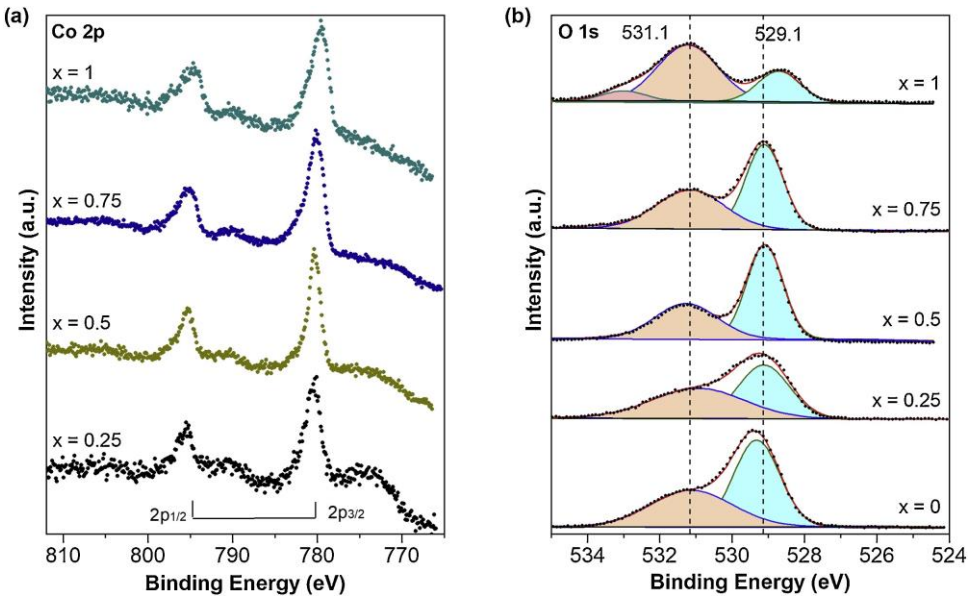

Figure 5.5. XPS spectra of Co 2p (a) and O 1s (b) of $LaAl_{1-x}Co_xO_3$ (x = 0, 0.25, 0.5, 0.75, 1).

Table 5.5. Relative abundances of oxygen species derived from the deconvolution of O 1s XPS spectra and Co/Al surface ratio.

Sample	$(Co/Al)_{surf.}$	Co $2p_{3/2}$	O_{ads}		O_{lat}		O_{ads}/O_{lat}
		BE (eV)	BE (eV)	%-atom	BE (eV)	%-atom	
$LaAlO_3$	0	-	531.1	43.5	529.3	56.5	0.77
$LaAl_{0.75}Co_{0.25}O_3$	0.4	780.4	531.2	44.4	529.2	55.6	0.80
$LaAl_{0.5}Co_{0.5}O_3$	0.6	780.4	531.3	39.4	529.1	60.6	0.65
$LaAl_{0.25}Co_{0.75}O_3$	3.2	780.0	531.1	42.9	529.1	57.1	0.75
$LaCoO_3$	-	779.5	531.2	66.2	528.7	25.4	2.60

5.3.1.4 NO_x-Temperature Programmed Desorption

For the NO_x-TPD measurement, the samples were adsorbed by equal quantities of NO and NO_2 (about 250 ppm of each balanced by N_2) at 250 °C until the saturation, cooled down under N_2, and followed by heating up under N_2 atmosphere with a rate of 5 °C min^{-1}. Figure 5.6A reveals the NO_x-TPD profiles of $LaAl_{1-x}Co_xO_3$ (x up to 0.75), while a similar figure for $LaCoO_3$ is plotted in Figure 5.6C. The first small NO_x desorption can be ascribed to physically adsorbed species which peaks at about 150 °C for $LaAlO_3$, and decreases by around 60 °C when Al is substituted by Co. It is reported that the NO_x desorption below 250 °C is mostly related to B-site of perovskite, while at high temperature the basic A-site may take a role [44]. The adsorbed species is reportedly in dependence with adsorption temperature [75]. When NO_x is adsorbed below 250 °C, it is mainly stored as nitrite species, which can convert into nitrate at higher

adsorption temperature [75]. In contrast, at high temperatures NO_x can be released by the nitrate decomposition followed by the oxides formation and the destruction of perovskite structure. [42]. It is also suggested that at low adsorption temperature NO_x is stored as chemisorbed NO_x and converted to nitrate by interaction with surface hydroxyl groups [76]. This chemisorbed species may be unstable, and it can be released during TPD experiment up to 350 °C. Generally, NO_2 is desorbed at a lower temperature in all studied samples compared to NO [77], and its desorption temperature drops with increased Co doping, from 351 °C for $LaAlO_3$ to 275 °C for $LaAl_{0.25}Co_{0.75}O_3$, and almost disappears in case of $LaCoO_3$ (Table 5.6). The quantity of desorbed gases is similar in all cases except $LaCoO_3$, varying from around 53 to 75 μmol g^{-1}. The values partially depend on the surface area which may be not promoted by high calcination temperature of perovskite oxides. Furthermore, deficient perovskites favor NO adsorption on oxygen vacancies before oxidizing to NO_2 [43,78] which may not be found in our compounds persevering charge neutrality. NO desorption temperature has the same trend of NO_2 but at a higher temperature. It decreases with Co content from 412 °C for $LaAlO_3$ to a similar range of 347-350 °C for both $LaAl_{0.75}Co_{0.25}O_3$ and $LaAl_{0.5}Co_{0.5}O_3$, and drops to the minimum of 320 °C for $LaAl_{0.25}Co_{0.75}O_3$. Surprisingly, a decrease in Al quantity weakens the bond with acidic NO_x, leading to lower desorption temperature. The introduction of Co may induce some modifications of the perovskite surface which leads to variation in desorption temperature of NO_x [44]. It is reported that calcination temperature up to 1000 °C induces the formation of oxygen-deficient $BaCoO_{3-\lambda}$ which promotes the trap of NO_x on oxygen vacancies; however, when the synthesis temperature is lower than 700 °C, surface areas may significantly contribute to the quantity of absorbed species [42]. For the sample $LaAl_{0.25}Co_{0.75}O_3$ calcined at different temperatures (Figure 5.6B), the one annealed at 500 °C releases the most NO_x with a value of 258 μmol g^{-1} in comparison with 45 and 61 μmol g^{-1} of $LaAl_{0.25}Co_{0.75}O_3$ calcined at 600 and 700 °C respectively. On the other hand, the specific surface areas of the sample decrease from ~ 22 to ~ 16 m^2 g^{-1} with calcination temperature from 500 to 600 °C, and drops to 13.1 m^2 g^{-1} at 700 °C. Furthermore, it can be seen that calcination temperature from 700 to 600 °C shifts the desorption peak of NO_x by around 96 °C, whereas sample calcined at 500 °C possesses the highest desorption temperature at 420 °C. The presence of La_2O_3 in the samples calcined at low temperatures may be attributed to a stronger bond with NO_x and higher adsorbed quantity since La_2O_3 is supposed as the main NO_x storage site [43].

In many works for NO_x storage and reduction, NO is fed with O_2 to be oxidized to NO_2 which is more readily trapped by basic catalysts [77]. In the present study, NO and NO_2 are supplied in an approximately equal amount at 250 °C without the presence of O_2. However, NO_2 almost disappears while NO is higher than its original value (250 ppm) during the adsorption process over $LaCoO_3$ (Figure 5.6D). This behavior cannot be found in other samples (for example $LaAl_{0.25}Co_{0.75}O_3$ in Figure 5.6B) where both NO and NO_2 gets saturated after around 10 minutes. This suggests that during the NO_x adsorption at 250 °C,

NO_2 may be adsorbed and partially reduced to NO. This is confirmed by the presence of more intense peaks of Co_3O_4 and La_2O_3 phases in XRD pattern of $LaCoO_3$ after TPD treatment, which may be a result of Co^{3+} to Co^{4+} oxidation by NO_2 reduction. Moreover, the NO_x-TPD of $LaCoO_3$ shows no NO_2 peaks whereas NO is desorbed at significantly higher than those of other samples (Figure 5.6C). The difference between NO adsorption (calculated by integration of NO adsorption curve with time) and desorption is 88.2 μmol g^{-1} , indicating the additional amount of NO from NO_2 reduction. It should be mentioned that NO_2 can be adsorbed by basic La_2O_3 observed in XRD pattern for $LaCoO_3$ to form nitrate salt, which can be decomposed at higher temperature than that in the experiment [79]. It may be suggested that NO_2 may be adsorbed on $LaCoO_3$ and completely reduced to other species together with both Co^{4+} formation and partially perovskite structure collapse.

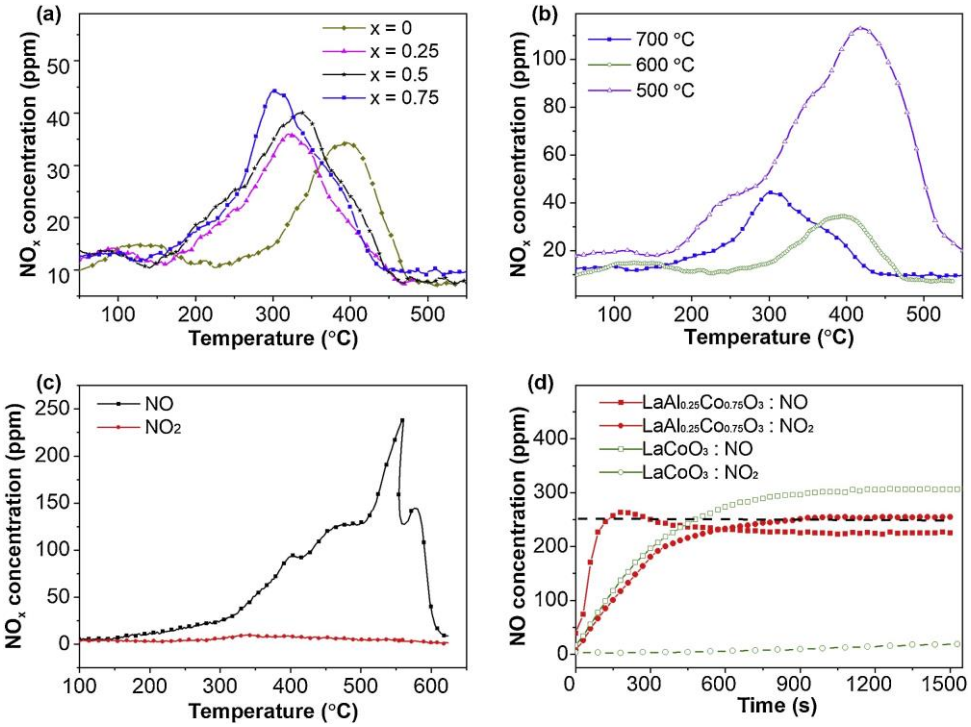

Figure 5.6. NO_x desorption curves of (a) $LaCo_{1-x}Al_xO_3$ calcined at 700 °C and (b) $LaAl_{0.25}Co_{0.75}O_3$ calcined at different temperatures; (c) NOx desorption of $LaCoO_3$ at 250 °C with time (250 ppm of NO_x and 250 ppm of NO_2 balance in N_2; 250 °C); (d) NO_x adsorption on $LaCoO_3$ and $LaAl_{0.25}Co_{0.75}O_3$ at 250 °C.

Table 5.6. Desorbed NO_x quantity and relative desorption temperature of $LaAl_{1-x}Co_xO_3$.

Catalysts	NO_2		NO		Total (μmol g^{-1})
	Amount (μmol g^{-1})	T_{max} (°C)	Amount (μmol g^{-1})	T_{max} (°C)	
$LaAlO_3$	26.8	351	26.2	412	53.0
$LaAl_{0.75}Co_{0.25}O_3$	27.8	294	25.8	347	52.9
$LaAl_{0.5}Co_{0.5}O_3$	36.5	289	38.7	350	75.2
$LaAl_{0.25}Co_{0.75}O_3$	24.7	275	36.3	320	61.0
$LaCoO_3$	-	-	410.2	558	411.7

5.3.2. Catalytic activities

5.3.2.1 NO oxidation

The NO oxidation tests aim at investigating the NO_2 production at low temperatures, which is beneficial for the NO_x storage/reduction process and soot combustion [77]. Figure 5.7A shows NO to NO_2 conversion profiles obtained from the isothermal mode, whereas the dashed line represents the thermodynamic equilibrium of NO oxidation reaction as a reference. The peaks of the curves indicate the temperatures where maximum NO_2 generation is achieved. At temperatures below the peak temperature the NO oxidation is kinetically limited, while at higher temperatures the thermodynamic equilibrium is the limiting factor. Among the as-prepared samples, $LaAl_{0.25}Co_{0.75}O_3$ perovskite presents the best performance (Table 5.7), with a maximum NO conversion of about 78 % at 320 °C. In contrast, $LaAlO_3$ exhibits the worst activity with 38 % at a remarkably high temperature of about 399 °C and the NO conversion increases with Co, from 38 % for $LaAlO_3$ to 56 and 60% for $LaAl_{0.75}Co_{0.25}O_3$ and $LaAl_{0.5}Co_{0.5}O_3$ catalysts, respectively. The conversion reaches the maximum value for $LaAl_{0.25}Co_{0.75}O_3$ before reverting to 68 % when Al is totally substituted by Co as reported for $LaCoO_3$ [20]. The same catalysts were also tested in the temperature ramping mode and under lower residence time (Figure 5.7C) in order to obtain the same test conditions as the soot oxidation tests and to get a closer correlation between the two kind of experiments. As can be appreciated, the order of the catalytic performance ($LaAl_{0.25}Co_{0.75}O_3$ > $LaCoO_3$ > $LaAl_{0.5}Co_{0.5}O_3$ > $LaAl_{0.75}Co_{0.25}O_3$ > $LaAlO_3$) remained unvaried from steady state to dynamic conditions.

Furthermore, by comparing the $LaAl_{0.25}Co_{0.75}O_3$ sample with a Pt/Al_2O_3 commercial oxidation catalyst, the NO oxidation rate of the perovskite is obviously lower although the equilibrium is reached by both catalysts at almost the same temperature, which is the one of interest for the soot oxidation, offering a viable alternative for the PGM-based catalysts under certain conditions.

It should be noticed that NO-to-NO_2 oxidation ability is due to the generation of oxygen defects and redox property [80], which can be created by adjusting cation doping at A or B sites in the perovskite compounds. Others suggest that higher oxidation capacity is associated with higher oxygen mobility and exchange between lattice oxygen and gas phase oxygen [20]. This may be related to $LaAl_{0.25}Co_{0.75}O_3$ with the higher amount of β-oxygen desorption (Table 5.4), implying the pivotal role of lattice oxygen species in the improvement of the oxidation reaction. Furthermore, all samples have negligible α-oxygen quantity released during O_2-TPD experiment, but still possess comparable NO oxidation activity. This result indicates that surface oxygen may not play a critical role in NO oxidation but the diffusion of lattice oxygen to the surface is more important [81].

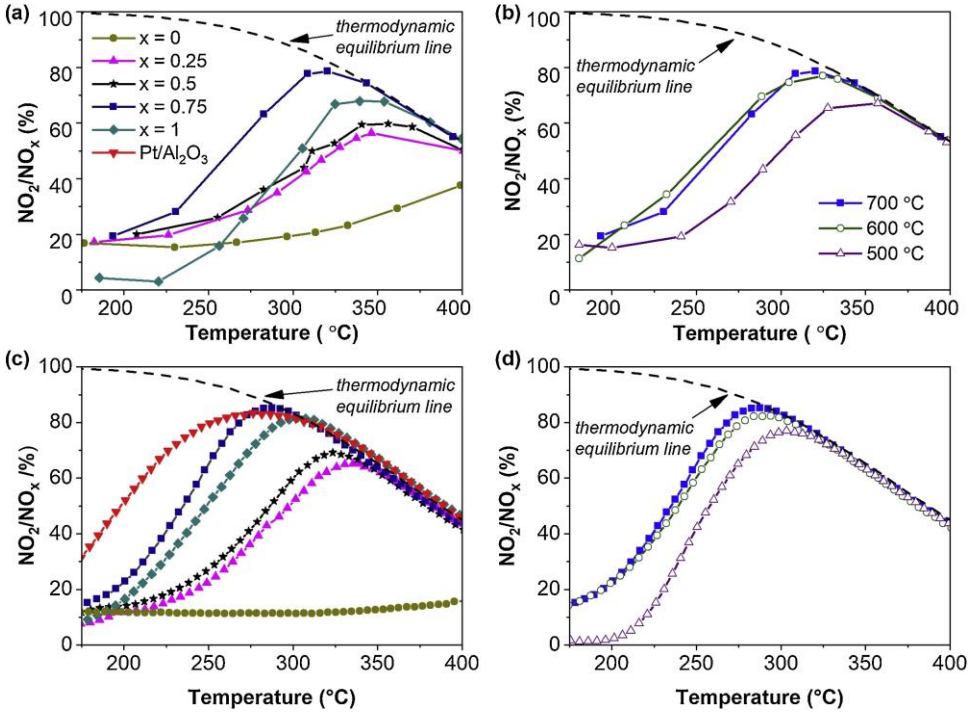

Figure 5.7. NO_2 percentage of (a) $LaAl_{1-x}Co_xO_3$ calcined at 700 °C and (b) $LaAl_{0.25}Co_{0.75}O_3$ calcined at different temperatures in steady state conditions and (c) $LaAl_{1-x}Co_xO_3$ calcined at 700 °C and (d) $LaAl_{0.25}Co_{0.75}O_3$ calcined at different temperatures in dynamic conditions.

Table 5.7. NO_x performances of $LaCo_{1-x}Al_xO_3$ calcined at 700 °C.

Catalysts	**$LaAl_{1-x}Co_xO_3$ (x)**	**NO_2/NO_x (%)**	**Peak NO_2/NO_x temperature (°C)**
$LaAlO_3$	0	38	399
$LaAl_{0.75}Co_{0.25}O_3$	0.25	56	346
$LaAl_{0.5}Co_{0.5}O_3$	0.5	60	356
$LaAl_{0.25}Co_{0.75}O_3$	0.75	78	320
$LaCoO_3$	1	68	339

However, $LaCoO_3$ desorbs significantly more oxygen than its rivals ($LaAl_{0.75}Co_{0.25}O_3$ and $LaAl_{0.5}Co_{0.5}O_3$) but its oxidation activity worsens despite more Co content. The higher NO_x desorption temperature for $LaCoO_3$ indicates strong interactions between NO_x and the catalyst, while partial doping Al slightly weakens the bonds facilitating the NO_x release at low temperatures. Thus, oxygen mobility may be not the only factor for NO oxidation but the synergetic interaction between two B-site cations (Al and Co) may enhance oxidation performance of the catalysts, as suggested by Ma et al. with a small substitution of Co by Fe to promote NO conversion [82]. Furthermore, under H_2/Ar flow in the H_2-TPR experiment, $LaAl_{0.25}Co_{0.75}O_3$ is reduced at a temperature of 437 °C, higher than 394 °C for $LaAl_{0.75}Co_{0.25}O_3$. However, the NO conversions of these samples reveal different trend for the reduction temperature, which may imply the negligible effects of reducibility on NO oxidation. Furthermore, $LaCoO_3$ produces less NO_2 at low temperatures but higher above 275 °C than $LaAl_{0.75}Co_{0.25}O_3$ and

$LaAl_{0.5}Co_{0.5}O_3$ (Figure 5.7A). This may be related to the fact that $LaCoO_3$ can adsorb NO_2 at low temperatures and partially reduce to NO, as can be seen in the NO_x-TPD experiment. Besides, the temperature of maximum NO_2 production is lowest for $LaAl_{0.25}Co_{0.75}O_3$ at 320 °C, and increases by around 30 °C with x = 0.25 and 0.5 (Table 5.7). A similar trend can be found for NO desorption profiles (Table 5.6), where NO desorbs at 320 °C for $LaAl_{0.25}Co_{0.75}O_3$ and increase to 350 and 347 °C for $LaAl_{0.5}Co_{0.5}O_3$ and $LaAl_{0.75}Co_{0.25}O_3$ respectively. This highlights the suggestion in which the oxidation reaction commences with the chemisorption of reactants NO and O_2, followed by the dissociation of O_2 and NO_2 on the surface [28].

Many works have found that substitutions of A-site generate oxygen vacancies, for example $La_{1-x}Sr_xBO_3$ [20,43], or of B-site to support the co-existence of multivalent states, e.g. $LaCo_{1-x}Mg_xO_3$ [67], in order to promote NO oxidation. Furthermore, it was shown that the partial substitution of cations can promote the formation of preferential oxidation active states (e.g. metallic isolated or biactive sites) that can promote the NO oxidation [83,84]. However, there are fewer investigations regarding the effect of the degree of perovskite crystallinity on the NO oxidation. Figure 5.7B shows profiles of NO_2 molar percentage in the NO_x mixture of $LaAl_{0.25}Co_{0.75}O_3$ which is calcined at 500, 600 and 700 °C. It is clear that the sample annealed at 500 °C reveals the lowest oxidation activity, with about 66 % at ~ 350 °C despite the highest surface area (21.9 $m^2\ g^{-1}$), probably due to the presence of segregated phases such as Co_3O_4 and La_2O_3 [20]. The samples calcined at 600 °C show superior oxidation performances at low temperatures, but at above 300 °C the solid calcined at 700 °C slightly outperforms. Despite the reduction in surface area, the calcination temperature up to 700 °C has positive effects on oxidation activity, which may be associated with higher crystallinity and less minor phases as detected in XRD profiles (Figure 5.2B). However, further increase calcination temperature beyond 700 °C may lead to deterioration of oxidation activity due to low surface area as studied elsewhere [20].

5.3.2.2 Soot Oxidation

Figure 5.8 reveals the results of soot oxidation tests over $LaAl_{0.25}Co_{0.75}O_3$ (calcined at 700 °C) in the presence and absence of NO_x gas. Table 5.8 shows the testing outputs: $T_{10\%}$ represents the ignition temperature, when 10 % of soot is burnt; $T_{50\%}$ and $T_{90\%}$ are the temperatures when 50 % and 90 % of soot is consumed respectively; T_{max} is the temperature when maximum CO_2 production is achieved, and $(NO_2/NO)_{max}/T$ is the maximum percentage of NO_2 over NO_x mixture and its temperature. Generally, the NO_x-assisted soot oxidation reaction starts with the oxidation of adsorbed NO to produce NO_2, which is a stronger oxidant than O_2 [38,45,85]. Soot can be also oxidized by O_2 but at a relatively higher temperature than with NO_2. In the presence of NO_2, it interacts with soot surface to form surface oxygen complexes (SOC), which decomposes further to

CO, CO_2 and NO [28,86]. O_2 is first adsorbed at the catalyst's surface and undergoes the dissociation to form active oxygen species. This species is possibly transferred to the surface of soot forming SOC via spill-over mechanism [86]. The results clearly show that soot is oxidized at a significantly lower temperature in the presence of NO_x ($T_{10\%}$ are 377 and 513 °C for with and without NO_x respectively). Moreover, NO_x also remarkably supports to reduce the temperature of 50 % of soot conversion by around 111 °C although at higher temperatures the role of NO_x in soot oxidation becomes less prominent with the decrease of $T_{90\%}$ by only 27 °C because of limited NO_x availability (Table 5.8). In terms of CO_2 production, NO_x promotes the total oxidation with CO_2 selectivity of 99.8 % compared to 98.5 % of that without NO_x. Without the presence of NO_x, the T_{max} increases by around 120 °C and the formation of CO is significant. The results highlight the vital role of NO_2 in soot oxidation and its further applications in NO_x reduction process by the selective catalytic reduction reaction.

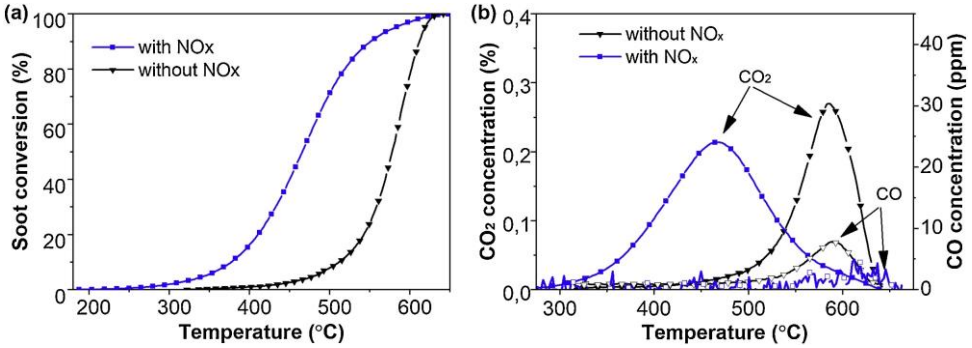

Figure 5.8. (a) Soot conversion and (b) CO_2 and CO concentration as functions of temperature during soot oxidation catalytic tests with and without NO_x supply over $LaAl_{0.25}Co_{0.75}O_3$ catalyst.

Figure 5.9 summarizes soot conversion, NO_2/NO_x percentage, CO and CO_2 concentrations as functions of temperature during the experiments with NO_x-assisted soot oxidation over $LaAl_{1-x}Co_xO_3$ catalysts. Among the prepared solids, $LaAlO_3$ possesses certainly the lowest activity with $T_{10\%}$, $T_{50\%}$ and $T_{90\%}$ of 470, 562 and 623 °C respectively. Doping Co shifts the reaction temperature to lower ranges, $LaAl_{0.75}Co_{0.25}O_3$ obviously outperforms $LaAlO_3$ by reducing these temperature values by about 60-80 °C. The improvement in the oxidation activity is likely to be related to not only the better performance in the NO_x oxidation but also the NO_x adsorption [35], as the Co doping reduces the NO_x desorption temperature thereby facilitating the oxidation reactions at a lower temperature range (Figure 5.6). As expected, both samples $LaAl_{0.75}Co_{0.25}O_3$ and $LaAl_{0.5}Co_{0.5}O_3$ (violet and black curves) exhibit similar soot oxidation activity, which is in line with the NO_x-TPD experiments. This suggests that the NO_x-assisted soot oxidation is mainly governed by the adsorption of NO_x on the catalyst's surface and directed to the soot-catalyst interface before initiation of the oxidation [35]. $LaAl_{0.25}Co_{0.75}O_3$ is the most active catalyst with $T_{10\%}$ of 377 °C, which is 12 °C lower than that of $LaCoO_3$. The complete substitution of Al by Co deteriorates the soot oxidation performance at low temperatures while there is no

difference at middle temperature with $T_{50\%}$ of 467 °C for both $LaAl_{0.25}Co_{0.75}O_3$ and $LaCoO_3$. The difference between these two catalysts is signified in terms of NO_2 production which plays an essential role in abatement reduction. $LaAl_{0.25}Co_{0.75}O_3$ maintains high formation of NO_2 with NO_2/NO_x of 0.71 at 321 °C compared to 0.42 at 352 °C for $LaCoO_3$. The low ignition temperature allows to uninterruptedly oxidize soot while keeping high NO_2 production. In comparison with soot-free NO oxidation, NO_2 production obtained from NO_x-soot oxidation for all catalysts is lower, confirming the participation of NO_2 as a strong oxidant in the reaction leading to its consumption. $LaAlO_3$ shows no formation of NO_2 at all, explaining that the soot oxidation is practically the same as non-catalytic [86]. The outstanding performance of $LaAl_{0.25}Co_{0.75}O_3$ is likely to be associated with the prominent lattice oxygen mobility which may be facilitated by co-incorporation of Co-Al elements in perovskite structure [86,87].

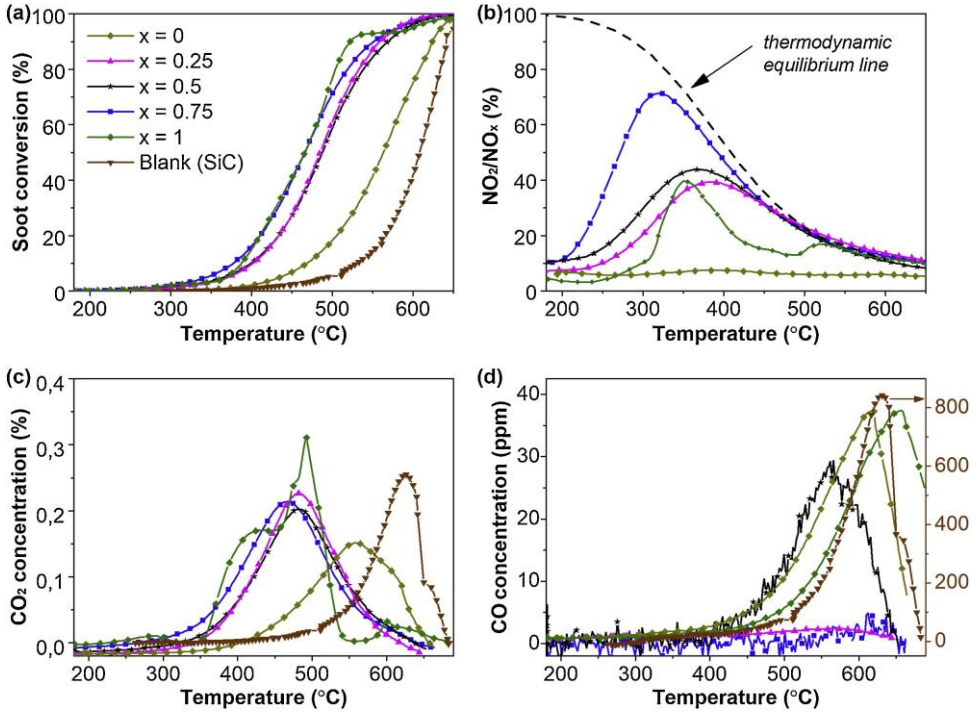

Figure 5.9. (a) Soot oxidation, (b) NO_2 percentage, (c) CO_2 and (d) CO concentrations of $LaAl_{1-x}Co_xO_3$ calcined at 700 °C.

Table 5.8. Catalytic performances of $LaCo_{1-x}Al_xO_3$ calcined at 700 °C.

$LaAl_{1-x}Co_xO_3$	X	$T_{10\%}$ (°C)	$T_{50\%}$ (°C)	T_{max} (°C)	$T_{90\%}$ (°C)	$(NO_2/NO_x)_{max}$ / T(°C)	CO_2 selectivity (%)
$LaAlO_3$	0	470	562	563	623	0.08 / 376	82.3
$LaAl_{0.75}Co_{0.25}O_3$	0.25	402	484	481	560	0.39 / 383	98.7
$LaAl_{0.5}Co_{0.5}O_3$	0.5	401	487	482	570	0.44 / 379	98.1
$LaAl_{0.25}Co_{0.75}O_3$	0.75	377	467	467	585	0.71 / 321	99.8
$LaCoO_3$	1	389	467	493	624	0.40 / 352	93.8
Without NO_x	-	513	578	587	612	-/-	98.5
SiC	-	532	610	626	640	-/-	50.7

Table 5.9. Catalytic performances of $LaAl_{0.25}Co_{0.75}O_3$ at different calcination temperatures.

Calcination Temperature (°C)	$T_{10\%}$ (°C)	$T_{50\%}$ (°C)	T_{max} (°C)	$T_{90\%}$ (°C)	$(NO_2/NO_x)_{max}$ / T (%/°C)	CO_2 selectivity (%)
700	377	467	467	585	71.0 / 321	99.8
600	370	478	478	578	64.9 / 330	99.5
500	399	492	499	583	47.9 / 368	98.7

Figure 5.9C and 9D show the evolution of CO_2 and CO concentration during the NO_x-assisted oxidation tests over the catalysts with various Co content. Obviously, $LaAlO_3$ has the highest T_{max} (the temperature at which the maximum CO_2 is produced) at 563 °C with low quantity of CO_2 formed, evidenced by the CO_2 selectivity of 82.3 %. The substitution of Co by Al shifts the T_{max} to lower range by about 81 °C for x=0.25 and 0.5, and by around 96 °C for $LaAl_{0.25}Co_{0.75}O_3$. However, $LaCoO_3$ shifts the temperature towards 493 °C which is similar to that reported elsewhere [27] and produces relatively a large amount of CO at high temperature. The CO_2 evolution profile for $LaCoO_3$ has a relatively similar trend as NO desorption curve with a broader shoulder at a low-temperature range (Figure 5.6C), indicating the key role of NO adsorption on soot oxidation. When SiC was used as a reference for the non-catalytic soot oxidation, the promotional effect of NO_x was lost as the peak of the soot oxidation rate was shifted to 626 °C coupled with a very high CO production.

Figure 5.10 summarizes soot conversion and NO_2/NO_x percentage as functions of temperature over catalyst $LaAl_{0.25}Co_{0.75}O_3$ calcined at different temperatures, and Table 5.9 sums up the oxidative characteristics of the catalyst. The calcination at lower temperatures enhances the surface areas but deteriorates the oxidation activity. The sample annealed at 500 °C has the highest $T_{10\%}$, $T_{50\%}$ and $T_{90\%}$ at 399, 492 and 583 °C respectively, compared to 370, 478 and 578 °C for $LaAl_{0.25}Co_{0.75}O_3$ calcined at 600 °C. Moreover, the treatment at 600 and 700 °C shows similar soot oxidation but the NO_2 production of the later is ameliorated with 71 % compared to 64.9 % for the former. It has been already mentioned that $LaAl_{0.25}Co_{0.75}O_3$ calcined at the lowest temperature adsorbs the largest amount of NO due to high surface area but releases this gas at the highest temperature, suggesting that stronger interaction between NO_x and substrate surface does not support the oxidation reaction and the products fail to dissociate as it can be described by the Sabatier principle [88]. This finding emphasizes the crucial role of crystallinity promoted by high calcination temperature in both NO and NO_x-assisted soot oxidation.

5.4. Conclusions

Among the prepared catalysts, $LaAl_{0.25}Co_{0.75}O_3$ exhibits superior catalytic activity for both NO oxidation and NO_x-assisted soot oxidation. For the NO oxidation, NO_2 production can reach 78 % at relatively low temperature (320 °C) which is considered as a potential alternative for noble metal catalysts. Furthermore, $LaAl_{0.25}Co_{0.75}O_3$ is also the most active catalyst for NO_x-assisted soot oxidation with $T_{10\%}$ of 377 °C and NO_2/NO_x of 0.71, and results in almost 100 % of CO_2 selectivity. The correlation between NO_x desorption and oxidation activity is well established suggesting that NO_x adsorption on catalyst surface is a key role in soot oxidation with NO_x. The presence of NO_2 for soot oxidation is obvious, the absence of which remarkably decreases the oxidation activity. The excellent performance of $LaAl_{0.25}Co_{0.75}O_3$ is likely to be linked with high lattice surface oxygen supported by well-crystallized perovskite structure. Full replacement of Al by Co deteriorates the catalytic activity, suggesting that the combination of Al-Co has synergetic effects on the catalysis.

References

[1] M.A. Pena, J.L.G. Fierro, Chem. Rev. 101 (2001) 1981–2017.

[2] J. Zhu, H. Li, L. Zhong, P. Xiao, X. Xu, X. Yang, Z. Zhao, J. Li, ACS Catal. 4 (2014) 2917–2940.

[3] U. Oemar, P.S. Ang, K. Hidajat, S. Kawi, Int. J. Hydrogen Energy 38 (2013) 5525–5534.

[4] C.P.B. Quitete, R.L. Manfro, M.M.V.M. Souza, Int. J. Hydrogen Energy 42 (2017) 9873–9880.

[5] Yasushi, D. Mukai, Y. Murai, S. Tochiya, Y. Izutsu, K. Sekiguchi, N. Hosomura, H. Arai, E. Kikuchi, Y. Sugiura, Appl. Catal. A Gen. 451 (2013) 160–167.

[6] K.H. Lin, C. Bin Wang, S.H. Chien, Int. J. Hydrogen Energy 38 (2013) 3226–3232.

[7] Q. Zhang, L. Li, B. Jiang, K. Wang, D. Tang, B. Dou, Int. J. Hydrogen Energy 42 (2017) 17102–17111.

[8] K. Zhao, F. He, Z. Huang, G. Wei, A. Zheng, H. Li, Z. Zhao, Appl. Energy 168 (2016) 193–203.

[9] L.D. Vella, J.A. Villoria, S. Specchia, N. Mota, J.L.G. Fierro, V. Specchia, Catal. Today 171 (2011) 84–96.

[10] T.H. Nguyen, A. Łamacz, P. Beaunier, S. Czajkowska, M. Domański, A. Krztoń, T. Van Le, G. Djéga-Mariadassou, Appl. Catal. B Environ. 152–153 (2014) 360–369.

[11] S. Ramesh, N.J. Venkatesha, ACS Sustanaible Chem. Eng. 5 (2017) 1339–1346.

[12] J. Yao, J. Liu, H. Hofbauer, G. Chen, B. Yan, R. Shan, W. Li, Energy Convers. Manag. 117 (2016) 343–350.

[13] G. Chen, J. Yao, J. Liu, B. Yan, R. Shan, W. Li, Bioresour. Technol. 198 (2015) 108–114.

[14] G. Chen, J. Yao, J. Liu, B. Yan, R. Shan, Renew. Energy 91 (2016) 315–322.

[15] K.A. Resende, C.N. Vila-Neto, R.C. Rabelo-Neto, F.B. Noronha, C.E. Hori, Catal. Today 242 (2015) 71–79.

[16] X. Yang, L. Yang, W. Fan, H. Lin, Catal. Today 269 (2016) 56–64.

[17] M.-Y. Chen, C.-B. Chen, B. Zada, Y. Fu, M.H. Qiao, K.N. Fan, X.X. Zhang, B.N. Zong, A. Sarkar, M.K. Nazeeruddin, M. Grätzel, S.I. Seok, Green Chem. 18 (2016) 3858–3866.

[18] H. Deng, L. Lin, Y. Sun, C. Pang, J. Zhuang, P. Ouyang, Z. Li, S. Liu, Catal. Letters 126 (2008) 106–111.

[19] H. Deng, L. Lin, Y. Sun, C. Pang, J. Zhuang, P. Ouyang, J. Li, S. Liu, Energy & Fuels 23 (2009) 19–24.

[20] J.A. Onrubia, J.R. González-velasco, Appl. Catal. B, Environ. 213 (2017) 198–210.

[21] X. Yang, L. Luo, H. Zhong, Catal. Commun. 6 (2005) 13–17.

[22] A.K. Ladavos, P.J. Pomonis, Appl. Catal. A Gen. 165 (1997) 73–85.

[23] N. Russo, S. Furfori, D. Fino, G. Saracco, V. Specchia, Appl. Catal. B Environ. 83 (2008) 85–95.

[24] S. Irusta, M.P. Pina, M. Men, J. Catal. 412 (1998) 400–412.

[25] A. Russell, W.S. Epling, Catal. Rev. - Sci. Eng. 53 (2011) 337–423.

[26] A. Namdeo, M.C. Bell, Environ. Int. 31 (2005) 565–573.

[27] R. Zhang, N. Luo, B. Chen, S. Kaliaguine, Energy and Fuels 24 (2010) 3719–3726.

[28] T. Andana, M. Piumetti, S. Bensaid, L. Veyre, C. Thieuleux, N. Russo, D. Fino, E. Alessandra, R. Pirone, Appl. Catal. B Environ. 209 (2017) 295–310.
[29] E. Xue, K. Seshan, J.R.H. Ross, Appl. Catal. B Environ. 11 (1996) 65–79.
[30] M. V. Twigg, Catal. Today 117 (2006) 407–418.
[31] A. Setiabudi, M. Makkee, J.A. Moulijn, Appl. Catal. B Environ. 50 (2004) 185–194.
[32] M. Koebel, M. Elsener, M. Kleemann, Catal. Today 59 (2000) 335–345.
[33] M. Koebel, G. Madia, M. Elsener, Catal. Today 73 (2002) 239–247.
[34] M.K. Majewski, W.A.; Khair, in: Diesel Emiss. Their Control. SAE Int., Warrendale, PA, 2006.
[35] T. Andana, M. Piumettia, S. Bensaida, L. Veyre, C. Thieuleux, N. Russo, D. Fino, E.A. Quadrelli, R. Pirone, Appl. Catal. B Environ. 226 (2018) 147–161.
[36] S. Liu, X. Wu, H. Luo, D. Weng, R. Ran, J. Phys. Chem. C 119 (2015) 17218–17227.
[37] H. Zhang, Y. Zhu, S. Wang, M. Zhao, M. Gong, Y. Chen, Fuel Process. Technol. J. 137 (2015) 38–47.
[38] S. Liu, X. Wu, D. Weng, M. Li, R. Ran, ACS Catal. 5 (2015) 909–919.
[39] C.H. Kim, G. Qi, K. Dahlberg, W. Li, Science (80-.). 327 (2010) 1624–1627.
[40] J. Wang, Y. Su, X. Wang, J. Chen, Z. Zhao, M. Shen, Catal. Commun. 25 (2012) 106–106.
[41] M.-S.S.-A.M.-J.I.G. Veronica Torregrosa-Rivero, Vicente Albaladejo-Fuentes, RSC Adv. Open 7 (2017) 35228–35238.
[42] V.G. Milt, M.A. Ulla, E.E. Miro, Appl. Catal. B Environ. 57 57 (2005) 13–21.
[43] N.T. and P.V. Xin-Gang Li, Yan-Hua Dong, Hui Xian, Willinton Yesid Hern andez, Ming Meng, Hong-Hu Zou, Ai-Jing Ma, Tian-Yong Zhang, Zheng Jiang, Energy Environ. Sci. 4 (2011) 3351–3354.
[44] J. Chen, M. Shen, X. Wang, J. Wang, Y. Su, Z. Zhao, Catal. Commun. 37 (2013) 105–108.
[45] F. Lin, X. Wu, S. Liu, D. Weng, Y. Huang, Chem. Eng. J. 226 (2013) 105–112.
[46] T.R. Sahoo, M. Armandi, R. Arletti, M. Piumetti, S. Bensaid, M. Manzoli, S.R. Panda, B. Bonelli, Appl. Catal. B Environ. 211 (2017) 31–45.
[47] H. Lehnert, H. Boysen, J. Schneider, F. Frey, D. Hohlwein, P. Radaelli, H. Ehrenberg, Zeitschrift Fur Krist. 215 (2000) 536.
[48] C.J. Howard, B.J. Kennedy, B.C. Chakoumakos, J. Phys. Condens. Matter 12 (2000) 349–365.
[49] G. Thornton, B.C. Tofield, A.W. Hewat, J. Solid State Chem. 61 (1986) 301–307.
[50] V. Aswin, P. Kumar, P. Singh, A. Gupta, S. Rayaprol, A. Dogra, J. Mater. Sci. 50 (2015) 366–373.
[51] R.D. Shannon, Acta Cryst. (1976) 751.
[52] X. Zhu, X. Tu, M. Chen, Y. Yang, C. Zheng, J. Zhou, X. Gao, Catal. Commun. 92 (2017) 35–39.
[53] N.A. Merino, B.P. Barbero, P. Ruiz, L.E. Cadús, J. Catal. 240 (2006) 245–257.
[54] J. Zhang, X. Weng, Z. Wu, Y. Liu, H. Wang, Appl. Catal. B Environ. 126 (2012) 231–238.
[55] S. Ivanova, A. Senyshyn, E. Zhecheva, K. Tenchev, V. Nikolov, R. Stoyanova, H. Fuess, J. Alloys Compd. 480 (2009) 279–285.
[56] N.A. Merino, B.P. Barbero, P. Grange, L.E. Cadús, J. Catal. 231 (2005) 232–244.

[57] B. Białobok, J. Trawczyński, W. Miśta, M. Zawadzki, Appl. Catal. B Environ. 72 (2007) 395–403.
[58] T. Nakamura, G. Petzow, L.J. Gauckler, Mat. Res. Bull. 14 (1979) 649–659.
[59] B. Levasseur, S. Kaliaguine, Appl. Catal. A Gen. 343 (2008) 29–38.
[60] L.B. Sis, G.P. Wirtz, S.C. Sorenson, J. Appl. Phys. 44 (1973) 5553.
[61] L. Huang, M. Bassir, S. Kaliaguine, Appl. Surf. Sci. 243 (2005) 360–375.
[62] O.O. James, S. Maity, J. Pet. Technol. Altern. Fuels 7 (2016) 1–12.
[63] R. Sarbajna, A.S. Devi, K. Purandhar, M. V Suryanarayana, Int. J. ChemTech Res. 5 (2013) 2810–2820.
[64] R. Zhang, A. Villanueva, H. Alamdari, S. Kaliaguine, Appl. Catal. B Environ. 64 (2006) 220–233.
[65] R. Pereñíguez, J.L. Hueso, F. Gaillard, J.P. Holgado, A. Caballero, Catal. Letters 142 (2012) 408–416.
[66] S. Royer, F. Bérubé, S. Kaliaguine, Appl. Catal. A Gen. 282 (2005) 273–284.
[67] J. Zhang, D. Tan, Q. Meng, X. Weng, Z. Wu, Appl. Catal. B, Environ. 172–173 (2015) 18–26.
[68] R.R. Solís, F.J. Rivas, O. Gimeno, "Applied Catal. B, Environ. 200 (2017) 83–92.
[69] M. O'Connell, A.. Norman, C.. Hüttermann, M.. Morris, Catal. Today 47 (1999) 123–132.
[70] C.A.F. Vaz, D. Prabhakaran, E.I. Altman, V.E. Henrich, Phys. Rev. B - Condens. Matter Mater. Phys. 80 (2009) 1–7.
[71] C.A. Chagas, F.S. Toniolo, R.N.S.H. Magalhães, M. Schmal, Int. J. Hydrogen Energy 37 (2012) 5022–5031.
[72] M.C. Biesinger, B.P. Payne, A.P. Grosvenor, L.W.M. Lau, A.R. Gerson, R.S.C. Smart, Appl. Surf. Sci. 257 (2011) 2717–2730.
[73] F. Fang, N. Feng, L. Wang, J. Meng, G. Liu, P. Zhao, P. Gao, J. Ding, Appl. Catal. B Environ. 236 (2018) 184–194.
[74] C. Lee, Y. Jeon, S. Hata, J. Park, R. Akiyoshi, H. Saito, Y. Teraoka, Y. Shul, H. Einaga, Appl. Catal. B Environ. 191 (2016) 157–164.
[75] X. He, M. Meng, J. He, Z. Zou, X. Li, Z. Li, Z. Jiang, Catal. Commun. 12 (2010) 165–168.
[76] R. You, Y. Zhang, D. Liu, M. Meng, Z. Jiang, S. Zhang, Y. Huang, Chem. Eng. J. 260 (2015) 357–367.
[77] S. Roy, A. Baiker, Chem. Rev. 109 (2009) 4054–4091.
[78] J. Liu, Z. Zhao, C. Xu, A. Duan, G. Jiang, J. Phys. Chem. C 112 (2008) 5930–5941.
[79] S. Mentus, D. Jelić, V. Grudić, J. Therm. Anal. Calorim. 90 (2007) 393–397.
[80] Y. Peng, W. Si, J. Luo, W. Su, H. Chang, J. Li, J. Hao, J. Crittenden, Environ. Sci. Technol. 50 (2016) 6442–6448.
[81] J. Chen, M. Shen, X. Wang, G. Qi, J. Wang, W. Li, Appl. Catal. B Environ. 134–135 (2013) 251–257.
[82] A.-J. Ma, S.Z. Wang, C. Liu, H. Xian, Q. Ding, L. Guo, M. Meng, Y.S. Tan, N. Tsubaki, J. Zhang, L.R. Zheng, X.G. Li, Appl. Catal. B Environ. 146 (2014) 24–34.
[83] J. Xiong, Q. Wu, X. Mei, J. Liu, Y. Wei, Z. Zhao, D. Wu, J. Li, ACS Catal. 8 (2018) 7915–7930.
[84] P. Ciambelli, S. Cimino, G. Lasorella, L. Lisi, S. De Rossi, M. Faticanti, G. Minelli, P. Porta, Appl. Catal. B Environ. 37 (2002) 231–241.
[85] K. Tikhomirov, O. Kröcher, M. Elsener, A. Wokaun, Appl. Catal. B Environ. 64 (2006) 72–78.

[86] N.D. Wasalathanthri, T.M. SantaMaria, D.A. Kriz, S.L. Dissanayake, C.H. Kuo, S. Biswas, S.L. Suib, Appl. Catal. B Environ. 201 (2017) 543–551.
[87] C.M. Marcos, V.T. Rivero, V.A. Fuentes, M.S.S. Adsuar, M.J.I. Gómez, Top. Catal. 0 (2018) 0.
[88] G. Rothenberg, Catalysis: Concepts and Green Applications, WILEY-VCH Verlag, 2008.

Supplementary material for Chapter 5

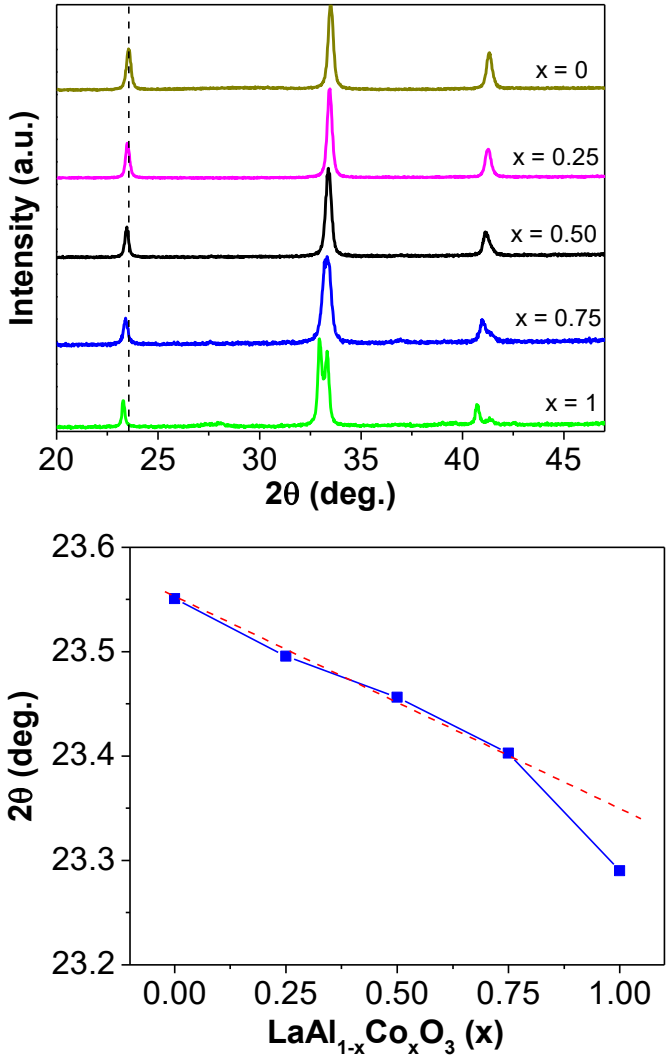

Figure S5.1 Magnification of XRD profiles of $LaAl_{1-x}Co_xO_3$ calcined at 700 °C (a) and 2θ peak position with Co content (b)

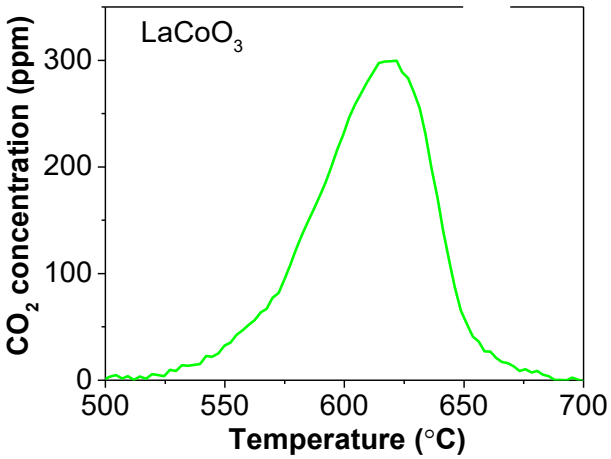

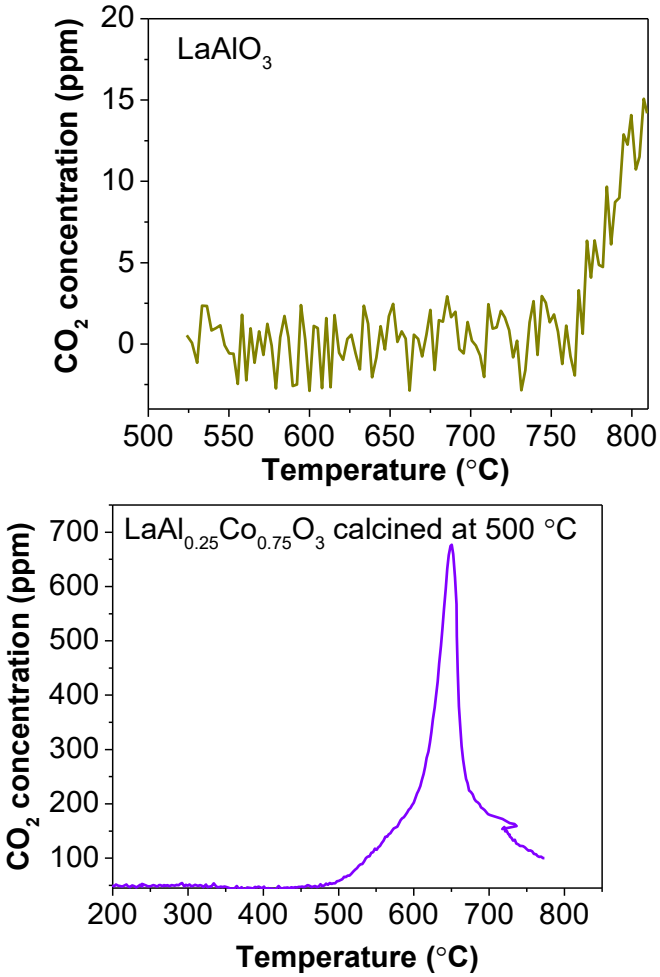

Figure S5.2 CO_2 desorption profiles of $LaCoO_3$ (a) $LaAlO_3$ (b) and (c) $LaAl_{0.25}Co_{0.75}O_3$ (c) during heat treatment under N_2

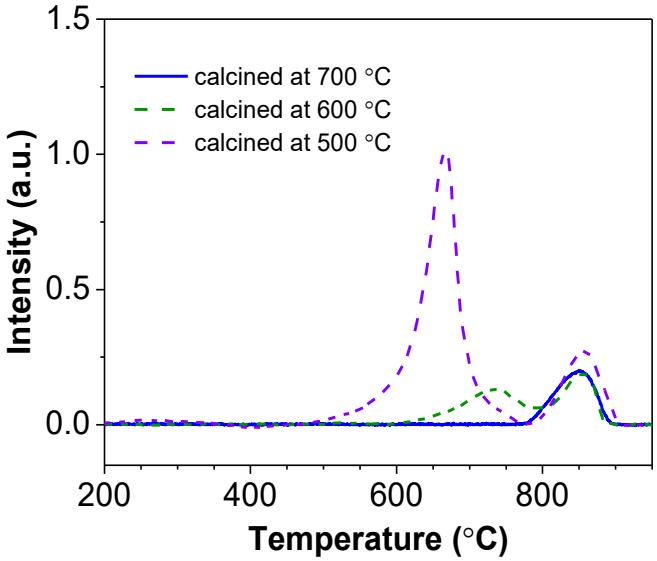

Figure S5.3 O_2 - TPD profiles of $LaAl_{0.25}Co_{0.75}O_3$ calcined at different temperatures.

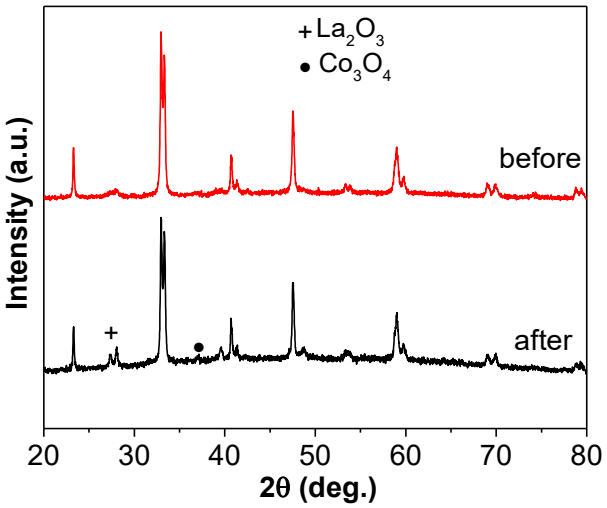

Figure S5.4 XRD patterns of $LaCoO_3$ after and before NO_x-TPD experiment (peaks are normalized)

Chapter 6

6. SO_2 deactivation mechanism of NO oxidation and regeneration of the $LaCoO_3$ perovskite

Chapter summary

In this chapter the SO_2 poisoning of $LaCoO_3$ as NO oxidation catalyst was investigated though various techniques and several regeneration methods investigated. At 300°C the SO_2 accumulated irreversibly during the deactivation in two stages. In the first stage the SO_2 competitively adsorbed to the same active sites as for the NO oxidation, while in the second stage lanthanum sulfates grew on the surface of the perovskite, without binding to cobalt. As evidenced through DRIFTS and soot-TPR the sulfates became mobile upon heating above 400 °C, while thermal desorption occurred only above 900 °C. The presence of soot induced the decomposition of the accumulated sulfates and triggered their release as low as 500 °C. The catalyst could be washed with distilled water at room temperature that removed the accumulated sulfates and completely recovered the NO oxidation activity, even after several poisoning-washing cycles. Finally the inclusion of adsorbent, $Ca(OH)_2$, could mitigate the second stage of the deactivation thereby delaying full deactivation.

Adapted from publication in Catalysis Science and Technology (2020) 10(7), 2193-2202

https://doi.org/10.1039/C9CY02478F

6.1. Introduction

Perovskite structured materials are an interesting type of catalysts due to their tunable catalytic activity, thermal stability and peculiar redox properties [1]. In the automotive exhaust treatment, they have been suggested as a potential low-cost substitute for the platinum group metals Pt-Pd (PGM) widely used in three way catalysts, diesel oxidation catalysts (DOC), catalyzed diesel particulate filters (cDPF) and lean NO_x traps (LNT) [1-6]. The most promising perovskites are lanthanides with $LaBO_3$ structure, where B is usually Fe, Mn and Co in the +3 oxidation state. Out of these three, $LaCoO_3$ has shown the highest activity in the automotive application, partly due to its interaction and high oxidation ability of NO_x [1-6].

Despite advances made in hydrodesulfurization, deep removal to produce low sulfur concentration in fuel (<10 ppm) remains a challenge. Hence, sulfur-based compounds are invariably present in the fuel and produce SO_2 during combustion. In different degrees, SO_2 represents a poison to almost all catalysts used in aftertreatment systems. The most sensitive to sulfur are catalysts that are characterized by an alkaline surface (e.g. barium in LNT), which can form stable

sulfates and deactivate the catalyst active site. While there are many detailed studies of SO_2 poisoning and deactivation on Pt-Ba based LNT systems [7-9], only few and conflicting reports are available on the deactivation of the perovskite-based catalysts [10-16]. The reason is that, in the deactivation studies, the applied reaction conditions are drastically different, depending on the application and/or the aims of the study. For example, in studies concerning the hydrocarbon catalytic oxidation at high temperature (>500 °C) the main results showed that sulfur diffuses in the bulk of the perovskite structure [12,14,17], whereas studies made at lower temperature concluded that the sulfur insertion was limited and the deactivation was mainly a surface phenomenon [10,13,16]. The point at which all agree is the competition for the same catalytic cycle and competition of SO_3 and NO_2 for the same active site characterized by alkaline character. The first goal of this work is to unravel the deactivation mechanism of NO oxidation by SO_2 under relevant reaction conditions that typically occur in diesel exhaust aftertreatment system.

The second goal of the work focuses on alternative methods of SO_2 poisoning management. The typical methods suggested for the regeneration of sulfur poisoned LNT catalysts involve the injection of large amounts of reductant (such as H_2, C_3H_6, NH_3) and high regeneration temperatures (>600 °C), which result in high fuel penalty and catalyst damage [8-10]. Based on the deactivation mechanism and different chemical nature of the perovskite-based catalysts compared to the PGM based LNT, several novel methods are suggested:

1. Use of inexpensive $Ca(OH)_2$ as SO_2 adsorbent and bed guard.
2. Use of soot for enhancing the release of SO_2. Soot is a pollutant abundant on the cDPF, which is one of the main catalytic potential applications of $LaCoO_3$.
3. Facile regeneration at room temperature, by washing with distilled water.

In this work all three alternative regeneration methods are investigated and discussed.

6.2. Experimental procedures

6.2.1. Catalyst preparation.

The $LaCoO_3$ catalyst was prepared by following the citrate sol-gel method. Proper equimolar amounts of $La(NO_3)_3 \cdot 6H_2O$ and $Co(NO_3)_2 \cdot 6H_2O$ (each 5 mmol) were dissolved in 60 mL of deionized water. 20 mmol citric acid monohydrate was added under stirring to the mixture and the pH adjusted to 7 by adding ammonia solution (10% v/v). The solution was heated to 80 °C and evaporated under stirring. As the liquid volume decreased, the chelated metallic ions were crosslinked by citric acid and the viscosity increased. The as-obtained gel was dried at 110 °C for 24 hours after which it was crushed and pre-calcined at 350 °C for 1 hour to decompose the citric acid. The obtained powder was ground in a mortar and calcined at 700 °C for 6 hours (5 °C/min heating rate).

Regeneration of the poisoned samples was made by placing the sulfated $LaCoO_3$ ($LaCoO_3$-S) in 20 mL of distilled water and by adjusting the pH to 7 by adding ammonia solution to avoid any metal leaching. The slurry was stirred for 30 min at room temperature, after which it was separated by centrifugation. The regenerated sample was dried at 200 °C for 12 h and tested again. Several successive deactivation-regeneration cycles were conducted, and the so obtained samples were referred to as $LaCoO_3$-R followed by a number indicating the number of regeneration cycles. A total of 5 poising-reactivation cycles was reached.

6.2.2. Catalyst characterization.

X-ray diffraction were recorded on a Philips PW 3040 X'Pert instrument with Cu anode for the Kα generation at 40 kV operating voltage. A pixel array detector enabled continuous data acquisition in the 2θ range 20-80°, with a step of 0.013°. The cell parameters and the crystallite sizes were evaluated by Rietveld refinement.

The specific surface area was determined by N_2 physisorption at -196 °C on Micrometrics Tristar 3020 instrument. Before the analysis, the samples were evacuated at 200 °C for 2 hours. The reported specific surface area was calculated according to the BET method.

X-ray photoelectron spectroscopy (XPS) was performed in a PHI Versaprobe apparatus, using Al Kα radiation with band-pass energy of 187.85 eV and 23.5 eV for the high-resolution scan, a 45° take off angle and a 100.0 μm diameter X-ray spot size. The lines of La, Co, O and S were detected. To observe the depth profile and the deactivation mechanism, the deactivated $LaCoO_3$-S was sputtered with Ar^+ gun to remove the top layer and the XPS analysis was repeated afterwards.

The hydrogen temperature programmed reduction (H_2-TPR) was performed on a ThermoScientific TPRDO 1100 instrument equipped with a thermal conductivity detector (TCD) detector. In a typical experiment, the catalyst was pre-treated in-situ under inert flow of Ar at 500 °C for 1 hour to remove any adsorbed species. Afterwards, the sample was cooled down and 20 mL/min of a gas mixture of 5% H_2 in Ar was flown over 60 mg of the sample with a 5°C/min rate of temperature increase until 900 °C. The H_2-TPR profile for the poisoned $LaCoO_3$-S sample was also repeated in the experimental setup described below, to detect by means of mass spectrometer the various potential species formed during reduction. The soot-TPR, H_2-TPR and temperature programmed desorption (TPD) of the poisoned sample was performed in a slightly different set-up, with the outlet connected to a mass spectrometer to follow the evolution of all the potential species. Typically, 60 mg of sample ($LaCoO_3$ and $LaCoO_3$-S) was used under 60 mL/min Ar flow and 5 °C/min heating rate. For the soot-TPR the fresh and poisoned catalyst was mixed with soot in a planetary ball mill in 10: 1 catalyst: soot mass ratio.

Morphology and elemental composition were determined by field emission scanning electron microscopy-Energy-dispersive X-ray spectroscopy (FESEM-EDS) under high vacuum, using Zeiss MERLIN Gemini II equipped with EDS at 3 keV accelerating voltage and different magnifications.

Diffuse Reflectance Infrared Fourier Transform Spectroscopy (DRIFTS) analysis was performed on Vertex-70 IR spectrometer equipped with Praying Mantis (Harrick) heated reaction cell. The samples $LaCoO_3$ or $LaCoO_3$-S were mixed to KBr in 100:2 mass ratio. The so-prepared samples were placed into an isolated cell and kept under inert N_2 flow during the test. $LaCoO_3$-S was heated to 400 °C, 500 °C, 550 °C and 600 °C and held at constant temperature for 30 min after which they were quenched at 200 °C/min cooling rate. All the IR spectra were collected in absorbance mode at 30 °C (2 cm^{-1} resolution; 64 scans; wavenumber range 1800-800 cm^{-1}).

6.2.3. Catalytic tests.

The catalytic tests were conducted in a glass tube reactor with i.d. 10 mm. The catalyst was placed on a glass membrane inside the reactor and heated in an isolated vertical furnace with a thermocouple in the catalytic bed for programmable heating. The outlet was connected to ABB Limas and Uras non-dispersive infrared and ultraviolet (NDIR and UV) analysers for continuous measurement of CO, CO_2, NO, NO_2.

The deactivation was performed by flowing 600 mL/min of 60 ppm SO_2, 500 ppm NO, 4% O_2 in N_2 over 200 mg of catalyst. To prepare the $LaCoO_3$-S sample, the deactivation was performed at constant temperature of 300 °C as it is a typical temperature found in diesel exhaust. Deactivation was considered complete when the NO oxidation rate dropped to 0, i.e. the NO_2/NO_x ratio after the catalytic bed was the same as at the inlet. The poisoning time typically lasted 90 minutes. To demonstrate the effectiveness of an adsorbent towards SO_2 management, 200 mg $LaCoO_3$ was mixed with 100 mg of $Ca(OH)_2$ before performing deactivation under the same conditions as before.

To show competitive adsorption of NO_x and SO_2, the catalyst was first saturated with NO_x at 200 °C. When the NO_x concentration was stable, NO_x flow was switched off and the catalyst purged with N_2 to remove weakly adsorbed NO_x. Once the NO_x concentration in the gas phase decreased to 0, 60 ppm of SO_2 in 4% O_2 and N_2 was introduced to the reactor and the desorbed NO_x species were measured. During the whole test, the temperature was kept constant at 200 °C.

NO oxidation tests were made under the aforementioned conditions, without SO_2 in the feed stream and at constant heating rate of 5 °C/min in the temperature range 150-600 °C. The NO oxidation performance of the fresh catalyst was compared to that of the regenerated $LaCoO_3$-R.

6.3. Results and discussion

6.3.1. Characterization results.

The XR-diffractograms of the samples $LaCoO_3$, $LaCoO_3$-S and $LaCoO_3$-R5 are presented in Figure 6.1. In all the samples, only the $LaCoO_3$ perovskite phase is detected without any Co_3O_4 or La_2O_3 phases, indicating good crystallization of the sample and the perovskite formation. The cell parameters of the rhombohedral perovskite structure (a = 5.441(5) and c = 13.10(5)) are not significantly affected by the treatments. The degree of crystallinity is the same with all the samples, as even after 5 regeneration cycles the normalized peak intensities are the same. The value of crystallite size as calculated by the Williamson-Hall method is 41 nm for the parent $LaCoO_3$ sample, decreases to 32 nm for $LaCoO_3$-S and stabilizes to 28 nm for regenerated samples from $LaCoO_3$-R1 to $LaCoO_3$-R5. The main diffraction peaks of $La_2(SO_4)_3$, Co_2O_3, orthorhombic La_2O_3 and cubic La_2O_3 (expected at the 2θ values 28.33°, 36.56°, 29.92° and 33.19° respectively) were not detected by XRD (25-30° magnified in Figure 6.1). Conversely several reports,[14,15,17] show the presence of peaks of $La_2(SO_4)_3$ as a result of SO_2 poisoning. The major difference is that for those, the deactivation by SO_2 was made at much higher temperature, well above 500 °C, and under different reaction conditions. At high temperature, changes in the perovskite structure can occur more readily and sulfates can diffuse into the bulk by forming a mixed phase. Here the deactivation proceeded at 300 °C (lower temperature) through a different mechanism and, as will be discussed later on, sulfates formed only at the surface, without affecting the crystalline structure of the perovskite. In fact, no changes in both the symmetry and lattice parameters were observed for $LaCoO_3$, $LaCoO_3$-S and $LaCoO_3$-R5. As the total quantity of sulfur was low and dispersed uniformly on the surface in a nm thin layer (vide infra), the sulfate containing phases could not be detected by XRD.

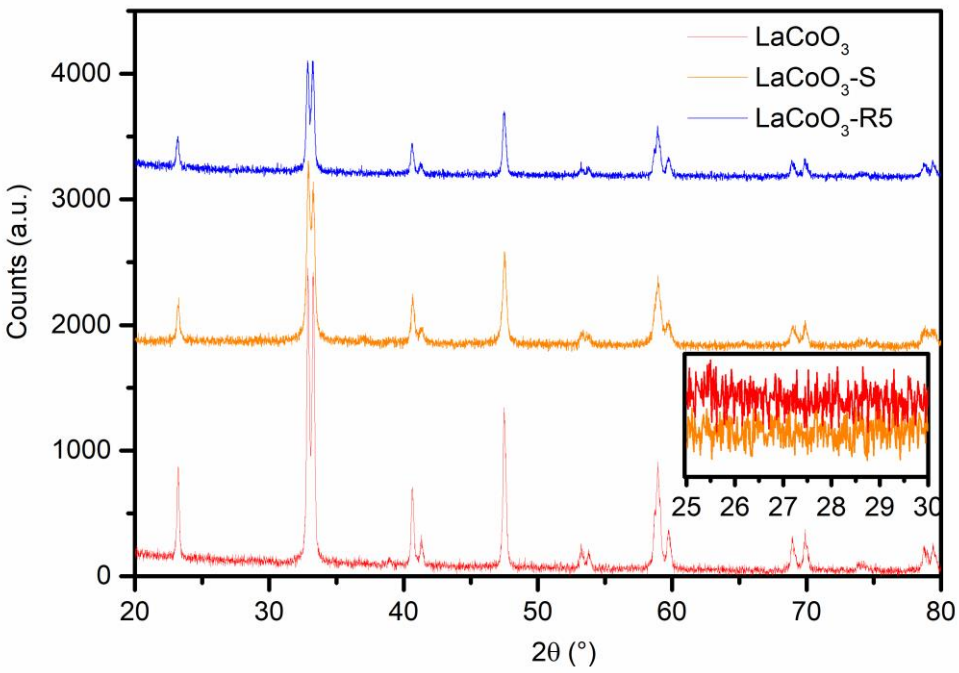

Figure 6.1. Powder XRD diffractograms of the $LaCoO_3$, $LaCoO_3$-S and $LaCoO_3$-R5 catalysts.

FE-SEM analysis (Figure S6.1) showed powders with a morphology typical of perovskites synthesized by citrate complexation method. The particles were round and interlinked, forming regular intergranular macropores. The $LaCoO_3$-S and the $LaCoO_3$-R5 presented no significant difference in the morphology as compared to the fresh catalyst (Figure S6.1) and no significant difference in the BET specific surface area was observed as well, specific surface areas being 12.64, 12.53, 9.12 m^2/g for the samples $LaCoO_3$, $LaCoO_3$-S and $LaCoO_3$-R5, respectively. The decrease of crystallite size, as observed by XRD linewidth, is not contradictory with the stability of grain size as observed by FE-SEM. As the decrease in crystallite size is mainly observed in the first catalytic use of the material, it seems likely that the largest grains have been fractured by thermal stress without physical separation of the sub-grains formed, hence with no changes of grain morphology. Conversely, significant decrease of the specific surface area was reported after deactivation by SO_2 albeit in different reaction conditions,[14,15,17] i.e. when the deactivation was made at high temperature (500-600 °C) for prolonged periods with catalysts calcined at lower temperature than in this study. In those cases, the decrease in the specific surface area could be attributable, at least partially, to thermal sintering during sulfation. In this work, instead, the calcination temperature was 700 °C and the sulfation temperature 300 °C and thus, the specific surface area was stabilized during the calcination and no significant decrease in the surface area was observed due to thermal effect, nor due to sulfation.

The total consumption of H_2 during H_2-TPR was 6.2 mmol/g for both the parent $LaCoO_3$ and the regenerated $LaCoO_3$-R5 (Figure 6.2). This amount

corresponds to the stochiometric reduction of Co^{3+} to metallic Co via the reduction steps: $Co^{3+} \rightarrow Co^{2+} \rightarrow Co^{0}$ [18]. It is generally accepted that the reduction of $LaCoO_3$ perovskites occurs along the reactions R1-2. This can explain the occurrence of two clearly separated reduction steps, at variance with the reduction of Co_3O_4 that has only a single peak in the low temperature region [19]. The reduction peak between 200-450 °C corresponds to the reduction of Co^{3+} to Co^{2+} (reaction R1) [18]. This first reduction step can be separated into several components, showing two distinct reduction temperatures at 325 and 400 °C. This is most likely due to the inhomogeneity and the presence of different types of Co^{3+} and O^{2-} species in the sample.

The second peak between 550-650 °C is due to the reduction of Co^{2+} to metallic Co^{0} with the consequent loss of the perovskite crystalline phase and the formation of Co/La_2O_3 system. Indeed, as expected, the H_2 consumption corresponding to the second peak of $LaCoO_3$ and $LaCoO_3$-R5 TPR profiles is twice the H_2 consumption of first peak. In contrast, the $LaCoO_3$-S sample did not show any H_2 consumption at low temperature, in that the first peak was absent and reduction started only at 400°C meaning that the Co^{3+} to Co^{2+} reduction is deactivated. The adsorbed sulfates had to be removed first by reducing them to H_2S (Figure 6.2B), before both the lattice and surface oxygen of perovskite could be accessible for the subsequent reduction with H_2. This provides evidence that the redox sites are blocked by strongly bound sulfates and the reactive oxygen species active for NO oxidation are inactivated. Only after the surface sulfate removal the reduction proceeds.

$2\ LaCoO_3 + H_2 \rightarrow 2\ LaCoO_{2.5} + H_2O$ R1 (200-420 °C)

$2\ LaCoO_{2.5} + 2\ H_2 \rightarrow 2Co + La_2O_3 + 2\ H_2O$ R2 (500-650 °C)

$LaCoO_3\text{-}xSO_3 + 4xH_2 \rightarrow LaCoO_3 + H_2O + xH_2S$ R3 (500-650 °C)

Figure 6.3 reports the XP-spectra concerning $LaCoO_3$, $LaCoO_3$-S, and $LaCoO_3$-R5 samples. The O 1s XP spectra shows a marked increase in the poisoned sample of the peak at 532 eV which corresponds to the characteristic electronic state of oxygen in sulfate form, originating from the SO_4^{2-} oxygen [14, 20]. Further evidence of surface sulfates comes from the S 2p peak as the band centered at 169 eV is a clear indicator for S in the SO_4^{2-} (i.e. S^{6+}) form [20]. The XPS analysis in the Co 2p binding energy region indicates that cobalt is present as Co^{3+} as its characteristic peaks are identified at 780 eV and 795 eV [20]. The lack of satellite peaks at 785 eV and at 803 eV allows excluding the occurrence of Co^{2+} species in the samples, in agreement with the H_2-TPR results. The XPS analysis of the poisoned sample does not indicate any change in the Co XP spectra and the characteristic peak assignable to cobalt sulfate, expected at 784 eV, is missing [20]. The La 3d XP spectra, in contrast, showed a clear transformation in the poisoned sample since La in the sulfate form was also detected besides the characteristic spectra of the oxide form found in the perovskite. The multiplet splitting in the La $3d_{3/2}$ and $3d_{5/2}$ regions of the $LaCoO_3$ presented a ΔE of 4.1 and 5.1 eV which is characteristic of La in the oxide form.[18,20] After poisoning, the resulting spectra was a combination of the oxide and sulfate form which features a

lower ΔE of 3.5 eV. The combination of these two forms were difficult to deconvolute unambiguously as the characteristic positions are only slightly shifted (difference of 0.15 eV) and significantly overlapping. Sputtering with an Ar^+ ion gun was used to remove ca. 30 nm surface layer from the $LaCoO_3$-S sample. The XP spectra taken after sputtering showed the same features of the fresh sample (not shown) and the absence of S, confirming that SO_2 poisoning mainly affected the surface rather than the bulk after the deactivation was performed at 300 °C.

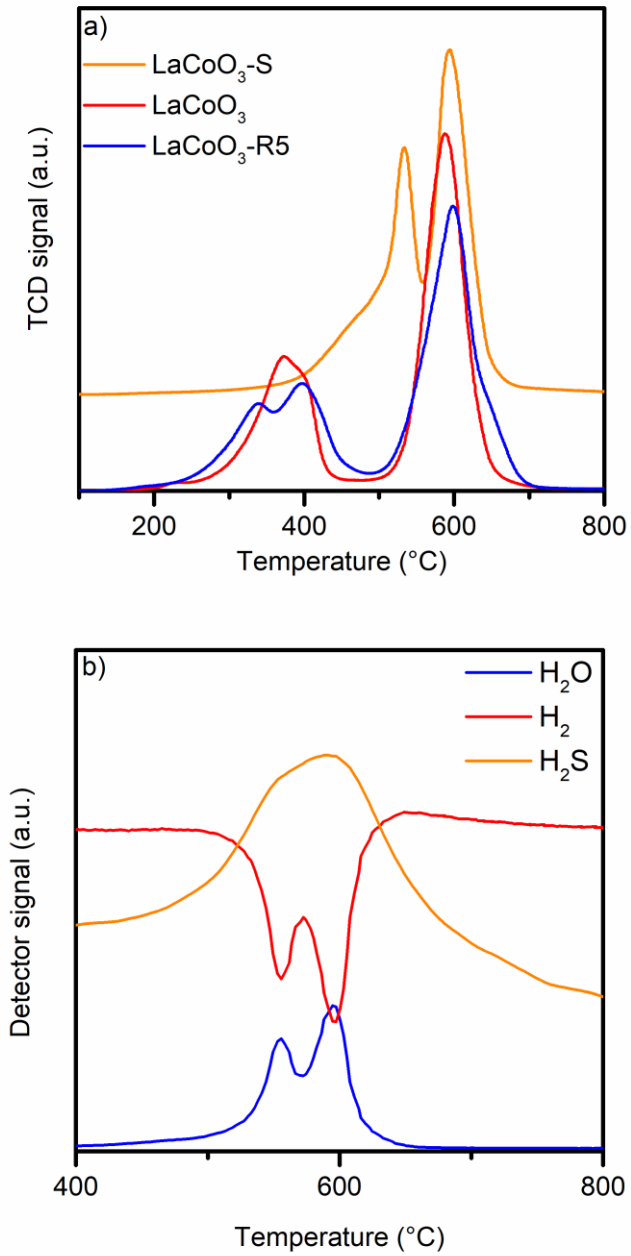

Figure 6.2. a) H_2 consumption during H_2-TPR b) H_2S and H_2O evolution during the reduction of $LaCoO_3$-S

The atomic ratios of different elements in the bulk (determined by EDS) and surface (XPS) of the samples are compared in Table 6.1. After SO_2 treatment the total sulfur content in the bulk is low (ca. 1 wt%), however on the surface the S/La

ratio reaches 0.4 which is much lower than the 1.5 ratio expected in the case of complete transformation into $La_2(SO_4)_3$. The poisoning is also accompanied by the enrichment of the surface by La relative to Co to La/Co 1.25 from 1.1. This provides further confirmation of the previous results that the sulfates are restricted to the surface and they are bound to the A and not the B site in the ABO_3 perovskite. It should be noted that the high La/Co ratio (2.15) after sputtering is most likely the consequence of the preferential ejection of the lighter Co (A = 58.93) with respect to the La (A = 138.91) during the ion sputtering, rather than a change in the chemical composition of the perovskite.

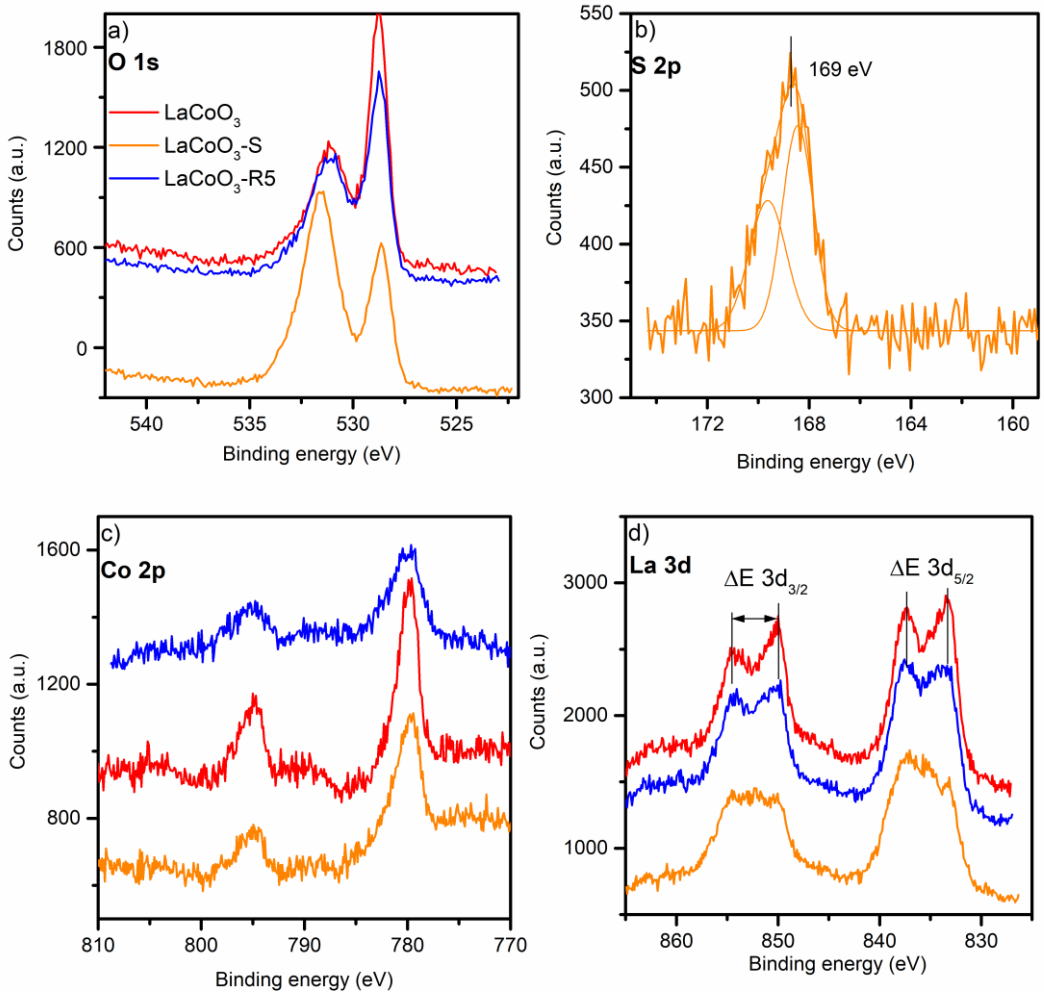

Figure 6.3. XPS spectra of a) O 1s, b) S 2p, c) Co 2p and d) La 3d band of the fresh, poisoned and regenerated by washing samples

Table 6.1. XPS and EDS analysis of the surface and bulk characteristics of the presented samples.

	La/Co		**S/La**	
	Total	Surface	Total	Surface
$LaCoO_3$	1	1.1	-	-
$LaCoO_3$-S	1	1.25	0.085	0.4
$LaCoO_3$-R5	1	1.1	-	-
After sputtering	1	2.15	0	0

Figure 6.4 reports the DRIFT spectra of the $LaCoO_3$ and $LaCoO_3$-S samples collected at room temperature after heating at 300, 400, 500, 550 and 600 °C to induce sulfate migration. The $LaCoO_3$-S at 300 °C presents two sulfate peaks at 990 and 1383 cm^{-1} and a broad band centered around 1130 cm^{-1}, likely a combination of a multitude of different vibration modes of amorphous sulfates differently bound to the surface, most commonly ascribed to bidentate sulfates [10, 21] . Detailed IR studies during sequential adsorption of NO followed by SO_2 showed that the replacement of the nitrites/nitrates was highly dependent of the adsorption mode [10]. Namely, at first the nitrates bound to multiple sites (meaning in bridging and bidentate configuration) were replaced while the monodentate nitrate form was the last to be substituted by SO_2. This implies that the formation and dissociation of the NO_2 is strongly hindered by the competitive adsorption. While a single free catalytic site is theoretically enough for the NO oxidation reaction to proceed, it is reasonable to expect that catalytic cycle is strongly inhibited when the fraction of the free sites (occupied by SO_4^{2-}) decreases below a critical value [22]. Between 400 and 600 °C, the characteristic peaks associated with bulk sulfates at the wavenumbers 1069, 1097 and 1204 cm^{-1} are progressively distinguished [10,17,21]. As the temperature increases, the sulfates become more mobile and migrate from the surface into the bulk of the perovskite and occupy energy states that are more favorable. This migration was also confirmed via XPS (see supplementary material Figure S6.2) and a uniform low concentration of S was observed through the whole depth profile on a $LaCoO_3$-S that was calcined at 600 °C. As will be discussed later in more detail, this increase sulfate mobility is also evident during the soot-TPR (Figure 6.6). As the sulfates spillover, the soot consumes one of the oxygen in the sulfate and CO_2 and SO_2 were simultaneously observed in the gas phase in the corresponding temperature range of 500-600 °C.

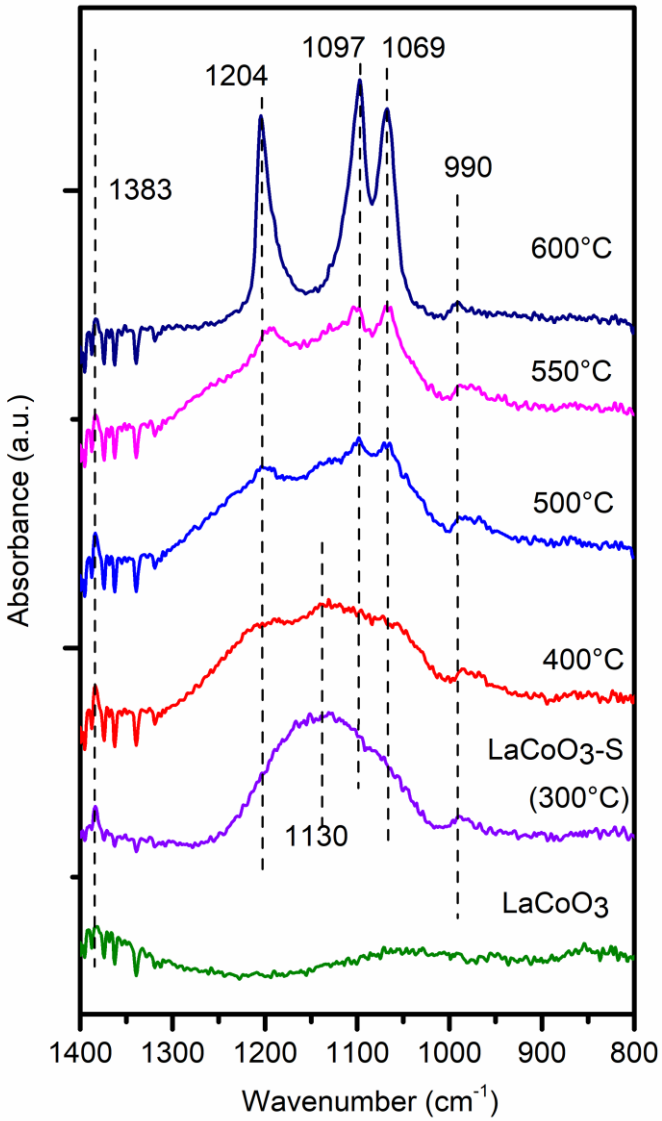

Figure 6.4. DRIFT spectra of the $LaCoO_3$ and $LaCoO_3$-S and the thermal evolution of the surface and bulk sulfates. $LaCoO_3$-S is heated to 400, 500, 550 and 600 °C with a hold time of 30 minutes each.

6.3.2. Catalytic activity and regeneration

The NO oxidation in the presence of the $LaCoO_3$ catalyst (Figure 6.5) initiated as low as 200 °C and rapidly increased, reaching very high NO_2/NO_x ratio (=0.8) and the thermodynamic equilibrium already at 300 °C, even at the high flowrates used in the study. This highlights the potential of $LaCoO_3$ as a low-cost alternative to PGM-based DOC and cDPF. The catalyst was however very sensitive to SO_2 (vide infra in Figure 6.7) and, despite the relatively low concentration of sulfur in the gas mixture, the catalyst fully deactivated within 90 min. The deactivation was irreversible, and no NO oxidation activity could be recovered after turning off the SO_2 flow. By considering that a total amount of 6

mmol SO_2/g_{cat} passed during 90 minutes of test and we assumed that a vehicle has a fuel consumption of 6 kg/100 km with 10 ppm of S in the fuel (Euro 5 fuel upper limit, EN 590:2009) and a total catalyst load of 200 g is present in the aftertreatment system, the amount of SO_2 equivalent to the laboratory test would be reached after ca. 15,000 km. This would imply that during its lifetime the DOC, cDPF etc. would have to be regenerated many times to recover its initial performance. Here, the first regeneration method was washing the catalyst with distilled water. The sulfates, present in small amount and only at the surface, can be easily dissolved and the catalyst activity is fully recovered. This method has been suggested before for the treatment of sulfur poisoned catalysts, including industrial SCR systems [21, 23-25]. Even after 5 regeneration cycles, no significant decrease in activity was observed. It should be noted that the same method could be not appropriate for the PGM-based catalysts, as the active component is expensive, and present only at very low (< 1%) amount and could be easily washed away.

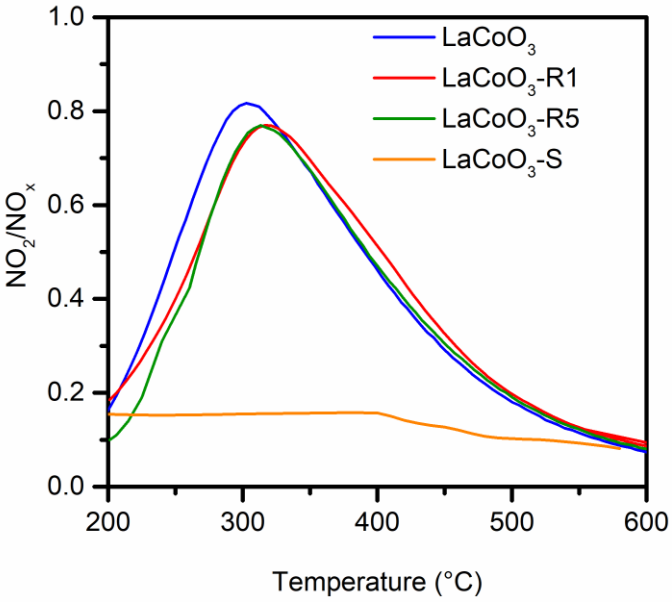

Figure 6.5. NO oxidation activity of the fresh and regenerated $LaCoO_3$ samples. Reaction conditions: 200 mg of catalyst, 600 mL/min flowrate of 500 ppm NO, 4% O_2 in N_2, 5 °C/min heating rate

The sulfur poisoned catalyst can be regenerated in-situ either by thermal desorption, to which temperatures above 900 °C are required, or at lower temperatures, however above 600 °C, if reducing atmosphere is used (Figure 6.2 and 6.6). The extremely high temperatures required for thermal regeneration can irreversibly damage the catalyst, which makes reducing treatment preferable and it is used for the Pt-Ba based LNT applications. Typical reductants for LNT are H_2, NH_3 and C_3H_6, with a corresponding increase of the regeneration temperature. Such a procedure not only requires large amount of fuel to be injected during the desulfurization, but also irreversibly damages the catalyst which is exposed to high temperature and consequent structural changes [4,8,26]. To avoid the high

fuel penalties associated with the regeneration by the injection of external reductant, soot was demonstrated here, for the first time, to be an efficient SO_2 regeneration medium. From the practical point of view, soot is an interesting alternative as it is a pollutant in the diesel exhaust and abundantly available on the cDPF. From the mechanistic point of view, soot is an interesting reacting species as, unlike most heterogeneous reactions which involve solid-gas interface, the soot oxidation involves solid-solid contact. For this reason, the soot-TPR is a good indicator for the differentiation of the highly reactive surface and lattice oxygen and the oxygen spillover rate. In Figure 6.6, the evolution of the different products during soot-TPR is shown. In contrast to the H_2-TPR, where bound sulfur is reduced to H_2S before being released in the gas phase, in the case of soot-TPR the bond between SO_4^{2-} and $LaCoO_3$-S is broken by releasing the more reactive oxygen in the soot oxidation. The reaction products are indeed SO_2 and CO_2, whereas almost no CO could be detected, despite oxygen free atmosphere, indicating oxygen spillover (reactions R5-9), in the temperature range between 500-600 °C. The increased sulfate mobility and spillover is also clearly observed during the DRIFTS analysis as the sulfate species rapidly change from surface to bulk sulfate at this temperature (Figure 6.4). The same mechanism occurs during the thermal decomposition as, without soot to accept the active oxygen species, the latter are released first by increasing the temperature before the desorption of SO_2, i.e. it is necessary that strongly bound sulfates decompose to sulfites before the SO_2 desorption. However, during thermal desorption there is no nearby oxygen acceptor and sulfates decomposition requires more energy. As with H_2-TPR, the lattice oxygen species are not available until the sulfur species are removed from the surface. This is evident since with the $LaCoO_3$ catalyst soot oxidation was started at lower temperatures, whereas on $LaCoO_3$-S significant soot oxidation is observed right after SO_2 is released (Figure 6.6).

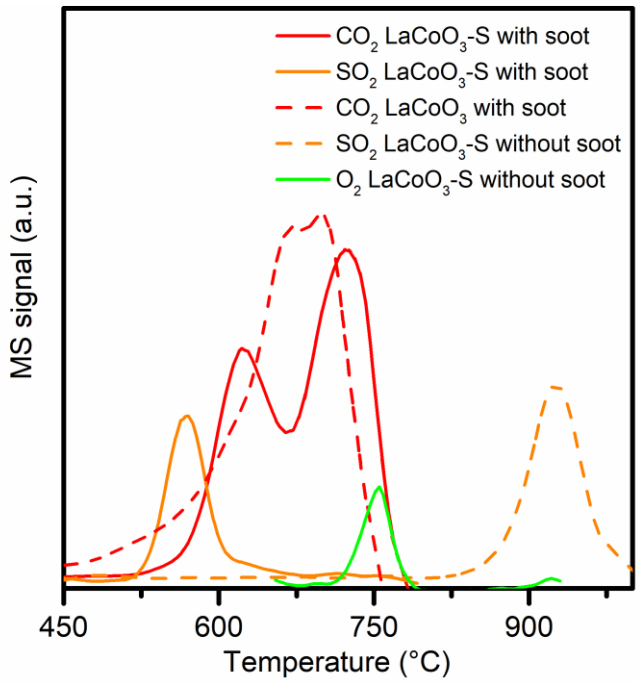

Figure 6.6. Soot-TPR and TPD of the $LaCoO_3$ and $LaCoO_3$-S samples. Reaction conditions: 60 mg of catalyst, 60 mL/min flowrate of Ar, 5 °C/min heating rate. Note that the different product species are not normalized.

As almost all the bound sulfur is released below 600 °C during soot-TPR, the required regeneration temperature is lower than that of H_2 regeneration (see Figure 6.2) as well as of thermal decomposition (above 900 °C). At the same time, the complete reduction and the consequent destruction of the perovskite structure is avoided. The reduction of $LaCoO_3$ and $LaCoO_3$-S by soot (R5-R7) and the thermal decomposition and desorption of sulfates (R8-R9) occur according to the following reactions:

$LaCoO_3\text{-}SO_3 + C \rightarrow LaCoO_3 + SO_2 + CO_2$ R5 (500-600 °C)

$4\ LaCoO_3 + C \rightarrow 4\ LaCoO_{2.5} + CO_2$ R6 (550-700 °C)

$2\ LaCoO_{2.5} + C \rightarrow Co/La_2O_3 + CO_2$ R7 (600-800 °C)

$LaCoO_3\text{-}SO_3 \rightarrow LaCoO_3\text{-}SO_2 + O_2$ R8 (700-800 °C)

$LaCoO_3\text{-}SO_2 \rightarrow LaCoO_3 + SO_2$ R9 (850-1000 °C)

The last phenomenon explored here is not regeneration, but deactivation prevention (Figure 6.7). The $LaCoO_3$ sample was physically mixed with small amounts of $Ca(OH)_2$, an alkaline compound apt to SO_2 capture. When SO_2 contacted with the ($LaCoO_3$ + $Ca(OH)_2$) physical mixture a temporary evolution of NO_2 was observed, as SO_3 substituted the previously adsorbed NO_2 according to reactions R10-12. The initial deactivation rate was fast since $Ca(OH)_2$ mainly adsorbed the oxidized form of SO_x (R8-10). After the initial deactivation stage, the catalyst maintained a stable ca. 50% initial activity for a prolonged time. Even after 6 hours of poisoning, a further decrease in activity was negligible. This method could offer an inexpensive and simple method for the delay and mitigation of deactivation.

The two-phase competitive deactivation was demonstrated more clearly (Figure 6.7B) on pure $LaCoO_3$, which was saturated with NO_x before switching off the NO_x flow and turning on SO_2. A clear evolution of NO_2 was observed upon SO_2 introduction, as the previously adsorbed NO_2 was being replaced by the SO_3 species having higher affinity during the competitive adsorption for the same catalytic active sites. The timespan of this substitution, ca. 20 minutes, corresponded to the timespan of the initial fast deactivation phase.

$Ca(OH)_2 + SO_3 \rightarrow CaSO_4 + H_2O$ R10

$Ca(OH)_2 + 2\ NO_2 \rightarrow Ca(NO_3)_2 + H_2O$ R11

$2\ Ca(NO_3)_2 + 2\ SO_3 \rightarrow 2\ CaSO_4 + 5\ NO_2$ R12

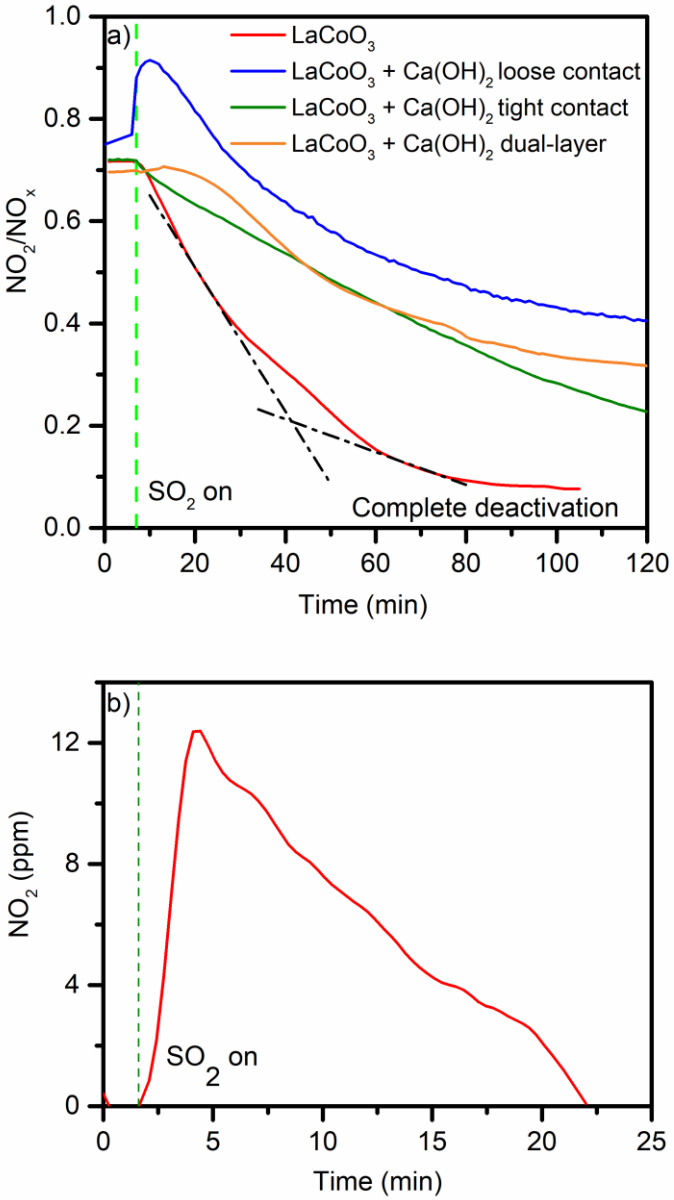

Figure 6.7. a) Deactivation of $LaCoO_3$ as pure and mixed with $Ca(OH)_2$. Reaction conditions: 200 mg catalyst, 100 mg $Ca(OH)_2$, 600 mL/min 500 ppm NO, 4 % O_2, in N_2 and 60 ppm SO_2 when added, T = 300 °C. b) The competitive adsorption of SO_2 on $LaCoO_3$ pre-saturated with NO_x, reaction conditions same as before, T = 200 °C.

6.4. Conclusions

The deactivation of $LaCoO_3$ by SO_2 was investigated under reaction conditions relevant to diesel aftertreatment. Although $LaCoO_3$ had excellent NO oxidation activity, it rapidly deactivated in the presence of SO_2. Investigation of the deactivated sample by XPS showed that sulfur occurred as sulfate species only at the surface, bound to lanthanum rather than to cobalt. As confirmed by DRIFTS and soot-TPR, sulfate mobility and diffusion into the bulk of the perovskite or

spillover to soot starts only above 500 °C and completed at 600 °C. The bound sulfates blocked gradually the active sites required for NO oxidation. After an initial fast deactivation, which can be ascribed to active site blocking, a second (slower) stage followed, during which multilayered lanthanum sulfates formed at the surface of the catalyst following the deactivation scheme proposed in Figure 6.8. The reported activity tests and characterization of the catalyst suggest a two-stage deactivation mechanism: a fast (initial) stage where deactivation occurs by competitive adsorption and *chemical blocking* of the active sites by sulfates, followed by a second (slower) stage where multilayer lanthanum sulfate forms on the catalyst surface *physically blocking* the sites.

Reactivity studies showed that the basic and redox sites on the catalyst were blocked by SO_4^{2-}, and for them to be reactivated, the strongly bound sulfur species had to be removed. Washing with water effectively removed the surface sulfates and the reactivated catalyst regained nearly the initial activity, even after 5 poisoning/regeneration cycles. Mixing small amounts of $Ca(OH)_2$ as an adsorbent delayed the complete deactivation and the catalyst retained nearly half of its initial activity for extended period. This method proved, however, ineffective in completely preventing the initial "fast" stage of the deactivation. Finally, soot was explored as a potential regenerating agent, since one of the main potential uses of $LaCoO_3$ would be in catalyzed diesel particulate filters. The soot acted as an oxygen acceptor from the surface sulfate and effectively released sulfur as SO_2 below 600 °C, a temperature lower than that required for H_2 mediated desulfurization.

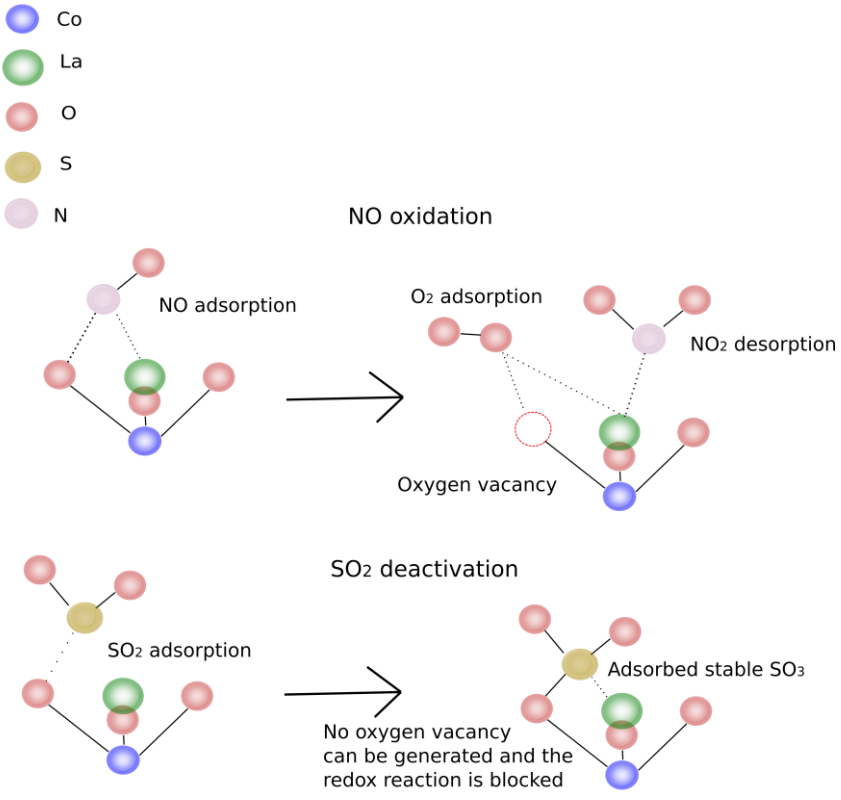

Figure 6.8. Proposed deactivation scheme.

References

[1] J. Zhu, H. Li, L. Zhong, P. Xiao, X. Xu, X. Yang, Z. Zhao and J. Li, ACS Catal., 4 (2014) 2917–2940.

[2] C. Zhou, Z. Feng, Y. Zhang, L. Hu, R. Chen, B. Shan, H. Yin, W. G. Wang and A. Huang, RSC Adv., 5 (2015) 28054–28059.

[3] R. You, Y. Zhang, D. Liu, M. Meng, L. Zheng, J. Zhang and T. Hu, J. Phys. Chem. C, 118 (2014) 25403–25420.

[4] X. He, J. He and M. Meng, Catal. Letters, 141 (2011) 1364–1370.

[5] H. Wang, Z. Zhao, P. Liang, C. Xu, A. Duan, G. Jiang, J. Xu and J. Liu, Catal. Letters, 124 (2008) 91–99.

[6] D. Fino, S. Bensaid, M. Piumetti and N. Russo, Appl. Catal. A Gen., 509 (2016) 75–96.

[7] A. Amberntsson, M. Skoglundh, S. Ljungström and E. Fridell, J. Catal., 217 (2003) 253–263.

[8] D. H. Kim, A. Yezerets, J. Li, N. Currier, H. Y. Chen, H. Hess, M. H. Engelhard, G. G. Muntean and C. H. F. Peden, Catal. Today, 197 (2012) 3–8.

[9] D. H. Kim, J. H. Kwak, J. Szanyi, X. Wang, G. Li, J. C. Hanson and C. H. F. Peden, J. Phys. Chem. C, 113 (2009) 21123–21129.

[10] M. Kurt, Z. Say, K. E. Ercan, E. I. Vovk, C. H. Kim and E. Ozensoy, Top. Catal., 60 (2017) 40–51.

[11] H. Xian, F. L. Li, X. G. Li, X. W. Zhang, M. Meng, T. Y. Zhang and N. Tsubaki, Fuel Process. Technol., 92 (2011) 1718–1724.

[12] H. Wang, Y. Zhu, R. Tan and W. Yao, Catal. Letters, 82 (2002) 199–204.

[13] A. Kumar, M. P. Harold and V. Balakotaiah, J. Catal., 270 (2010) 214–223.

[14] S. Royer, A. Van Neste, R. Davidson, B. McIntyre and S. Kaliaguine, Ind. Eng. Chem. Res., 43 (2004) 5670–5680.

[15] Y. Zhu, R. Tan, J. Feng, S. Ji and L. Cao, Appl. Catal. A Gen., 209 (2001) 71–77.

[16] S. Hodjati, C. Petit, V. Pitchon and A. Kiennemann, Appl. Catal. B Environ., 30 (2001) 247–257.

[17] R. Zhang, H. Alamdari and S. Kaliaguine, Appl. Catal. A Gen., 340 (2008) 140–151.

[18] Q. N. Tran, F. Martinovic, M. Ceretti, S. Esposito, B. Bonelli, W. Paulus, F. Di Renzo, F. A. Deorsola, S. Bensaid and R. Pirone, Appl. Catal. A Gen., 589 (2020) 117304.

[19] B. M. Abu-Zied, S. M. Bawaked, S. A. Kosa and W. Schwieger, J. Nanomater., (2015) 580582.

[20] D. Briggs, Handbook of X-ray Photoelectron Spectroscopy C. D. Wanger, W. M. Riggs, L. E. Davis, J. F. Moulder and G. E.Muilenberg Perkin-Elmer Corp., Physical Electronics Division, Eden Prairie, Minnesota, USA, 1979. 190 pp. $195, 1981, vol. 3.

[21] I. Rosso, G. Saracco and V. Specchia, Korean J. Chem. Eng., 20 (2003) 222–229.

[22] C. Barroo, V. Voorsluijs, T. Visart De Bocarmé, P. Gaspard and Y. De Decker, Phys. Chem. Chem. Phys., 20 (2018) 21302-21312.

[23] X. Shang, G. Hu, C. He, J. Zhao, F. Zhang, Y. Xu, Y. Zhang, J. Li and J. Chen, J. Ind. Eng. Chem., 18 (2012) 513–519.

[24] Y. Yu, C. He, J. Chen, L. Yin, T. Qiu and X. Meng, Catal. Commun., 39 (2013) 78–81.

[25] Y. Wang, D. Ge, M. Chen, S. Gao and Z. Wu, Catal. Commun., 117 (2018) 69–73.

[26] J. McCarthy and J. Holtgreven, in SAE Technical Papers, 2008.

Supplementary material to Chapter 6

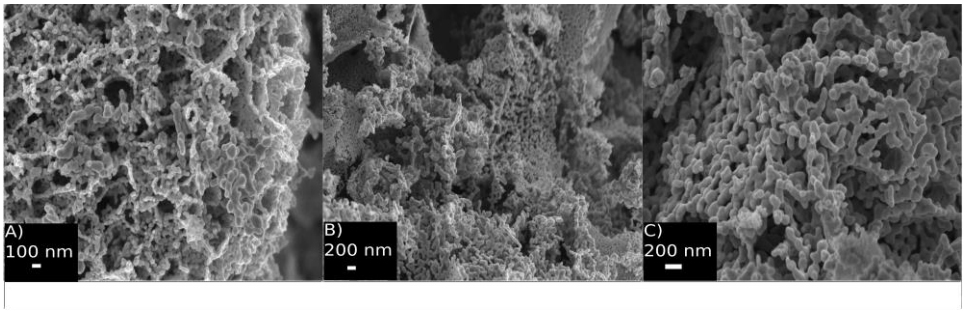

Figure S6.1 SEM images of the a) $LaCoO_3$ b) $LaCoO_3$-S and c) $LaCoO_3$-R5 catalysts.

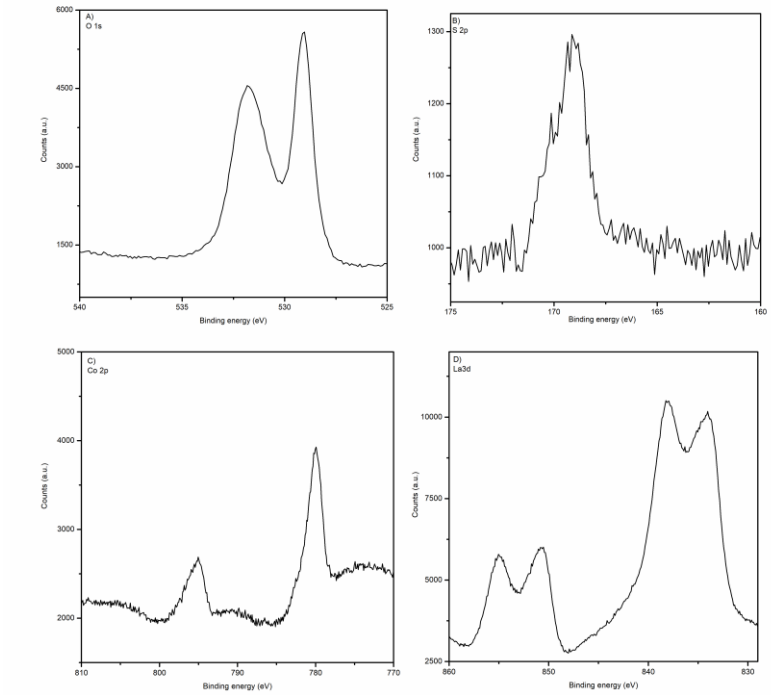

Figure S6.2. XP spectra of the sputtered $LaCoO_3$-S after calcination at 700 °C.

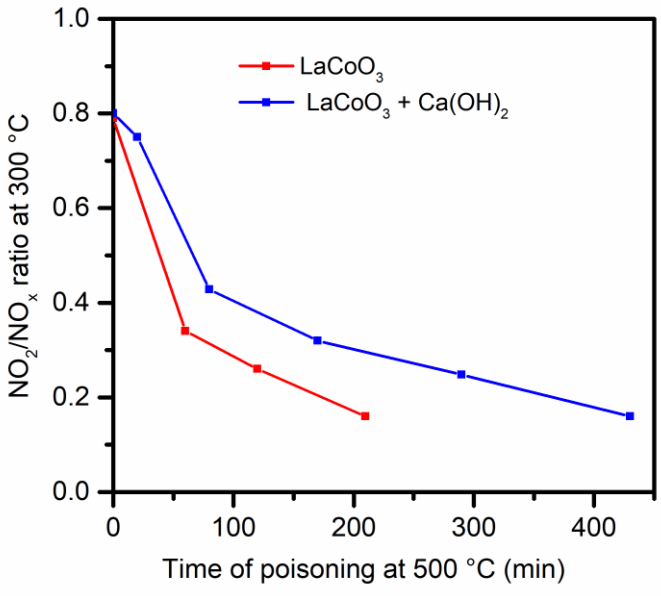

Figure S6.3. Deactivation of $LaCoO_3$ as pure and mixed with $Ca(OH)_2$. Reaction conditions: 200 mg catalyst, 100 mg $Ca(OH)_2$, 600 mL/min 500 ppm NO, 4 % O_2, in N_2 and 60 ppm SO_2 when added, T = 500 °C.